International Journal of Engineering (IJE)

ISSN : 1985-2312

VOLUME 3, ISSUE 6

PUBLICATION FREQUENCY: 6 ISSUES PER YEAR

International Journal of Engineering (IJE)

Volume 3, Issue 6, 2010

Edited By
Computer Science Journals
www.cscjournals.org

Editor in Chief Dr. Kouroush Jenab

International Journal of Engineering (IJE)

Book: 2010 Volume 3, Issue 6

Publishing Date: 31-01-2010

Proceedings

ISSN (Online): 1985-2312

IJE Journal is a part of CSC Publishers

http://www.cscjournals.org

Published in Malaysia

Typesetting: Camera-ready by author, data conversation by CSC Publishing Services – CSC Journals, Malaysia

CSC Publishers

Editorial Preface

This is the sixth issue of volume three of International Journal of Engineering (IJE). The Journal is published bi-monthly, with papers being peer reviewed to high international standards. The International Journal of Engineering is not limited to a specific aspect of engineering but it is devoted to the publication of high quality papers on all division of engineering in general. IJE intends to disseminate knowledge in the various disciplines of the engineering field from theoretical, practical and analytical research to physical implications and theoretical or quantitative discussion intended for academic and industrial progress. In order to position IJE as one of the good journal on engineering sciences, a group of highly valuable scholars are serving on the editorial board. The International Editorial Board ensures that significant developments in engineering from around the world are reflected in the Journal. Some important topics covers by journal are nuclear engineering, mechanical engineering, computer engineering, electrical engineering, civil & structural engineering etc.

The coverage of the journal includes all new theoretical and experimental findings in the fields of engineering which enhance the knowledge of scientist, industrials, researchers and all those persons who are coupled with engineering field. IJE objective is to publish articles that are not only technically proficient but also contains information and ideas of fresh interest for International readership. IJE aims to handle submissions courteously and promptly. IJE objectives are to promote and extend the use of all methods in the principal disciplines of Engineering.

IJE editors understand that how much it is important for authors and researchers to have their work published with a minimum delay after submission of their papers. They also strongly believe that the direct communication between the editors and authors are important for the welfare, quality and wellbeing of the Journal and its readers. Therefore, all activities from paper submission to paper publication are controlled through electronic systems that include electronic submission, editorial panel and review system that ensures rapid decision with least delays in the publication processes.

To build its international reputation, we are disseminating the publication information through Google Books, Google Scholar, Directory of Open Access Journals (DOAJ), Open J Gate, ScientificCommons, Docstoc and many more. Our International Editors are working on establishing ISI listing and a good impact factor for IJE. We would like to remind you that the success of our journal depends directly on the number of quality articles submitted for review. Accordingly, we would like to request your participation by submitting quality manuscripts for review and encouraging your colleagues to submit quality manuscripts for review. One of the great benefits we can provide to our prospective authors is the mentoring nature of our review process. IJE provides authors with high quality, helpful reviews that are shaped to assist authors in improving their manuscripts.

Editorial Board Members
International Journal of Engineering (IJE)

Editorial Board

Editor-in-Chief (EiC)

Associate Editors (AEiCs)

Editorial Board Members (EBMs)

Table of Contents

Volume 3, Issue 6, January 2010.

Pages

Influence of Helicopter Rotor Wake Modeling on Blade Airload Predictions

Christos K. Zioutis zioutis@mech.upatras.gr
Mechanical Engineering and Aeronautics Department University of Patras Rio Patras, 26500, Greece

Apostolos I. Spyropoulos spyrop@mech.upatras.gr
Mechanical Engineering and Aeronautics Department University of Patras Rio Patras, 26500, Greece

Anastasios P. Fragias fragias@mech.upatras.gr
Mechanical Engineering and Aeronautics Department University of Patras Rio Patras, 26500, Greece

Dionissios P. Margaris margaris@mech.upatras.gr
Mechanical Engineering and Aeronautics Department University of Patras Rio Patras, 26500, Greece

Dimitrios G. Papanikas papanikas@mech.upatras.gr
Mechanical Engineering and Aeronautics Department University of Patras Rio Patras, 26500, Greece

Abstract

In the present paper a computational investigation is made about the efficiency of recently developed mathematical models for specific aerodynamic phenomena of the complicated helicopter rotor flowfield. A developed computational procedure is used, based on a Lagrangian type, Vortex Element Method. The free vortical wake geometry and rotor airloads are computed. The efficiency of special models concerning vortex core structure, vorticity diffusion and vortex straining regarding rotor airloads prediction is tested. Investigations have also been performed in order to assess a realistic value for empirical factors included in vorticity diffusion models. The benefit of using multiple vortex line to simulate trailing wake vorticity behind blade span instead of isolated lines or vortex sheets, despite their computational cost, is demonstrated with the developed wake relaxation method. The computational results are compared with experimental data from wind tunnel tests, performed during joined European research programs.

Keywords: Helicopter aerodynamics, rotor wake, vortex core.

1. INTRODUCTION

Computational research on helicopter rotors focuses on blade airloads prediction, trying to identify the effects of important operational, structural and flowfield parameters such as wake formation, blade planform, flight conditions etc on blade vibrations and noise emissions. Improved helicopter performance is a continuous research challenge as aeronautical industry is always seeking for a more efficient, vibration free and "quiet" rotorcraft with increased public acceptance.

The main issue in helicopter aerodynamics examined by many computational and experimental efforts is the interaction of rotor blades with wake vortices, a phenomenon which characterizes helicopters and is the source of blade vibration and noise emission. As in other similar aerodynamic flowfields, such as the trailing wake of aircrafts or wind turbines, the velocity field in the vicinity of a helicopter rotor must be calculated from the vorticity field. A prerequisite for such a calculation is that the physical structure and the free motion of wake vortices are adequately simulated.

Vortex Element Methods (VEM) have been established during recent years computational research as an efficient and reliable tool for calculating the velocity field of concentrated three-dimensional, curved vortices [1,2]. Wake vortices are considered as vortex filaments which are free to move in Lagrangian coordinates. The filaments are descritized into piecewise segments and a vortex element is assigned to each one of them. Since the flow is considered inviscid except for the vortices themselves, the Biot-Savart low is applied in closed-form integration over each vortex element for the velocity field calculation. Marked points are traced on vortex filaments as they move freely due to the mutual-induced velocity field, either by externally imposing geometrical periodicity (relaxation methods) or not (time marching methods). Thus, VEM can computationally reproduce an accurate geometry of the concentrated wake vortices spinning close to rotor disk. As a result the non-uniform induced downwash of lifting helicopter rotors can be computed, which is responsible for rotor blade vibratory airloads.

From the first simplified approaches [3,4], to recent advanced procedures [5-9], the vorticity elements used are vortex lines and vortex sheets [5,10]. The sophistication level of rotor wake analysis can vary from preliminary to advanced manufacture calculations. The basic formulation of VEM is closely related to classical vortex methods for boundary layer and vortical flow analysis extensively applied by Chorin [11], Leonard [12] and other researchers [13,33].

The extensive effort made by a number of researchers has resulted to several models proposed for simulating viscous vortex core structure, vorticity diffusion, trailing vortex rollup process, rotor blade dynamic stall and other phenomena [14]. These different physico-mathematical models have a significant influence on computed blade airload distributions, while their reliability for the majority of helicopter rotor flow conditions is always under evaluation.

The contribution of the work presented here is to investigate the influence of specific aerodynamic models on computed blade airloads, evaluating their reliability by comparisons of computed results with experimental data. In addition, the values of empirical factors included in these models are computationally verified. The applied method consists of a free wake analysis, using a wake-relaxation type VEM [15,16,29] and a coupled airload computation module which has the flexibility to adopt either lifting line or lifting surface methods. Blade motion calculations include provisions for articulated or hingeless blades and the main rigid and elastic flapping modules can be regarded separately or coupled.

When helicopter rotor wakes are simulated, then the line segment discretization of wake vortices is prevailed. Methods with straight [8,10] or curved [6,17] line segments have been proposed and their accuracy was found to be of second order comparing to vortex ring analytical solution [18,19]. Rarely, the distributed vorticity behind the inner part of blade span is modeled by surface elements such as vortex sheets [10]. For the present investigation, a model of multiple trailing lines is adopted and compared with models of simpler discretization.
Viscous effects on wake vorticity have also been the subject of computational and experimental efforts because of their significant impact on induced velocity calculations especially for large wake ages [20-22]. These effects are the vortex core formation in the center of vortex lines and the diffusion of the concentrated vorticity as time progresses. Both of these phenomena are found to be of crucial importance for a reliable wake representation. In the present paper several models are compared, assuming both laminar and turbulent vortex core flow, in order to demonstrate their effectiveness and a parametric investigation is performed concerning empirical factors employed by these models.

The experimental data used for comparisons include test cases executed during cooperative European research programs on rotorcraft aerodynamics and aeroacoustics performed in the open test section of the German-Dutch Wind Tunnel (DNW) The Netherlands [23].

2. AERODYNAMIC FORMULATION

2.1 Rotor Wake Model

The vorticity generated in rotor wake is distinguished regarding its source in two main parts, the trailing and the shed vorticity. Conservation of circulation dictates that the circulation gradients on a rotor blade determine the vorticity shed at specific spanwise locations behind the blade. Thus spanwise circulation variations generate trailing vorticity, g_n, whose direction is parallel to the local flow velocity (Figure 1). On the other hand, azimuthal variations produce shed vorticity radially oriented, g_s, due to the transient periodical nature of the rotor blade flowfield. In general, bound circulation has a distribution as shown in Figure 1, where the pick is located outboard of the semi-span and a steep gradient appears closely to blade tip. This gradient generates a high strength trailing vortex sheet just behind the blade which quickly rolls up and forms a strong tip vortex.

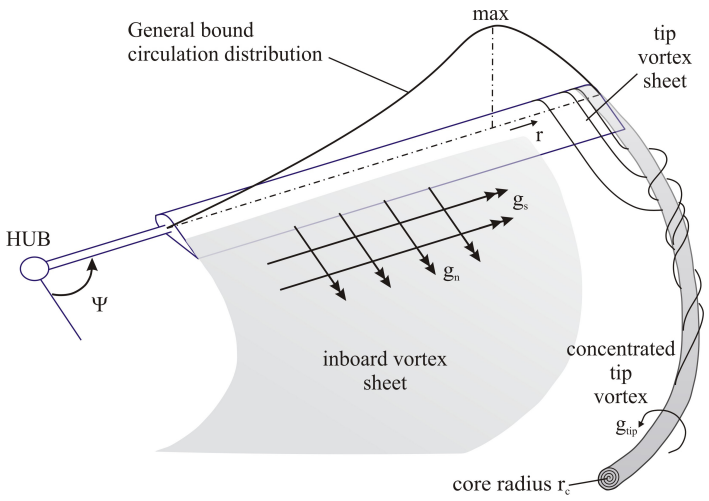

FIGURE 1: Rotor wake physicomathematical modeling.

The continuous distribution of wake vorticity shown in Figure 1 is discretized into a series of vortex elements. Depending on the degree of analysis of wake flowfield and on targeted computational consumption, some VEMs use simple disretization as shown in Figure 2. In this

case, bound circulation is assumed as a linearized distribution, as shown in the figure. According to such an assumption, trailing vorticity emanates from the inner part of blade span and is modeled with vortex sheets extending from A to C. Shed vorticity is modeled either with vortex sheets extending from B to E or with vortex lines parallel to blade span as shown in Figure 2. Vortex line discretization is used for tip vortex, except for the area just behind the blade where a rolling up vortex sheet is used. Roll up is simulated with diminishing vortex sheets together with line segments of correspondingly increasing circulation. This type of discretization simulates the basic features of rotor wake with acceptable accuracy and reduces computational consumption especially when VEMs are used in conjunction with CFD simulations of rotor wake in hybrid schemes.

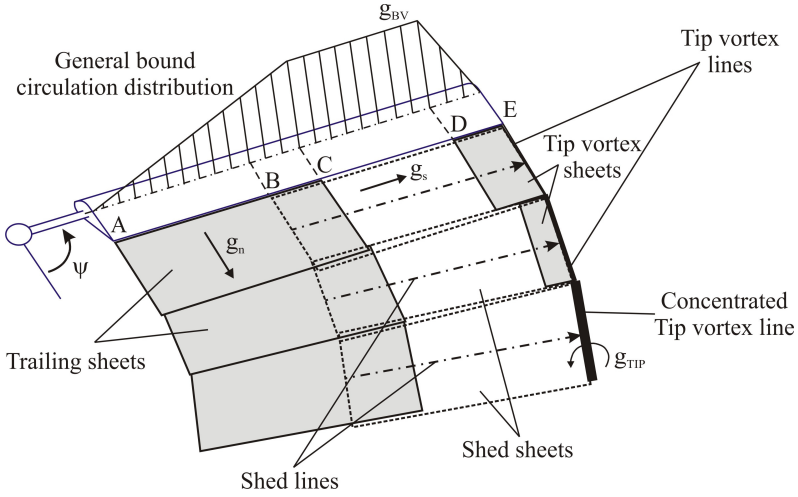

FIGURE 2: Rotor wake simulation, where the trailing wake is represented by vortex sheets, the shed wake either by vortex sheets or vortex lines and the concentrated tip vortex by vortex lines.

Despite the computational efficiency of the above approach, the simplification made in bound circulation distribution can lead to unrealistic results for certain blade azimuth angles. For example, in the cases of reverse flow regions or low advance ratios, where the air hits the rotor blades at the trailing edge or when the rotor blades cut the concentrated tip vortices respectively, a phenomenon known as Blade Vortex Interaction (BVI) is apparent. In these cases the bound circulation distribution departs from the form of Figure 2 and a more detailed discretization is needed in order to catch the specific circulation variations.

In this work, the wake vorticity is discretized in a multitude of trailing and shed vortex lines as shown in Figure 3, in order to simulate the bound circulation distribution in a way that takes into account the fluctuations produced in the majority of blade azimuth angles.

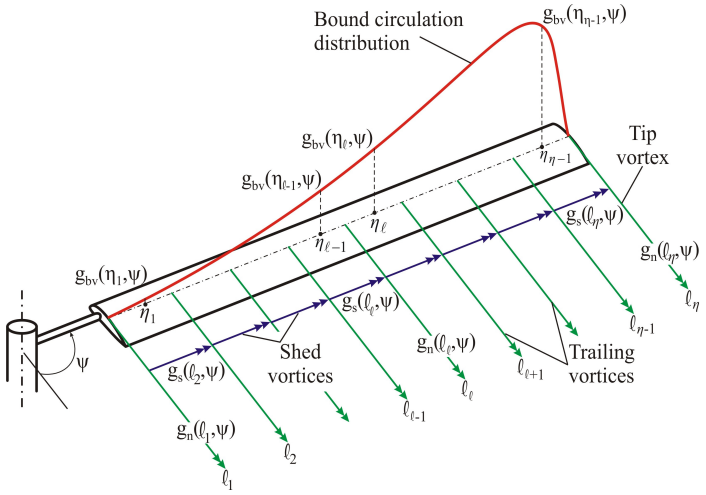

FIGURE 3: Modeling of rotor blade bound circulation distribution and wake vorticity formations with multiple vortex lines.

Trailing vorticity is simulated by n-straight line vortex segments, labeled ℓ_ℓ, which run from ℓ_1 at the root to ℓ_n at the tip. There are η_ℓ=n-1 radial stations where bound circulation is computed, where η_ℓ runs from η_1 between ℓ_1 and ℓ_2 to η_{n-1} between ℓ_{n-1} and ℓ_n. The strength of each segment is equal to the gradient of the bound circulation g_{bv} between two successive radial stations. This means that for all intermediate segments at azimuthal angle ψ:

$$g_n(\ell_\ell,\psi) = g_{bv}(\eta_{\ell-1},\psi) - g_{bv}(\eta_\ell,\psi) \tag{1}$$

The first term is equal to zero at the root because there is no bound circulation inboard the root. Analogically the second term is zero at the tip. The shed vorticity is simulated by n-1 straight line vortex segments which are extended radially between two adjacent trailing vortices as shown in Figure 3. The strength of each segment is equal to the azimuthal variation of bound circulation for each radial station:

$$g_s(\ell_\ell,\psi) = g_{bv}(\eta_{\ell-1},\psi+\Delta\psi) - g_{bv}(\eta_{\ell-1},\psi) \tag{2}$$

where Δψ is the azimuthal step. A number of 50 trailing and shed vortex line segments per azimuthal step were found adequate to discretize the wake vorticity. More detailed discretization will increase computational cost without any tangible improvement of accuracy.

2.2 Induced Velocity Calculation

The distortion of the initial helical geometry of the rotor wake vortices, makes the calculation of the rotor downwash almost impossible with direct numerical integration of the Biot-Savart law, over the actual wake geometry. This procedure is used only for simplified approaches such as the rigid or semi-rigid wake assumptions [3,4]. The utilization of discrete computational elements (vortex lines and sheets) by VEM, converts direct integration in a closed form integration of the Biot-Savart law over the known spatial locations of these elements. The contribution of a vortex line segment i to the induced velocity $\vec{w}_{ij}$ at an arbitrary point in space j, is given by the relation

$$\vec{w}_{ij} = -\frac{1}{4\pi}\int \frac{g_i\left(\vec{r}_{ijm} - k\cdot\vec{e}_k\right)\times d\vec{k}}{\left|\vec{r}_{ijm} - k\cdot\vec{e}_k\right|^3} \tag{3}$$

where $\vec{r}_{ijm}$ is the minimum distance from vortex line i to the point j, $\vec{e}_k$ the unit vector in the direction of the vortex segment, g_i the circulation strength of the vortex segment and k the coordinate measured along the vortex segment. With a reasonable step of discretization, the simplification made to the actual wake geometry can be overcome. After computational investigation the azimuthal step for realistic rotor wake simulations has been proposed by different researchers to be from 2 to 5 degrees [5,32]. The calculation of velocity induced by vortex sheet can be found in [15].

Free vortical wake computation is an iterative procedure, which initiates from rigid wake geometry. Each iteration defines a new position of each vortex element, and takes into account the contribution of all the wake elements to the local flow velocity. At the end of each iteration a new distorted wake geometry is calculated, which is the starting point for the next cycle. This scheme continues until distortion convergence is achieved.

Rotor blade dynamics influence the angle of attack distribution seen by the blade, and therefore alter the bound circulation distribution. Due to out-of-plane motion, rotor blade balances the asymmetry of rotor disk loading. For studying rotor aerodynamics, blade flapwise bending can be represented by a simple mode shape, without significant loss of accuracy [10]. In general the out of plane deflection z(r,t) can be written as a series of normal modes describing the spanwise deformation

$$z(r,t) = \sum_{k=1}^{\infty} n_k(r) q_k(t) \tag{4}$$

where n_κ is the mode shape and $q_\kappa(t)$ is the corresponding degree of freedom. For the developed procedure rigid blade motion and the first flapwise bending mode shape, $n=4r^2-3r$, which is appropriate for blade's basic bending deformation can be used alternatively [15].
By these means a detailed rotor induced downwash distribution is obtained by free wake calculations. Sequentially, the blade section angle of attack distribution is computed by

$$\alpha(r,\psi) = \theta(r) - tan^{-1}(u_P/u_T) \tag{5}$$

where u_P is the air velocity perpendicular to No Feathering Plane (NFP), which includes nonuniform rotor downwash, u_T is the tangential velocity to blade airfoil, both normalized by the rotor tip speed ΩR, and θ(r) is the collective pitch angle (since NFP is taken as reference). With known angle of attack and local velocity, a blade-element type methodology is applied for blade section lift calculations. The above computational procedure is extensively documented in [15].

2.3 Vortex Core Structure

As mentioned above, rotor induced velocity calculation is based on potential field solution such as Biot-Savart law. Due to the absence of viscosity, the induced velocity calculated at a point lying very close to a vortex segment, tends to be infinite which is unrealistic. In order to remove such singularities and model the effects of viscosity in a convenient way the vortex core concept is introduced. A great deal of the current knowledge about the role of viscosity in a vortex core has been derived mainly from experimental measurements. As a result empirical relations are commonly used for the vortex core radius, the velocity distribution at the core region and the viscous core growth.
The core radius is defined as the distance from the core center where the maximum tangential velocity is observed. A corresponding expression for the radial circulation distribution inside the core region is introduced in the computations, which alters the velocity induced from a vortex element. Outside the core region the induced velocity has an approximately potential distribution which tends to coincide with the Biot-Savart distribution fairly away from the vortex line.

Several algebraic models for the vortex induced velocity have been introduced due to their simplicity and computational efficiency in engineering applications [24-26]. According to Vatistas [26] a series of tangential velocity profiles in the vortex core is given by the relation

$$V_\theta(r) = \frac{g\, r}{2\pi\left(r_c^{2n} + r^{2n}\right)^{1/n}} \tag{6}$$

where g is the circulation of the vortex line, n is an integer variable, r is the radial distance from the vortex center and r_c is the core radius. Using this relation for different values of n, the velocity r profiles of some well-known core models can be derived using the nondimensional radius $\bar{r} = r/r_c$ For n=1 the core model suggested by Scully and Sullivan [27] is derived

$$V_\theta(\bar{r}) = \frac{g}{2\pi r_c}\frac{\bar{r}}{(1+\bar{r}^2)} \tag{7}$$

For n=2 the model proposed by Bagai-Leishman in [32] is derived

$$V_\theta(\bar{r}) = \frac{g}{2\pi r_c}\frac{\bar{r}}{\sqrt{1+\bar{r}^4}} \tag{8}$$

Taking these models into account, the present investigation also applies the Rotary Wing vortex model [10] and of the Lamb-Oseen model [28] for the representation of the vortex core structure.

2.4 Core Growth

Unlike airplanes, helicopter rotors remain in close proximity to their tip vortices, more so in descent and maneuvers. This feature leads to close encounters of rotor blades with tip vortices, which as already mentioned are known as blade vortex interactions or BVIs. As a consequence, it is important to understand not only the initial core size after roll-up, but also the subsequent growth of the vortex core [29].

The effect of diffusion on tip vortices is taken into account by increasing the vortex core radius and decreasing its vorticity as time advances. The simplest viscous vortex is the Lamb-Oseen vortex model. This is a two-dimensional flow with circular symmetry in which the streamlines are circles around the vortex filament. The vorticity vector is parallel to the vortex filament and a function of radial distance r and time t. Solving the Navier-Stokes equations for this case an exact solution for the tangential or swirl velocity surrounding the vortex filament arises as

$$V_\theta(r) = \frac{g_{TIP}}{2\pi r}\left(1 - e^{-r^2/4vt}\right) \tag{9}$$

where g_{TIP} is the tip vortex strength and v is the kinematic viscosity. The core growth with time, predicted by the Lamb-Oseen model is given by

$$r_{diff}(t) = 2.24181\sqrt{vt} \tag{10}$$

This result came up by differentiating equation 9 with respect to r and setting the derivative to zero. The Lamb-Oseen vortex can be regarded as the "desingularisation" of the rectilinear line vortex, in which the vorticity has a delta-function singularity.
Squire [30] showed that the solution for a trailing vortex is identical to the Lamb-Oseen solution. So the downstream distance z from the origin of the vortex can be related to time as $t=z/V_4$. In order to account for effects on turbulence generation, Squire introduced an eddy viscosity coefficient δ. In the case of a helicopter rotor, time t is related to the wake age δ_ℓ as $\delta_\ell = \Omega t$, where Ω is the angular velocity of the rotor. Thus, including these parameters equation 10 can be written as

$$r_{diff}(\delta_\ell) = 2.24181\sqrt{\delta v\left(\frac{\delta_\ell + \delta_0}{\Omega}\right)} \tag{11}$$

In the above equation δ_0 is an effective origin offset, which gives a finite value of the vortex core radius at the instant of its generation ($\delta_\ell=0$) equals to

$$r_{diff}(\delta_\ell = 0) \equiv r_0 = 2.24181\sqrt{\delta v\left(\frac{\delta_0}{\Omega}\right)} \tag{12}$$

At this work δ_0 was selected to have an age between 15° and 30°. According to Squire, the eddy viscosity coefficient is proportional to the vortex Reynolds number Re_v and equals to

$$\delta = 1 + a_S\, Re_v \tag{13}$$

where a_s is the Squire's parameter and its value is determined from experimental measurements. A phenomenon often opposing vortex diffusion is the straining of vortex filaments due to their freely distorted geometry. In fact the steep gradients of wake induced velocities cause them to stretch or to squeeze and their core radius to decrease or to increase correspondingly. For straining effects, the following fraction is defined

$$\varepsilon = \frac{\Delta\ell}{\ell} \tag{14}$$

as the strain imposed on the filament over the time interval Δt, where Δℓ is the deformation from its initial length ℓ. Now assume that the filament has a core radius $r_{diff}(\delta_\ell)$ at time δ_ℓ. At time $\delta_\ell+\Delta\psi$ the filament will have a core radius $r_{diff}(\delta_\ell+\Delta\psi)-\Delta r_{diff}(\delta_\ell)=r_{strain}$ because of straining. Applying the principle of conservation of mass leads to the following result

$$r_{strain}(\delta_\ell + \Delta\psi) = r_{diff}(\delta_\ell)\frac{1}{\sqrt{1+\varepsilon}} \tag{15}$$

Combining equations (11) and (15) a vortex core radius including both diffusion and straining effects can be defined as

$$r_c(\delta_\ell) = r_{diff}(\delta_\ell) - r_{strain}(\delta_\ell) = r_{diff}(\delta_\ell) - r_{diff}(\delta_\ell - \Delta\psi)\frac{1}{\sqrt{1+\varepsilon}} \qquad (16)$$

3. RESULTS AND DISCUSSION

Table 1 summarizes the basic parameters of the test cases used at the present work. For all of the test cases the rotor blade radius and the chord length were equal to 2.1 m and 0.14 m respectively.

TABLE 1: Basic parameters of the experimental flight test cases used at the present work.

Test Case	Advance Ratio μ	Tip Path Plane Angle a_{TPP}	Thrust Coefficient C_T	Tip Mach Number M_{TIP}	Type of Flight
1	0.168	6.0°	0.0069	0.616	Ascent
2	0.264	3.0°	0.0071	0.662	Ascent
3	0.166	-1.8°	0.0069	0.617	Descent
4	0.166	-5.7°	0.0070	0.617	Descent

Table 2 shows three different wake models which are compared for the present work. Each of these wake models has been tested with the developed computational procedure and its influence on the rotor aerodynamic forces has been studied.

TABLE 2: Different wake models used for rotor wake simulation.
SLV = Straight Line Vortex, VS = Vortex Sheet

Wake Model	Shed Wake	Inboard Wake	Tip Vortex
1	50 SLV	50 SLV	1 SLV
2	1 SLV	VS	1 SLV
3	VS	VS	1 SLV

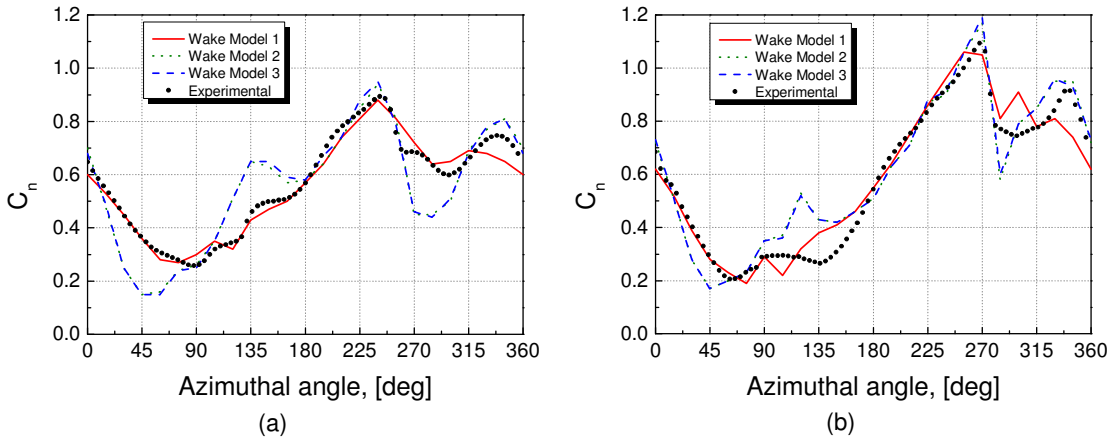

FIGURE 4: Influence of different wake models on the normal force coefficient at radial station 0.82 for two climb cases with different advance ratio, (a) Test Case 1, μ=0.168, (b) Test Case 2, μ=0.268.

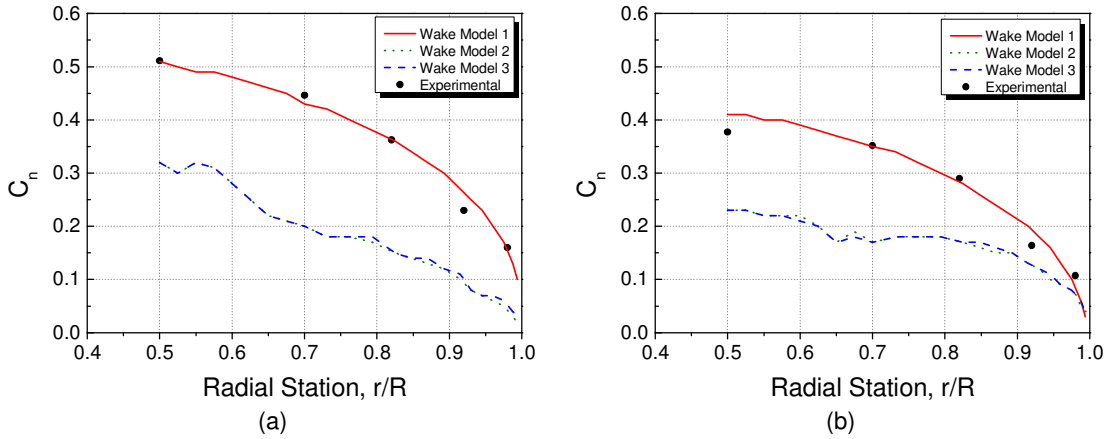

FIGURE 5: Influence of different wake models on the normal force coefficient at azimuth angle $\Psi=45^o$ for two climb cases with different advance ratio, (a) Test Case 1, $\mu=0.168$, (b) Test Case 2, $\mu=0.268$.

In Figure 4 the resulting azimuthal distribution of normal force coefficient C_n is compared with experimental data for the first two test cases of Table 1. For the same test cases the radial distribution of normal force coefficient C_n is compared with experimental data as shown in Figure 5.

It is evident from these figures that representing the total rotor wake with n-straight line vortices is preferable than using vortex sheets for trailing or shed wake. Especially at rotor disk areas where Blade Vortex Interaction phenomena are likely to occur, as for azimuth angles 90^o to 180^o and 270^o to 360^o, wake model 1 gives substantially better results because the existing fluctuations of bound circulation distribution are adequate simulated. For the test cases shown, radial airloads distribution also differs at 45^o where the results of wake model 1 follow closely the experimental values. For this reason wake model 1 is used hereafter.

Another observation is that wake models 2 and 3 give better results by the increment of the advance ratio, which demonstrates that helicopter rotor wake representation could be simpler for high speed flights, saving extra computational time. On the other hand an elaborate rotor wake model is crucial for low speed flights.

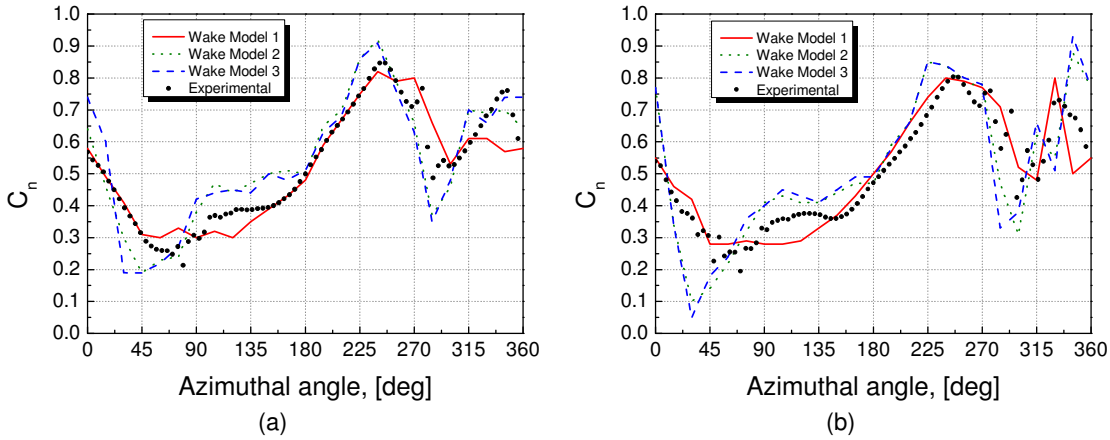

FIGURE 6: Influence of different wake models on the normal force coefficient at radial station 0.82 for two descent cases with different TPP angle, (a) Test Case 3, $a_{TPP}=-1.8^o$, (b) Test Case 4, $a_{TPP}=-5.7^o$.

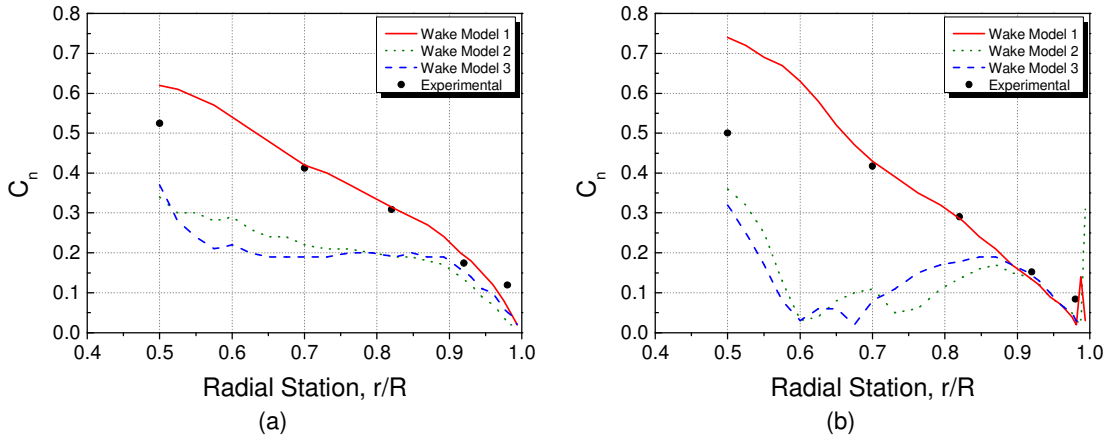

FIGURE 7: Influence of different wake models on the normal force coefficient at azimuth angle $\Psi=45^{o}$ for two descent cases with different TPP angle, (a) Test Case 3, $a_{TPP}=-1.8^{o}$, (b) Test Case 4, $a_{TPP}=-5.7^{o}$.

In Figures 6 and 7 the azimuthal and radial distribution of normal force coefficient respectively is compared with experimental data for test cases 3 and 4 of Table 1. The multiple vortex lines model gave better results than the other two wake models although there is considerable deviation from the experimental data especially for test case 4, where $a_{TPP}=-5.7^{o}$. This is due to the intensive Blade Vortex Interactions (BVI) occurred at descent flight cases and especially at the specific region of TPP angle, as demonstrated from wind tunnel results [16,23].

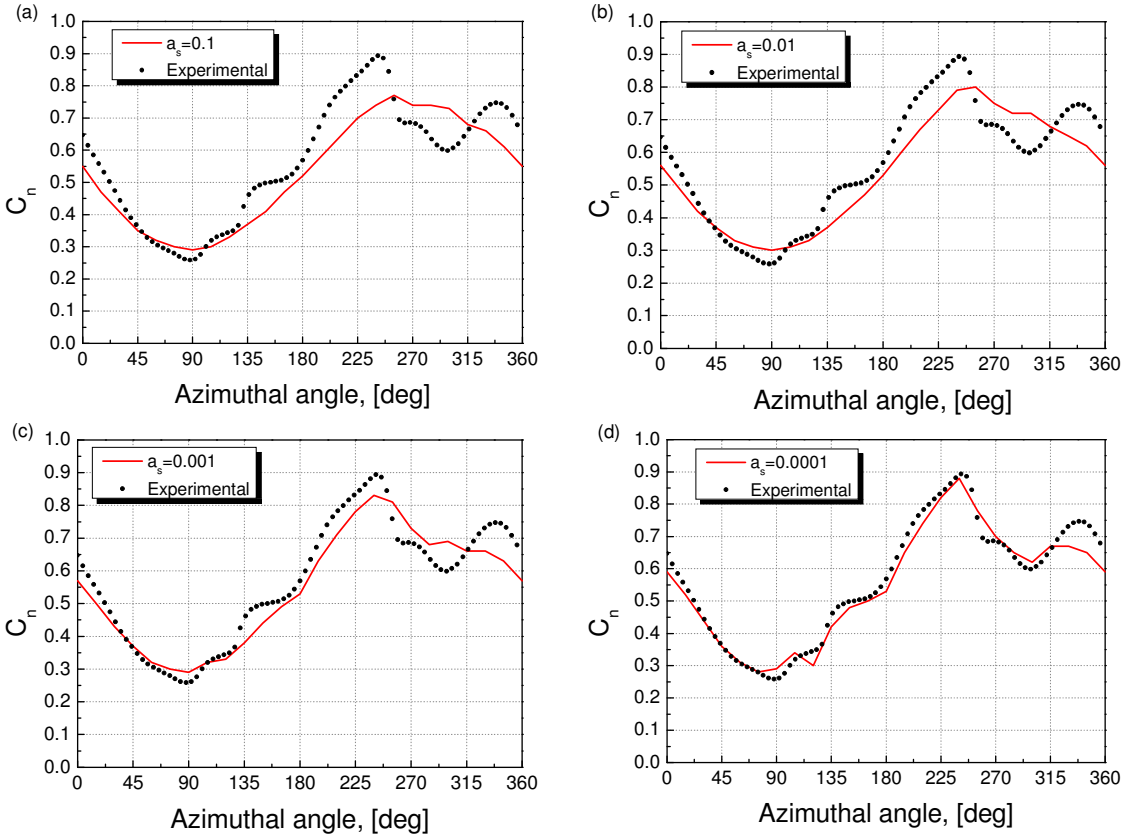

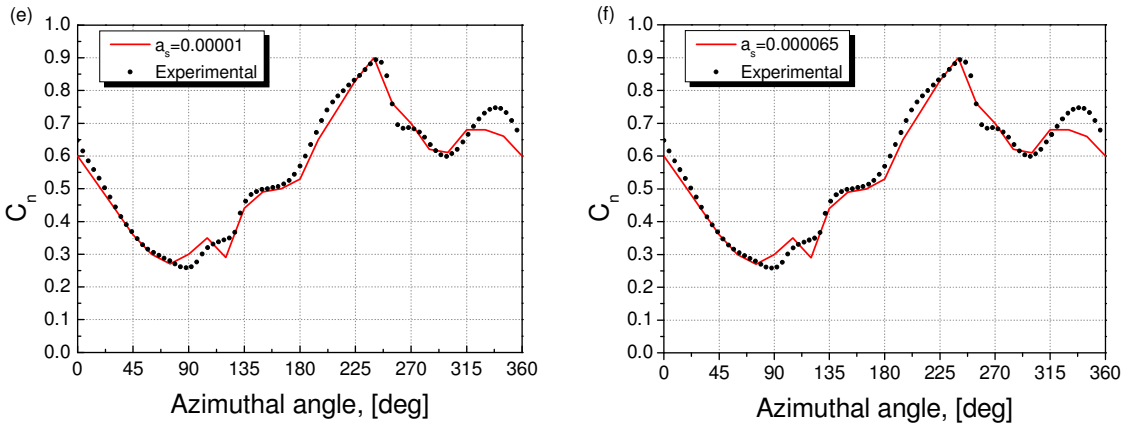

FIGURE 8: Computational investigation for the definition of Squire's parameter a_s. The diagrams correspond to the test case 1 flight conditions.

As mentioned before in order to include diffusion effects in the vortex core, Squire's parameter a_s must be defined. For this purpose a computational investigation has been done for the derivation of an acceptable value of a_s.

Figure 8 shows the azimuthal distribution of the normal force coefficient for several values of a_s varying from 10^{-1} to 10^{-5}. Comparing the computed results with the corresponding experimental ones for test case 1, a value of the order 10^{-4} to 10^{-5}, as indicated in diagrams (d) and (e) in Figure 8, seems to achieve best results. This value for a_s has also been suggested by Leishman [31]. At this work a value of 0.000065 was selected for a_s as shown in the diagram (f) in Figure 8.

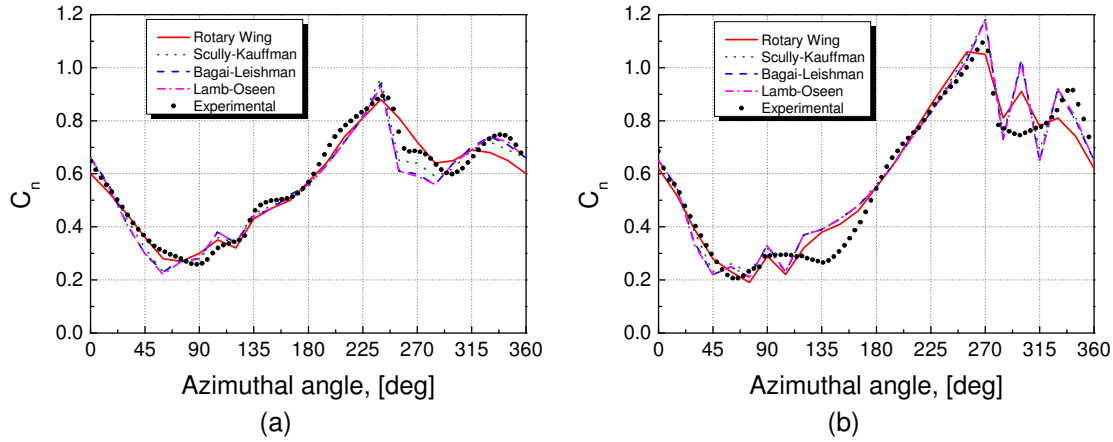

FIGURE 9: Influence of different core models on the normal force coefficient at radial station 0.82 for two climb cases with different advance ratio, (a) Test Case 1, μ=0.168, (b) Test Case 2, μ=0.268.

Having found an appropriate value for a_s, several core models are applied to simulate the tip vortex core structure. In Figures 9 and 10 the azimuthal and radial distribution of normal force coefficient respectively is compared with experimental data for test cases 1 and 2 as presented in Table 1. Four different core models are tested. As expected, Scully-Kauffman, Bagai-Leishman and Lamb-Oseen core models give about the same results. This is due to the fact that these core models were obtained from the same series family proposed by Vatistas. The rotary wing gave better results than the other three core models, demonstrating that this model is suitable for helicopter climb test cases.

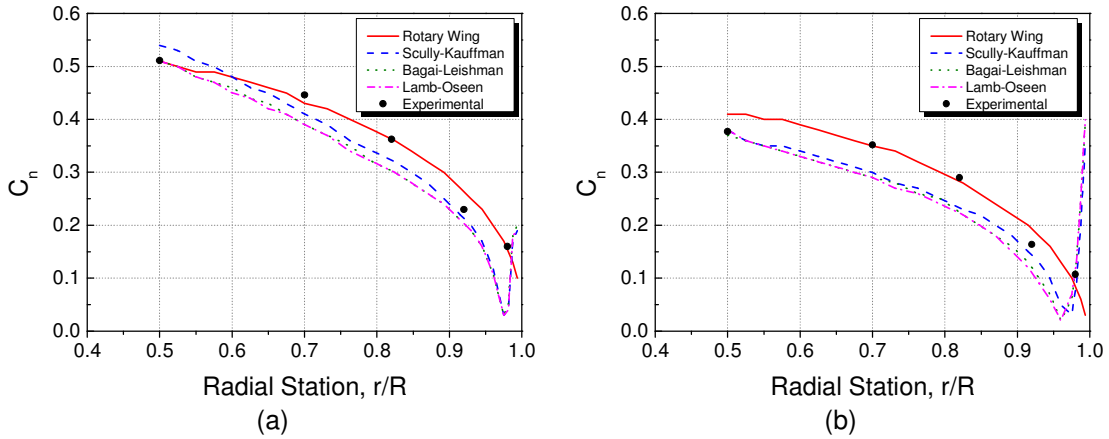

FIGURE 10: Influence of different core models on the normal force coefficient at azimuth angle $\Psi=45^o$ for two climb cases with different advance ratio, (a) Test Case 1, $\mu=0.168$, (b) Test Case 2, $\mu=0.268$.

The same core models were applied for the two descent test cases 3 and 4 (Table 1). As shown in Figure 11 all core models give about the same overall results, underestimating the value of C_n at azimuthal angles between 90^o and 135^o. The three core models which belong to the same series family fit better to the experimental data than the rotary wing, for azimuthal angles between 315^o and 360^o. Also from Figure 12 seems that these models correspond better to the experimental data and especially for the second descent test case, as shown in Figure 12b where intense BVI phenomena occurred as mentioned previously. Due to its simplicity the Scully-Kauffman core model is an option, but in order to include diffusion and straining effects the Lamb-Oseen model is preferable.

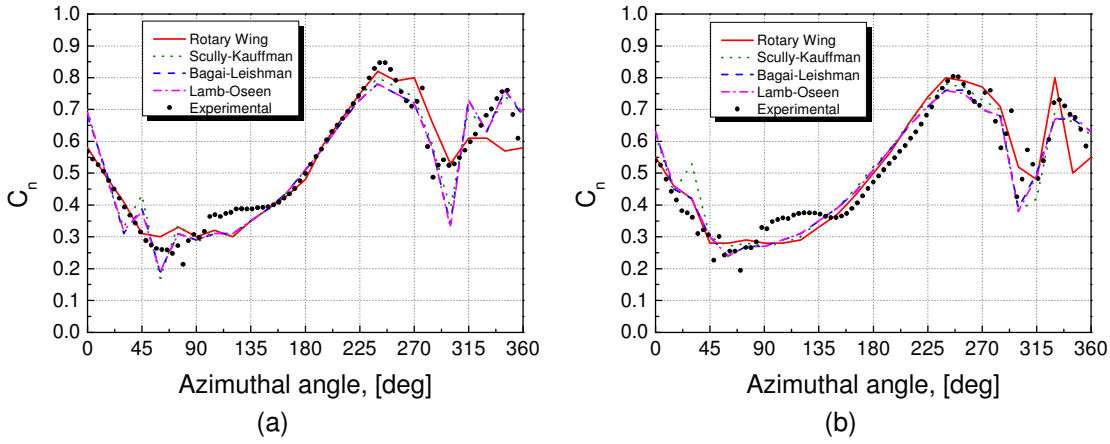

FIGURE 11: Influence of different core models on the normal force coefficient at radial station 0.82 for two descent cases with different TPP angle, (a) Test Case 3, $a_{TPP}=-1.8^o$, (b) Test Case 4, $a_{TPP}=-5.7^o$.

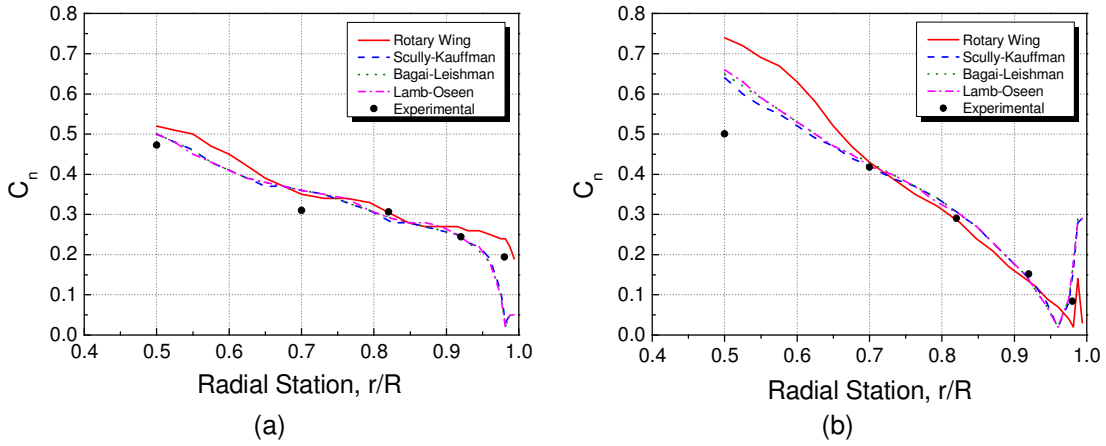

FIGURE 12: Influence of different wake models on the normal force coefficient at azimuth angle $\Psi=45^o$ for two descent cases with different TPP angle, (a) Test Case 3, $a_{TPP}=-1.8^o$, (b) Test Case 4, $a_{TPP}=-5.7^o$.

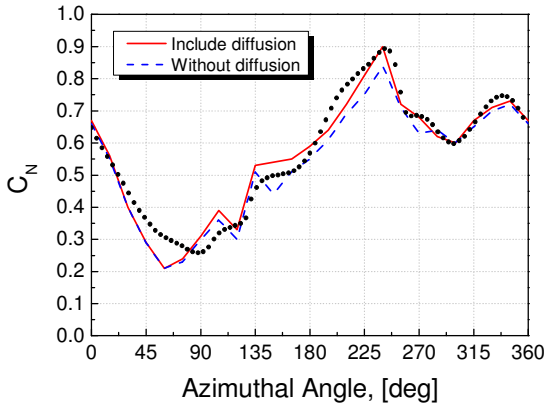

FIGURE 13: Comparison of experimental and computed azimuthal distribution of normal force coefficient C_n for the test case 1 flight conditions, when diffusion effects are included and neglected respectively.

The importance of diffusion effects was also studied. Using the Lamb-Oseen model for the straight line tip vortex core structure, a comparison is made between experimental and computed C_n for the cases where diffusion effects are included and neglected respectively. The diagram in Figure 13 shows that better results can be obtained when diffusion effects are included, although the differences are small.

An effort was also made in order to include straining effects at the tip vortex core growth. This phenomenon is often opposing diffusion as already mentioned. Figure 14 shows the computed azimuthal distribution of C_n for the cases where straining effects are included and neglected respectively. The results are compared with experimental data. For the current test case it seems that straining effects do not play an important role as diffusion.

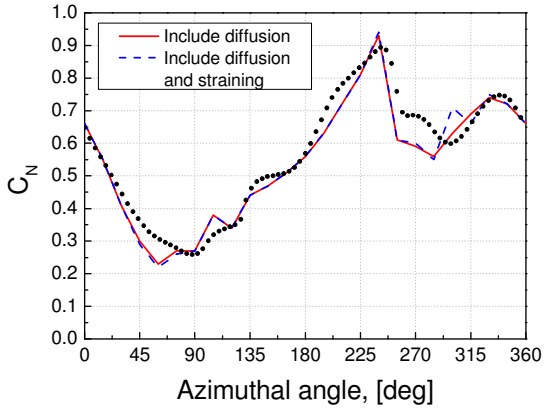

FIGURE 14: Comparison of experimental and computed azimuthal distribution of normal force coefficient C_n for the test case 1 flight conditions, when straining effects are included and neglected respectively.

4. CONSLUSIONS

A computational model for the simulation of helicopter rotor wake has been developed using multiple trailing vortex lines. Diffusion and straining effects of the tip vortex have been appropriate incorporated in order to investigate their influences. To include viscous effects several core models have been tested.

The conclusions from this study are summarized as follows:

1. Despite the extra computational cost, simulating the rotor wake by multiple trailing vortex lines is preferable than using vortex sheets for the inboard or the shed wake. This is crucial especially for low speed helicopter flight.
2. In order to include diffusion effects, Squire's parameter a_s has been found to be of the order of 10^{-4} to 10^{-5}. At this work a value equal to 0.000065 was selected.
3. The rotary wing core model seems to be more suitable for helicopter climb flight cases.
4. For descent flight cases, where intense BVI phenomena occurred, the Lamb-Oseen core model is preferable due to its ability to include diffusion and straining effects. The Scully-Kauffman core model is an option because of its simplicity.
5. Diffusion effects are important on the calculation of helicopter rotor aerodynamic forces, but straining effects do not influence computational results as much as diffusion.

5. REFERENCES

1. W. Johnson. "*Rotorcraft aerodynamics models for a comprehensive analysis"*. Proceedings of 54th Annual Forum of American Helicopter Society, Washington, DC, May 20-22, 1998.
2. G. J. Leishman, M. J. Bhagwat and A. Bagai. "*Free-vortex filament methods for the analysis of helicopter rotor wakes"*. Journal of Aircraft, 39(5):759-775, 2002.
3. T. A. Egolf and A. J. Landgrebe. "*A prescribed wake rotor inflow and flow field prediction analysis"*. NASA CR 165894, June 1982.
4. T. S. Beddoes. "*A wake model for high resolution airloads*". Proceedings of the 2nd International Conference on Basic Rotorcraft Research, Univ. of Maryland, College Park, MD, 1985.
5. M. J. Bhagwat and G. J. Leishman. "*Stability, consistency and convergence of time-marching free-vortex rotor wake algorithms*". Journal of American Helicopter Society, 46(1):59-71, 2001.
6. T. R. Quackenbush, D. A. Wachspress and Boschitsch. "*Rotor aerodynamic loads computation using a constant vorticity contour free wake model*". Journal of Aircraft, 32(5):911-920, 1995.
7. K. Chua and T.R. Quackenbush. "*Fast three-dimensional vortex method for unsteady wake calculations*". AIAA Journal, 31(10):1957-1958, 1993.

8. M. J. Bhagwat and G. J. Leishman. "*Rotor aerodynamics during manoeuvring flight using a time-accurate free vortex wake*". Journal of American Helicopter Society, 48(3):143-158, 2003.
9. G. H. Xu and S. J. Newman. "*Helicopter rotor free wake calculations using a new relaxation technique*". Proceedings of 26th European Rotorcraft Forum, Paper No. 37, 2000.
10. M. P. Scully. "*Computation of helicopter rotor wake geometry and its influence on rotor harmonic airloads*". ASRL TR 178-1, 1975
11. A. J. Chorin. "*Computational fluid mechanics*". 1st edition, Academic Press, (1989).
12. T. Leonard. "*Computing three dimensional incompressible flows with vortex elements*". Annual Review of Fluid Mechanics, 17: 523-559, 1985.
13. T. Sarpkaya. "*Computational methods with vortices - The 1988 Freeman scholar lecture*". ASME Journal of Fluids Engineering, 111(5):5-52, March 1989.
14. N. Hariharan and L. N. Sankar. "*A review of computational techniques for rotor wake modeling*". Proceedings of AIAA 38th Aerospace Sciences Meeting, AIAA 00-0114, Reno NV, 2000.
15. A. I. Spyropoulos, A. P. Fragias, D. G. Papanikas and D. P. Margaris. "*Influence of arbitrary vortical wake evolution on flowfield and noise generation of helicopter rotors*". Proceedings of the 22nd ICAS Congress, Harrogate, United Kingdom, 2000.
16. A. I. Spyropoulos, C. K. Zioutis, A. P. Fragias, E. E. Panagiotopoulos and D. P. Margaris. "*Computational tracing of BVI phenomena on helicopter rotor disk*". International Review of Aerospace Engineering (I.RE.AS.E), 2(1):13-23, February 2009.
17. D. B. Bliss, M. E. Teske and T. R. Quackenbush. "*A new methodology for free wake analysis using curved vortex elements*". NASA CR-3958, 1987.
18. S. Gupta and G. J. Leishman. "*Accuracy of the induced velocity from helicoidal vortices using straight-line segmentation*". AIAA Journal, 43(1):29-40, 2005.
19. D. H. Wood and D. Li. "*Assessment of the accuracy of representing a helical vortex by straight segments*". AIAA Journal, 40(4):647-651, 2005.
20. M. Ramasamy, G. J. Leishman. "*Interdependence of diffusion and straining of helicopter blade tip vortices*". Journal of Aircraft, 41(5):1014-1024, 2004.
21. C. Tung and L. Ting. "*Motion and decay of a vortex ring*". Physics of Fluids, 10(5):901-910, 1967.
22. J. A. Stott and P. W. Duck. "*The effects of viscosity on the stability of a trailing-line vortex in compressible flow*". Physics of Fluids, 7(9):2265-2270, 1995.
23. W. R. Splettstoesser, G. Niesl, F. Cenedese, F. Nitti and D. G. Papanikas. "*Experimental results of the European HELINOISE aeroacoustic rotor test*". Journal of American Helicopter Society, 40(2):3-14, 1995.
24. S. E. Windnall and T. L. Wolf. "*Effect of tip vortex structure on helicopter noise due to blade vortex interactions*". AIAA Journal of Aircraft, 17(10):705-711, 1980.
25. J. M. Bhagwat and G. J. Leishman. "*Correlation of helicopter rotor tip vortex measurements*". AIAA Journal, 38(2):301-308, 2000.
26. G. H. Vatistas, V. Kozel and W. C. Mih. "*A simpler model for concentrated vortices*". Experiments in Fluids, 11(1):73-76, 1991.
27. M. P. Scully and J. P. Sullivan. "*Helicopter rotor wake geometry and airloads and development of laser Doppler velocimeter for use in helicopter rotor wakes*". Massachusetts Institute of Technology Aerophysics Laboratory Technical Report 183, MIT DSR No. 73032, 1972.
28. G. K. Batchelor, "*Introduction to fluid dynamics*". Cambridge University Press, (1967).
29. C. K Zioutis, A. I. Spyropoulos, D. P. Margaris and D. G. Papanikas. "*Numerical investigation of BVI modeling effects on helicopter rotor free wake simulations*". Proceedings of the 24th ICAS Congress, 2004, Yokohama, Japan.
30. H. B. Squire. "*The growth of a vortex in turbulent flow*". Aeronautical Quarterly, 16(3):302-306, 1965.
31. J. M. Bhagwat and G. J. Leishman. "*Generalized viscous vortex model for application to free-vortex wake and aeroacoustic calculations*". Proceedings of American Helicopter Society 58th Annual Forum and Technology Display, Montreal, Canada, 2002.

32. G. J. Leishman, A. Baker and A. Coyne *"Measurements of rotor tip vortices using three-component laser doppler velocimetry"*. Journal of American Helicopter Society, 41(4):342-353, 1996.
33. C. Golia, B. Buonomo and A. Viviani. "*Grid Free Lagrangian Blobs Vortex Method with Brinkman Layer Domain Embedding Approach for Heterogeneous Unsteady Thermo Fluid Dynamics Problems".* International Journal of Engineering, 3(3):313-329, 2009.

CFD Transonic Store Separation Trajectory Predictions with Comparison to Wind Tunnel Investigations

Elias E. Panagiotopoulos hpanagio@mech.upatras.gr
Hellenic Military Academy
Vari, Attiki, 16673, Greece

Spyridon D. Kyparissis kyparis@mech.upatras.gr
Mechanical Engineering and
Aeronautics Department
University of Patras
Patras, Rio, 26500, Greece

Abstract

The prediction of the separation movements of the external store weapons carried out on military aircraft wings under transonic Mach number and various angles of attack is an important task in the aerodynamic design area in order to define the safe operational-release envelopes. The development of computational fluid dynamics techniques has successfully contributed to the prediction of the flowfield through the aircraft/weapon separation problems. The numerical solution of the discretized three-dimensional, inviscid and compressible Navier-Stokes equations over a dynamic unstructured tetrahedral mesh approach is accomplished with a commercial CFD finite-volume code. A combination of spring-based smoothing and local remeshing are employed with an implicit, second-order upwind accurate Euler solver. A six degree-of-freedom routine using a fourth-order multi-point time integration scheme is coupled with the flow solver to update the store trajectory information. This analysis is applied for surface pressure distributions and various trajectory parameters during the entire store-separation event at various angles of attack. The efficiency of the applied computational analysis gives satisfactory results compared, when possible, against the published data of verified experiments.

Keywords: CFD Modelling, Ejector Forces and Moments, Moving-body Trajectories, Rigid-body Dynamics, Transonic Store Separation Events.

1. INTRODUCTION

With the advent and rapid development of high performance computing and numerical algorithms, computational fluid dynamics (CFD) has emerged as an essential tool for engineering and scientific analyses and design. Along with the growth of computational resources, the complexity of problems that need to be modeled has also increased. The simulation of aerodynamically driven, moving-body problems, such as store separation, maneuvering aircraft, and flapping-wing flight are important goals for CFD practitioners [1].

The aerodynamic behavior of munitions or other objects as they are released from aircraft is critical both to the accurate arrival of the munitions and the safety of the releasing aircraft [2]. In

the distant past separation testing was accomplished solely using flying tests. This approach was very time-consuming, often requiring years to certify a projectile. It was also expensive and occasionally led to the loss of an aircraft due to unexpected behavior of the store being tested.

In the past, separation testing was accomplished solely via flight tests. In addition to being very time consuming, often taking years to certify a weapon, this approach was very expensive and often led to loss of aircraft. In the 1960s, experimental methods of predicting store separation in wind tunnel tests were developed. These tests have proven so valuable that they are now the primary design tool used. However, wind tunnel tests are still expensive, have long lead times, and suffer from limited accuracy in certain situations, such as when investigating stores released within weapons bays or the ripple release of multiple moving objects. In addition, because very small-scale models must often be used, scaling problems can reduce accuracy.

In recent years, modelling and simulation have been used to reduce certification cost and increase the margin of safety of flight tests for developmental weapons programs. Computational fluid dynamics (CFD) approaches to simulating separation events began with steady-state solutions combined with semi-empirical approaches [3] - [7]. CFD truly became an invaluable asset with the introduction of Chimera overset grid approaches [8]. Using these methods, unsteady full field simulations can be performed with or without viscous effects.

The challenge with using CFD is to provide accurate data in a timely manner. Computational cost is often high because fine grids and small time steps may be required for accuracy and stability of some codes. Often, the most costly aspect of CFD, both in terms of time and money, is grid generation and assembly. This is especially true for complex store geometries and in the case of stores released from weapons bays. These bays often contain intricate geometric features that affect the flow field.

Aerodynamic and physical parameters affect store separation problems. Aerodynamic parameters are the store shape and stability, the velocity, attitude, load factor, configuration of the aircraft and flow field surrounding the store. Physical parameters include store geometric characteristics, center of gravity position, ejector locations and impulses and bomb rack. The above parameters are highly coupled and react with each other in a most complicated manner [9] - 11]. An accurate prediction of the trajectory of store objects involves an accurate prediction of the flow field around them, the resulting forces and moments, and an accurate integration of the equations of motion. This necessitates a coupling of the CFD solver with a six degree of freedom (6-DOF) rigid body dynamics simulator [12]. The simulation errors in the CFD solver and in the 6-DOF simulator have an accumulative effect since any error in the calculated aerodynamic forces can predict a wrong orientation and trajectory of the body and vice-versa. The forces and moments on a store at carriage and various points in the flow field of the aircraft can be computed using CFD applied to the aircraft and store geometry [13].

The purpose of this paper is to demonstrate the accuracy and technique of using an unstructured dynamic mesh approach to store separation. The most significant advantage of utilizing unstructured meshes [14] is the flexibility to handle complex geometries. Grid generation time is greatly reduced because the user's input is limited to mainly generation of a surface mesh. Though not utilized in this study, unstructured meshes additionally lend themselves very well to solution-adaptive mesh refinement/coarsening techniques, especially useful in capturing shocks. Finally, because there are no overlapping grid regions, fewer grid points are required.

The computational validation of the coupled 6-DOF and overset grid system is carried out using a simulation of a safe store separation event from underneath a delta wing under transonic conditions (Mach number 1.2) at an altitude of 11,600 m [15] and various angles of attack (0°, 3° and 5°) for a particular weapon configuration with appropriate ejection forces. An inviscid flow is assumed to simplify the above simulations. The predicted computed trajectories are compared with a 1/20 scale wind-tunnel experimental data conducted at he Arnold Engineering Development Center (AEDC) [16] - [17].

2. WEAPON / EJECTOR MODELLING

In the present work store-separation numerically simulation events were demonstrated on a generic pylon/store geometric configuration attached to a clipped delta wing, as shown in FIGURE 1. Benchmark wind-tunnel experiments for these cases were conducted at the Arnold Engineering Development Center (AEDC) [16], and the details of the data can be found in Lijewski and Suhs [18]. Results available from these studies include trajectory informations and surface pressure distributions at multiple instants in time. The computational geometry matches the experimental model with the exception of the physical model being 1/20 scale.

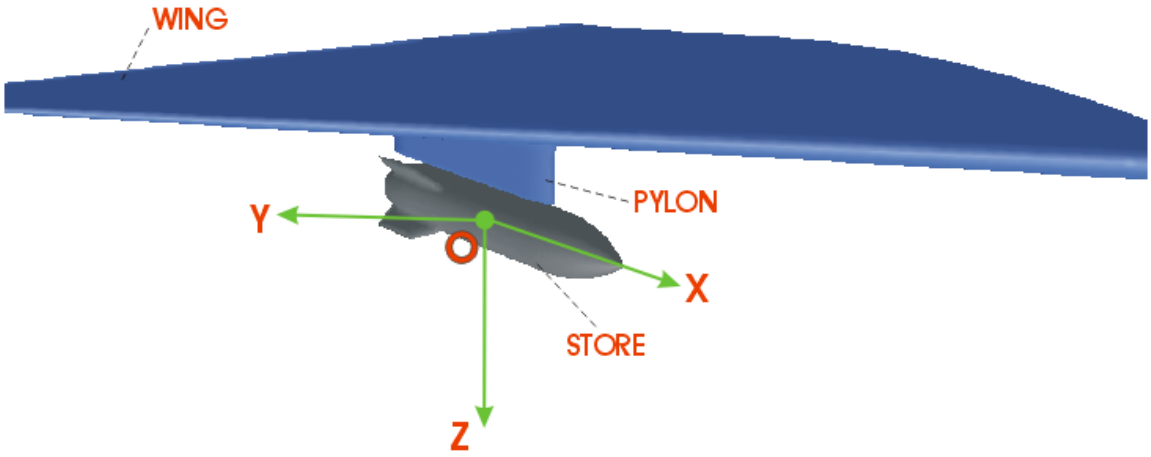

FIGURE 1: Global coordinate system OXYZ for store separation trajectory analysis.

It can be seen from FIGURE 1 the global coordinate system orientation OXYZ for the store separation simulation analysis. The origin O is located at the store center of gravity while in storage. X-axis runs from the tail to nose of the store, Y-axis points away from the aircraft and Z-axis points downward along the direction of the gravity.

The aircraft's wing is a 45-degree clipped delta with 7.62 m (full scale) root chord length, 6.6 m semi-span, and NACA 64A010 airfoil section. The ogive-flat plate-ogive pylon is located spanwise 3.3 m from the root, and extends 61 cm below the wing leading edge. The store consists of a tangent-ogive forebody, clipped tangent-ogive afterbody, and cylindrical centerbody almost 50 cm in diameter. Overall, the store length is approximately 3.0 m. Four fins are attached, each consisting of a 45-degree sweep clipped delta wing with NACA 008 airfoil section. To accurately model the experimental setup, a small gap of 3.66 cm exists between the missile body and the pylon while in carriage.

In the present analysis the projectile is forced away from its wing pylon by means of identical piston ejectors located in the lateral plane of the store, -18 cm forward of the center of gravity (C.G.), and 33 cm aft. While the focus of the current work is not to develop an ejector model for the examined projectile configuration, simulating the store separation problem with an ejector model which has known inaccuracies serves little purpose [9].

The ejector forces were present and operate for the duration of 0.054 s after releasing the store. The ejectors extend during operation for 10 cm, and the force of each ejector is a constant function of this stroke extension with values 10.7 kN and 42.7 kN, respectively. The basic geometric properties of the store and ejector forces for this benchmark simulation problem are tabulated in TABLE 1 and are depicted in a more detail drawing in FIGURE 2.

As the store moves away from the pylon, it begins to pitch and yaw as a result of aerodynamic forces and the stroke length of the individual ejectors responds asymmetrically.

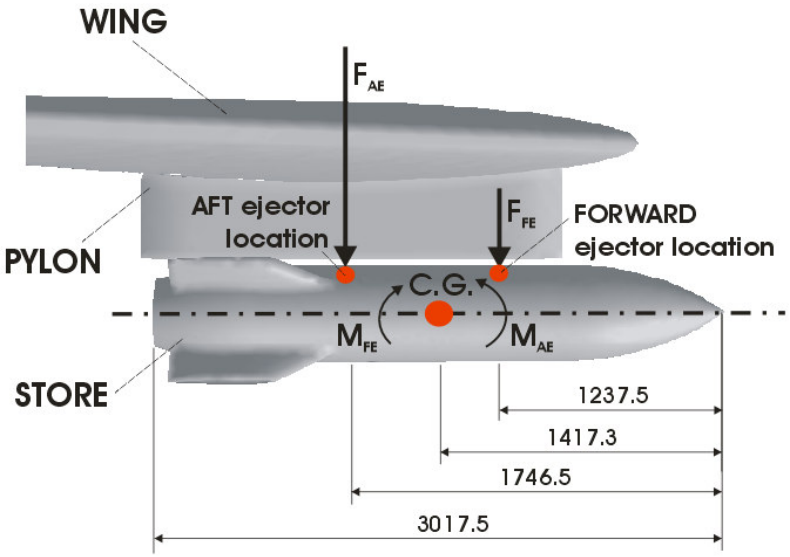

FIGURE 2: Ejector force model for the store separation problem.

Characteristic Magnitudes	Values
Mass m, kg	907
Reference Length L, mm	3017.5
Reference Diameter D, mm	500
No. of fins	4
Center of gravity $x_{C.G.}$, mm	1417 (aft of store nose)
Axial moment of inertia I_{XX}, kg·m^2	27
Transverse moments of inertia I_{yy} and I_{zz}, kg·m^2	488
Forward ejector location $L_{FE.}$, mm	1237.5 (aft of store nose)
Forward ejector force F_{FE}, kN	10.7
Aft ejector location L_{AE}, mm	1746.5 (aft of store nose)
Aft ejector force F_{AE}, kN	42.7
Ejector stroke length L_{ES}, mm	100

TABLE 1: Main geometrical data for the examined store separation projectile.

3. FLOWFIELD NUMERICAL SIMULATION

The computational approach applied in this study consists of three distinct components: a flow solver, a six degree of freedom (6DOF) trajectory calculator and a dynamic mesh algorithm [12]. The flow solver is used to solve the governing fluid-dynamic equations at each time step. From this solution, the aerodynamic forces and moments acting on the store are computed by integrating the pressure over the surface. Knowing the aerodynamic and body forces, the

movement of the store is computed by the 6DOF trajectory code. Finally, the unstructured mesh is modified to account for the store movement via the dynamic mesh algorithm.

3.1 Flow Solver

The flow is compressible and is described by the standard continuity and momentum equations. The energy equation incorporates the coupling between the flow velocity and the static pressure. The flow solver is used to solve the governing fluid dynamic equations that include an implicit algorithm for the solution of the Euler Equations [11] - [14]. The Euler equations are well known and hence, for purposes of brevity, are not shown. The present analysis employs a cell-centered finite volume method based on the linear reconstruction scheme, which allows the use of computational elements with arbitrary polyhedral topology. A point implicit (block Gauss-Seidel) linear equation solver is used in conjunction with an algebraic multigrid (AMG) method to solve the resultant block system of equations for all dependent variables in each cell. Temporally, a first order implicit Euler scheme is employed [14] - [23].

The conservation equation for a general scalar f on an arbitrary control volume whose boundary is moving can be written in integral form as:

$$\frac{\partial}{\partial t}\int_V \rho f dV + \int_{\partial V} \rho f\left(\vec{u}-\vec{u}_g\right)d\vec{A} = \int_{\partial V} I\nabla f d\vec{A} + \int_V S_f dV \tag{1}$$

The time derivative in Eq.(1) is evaluated using a first-order backward difference formula:

$$\frac{d}{dt}\int_V \rho f dV = \frac{\left(\rho f V\right)^{k+1} - \left(\rho f V\right)^{k}}{\Delta t} \tag{2}$$

where the superscript denotes the time level and also

$$V^{k+1} = V^{k} + \frac{dV}{dt}\Delta t \tag{3}$$

The space conservation law [24] is used in formulating the volume time derivative in the above expression Eq.(3) in order to ensure no volume surplus or deficit exists.

3.2 Trajectory Calculation

The 6DOF rigid-body motion of the store is calculated by numerically integrating the Newton-Euler equations of motion within Fluent as a user-defined function (UDF). The aerodynamic forces and moments on the body store are calculated based on the integration of pressure over the surface. This information is provided to the 6DOF from the flow solver in inertial coordinates. The governing equation for the translational motion of the center of gravity is solved for in the inertial coordinate system, as shown below:

$$\dot{\vec{v}}_G = m\sum \vec{f}_G \tag{4}$$

where $\dot{\vec{v}}_G$ is the translational motion of the center of gravity, m is the mass of the store and $\vec{f}_G$ is the force vector due to gravity.

The angular motion of the moving object $\vec{\omega}_{\mathrm{B}}$, on the other hand, is more readily computed in body coordinates to avoid time-variant inertia properties:

$$\dot{\vec{\omega}}_{\mathrm{B}} = L^{-1}\left(\sum \vec{M}_B - \vec{\omega}_{\mathrm{B}} \times L\vec{\omega}_{\mathrm{B}}\right) \tag{5}$$

where L is the inertia tensor and $\vec{M}_B$ is the moment vector of the store.
The orientation of the store is tracked using a standard 3-2-1 Euler rotation sequence. The moments are therefore transformed from inertial to body coordinates via

$$\vec{M}_B = R\vec{M}_G \tag{6}$$

where R is the transformation matrix

$$R \equiv \begin{bmatrix} c_\theta c_\psi & c_\theta s_\psi & -s_\theta \\ s_\phi s_\theta c_\psi - c_\phi s_\psi & s_\phi s_\theta s_\psi + c_\phi c_\psi & c_\theta s_\phi \\ c_\phi s_\theta c_\psi + s_\phi s_\psi & c_\phi s_\theta s_\psi - s_\phi c_\psi & c_\theta c_\phi \end{bmatrix} \tag{7}$$

with the shorthand notation $c_\xi = \cos(\xi)$ and $s_\xi = \sin(\xi)$ has been used.
Once the translational and angular accelerations are computed from Eqs (4) and (5), the angular rates are determined by numerically integrating using a fourth-order multi-point Adams-Moulton formulation:

$$\xi^{k+1} = \xi^k + \frac{\Delta t}{24}\left(9\dot{\xi}^{k+1} + 19\dot{\xi}^k - 5\dot{\xi}^{k-1} + \dot{\xi}^{k-2}\right) \tag{8}$$

where ξ represents either $\vec{v}_G$ or $\vec{\omega}_B$.

The dynamic mesh algorithm takes as input $\vec{v}_G$ and $\vec{\omega}_G$. The angular velocity, then, is transformed back to inertial coordinates via

$$\vec{M}_G = R^T\vec{M}_B \tag{9}$$

where R is given in Eq.(7).

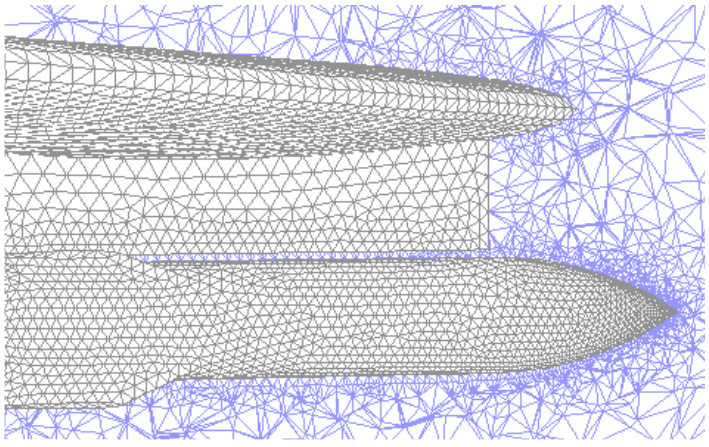

FIGURE 3: Refined mesh in the region near the store.

3.3 Dynamic Mesh

The geometry and the grid were generated with Fluent's pre-processor, Gambit® using tetrahedral volume mesh [25]. As shown in FIGURE 3, the mesh of the fluid domain is refined in the region near the store to better resolves the flow details. In order to simulate the store separation an unstructured dynamic mesh approach is developed. A local remeshing algorithm is

used to accommodate the moving body in the discretized computational domain. The unstructured mesh is modified to account for store movement via the dynamic mesh algorithm.

FIGURE 4: Surface mesh of the examined store.

When the motion of the moving body is large, poor quality cells, based on volume or skewness criteria, are agglomerated and locally remeshed when necessary. On the other hand, when the motion of the body is small, a localized smoothing method is used. That is, nodes are moved to improve cell quality, but the connectivity remains unchanged. A so-called spring-based smoothing method is employed to determine the new nodal locations. In this method, the cell edges are modeled as a set of interconnected springs between nodes.

The movement of a boundary node is propagated into the volume mesh due to the spring force generated by the elongation or contraction of the edges connected to the node. At equilibrium, the sum of the spring forces at each node must be zero; resulting in an iterative equation:

$$\Delta\vec{x}_i^{m+1} = \frac{\sum_{j=1}^{n_i} k_{ij}\Delta\vec{x}_i^{m}}{\sum_{j=1}^{n_i} k_{ij}} \tag{10}$$

where the superscript denotes iteration number. After movement of the boundary nodes, as defined by the 6DOF, Eq.(10) is solved using a Jacobi sweep on the interior nodes, and the nodal locations updated as

$$\vec{x}_i^{k+1} = \vec{x}_i^{k} + \Delta\vec{x}_i \tag{11}$$

where here the superscript indicates the time step.

In FIGURE 4 the surface mesh of the store is illustrated. A pressure far field condition was used at the upstream and downstream domain extents. The initial condition used for the store-separation simulations was a fully converged steady-state solution [26] - [28]. This approach was demonstrated on a generic wing-pylon-store geometry with the basic characteristics shown on the previous section. The domain extends approximately 100 store diameters in all directions around the wing and store.

The working fluid for this analysis is the air with density ρ = 0.33217 kg/m^3. The studied angles of attack are 0°, 3° and 5°, respectively. The store separation is realized to an altitude of 11,600 m, where the corresponding pressure is 20,657 Pa and the gravitational acceleration is g = 9.771 m/s^2. The Mach number is M = 1.2 and the ambient temperature is T = 216.65 K [15], [29], [30].

4. NUMERICAL ANALYSIS RESULTS

The full-scale separation events are simulated under transonic conditions (Mach number 1.2) at an altitude of 11,600 m and various angles of attack (0°, 3° and 5°) using CFD-FLUENT package

[31] - [32]. The initial condition used for the separation analysis was a fully converged steady-state solution. Because an implicit time stepping algorithm is used, the time step Δt is not limited by stability of the flow solver. Rather, Δt is chosen based on accuracy and stability of the dynamic meshing algorithm. Time step Δt = 0.002 sec is chosen for the convergence of store-separation trajectory simulations.

Four trajectory parameters are examined and compared with the experimental data: center of gravity (CG) location, CG velocity, orientation, and angular rate. These parameters are plotted in FIGURE 5 - 8 for total store separation process in 0.8 sec. In each plot are shown the experimental data at α = 0 deg [30], [33], [34] and CFD data for the three examined angles of attack.

FIGURE 5 shows the store CG location in the global coordinate system as a function of store-separation time. It is apparent that the z (vertical) position matches very closely with the experimental data for the three examined angles of attack. This is because the ejector and gravity forces dominate the aerodynamic forces in this direction. In the x and y direction the agreement is also very good. The store moves rearward and slightly inboard as it falls. The small discrepancy in the x direction is expected because the drag is underestimated in the absence of viscous effects. This is also seen in the CG velocities, shown in FIGURE 6. As expected, the store continuously accelerates rearward, with the CFD results underpredicting the movement for the three examined angles of attack. The store is initially pulled slightly inboard, but soon begins to move slowly outboard with the wing outwash. As with position, the velocity in the z direction matches very well with the experiments for zero angle of attack. In this plot the effect of the ejectors is seen clearly at the beginning of the trajectory via a large z-velocity gradient. After approximately t = 0.05 seconds, the store is clear of the ejectors.

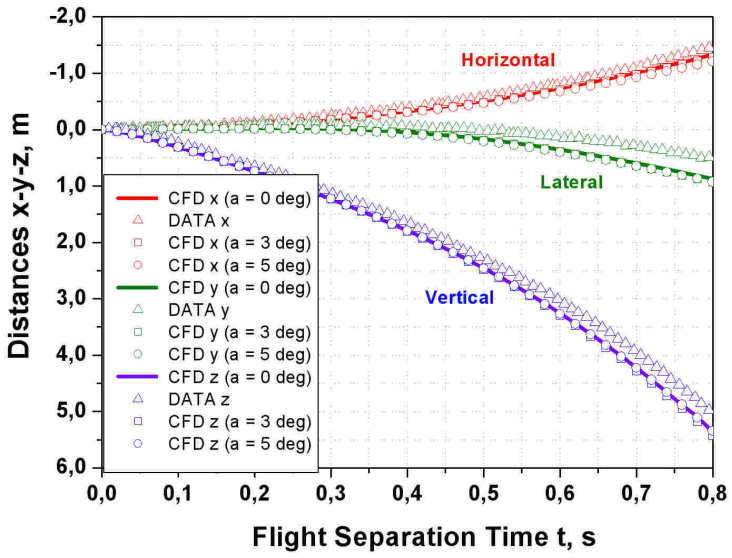

FIGURE 5: Center of gravity location.

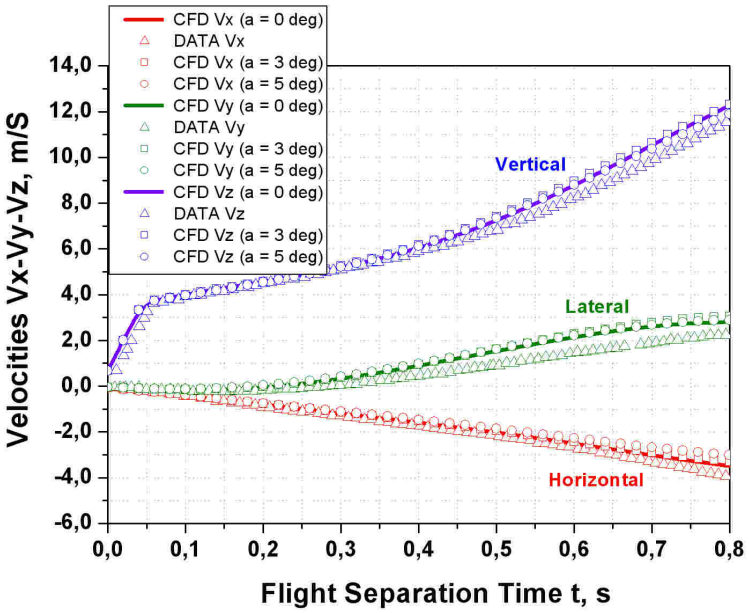

FIGURE 6: Center of gravity velocity.

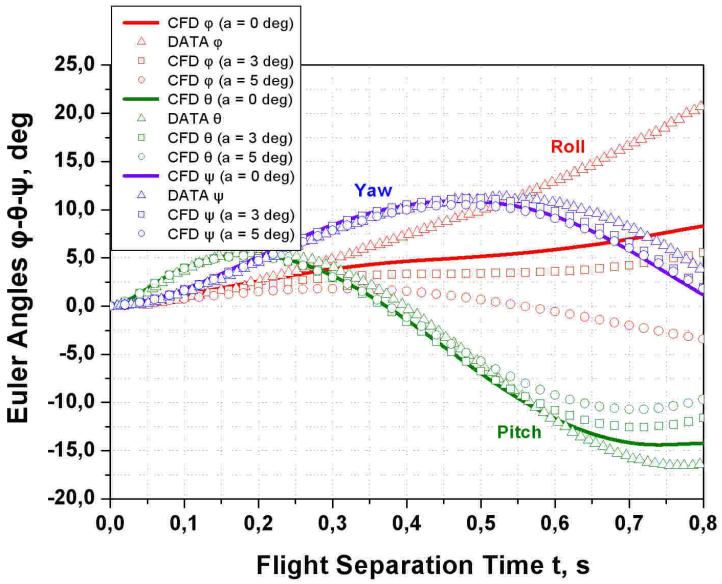

FIGURE 7: Angular orientation of projectile separation process.

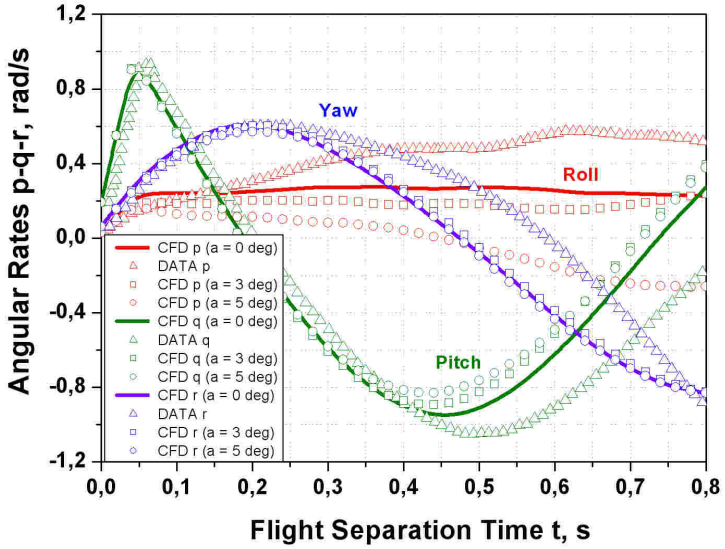

FIGURE 8: Angular rate of the examined store movement.

The orientation of the store is more difficult to model than the CG position. This is evident in FIGURE 7, which shows the Euler angles as a function of time. The pitch and yaw angles agree well with the experiment for α = 0, 3 and 5 degrees, respectively. The store initially pitches nose-up in response to the moment produced by the ejectors, as shown in FIGURE 2. Once free of the ejectors after 0.05 seconds, though, the nose-down aerodynamic pitching moment reverses the trend. The store yaws initially outboard until approximately 0.55 seconds, after which it begins turning inboard. The store rolls continuously outboard throughout the first 0.8 seconds of the separation. This trend is under-predicted by the CFD simulation analysis, and the curve tends to diverge from the experiments after approximately 0.3 seconds for all the examined angles of attack. The roll angle is especially difficult to model because the moment of inertia about the roll axis is much smaller than that of the pitch and yaw axes, see TABLE 1. Consequently, roll is very sensitive to errors in the aerodynamic force prediction. The body angular rates are plotted in FIGURE 8. Here again it is shown that the pitch and yaw rates compare well with the experiments at α = 0 deg, while the roll rate is more difficult to capture.

It is obvious, that the CFD performs very well in modelling the whole store separation events. This is reiterated in FIGURE 9, in which views of the simulated store movements at α = 0 and α = 5 deg, respectively, are compared at discrete instants in time throughout the separation for the first 0.8 seconds. In the examined two cases the stores pitch down even though the applied ejector forces causes a positive (nose up) ejector moment and roll inboard and yaw outboard. This downward pitch of the store is a desirable trait for safe separation of a store from a fighter aircraft [2].

The fluid dynamics prediction analysis also gives pressure coefficient distributions for the total separation history along axial lines on the store body at four circumferential locations and three instants in time. The simulation data are compared with experimental surface pressure data from the wind tunnel tests [31], [33], 34], as depicted in FIGURES 10 up to 13.

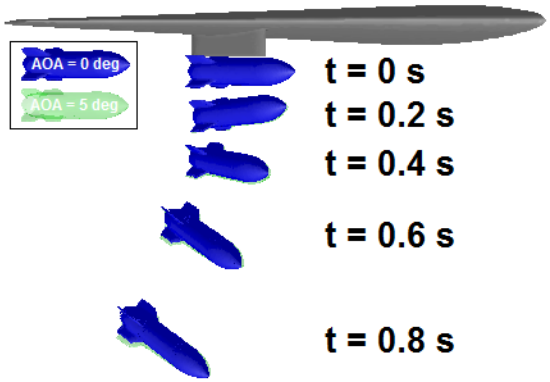

(a) Front view with side angles

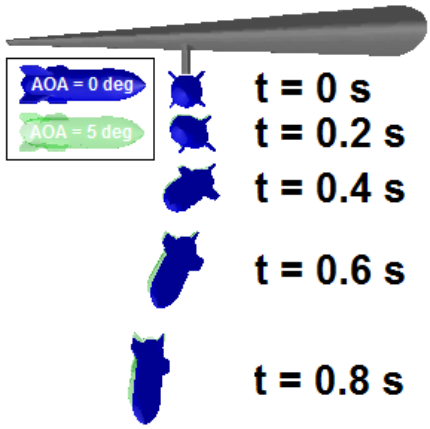

(b) Front view

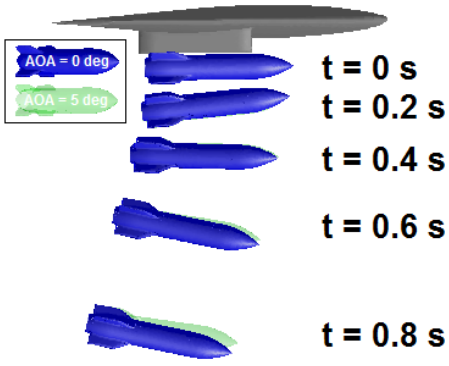

(c) Side view

FIGURE 9: Store separation events with ejectors at Mach 1.2 for 0 and 5 deg angle of attacks, respectively.

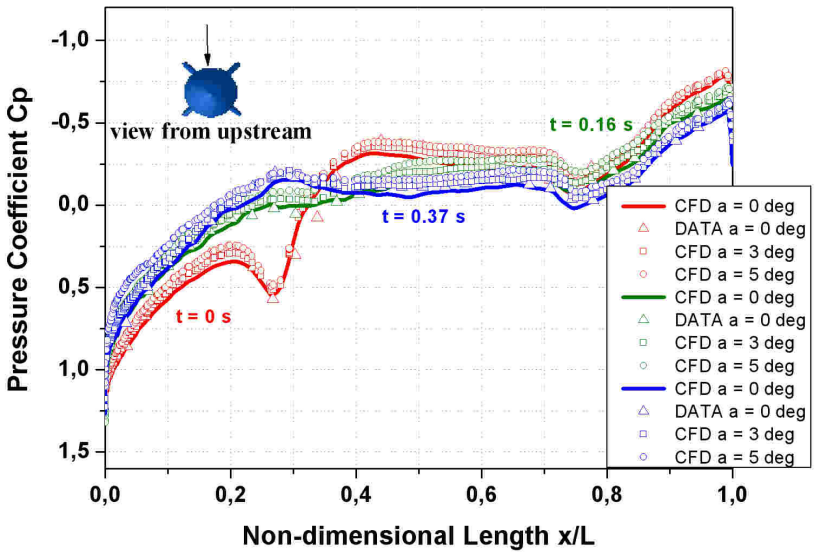

FIGURE 10: Surface pressure profile for phi = 5 deg.

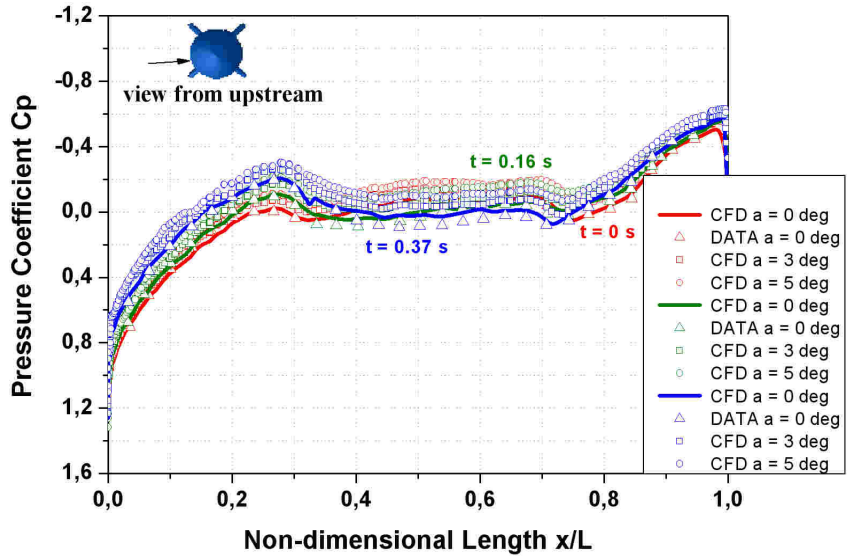

FIGURE 11: Surface pressure profile for phi = 95 deg.

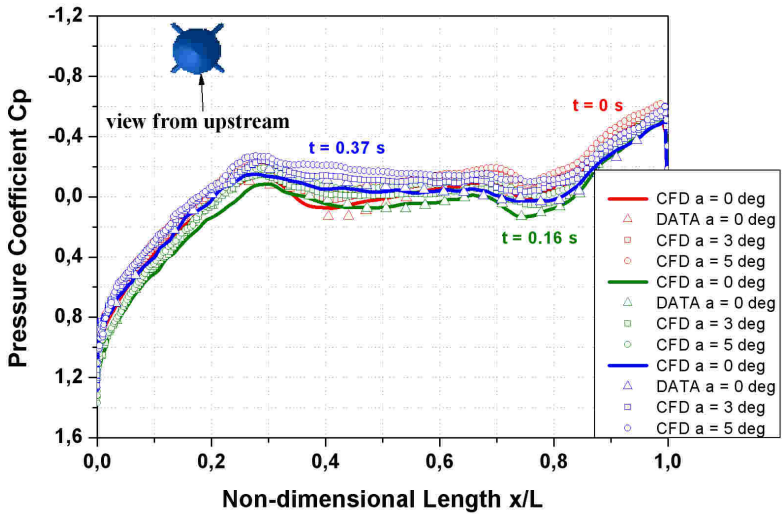

FIGURE 12: Surface pressure profile for phi = 185 deg.

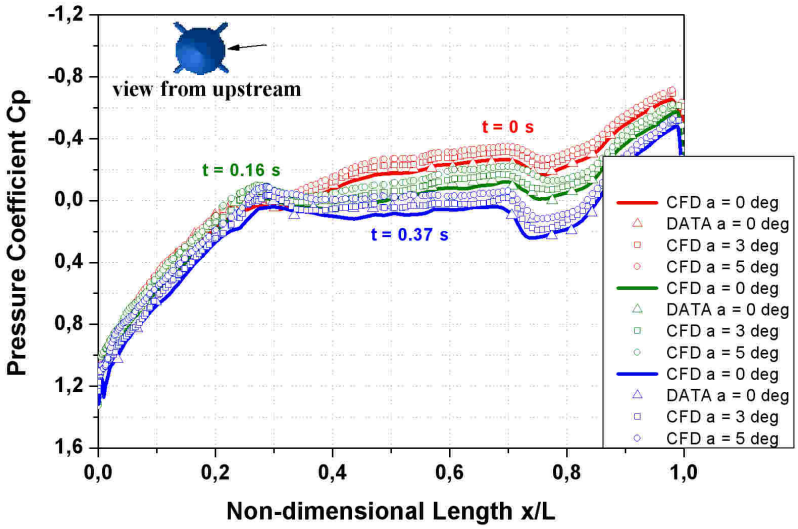

FIGURE 13: Surface pressure profile for phi = 275 deg.

The circumferential locations are denoted by the angle phi. The value phi = 0 is located at the top (y = 0, nearest the pylon) of the store while in carriage and is measured counter clockwise when viewed from upstream. FIGURES 10 - 13 show the pressure profiles along the non-dimensional axis of symmetry length x/L at phi = 5, 95, 185, and 275 deg for three time instants t = 0.0, 0.16, and 0.37 seconds with 0°, 3° and 5° degrees angle of attack (blue, green and red solid lines), respectively. It is obvious the agreement between computational and experimental data, especially in the region near the nose of projectile where the pressure coefficient Cp takes positive values.

The CFD numerical results correspond to the nominal grid with time step Δt = 0.002 sec run. Agreement is exceptional. Of particular interest is the phi = 5 deg line at t = 0.0 because it is

located in the small gap between the pylon and store. The deceleration near the leading edge of the pylon is apparent at x/L = 0.25, and is well captured.

Also FIGURE 14 shows the zero angle of attack Cp computational results at five different times of the store separation process along the axis of symmetry passing from the fin tail. Strong disturbances are noticed in this diagram in the fin tail region x/L = 0.7 to 1.0 where the presence of the fin influences the air flow field environment around the projectile process separation. The computational results show that Cp takes positive values not only at distances close to projectile's nose region but also at the leading edge region of the backward fin tail.

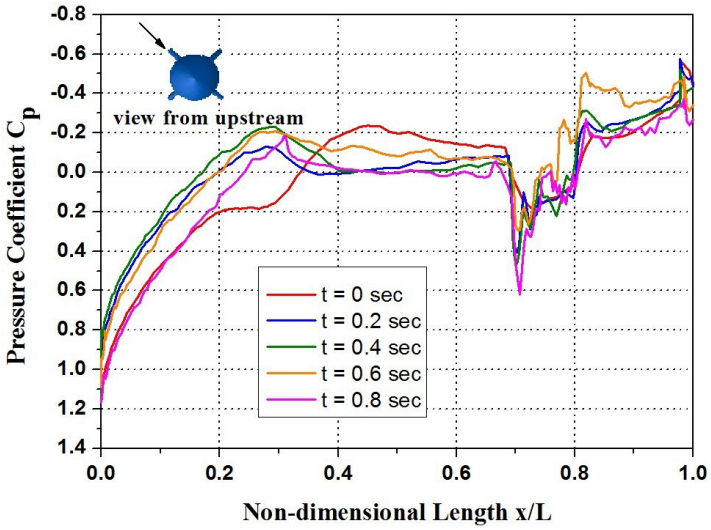

FIGURE 14: Surface pressure profiles along the non-dimensional axis of symmetry passing from the projectile fin tail at zero angle of attack.

The above results showed that CFD performed very well in modelling a separation event at transonic Mach number 1.2 for 11,600 m altitude at the three examined angles of attack. The store moved rearward and slightly inboard as it fell in all cases. Consequently the roll is very sensitive to errors in aerodynamic force prediction. In this case, the store initially pitched nose-up in response to the moment produced by the ejectors. Once free of the ejectors, the nose-down aerodynamic pitching moment reversed the trend. The store yawed initially outboard until about 0.55 s, after which it began turning inboard. The store rolled continuously outboard throughout the first 0.8 s of the separation process.

5. CONSLUSION & FUTURE WORK

The current work demonstrates an integrated package for performing 6-DOF simulations coupled with an Euler code. The feasibility of numerical simulation for store separation has been successfully demonstrated in this work. CFD has gradually become a valuable tool for supporting store separation studies and assessments. CFD is very useful and allows the complex geometries associated with real aircraft to be modelled. The modelling of a full aircraft configuration for the Navier-Stokes solution using structured grids is a challenge.

This study has shown that CFD with unstructured dynamic meshing can be an effective and successful tool for modelling transonic store separation at various angles of attack. The simulation captured the experimental location, velocity, orientation, and angular rate trends. Surface pressure distributions were also in good agreement with experiments at three times during the whole separation event.

This approach offers the ability to obtain accurate store separation predictions with quick turn-around times. Benefits include fast grid generation due to the use of unstructured tetrahedral

meshes, and a fully parallelized, accurate, and stable solver that allows small grids and relatively large time steps. Grid generation can be accomplished in a matter of hours, and runs such as the nominal grid case with time step $\Delta t = 0.002$ seconds examined in this study can be completed overnight on a desktop workstation.

Some error did exist between the simulation and experiment, most prominently in the roll angle. Sources of error include the inviscid assumption (resulting in an under-prediction of drag forces) and the quasi-steady nature of the experiment.

Future work is planned to address the viscous effects. Modeling of the boundary layer requires construction of a rigid viscous mesh attached to the store. Additionally, an adaptive grid refinement algorithm is to be added to the solution procedure, providing more accurate prediction of shock strengths and locations to improve the aerodynamic model.

6. REFERENCES

1. A. Arabshahi, D. L. Whitfield. *"A Multi-Block Approach to Solving the Three-Dimensional Unsteady Euler Equations about a Wing-Pylon-Store Configuration".* AIAA Paper 89-3401, August 1989
2. E. E. Covert. *"Conditions for Safe Separation of External Stores".* Journal of Aircraft, 18(8), 1981
3. W. L. Sickles, C. H. Morgret, A. G. Denny and R. H. Nichols. *"Comparison of Time-Accurate CFD and Engineering Methods for the JDAM Separation from an F-18C Aircraft"*. In proceedings of the Aircraft-Store Compatibility Symposium sponsored by International Test and Evaluation Association, Joint Ordinance Commanders Group, Aircraft Store Compatibility Subgroup, Destin, FL, March 5–8, 2001
4. W. L. Sickles, A. G. Denny and R. H. Nichols. *"Time-Accurate CFD Store Separation Predictions with Comparison to Flight Data"*. AIAA Paper No. 2000-0796, In proceedings of the 37th Aerospace Sciences Meeting and Exhibit, Reno, NV, January 10–13, 2000
5. A. Cenko, E. N. Tinoco, R. D. Dyer and J. DeJongh. *"PANAIR Applications to Weapons Carriage and Separation"*. Journal of Aircraft, 18:128–134, 1981
6. E. Ray. *"CFD Applied to Separation of SLAM-ER from the S-3B".* AIAA Paper No. 2003-4226, In proceedings of the AIAA 21st Applied Aerodynamics Conference, Orlando, Florida, June 23–26, 2003
7. S. M. Murman, M. J. Aftosmis and M. J. Berger. *"Simulations of Store from an F/A-18 with a Cartesian Method".* Journal of Aircraft, 41(4):870–878, 2004
8. N. C. Prewitt, D. M. Belk, Soni and W. Shyy. *"Parallel Computing of Overset Grids for Aerodynamic Problems with Moving Objects".* Progress in Aerospace Sciences, 36(2):117-172, 2000
9. K. S. Keen. *"New Approaches to Computational Aircraft/Store Weapons Integration"*. AIAA Paper No. 90-0274, In proceedings of the AIAA 28th Aerospace Sciences Meeting, Reno, NV, January 8–11, 1990
10. T. L. Donegan, J. H. Fox. *"Analysis of Store Trajectories from Tactical Fighter Aircraft".* AIAA Paper No. 91-0183, In proceedings of the AIAA 29th Aerospace Sciences Meeting, Reno, NV, January 7–10, 1991
11. W. L. Sickles, M. J. Rist, C. H. Morgret, S. L. Keeling, K. N. Parthasarathy. *"Separation of the Pegasus XL from an L-1011 Aircraft".* AIAA Paper No. 94-3454, In proceedings of the AIAA Atmospheric Flight Mechanics Conference, August 1–3, 1994
12. R. Koomullil, G. Cheng, B. Soni, R. Noack and N. Prewitt. *"Moving-body Simulations Using Overset Framework with Rigid Body Dynamics".* Mathematics and Computers in Simulation, 78(5-6):618-626, 2008
13. R. Meyer, A. Cenko and S. Yaros. *"An Influence Function Method for Predicting Aerodyanmic Characteristics During Weapon Separation".* In proceedings of the 12th Navy Symposium on Aeroballistics, May 1981

14. S. E. Kim, S. R. Mathur, J. Y. Murthy and D. Choudhury. *"A Reynolds –Averaged Navier-Stokes Solver Using Unstructured Mesh-Based Finite-Volume Scheme"*. AIAA Paper 98-0231, 1998
15. E. E. Panagiotopoulos and S. D. Kyparissis. *"Computational Flowfield Investigation of Store Separation Trajectories from Transonic Aircraft Wing".* International Review of Aerospace Engineering, 2(3):139-144, 2009
16. R. R. Heim. *"CFD Wing/Pylon/Finnned Store Mutual Interference Wind Tunnel Experiment".* AEDC-TSR-91-P4, 1991
17. L. E. Lijewski. *"Comparison of Transonic Store Separation Trajectory Predictions Using the Pegasus/DXEagle and Beggar Codes".* AIAA Paper 97-2202, 1997
18. L. E. Lijewski, N. E. Suhs. *"Time-Accurate Computational Fluid Dynamics Approach to Transonic Store Separation Trajectory Prediction".* Journal of Aircraft, 31(4):886-891, July 1994
19. L. H. Hall, C. R. Mitchell and V. Parthasarathy. *"An Unsteady Simulation Technique for Missile Guidance and Control Applications".* AIAA Paper AIAA97-0636, 1997
20. S. Westmoreland. *"A Comparison of Inviscid and Viscous Approaches for Store Separations".* AIAA Paper AIAA2002-1413, 2002
21. A. Benmeddour, F. Fortin, T. Amirlatifi and N. Stathopoulos. *"Prediction of the CF-18/MK-83 LD Store Separation Characteristics Using a Quasi-Steady CFD Approach".* AIAA Paper No. 2003-4222, In proceedings of the AIAA 21st Applied Aerodynamics Conference, Orlando, Florida, June 23–26, 2003
22. L. Formaggia, J. Peraire and K. Morgan. *"Simulation of a Store Separation Using the Finite Element Method"*. Journal of Applied Mathematical Modelling, 12(2):175–181, 1988
23. E. Lath, K. Kailasanath and R. Lockner. *"Supersonic Flow over an Axisymmetric Backward-Facing Step"*. Journal of Spacecraft and Rockets, 29(3): 352-359, 1992
24. I. Demirdzic, M. Peric. "*Space Conservation Law in Finite Volume Calculations of Fluid Flow*". International Journal for Numerical Methods in Fluids, 8: 1037-1050, 1988
25. R. W. Tramel, R.H. Nichols. *"A Highly Efficient Numerical Method for Overset-Mesh Moving-Body Problems".* AIAA Paper 97-2040, In proceedings of the AIAA 13th Computational Fluid Dynamics Conference, Snowmass Village, CO, June 29–July 2, 1997
26. R. D. Thomas, J. K. Jordan. *"Investigation of Multiple Body Trajectory Prediction Using Time Accurate Computational Fluid Dynamics"*. AIAA Paper AIAA95-1870, 1995
27. R. M. Lee. *"Beggar Code Implementation of the 6DOF Capability for Stores with Moving Components".* AIAA Paper AIAA2004-1251, 2004
28. J. K. Jordan, N. E. Suhs, R. D. Thoms, R. W. Tramel, J. H. Fox and J. C. Erickson. *"Computational Time-Accurate Body Movement Methodology, Validation, and Application".* AEDC-TR-94-15, October 1995
29. J. H. Fox, T. L. Donegan, J. L. Jacocks and R. H. Nichols. *"Computed Euler Flowfield for a Transonic Aircraft with Stores"*. Journal of Aircraft, 28(6):389–396, 1991
30. L. E. Lijewski. *"Transonic Euler Solutions on Mutually Interfering Finned Bodies".* AIAA Journal, 28(6):982-988, June 1990
31. Gambit Modeling Guide, Fluent Incorporated, Lebanon, NH, 1998
32. TGrid 3.4 User's Guide, Fluent Incorporated, Lebanon, NH, 2001
33. J. B. Carman, D. W. Hill and J. P. Christopher. *"Store Separation Testing Techniques at the Arnold Engineering Development Center, Volume II: Description of Captive Trajectory Store Separation Testing in the Aerodynamic Wind Tunnel (4T)".* AEDC-TR-79-1, Vol. II (AD-A087561), 1980
34. C. H. Morgret, R. E. Dix and L. E. Lijewski. *"Development of Analytical and Experimental Techniques for Determining Store Airload Distribution".* Journal of Spacecraft and Rockets, 19(6):489–495, 1982

An efficient Bandwidth Demand Estimation for Delay Reduction in IEEE 802.16j MMR WiMAX Networks

Fath Elrahman Ismael fathi_sml@yahoo.com

UTM MIMOS CoE Telecommunication Technology,
Faculty of Electrical Engineering (FKE)
Universiti Teknologi Malaysia (UTM)
Johor, 81300, Malaysia

Sharifah K. Syed Yusof kamilah@fke.utm.my

UTM MIMOS CoE Telecommunication Technology,
Faculty of Electrical Engineering (FKE)
Universiti Teknologi Malaysia (UTM)
Johor, 81300, Malaysia

Norsheila Fisal Sheila@fke.utm.my

UTM MIMOS CoE Telecommunication Technology,
Faculty of Electrical Engineering (FKE)
Universiti Teknologi Malaysia (UTM)
Johor, 81300, Malaysia

Abstract

IEEE 802.16j MMR WiMAX networks allow the number of hops between the user and the MMR-BS to be more than two hops. The standard bandwidth request procedure in WiMAX network introduces much delay to the user data and acknowledgement of the TCP packet that affects the performance and throughput of the network. In this paper, we propose a new scheduling scheme to reduce the bandwidth request delay in MMR networks. In this scheme, the MMR-BS allocates bandwidth to its direct subordinate RSs without bandwidth request using Grey prediction algorithm to estimate the required bandwidth of each of its subordinate RS. Using this architecture, the access RS can allocate its subordinate MSs the required bandwidth without notification to the MMR-BS. Our scheduling architecture with efficient bandwidth demand estimation able to reduce delay significantly.

Keywords – IEEE 802.16j, Grey prediction, Delay, throughput, wireless networks.

1. INTRODUCTION

The IEEE 802.16 WiMAX is a standard for the wireless broadband access networks and is recognized as one of the strongest contenders of the wired networks to provide internet connection to the end users. However, the existing WiMAX products have limited coverage and provide poor signal strength for indoor users as well as users at cell boundaries [1].

Mobile Multi-hop Relay (MMR) WiMAX systems have the potential to offer improved coverage and capacity over single-hop radio access systems. Standards development organizations are considering how to incorporate such techniques into new standards. One such initiative is the

IEEE 802.16j standardization activity, adding relay capabilities to IEEE 802.16e systems [2]. The Relay Station (RS) significantly reduces the installation and operation cost [3]. Moreover, the RS increases the overall network capacity as a result of enhancing CINR in a poor coverage area.

Transmission Control Protocol (TCP) is the most commonly used transport protocol on the Internet [16]. But conventional TCP requires acknowledgement from the receiver side to know that the sent packet is received correctly or not.

The bandwidth request- grant mechanism in the standard WiMAX when applied to multi- hop systems affects the performance of the TCP traffic. It introduces much delay to the transmitted data in the uplink and also to the TCP acknowledgement, which increases the Round Trip Time (RTT) and leads to unnecessary retransmission and reduces the throughput.

The paper is organized as follows. Section 2 introduces general overview on MMR network architecture. In 3 scheduling algorithm of WiMAX networks are discussed. The Problem definition is stated in 4. The literature and related work is given in 5. The proposed scheduling architecture is explained in 6, the grey prediction algorithm is discussed in 7, the performance of the proposed scheme is evaluated in 8, and the conclusion in 9.

2. Mmr networks architecture

The MMR networks consist of three types of station: the MMR-BS, a fixed (RS), and the (MS) as shown in FIGURE 1. The MS can communicate with a MMR-BS either directly or over a two-hop via the RS, and also more than two hops can be exploited via multiple RSs. The direct link between the MS and the MMR-BS or RS is referred to as an access link, while the backhaul link between the RS and the MMR-BS referred to as a relay link.

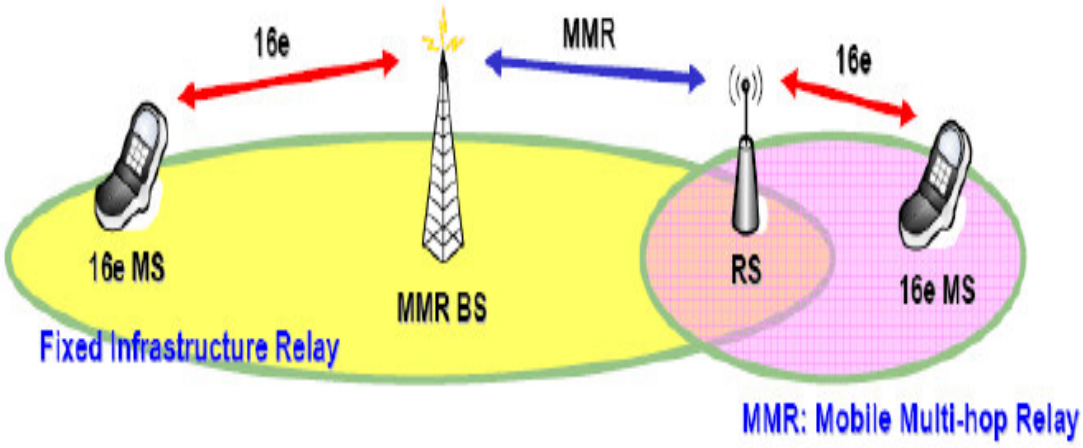

FIGURE 1: MMR network architecture

In WiMAX OFDMA the most common duplexing mode is frame structure TDD, in which the frame is divided into downlink and uplink sub frame that are separated by a guard interval. At the beginning of each Downlink (DL) frame there are several symbols that used for frame control as shown in FIGURE 2. The Preamble enables MS to synchronize to the MMR-BS. DL MAP maps each MS the location of its pertinent burst in the DL sub frame. UL MAP that define for the MS the burst location and size in the coming UL sub frame. Frame Check Header (FCH) which is a special management burst that is used for the MMR-BS to advertize the system configuration The relay operation is classified in two different modes: transparent and non-transparent relay (NTR): The transparent relay is an element that is located in the network between the MMR-BS and the MS, without the MS being aware of its existence. It does not transmit any control data. The MS

receives directly all the control data such as preamble, FCH, DL MAP and UL MAP directly from the MMR-BS. The transparent relay usually does not extend coverage; its main function is channel quality improvement that as a result increases the link capacity [1] [2].

NTR is a network element that the MS is totally aware of it. The MS which is IEEE 802.16e compatible is not aware of any relaying operation, from the MS point of view the NTR is its conventional serving BS. So, the NTR should support most of the capabilities of a plain 802.16e BS like sending frame control data that includes preamble, UL/DL MAP, FCH. Furthermore, the NTR supports handover, network entry and MS ranging. The NTR serves MSs that are beyond reach of the MMR-BS. As so the NTR is perfect tool for achieving extension of cell and coverage. In addition it can also act as a capacity enhancer because of significant improvement in the

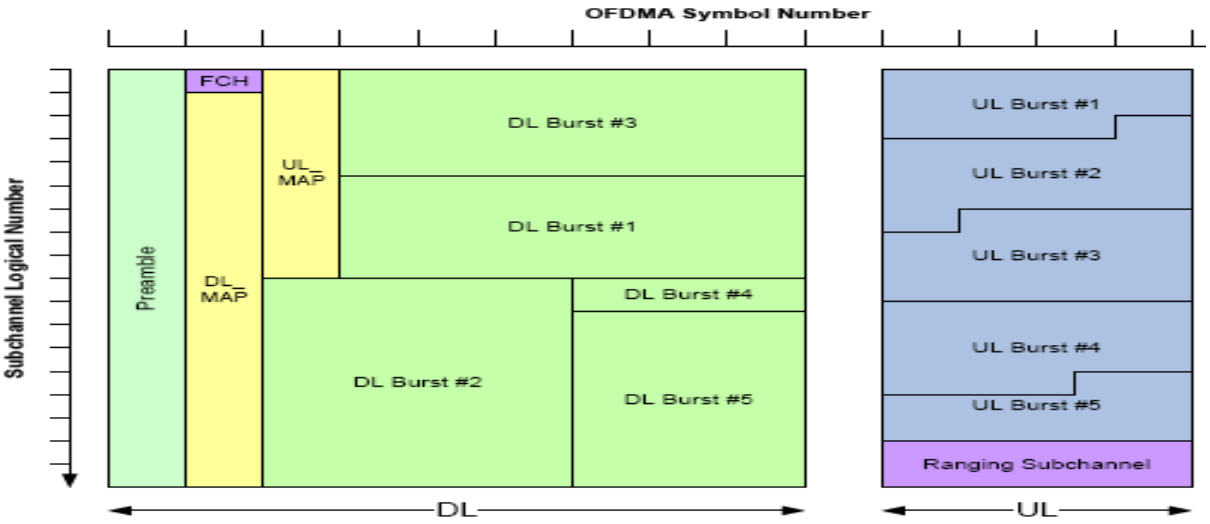

channel quality of both access and relay links [1] [2].

FIGURE 2: OFDMA frame structure

3. Scheduling algorithms of wimax

Scheduling is a sequence of allocating fixed-length time slots to users, where each possible transmission is assigned a time slot. The scheduling challenges are how to develop scheduling architecture that overcomes the problems of increased delay and signaling overhead, and design scheduling algorithm that guarantees the QoS requirements of each service flow [13].

All transparent relays must (and NTRs may) operate in centralized scheduling mode. In this option the MMR-BS is doing all scheduling tasks as it is defined in IEEE 802.16e. It supports optimal centralized radio resource management (RRM), and enables network load balancing among the subordinate relays. However, it requires heavy management traffic within the network, and it is slow in granting bandwidth, which make it not feasible in heavy multi-hop network [4][5].

In distributed scheduling, some MAC intelligence can be given to the RSs. IEEE 802.16j allows NTR relays to operate in distributed scheduling mode, where they make decisions about resource allocation to their subordinate stations most always in coordination with the MMR-BS. In distributed scheduling there is no heavy management traffic within the network and it allows fast bandwidth request grants for high priority requests, which it a suitable technique in heavy multi-hop architecture. But it does not give option for load balancing between relays, and there is no option for centralized RRM [4] [5].

Five scheduling services are defines in the IEEE 802.16j, these are Unsolicited Grant Service (UGS), Real Time Polling Service (rtps), Extended Real Time Polling Service (ertps), Non Real

Time polling Service (nrtps), and Best Effort (BE). The selected network service should allocate sufficient amount of bandwidth in order to actually guarantee network QoS provisioning [17].

4. Problem definition

In WiMAX network when the MS wants to send data, it first sends a bandwidth request message to the corresponding base station (BS), and then the BS grants the appropriate amount of bandwidth to the MS based on the uplink scheduling algorithm. In MMR networks, the control messages used for network entry or bandwidth request are doubled for every RS introduced between MS and MMR-BS, as shown in FIGURE 3. The main reason of the increasing overhead and latency is because all service flow management decisions should be made by MMR-BS in spite of centralized or distributed scheduling. In the centralized scheduling all the functions of network entry and bandwidth request are performed by the MMR-BS. The signaling messages received by the RS from the MSs are forwarded to the MMR-BS, which decides and sends a response messages to the MSs through the intermediate RSs, this process increases the signaling messages exchanged and the delay. Although in the distributed scheduling the RS have an ability to respond to the bandwidth request from their subordinate stations, the relay station requires also a bandwidth request to relay received data to the MMR-BS, which also increase the signaling overhead and delay. Considering that, a signaling message from one hop to another cannot be transmitted in one frame's duration, the delay of control messages transfer from MMR-BS to the MS will increase significantly due to the multi-hop added.

The increased delay affects the performance of the services offered by the MMR WiMAX, because in UGS, rtps, and ertps services the lower latency is required as a QoS metric. Furthermore, even for the BE using TCP as transport protocol, the increased delay increases Round Trip Time (RTT) which degrades the throughput.

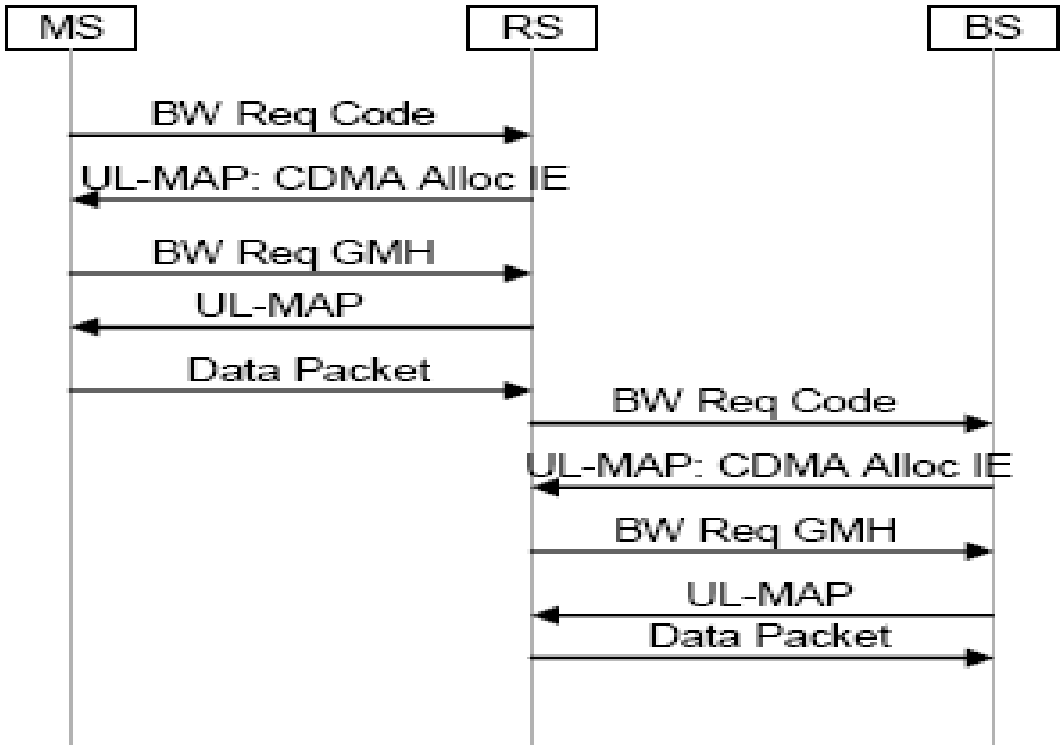

FIGURE 3: Bandwidth request procedure

5. Related works

In the literature there is some works done to reduce the signaling overhead and delay in one hop WiMAX networks such as IEEE 802.16e.

The authors of [8, 9] suggest bandwidth grant mechanism without bandwidth request to fully utilize the available bandwidth for the BE traffic. The BE traffic has a lower priority among services supported by WiMAX; this will result in small amount of bandwidth for this type of service. In addition the BE uses contention based bandwidth request, in which BE connections contend limited number of shared slots for sending their request, and if there is more than one SS attempts to send their requests via a slot, the requested are corrupted.

In this scheme, the BS allocate bandwidth to the SSs without bandwidth request, the amount of granted bandwidth is determined from the current sending rate, this scheme is suitable for large scale network. On the other hand, it may waste the bandwidth when the sending rate is highly fluctuated, and it's hard to estimate the required bandwidth accurately.

In the downlink TCP flow, the standard bandwidth request- grant mechanism in single hop networks introduces much delay to transmit uplink TCP acknowledgement, which increase the Round Trip Time (RTT) and causes unnecessary retransmission that reduce the TCP traffic performance. The authors of [11] introduce new bandwidth scheme that simultaneously allocate bandwidth for both downlink TCP data and uplink TCP acknowledgement.

In the uplink TCP traffic, since the BS controls the uplink transmission and the MS needs to get permission before transmission, these steps severely limit the performance of the TCP by introducing much delay and degrade the throughput. The authors of [12] propose scheme allocating uplink bandwidth in advance. When the BS receive acknowledgement to be sent to the MS, it relays the TCP ACK and at the same time allocate bandwidth for the uplink TCP data packet without bandwidth request from the SS. These schemes for bidirectional bandwidth allocation require more information about the actual SS needs to not waste the bandwidth.

For MMR networks there are a little work done to reduce the signaling overhead and delay. In [6] MSs send their bandwidth request to their super ordinate RS at their respective polling intervals. The RS collects all bandwidth requests from MSs and generates an aggregated bandwidth request to the MMR-BS. The MMR-BS, instead of allocating the bandwidth to the MSs directly, it grants bandwidth to the intermediate RS, which then allocates bandwidth to individual MSs. This scheme decreases the signaling overhead, but not decreases the delay.

The authors of [7], has defined an operation called concatenation, whereby multiple packet data units (MPDUs) can be concatenated into a single transmission burst in either uplink or downlink directions, regardless whether these MPDUs belong to the same connection or not. Also multiple service data units (MSDUs) belong to the same connection can be aggregated to form one MPDU. These schemes reduce the signaling overhead but there is still much delay.

In [10], the authors propose Extra Resource Reservation (ERR) scheme in which the MMR-BS pre-allocate some resources to the RSs for purpose of transporting control messages or data traffic. So the RS can admit its MSs without MMR-BS notification. This scheme can reduce the delay but it wastes the channel resources if the ERR is used ineffectively in the RS.

Grey theory has been widely applied to many disciplines such as economics, sociology, engineering, and so forth. The authors of [14] use the grey prediction to estimate the demand value of the electricity on line. In [15] it is used for internet access forecasting.

6. The proposed scheduling algorithm

The IEEE 802.16j support tree architecture in which all the traffic go through the MMR-BS, so it should be managed in a centralized manner. But to reduce the signaling overhead and delay its better to distribute the management of the bandwidth request in the access RS. So, our scheme manages the relay links centrally in the MMR-BS, and the bandwidth request for the end users distributed in the RS to take the advantages of both scheduling architectures.

The aims of the proposed scheduling scheme are to fully utilize the available bandwidth, and effectively respond to the demand changes of the subordinate Relay Stations.

In the proposed scheduling architecture in FIGURE 4, the MMR-BS manages its subordinate RSs as one hop stations. The same procedure is applied in the intermediate RS in the case of more than two hops, and in the access RS the conventional bandwidth request can be deployed.

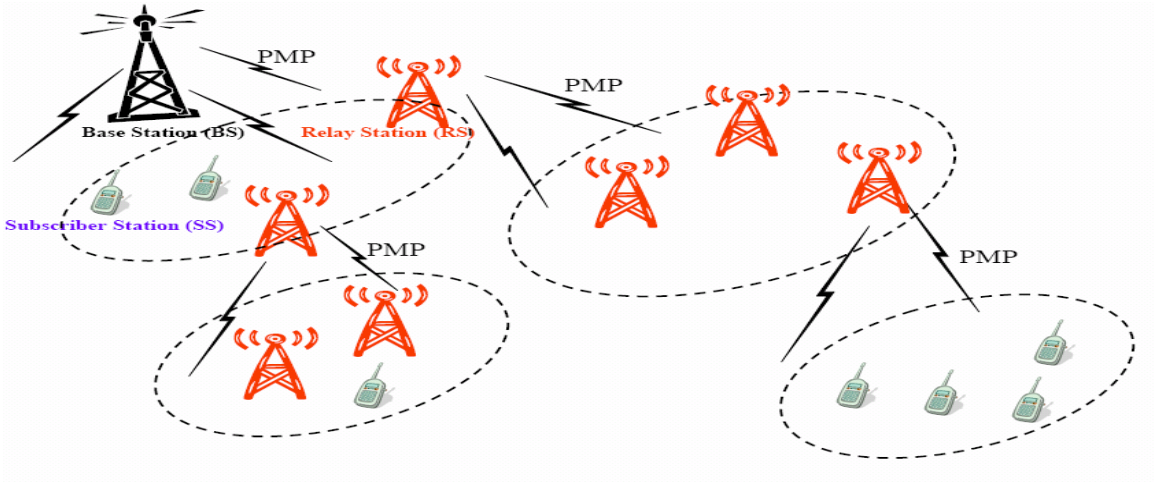

FIGURE 4: Proposed Scheduling Architecture

In this scheme the bandwidth request is not needed, instead MMR-BS measures the existing sending rate of its subordinate RSs, estimates the future demand of each RS using Grey prediction algorithm and grants them a suitable bandwidth without request.

Grey prediction theory [14] aims to find the optimized system parameters of a Grey differential equation such that the dynamic behavior of the traffic demand could be best fitted with the differential equation.

One of the major advantages of Grey prediction theory is that only small amounts of data are needed to describe the demand behavior and reveal the continuous changing in the required bandwidth.

7. The grey prediction algorithm

The grey prediction algorithm is used in the proposed scheme to estimate the required bandwidth of each RS from the previous values. In this paper, the GM (1, 1) model is adopted to perform the prediction of the required bandwidth for each RS. The standard procedure is as follows:

Step 1: Collecting the original data sequence, those are at least four consequence values of the measured traffic for the RS that is used in the estimation process.

$$x^{(0)} = \left\{x^{(0)}(1), x^{(0)}(2), \ldots\ldots .x^{(0)}(m)\right\} \qquad m \geq 4 \quad (1)$$

Step 2: Calculating an accumulated generation operation, AGO, on the original data sequence in order to diminish the effect of data uncertainty.

$$x^{(1)}(k) = \sum_{i=1}^{k} x^{(0)}(i) \qquad k = 1,2,....., \ m \qquad (2)$$

Step 3: Establishing Grey differential equation and then calculating its background values: First we define z (1) as the sequence obtained by the MEAN operation to x (1) as:

$$z^{(1)}(k) = \left[\alpha * x^{(1)}(k) + (1-\alpha)x^{(1)}(k-1)\right] \quad (3)$$

$$for \qquad k = 2,3,...m$$

Secondly Grey differential equation can be obtained the as follow:

$$x^{(0)}(k) + az^{(1)}(k) = b \qquad (4)$$

Where the parameters a, b are called the development coefficient and the grey input, respectively. The equation (5) is called the whitening equation corresponding to the grey differential equation.

$$\frac{dx^{(1)}}{dt} + ax^{(1)} = b \qquad (5)$$

Step 4: calculate the value of a, b by means of the least square method.

$$\begin{bmatrix} a \\ b \end{bmatrix} = (B^T B)^{-1} B^T x^N \qquad (6)$$

$$B = \begin{bmatrix} -z^{(1)}(2) & 1 \\ -z^{(1)}(3) & 1 \\ . & \\ . & \\ . & \\ -z^{(1)}(m) & 1 \end{bmatrix} \qquad (7)$$

Where

And $x^N = \left[x^{(0)}(2)\, x^{(0)}(3)... \ x^{(0)}(m)\right]^T \qquad (8)$

Step 5: Deriving the solution to the Grey difference equation:

$$\hat{x}^{(1)}(k+1) = \left[x^{(0)}(1) - \frac{b}{a}\right]e^{-a(k)} + \frac{b}{a} \qquad (9)$$

Where the parameter (k) is the forecasting step size and the up script "^" means the value $\hat{x}$ is a forecasting value of traffic demand.

Step 6: conducting the inverse accumulated generation operation (IAGO) on $\hat{x}^{(1)}$ to obtain a prediction value as follow:

$$\hat{x}^{(0)}(k) = \hat{x}^{(1)}(k) - \hat{x}^{(1)}(k-1) \qquad (10)$$

$$K = 2,3,....., \ n$$

Combining the equations (9) and (10) gives the predicted value of the traffic demand as stated in (11)

$$\hat{x}^{(0)}(k) = (1-e^{a})\left[x^{(0)}(1) - \frac{b}{a}\right]e^{-a(k-1)} \qquad (11)$$

Step 7: The parameters are changed and the accuracy of the estimated value is calculated using the formula:

$$e(k) = \frac{\hat{x}_i^{(0)}(k) - x_i^{(0)}(k)}{\hat{x}_i^{(0)}(k)} * 100 \ \% \qquad (12)$$

$$K <= n$$

The average error percentage can be calculated as below:

$$e = \frac{1}{(n-m)} * \sum_{k=4}^{n-1} \left\| e(k+1) \right\| * 100 \ \% \qquad (13)$$

$$m = 4, 5 or\ 6$$

The accuracy of the traffic demand prediction can be given by:

$$\varepsilon = (1 - e) * 100 \ \% \qquad (14)$$

8. Performance evaluation

In the Grey prediction, the parameter settings are highly relevant to accuracy of prediction. To get more accurate predicted value, there are three parameters should be optimized, these are: the number of modeling points , those are the previous values used in the estimation (m), the parameter α used to construct the matrix z in equation (3), and the time difference between successive estimations or the number of estimated values in a given time (n).

To evaluate the Grey prediction algorithm, we write a MATLAB program, in which the traffic sequence is generated using random function that generates traffic between 10 Kbps and 40 Kbps. Initially we begin with minimum values, in this case it's taken as 10 Kbps for all modeling points, then after each cycle we shift the old values left and insert the actual measured traffic value, and so after m cycles all the modeling points should be replaced by the actual traffic values.

In the simulation program we use the equations from (1) to (11) to estimate the next traffic value and then we used the equations from (12) to (14) to calculate the accuracy and the error percentage

We changed the time difference between the successive samples, the modeling points, and the parameter α to select the suitable values of these parameters that give best estimation accuracy. Our experimental results shows that the optimal parameters settings of the Grey prediction are that it is better to take the sampling time as short as possible or n maximum, the Modeling points maximum (m=6), and the Parameter α=0.5. The selection of this parameters give an accuracy of (ε=97.8992 %) and error of (e=2.1008 %).

The optimum parameters of Grey prediction are chosen to give the highest accuracy and then we plot the FIGURE 5 for the increasing traffic and the decreasing one.

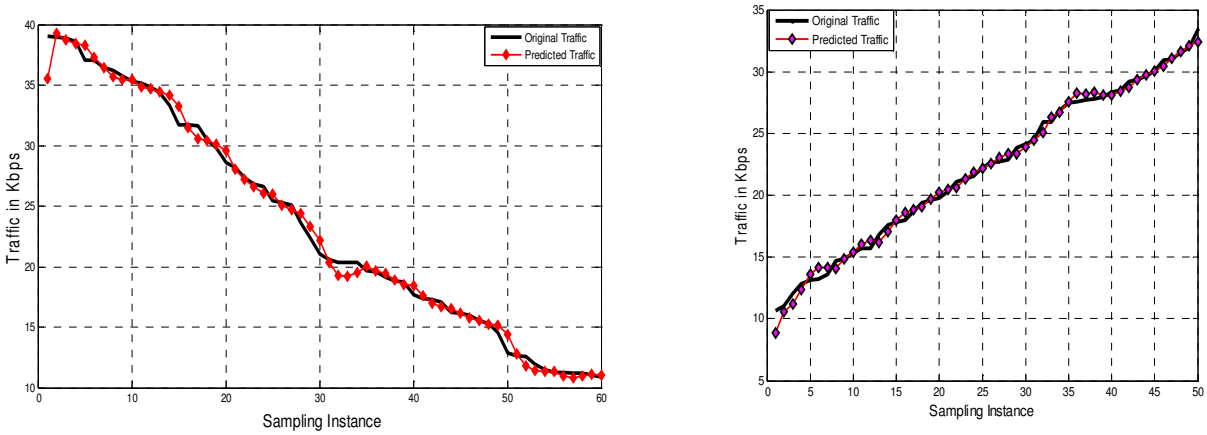

FIGURE 5: Predicted RS traffic using Grey prediction algorithm

The gained prediction accuracy makes the deployment of our scheduling algorithm to overcome the effects of the delay in MMR networks applicable. To evaluate the performance of the proposed scheduling algorithm, we assume that the RS uses the next frame to relay the data received in the current frame and there are no errors in the transmission, and the frame duration is τ =10 ms, and the number of hops is n<=10. The delay associated a data packet a cross n hops with a conventional bandwidth request scheme given by:

$$D = 4 * \tau * n \qquad (15)$$

The delay for n hops using our proposed scheduling architecture can be given by:

$$D = 4 * \tau + (n - 1) * \tau \qquad (16)$$

FIGURE 6 indicates that, as the number of hops increased the delay rapidly increased in the conventional bandwidth allocation (CBR) scheme, but in our enhanced bandwidth allocation (EBA) scheme it increased slightly. This figure shows that our algorithm can be more useful to reduce the signaling overhead and the delay when the number of hops is high.

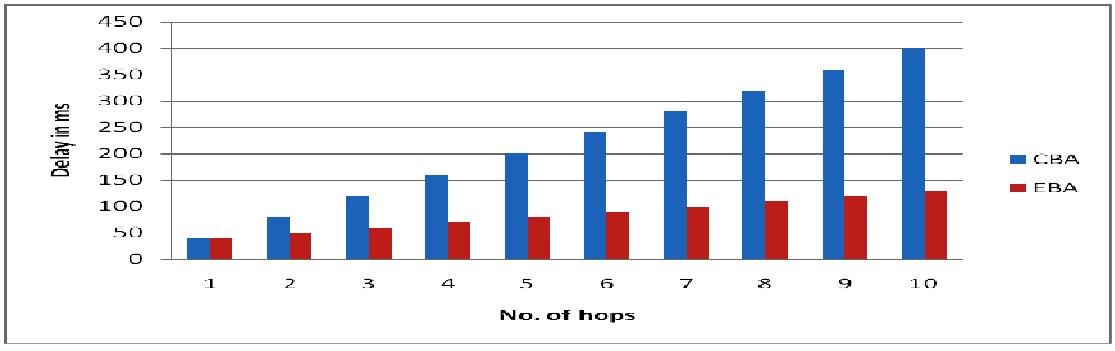

FIGURE 6: Delay in MMR network

9. Conclusion

In this paper we have presented an efficient bandwidth demand estimation to estimate the required bandwidth of the RS in IEEE 802.16j using the Grey prediction algorithm. The high accuracy offered by Grey prediction algorithm make the use of hybrid centralized and distributed

scheduling architecture applicable solution of the increased signaling overhead and delay in IEEE 802.16j MMR WiMAX networks.

In this scheme, the MMR-BS allocates bandwidth to its direct subordinate station without bandwidth request. Using this scheduling architecture, each RS can admit its subordinate SSs the required bandwidth without notification to the MMR-BS. Our scheme can reduce the delay in MMR WiMAX networks significantly.

10. References

1. Steven W. Peters and Robert W. Heath, “The future of WiMAX: Multihop relaying with IEEE 802.16j”, IEEE communication magazine, January 2009.
2. Vasken Genc, Sean Murphy, Yang Yu, and John Murphy, “IEEE 802.16j Relay Based Wireless Access Networks: An overview”, IEEE wireless communications, October 2008.
3. Bharathi Upase, and Mythri Hunukumbure, “Dimensioning and cost analysis of Multihop relay enabled WiMAX networks”, FUJITSU Sci. Tech. J., 44, 3, p.303-317(July 2008).
4. Masato Okuda, Chenxi Zhu, and Dorin Viorel, “Multihop relay extension for WiMAX Networks overview and benefits of IEEE 802.16j standard”, Fujtsu Sci. Tech. J., 44, 3, p.292-302(July 2008).
5. REWIND project, " D4.1: Summary of Network Architecture Analysis and Selected Network Architecture”, December 2008.
6. Chun Nie, Thanasis Korakis, and Shivendra Panwar, “ A Multihop polling service with bandwidth request aggregation in IEEE 802.16j networks”, 978-1- 4244-1645-5/08/2008 IEEE.
7. Zhifeng Tao, Koon Hoo Teo, and Jinyun Zhang,” Aggregation and Concatenation in IEEE 802.16j Mobile Multihop Relay (MMR) networks”, 1-4244-0957-8/07, 2007 IEEE.
8. Seungwoon Kim, Minwook Lee, and Ikjun Yeom, “ Impact of bandwidth request schemes for Best Effort traffic in IEEE 802.16 networks”, Science Direct, Computer Communications 32 (2009) 235-245.
9. Seungwoon Kim, and Ikjun Yeom, “TCP aware uplink scheduling for IEEE 802.16”, IEEE communication letters (February) (2) (2007) 146-148.
10. Junkai Zhang, Suili Feng, We Ye, and Hongcheng Zhung,” Reducing signaling overhead and latency of 802.16j service flow management”, 978-1-4244-2108-4/08, 2008 IEEE
11. Eun Chan Park, Jae Young Kim, Hwangnam Kim, and Han Seok Kim, “Bidirectional bandwidth allocation for TCP performance enhancement in IEEE 802.16 broadband wireless access networks”, WiBro system Lab, Telecommunication and networking devision, Samsung Electronics Co., LTD, Korea.
12. Noureddine Lasfar, Jeonghoon Mo, and Byongkwon Moon, “ TCP ACK Triggered bandwidth request scheme in IEEE 802.16e systems”, School of Engineering, Information and Communications University, Korea.
13. Carlos G. Bilich, “TCP over WiMAX Networks”, Wireless Access networks project number II, University of Trento, Trento, TN 38100 italy.
14. Albert W.L. Yao, S.C. Chi, “Analysis and design of a Taguchi–Grey based electricity demand predictor for energy management systems”, Elsevier, Energy Conversion and Management 45 (2004) 1205–1217.
15. Wann-Yih Wu, Shuo-Pei Chen, “A prediction method using the grey model GMC(1,n) combined with the grey relational analysis: a case study on Internet access population forecast”, Elsevier, Applied Mathematics and Computation 169 (2005) 198–217.
16. Sachin Shetty, Ying Tang & William Collani, “A Cross-Layer Packet Loss Identification Scheme to Improve TCP Veno Performance”, International Journal of Computer Networks (IJCN), Volume (1): Issue (1), November 2009.
17. Qiang Duan, Enyue Lu, “Network Service Description and Discovery for the Next Generation Internet”, International Journal of Computer Networks (IJCN), Volume (1): Issue (1), November 2009.

18. Syed S. Rizvi, Aasia Riasat, & Khaled M. Elleithy, “Deterministic Formulization of End-to-End Delay and Bandwidth Efficiency for Multicast Systems”, International Journal of Computer Networks (IJCN), Volume (1): Issue (1), November 2009.

Prediction of 28-day compressive strength of concrete on the third day using artificial neural networks

Vahid. K. Alilou ailab@srbiau.ac.ir
Department of Computer Engineering
Science and Research Branch, Islamic
Azad University, Tehran, Iran
Khvoy, 58197-38131, IRAN

Mohammad. Teshnehlab teshnehlab@eetd.kntu.ac.ir
Department of Electronic Engineering
K.N. Toosi University of Technology, Tehran, Iran
Tehran, IRAN

Abstract

In recent decades, artificial neural networks are known as intelligent methods for modeling of behavior of physical phenomena. In this paper, implementation of an artificial neural network has been developed for prediction of compressive strength of concrete. A MISO (Multi Input Single Output) adaptive system has been introduced which can model the proposed phenomenon. The data has been collected by experimenting on concrete samples and then the neural network has been trained using these data. From among 432 specimens, 300 data sample has been used for train, 66 data sample for validation and 66 data sample for the final test of the network. The 3-day strength parameter of concrete in the introduced structure also has been used as an important index for predicting the 28-day strength of the concrete. The simulations in this paper are based on real data obtained from concrete samples which indicate the validity of the proposed tool.

Keywords: Concrete, Strength, Prediction, Artificial, Neural Networks.

1. INTRODUCTION

Different sciences are developing fast in today's world. In recent decades, man has seen increased relationship of sciences in different fields and the more relationship has led to the appearance of the more new knowledge and technology. Nowadays, one of the most important problems of man are technical and engineering problems. The complexity of the most of the problems in this field has made the experts of this field use the new mathematical and modeling methods for solving this type of problems. Intelligent systems can be used as suitable tools for identifying complex systems, due to their ability of learning and adaptation.

One of the complex problems in our world is the problem of the concrete. The main criterion for evaluating the compressive strength of concrete is the strength of the concrete on 28^{th} day. The concrete sample is tested after 28 days and the result of this test is considered as a criterion for quality and rigidity of that concrete.

Concrete is the most widely used structural material in constructions in the world. Massive concreting in huge civil projects like dams, power plants, bridges and etc… usually is not practicable and it is necessary to be performed in several layers and the compressive strength of each layer should not be less than the specified compressive strength. Therefore one should wait 28 days to achieve 28-day strength of each layer of concrete. Thereupon if we have *n* layers of concrete we need $28 \times n$ days to complete the total project. [1]

2. CONCRETE

Concrete is the only major building material that can be delivered to the job site in a plastic state. This unique quality makes concrete desirable as a building material because it can be molded to virtually any form or shape. Concrete provides a wide latitude in surface textures and colors and can be used to construct a wide variety of structures, such as highways and streets, bridges, dams, large buildings, airport runways, irrigation structures, breakwaters, piers and docks, sidewalks, silos and farm buildings, homes, and even barges and ships.

The two major components of concrete are a cement paste and inert materials. The cement paste consists of Portland cement, water, and some air either in the form of naturally entrapped air voids or minute, intentionally entrained air bubbles. The inert materials are usually composed of fine aggregate, which is a material such as sand, and coarse aggregate, which is a material such as gravel, crushed stone, or slag.

When Portland cement is mixed with water, the compounds of the cement react to form a cementing medium. In properly mixed concrete, each particle of sand and coarse aggregate is completely surrounded and coated by this paste, and all spaces between the particles are filled with it. As the cement paste sets and hardens, it binds the aggregates into a solid mass.

Under normal conditions, concrete grows stronger as it grows older. The chemical reactions between cement and water that cause the paste to harden and bind the aggregates together require time. The reactions take place very rapidly at first and then more slowly over a long period of time. [2]

3. CEMENT

Cement is a material that has adhesive and cohesive properties enabling it to bond mineral fragments into a solid mass. Cement consists of silicates and aluminates of lime made from limestone and clay (or shale) which is ground, blended, fused in a kiln and crushed to a powder. Cement chemically combines with water (hydration) to form a hardened mass. The usual hydraulic cement is known as Portland cement because of its resemblance when hardened to Portland stone found near Dorset, England. The name was originated in a patent obtained by Joseph Aspdin of Leeds, England in 1824.

Typical Portland cements are mixtures of tricalcium silicate ($3CaO \bullet SiO2$), tricalcium aluminate ($3CaO \bullet Al2O3$), and dicalcium silicate ($2CaO \bullet SiO2$), in varying proportions, together with small amounts of magnesium and iron compounds. Gypsum is often added to slow the hardening process. [2,3]

4. WATER

The water has two roles in concrete mixture: First is the chemical composition with cement and perform cement hydration and second is to make the concrete composition fluent and workable. The water which is used to make the concrete is drink water. The impurity of water can have undesirable effect on concrete strength. [4]

5. AGGREGATES

Since aggregate usually occupies about 75% of the total volume of concrete, its properties have a definite influence on behavior of hardened concrete. Not only does the strength of the aggregate affect the strength of the concrete, its properties also greatly affect durability (resistance to deterioration under freeze-thaw cycles). Since aggregate is less expensive than cement it is

logical to try to use the largest percentage feasible. Hence aggregates are usually graded by size and a proper mix has specified percentages of both fine and coarse aggregates. Fine aggregate (sand) is any material passing through a No. 4 sieve. Coarse aggregate (gravel) is any material of larger size.
Fine aggregate provides the fineness and cohesion of concrete. It is important that fine aggregate should not contain clay or any chemical pollution. Also, fine aggregate has the role of space filling between coarse aggregates. Coarse aggregate includes: fine gravel, gravel and coarse gravel
In fact coarse aggregate comprises the strongest part of the concrete. It also has reverse effect on the concrete fineness. The more coarse aggregate, the higher is the density and the lower is the fineness. [3,5]

6. COMPRESSIVE STRENGTH OF CONCRETE

The strength of concrete is controlled by the proportioning of cement, coarse and fine aggregates, water, and various admixtures. The ratio of the water to cement is the chief factor for determining concrete strength as shown in figure1. The lower the water-cement ratio, the higher is the compressive strength. A certain minimum amount of water is necessary for the proper chemical action in the hardening of concrete; extra water increases the workability (how easily the concrete will flow) but reduces strength. A measure of the workability is obtained by a slump test.
Actual strength of concrete in place in the structure is also greatly affected by quality control procedures for placement and inspection. The strength of concrete is denoted in the United States by $f_c^{'}$ which is the compressive strength of test cylinder 6 in. in diameter by 12 in. high measured on the 28th day after they are made. [3]

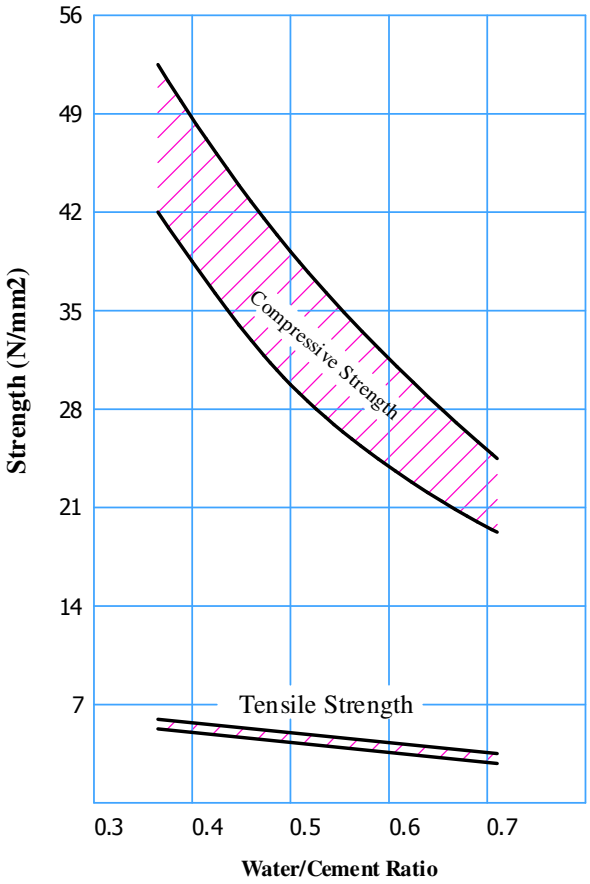

FIGURE 1: illustration of the effect of water/cement ratio in concrete strength [1]

7. CONCRETE SAMPLING

Acceptance of the concrete in the site is performed based on the results of the compressive tests of concrete samples. The concrete samples must be taken from the final consumption place.
The purpose of the concrete sampling is to prepare two specimens of concrete which their compressive tests will be performed after 28 days or in any predetermined day. To predict the 28-day compressive strength of concrete we can also have another sample to be tested earlier than 28 days. [1]

8. CONCRETE MIX DESIGN

The concrete mix design is a process of selecting the suitable ingredients of concrete and determining their most optimum proportion which would produce, as economically as possible, concrete that satisfies a certain compressive strength and desired workability. [6]
The concrete mix design is based on the principles of

- Workability
- Desired strength and durability of hardened concrete
- Conditions in site, which helps in deciding workability, strength and durability requirements

9. ADAPTIVE SYSTEMS

Adaptability, in essence, is the ability to react in sympathy with disturbances to the environment. A system that exhibits adaptability is said to be adaptive. Biological systems are adaptive systems; animals, for example, can adapt to changes in their environment through a learning process [7]. A generic adaptive system employed in engineering is shown in Figure 2. It consists of

- set of adjustable parameters (weights) within some filter structure;
- An error calculation block (the difference between the desired response and the output of the filter structure);
- A control (learning) algorithm for the adaptation of the weights.

The type of learning represented in Figure 2 is so-called supervised learning, since the learning is directed by the desired response of the system. Here, the goal is to adjust iteratively the free parameters (weights) of the adaptive system so as to minimize a prescribed cost function in some predetermined sense. [8]

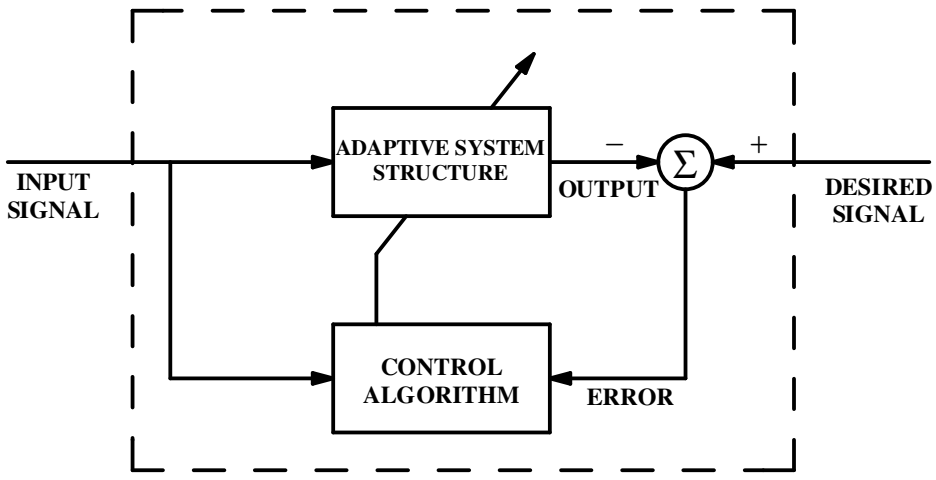

FIGURE 2: Block diagram of an adaptive system

10. ARTIFICIAL NEURAL NETWORKS

Artificial Neural Network (ANN) models have been extensively studied with the aim of achieving human-like performance, especially in the field of pattern recognition and system identification. These networks are composed of a number of nonlinear computational elements which operate in parallel and are arranged in a manner reminiscent of biological neural inter-connections.
The property that is of primary significance for a neural network is the ability of the network to learn from its environment, and to improve its performance through learning. The improvement in performance takes place over time in accordance with some prescribed measure. A neural network learns about its environment through an interactive process of adjustments applied its synaptic weights and bias levels. Ideally, the network becomes more knowledgeable about its environment after each iteration of the learning process. [7]

11. CONCRETE STRENGTH PREDICTION

To predict 28-day strength of concrete, It should identify the effective parameters of the concrete strength. The more accurately identified the parameters, the better is the result.
The studies in this paper were performed in two phases:

1. Phase one, includes the studies about the concrete and effective factors of the concrete compressive strength and also performing the experiments in the real environment and collecting data.
2. Phase two, include studies about how to use artificial neural networks to identify the presented system and to achieve accurate prediction of concrete 28-day compressive strength. [1]

12. PERFORMING EXPERIMENTS

In this study the ACI method is used to perform experiments. Experiments were performed in Aghchay dam in west Azerbaijan in IRAN. The cement used in the experiments was provided from Sofiyan cement plant and the aggregates were provided from the natural materials of the Aghchay dam site. [1]

13. COLLECTING DATA

There are lots of Parameters affect on compressive strength of concrete. But the most important parameters were collected in table 1. It is important that the range of each parameter is limited due to regarding ACI standard.

TABLE 1: Effective parameters of the compressive strength of the concrete

Row	Parameter	Unit	Range
1	Mix Design	-	A-L
2	Water/Cement Ratio	%	35.0 - 75.0
3	Density	ton/m3	2.30 - 2.60
4	Slump	mm	70 - 150
5	Air	%	1.0 - 7.0
6	Silica fumes	gr	0 - 400
7	Super-Plasticizer	kg	0.0 - 3.5
8	Age	day	3, 7, 14, 28, 42
9	Compressive Strength	kg/cm2	70.00 - 420.00

The concrete mix design is affected by these factors:
Cement, Fine aggregate, Fine gravel, gravel, coarse gravel, air

The 1st to 7th parameters are determined in the first day. There is a salient point about 8th parameter (age). As previously mentioned, the concrete age has a direct arithmetic relation with the concrete strength. The more aged the concrete the higher is the compressive strength. [1]
Here is an interesting point so that the 3-day compressive strength of concrete has a mathematical relation with the compressive strength of the same concrete in 7th, 14th, 28th and 42th day. Therefore it can be used as an important parameter for prediction of this system. In other words, the 3-day compressive strength of concrete is a very good criterion to achieve the 28-day compressive strength.
It is conceived from figure.3 that the higher the 3-day compressive strength the higher is the 28-day compressive strength of the concrete. Figure.4 shows the relationship between 3-day compressive strength and 28-day compressive strength for 4 types of concrete with variable w/c ratios, this relation is linear relatively.

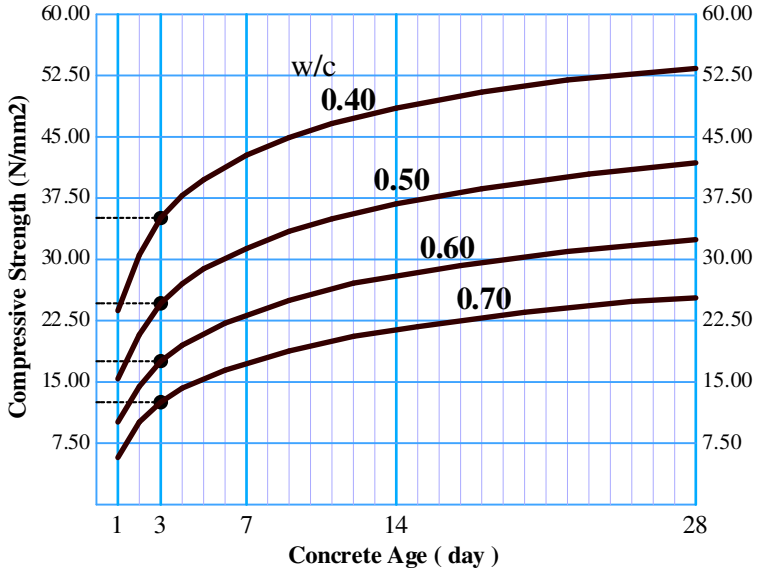

FIGURE 3: illustration of relationship between age and compressive strength of concrete [1]

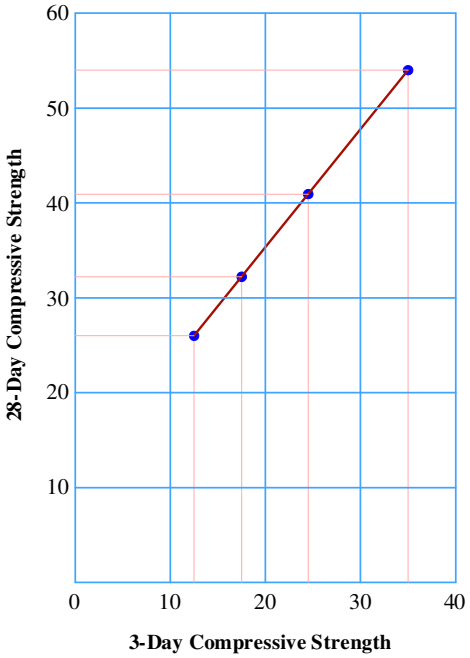

FIGURE 4: illustration of relationship between 3-day and 28-day strength of concrete [1]

14. METHODOLOGY OF CONCRETE STRENGTH NEURAL IDENTIFICATION

A methodology for concrete strength neural identification was developed. It is shown schematically in Figure 5. Three blocks can be distinguished in the scheme. Experimental results, forming a set of data on concrete, used for training and testing the neural network are an integral part of block1.

The experimental results as a set of patterns were saved in a computer file which was then used as the input data for the network in block 2. The data were divided into data for training and testing the neural network. The training patterns were randomly input into the network as following:

1. 70% of total data for training of the neural network
2. 15% of total data for validation of the neural network
3. 15% of total data for testing of the neural network,

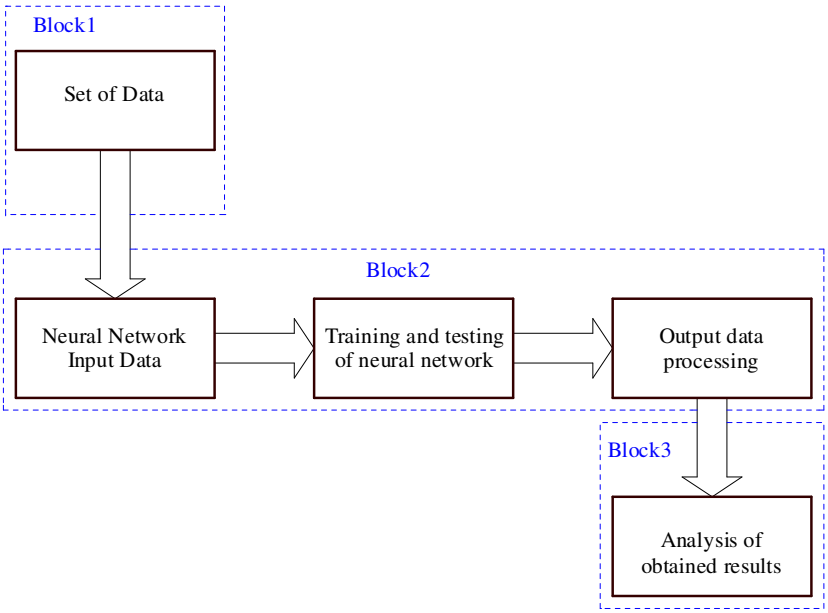

FIGURE 5: Block diagram of concrete compressive strength identification by means of neural networks [9]

If the neural network correctly mapped the training data and correctly identified the testing data, it was considered trained. The obtained results were analyzed in block 3 whose output was identified concrete compressive strength f'_c. [9]

15. FEED-FORWARD NEURAL NETWORK

The Feed-forward neural network structure for prediction of concrete compressive strength is shown in Figure 6. Feed-forward networks often have one or more hidden layers of sigmoid neurons followed by an output layer of linear neurons. Multiple layers of neurons with nonlinear transfer function allow the network to learn nonlinear and linear relationships between inputs and outputs. [10]

The process of learning with teacher in this network is executed through a back-propagation algorithm so that the network output converges to the desired output. The key distinguishing characteristic of this feed-forward neural network with the back-propagation learning algorithm is that it forms a nonlinear mapping from a set of input stimuli to a set of output using features extracted from the input patterns. The network can be designed and trained to accomplish a wide variety of nonlinear mappings, some of which are very complex. This is because the neural units in the neural network learn to respond to features found in the input. [11]

The number of input and output units is determined by dimensions of the data set whereas the number of hidden layer (M) is a free parameter which is adjusted to achieve the maximum performance. Note that, M determines the degree of freedom of the system. Therefore we expect that there was an optimum value for M. The criterion to achieve the optimum M is defined as: "The smallest M which causes minimum mse while the maximum error is small"

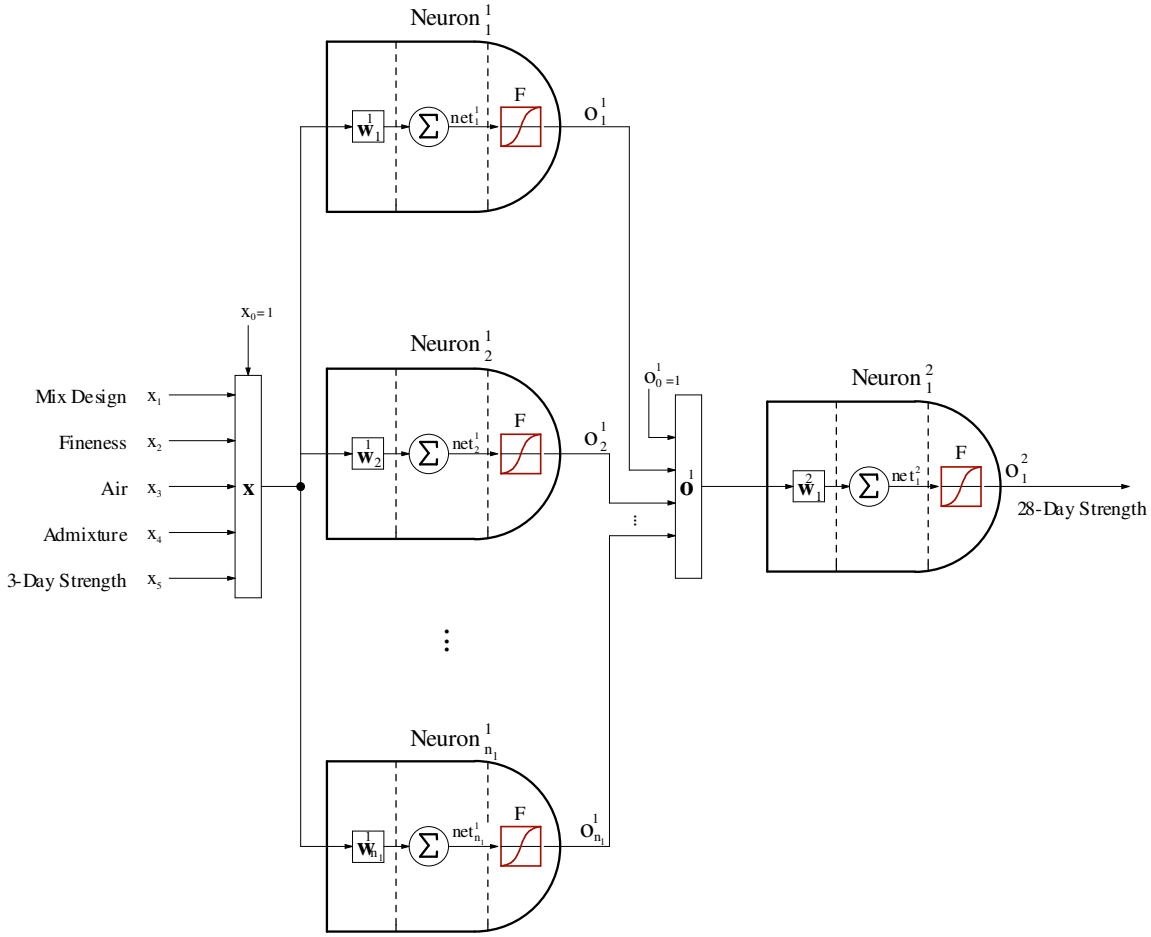

FIGURE 6: Diagram of the feed-forward neural network used for concrete compressive strength prediction

Figure.7 shows the mean squared error of the network output for validation and test data with 10 iterations for each number of hidden neurons. Figure.8 shows the maximum error between desired outputs and the network outputs with 10 iterations for each number of hidden neurons.
The optimum value in this structure is to choose *M=11* for the number of hidden neurons.
In order to backpropagage the error and update the network weights, Gradient-Descent, Quasi-Newton, Conjugate-Gradient and Levenberg-Marquardt Algorithms were used.

- Gradient Descent $W(k+1) = W(k) - \alpha_\kappa g_k$
- Quasi Newton $W(k+1) = W(k) - H_K^{-1} g_K$
- Conjugate Gradient $W(k+1) = W(k) - g_{k+1} + \alpha_\kappa \Delta W_\kappa$

Where *W* is the weight matrix, *α* is the learning rate, *g* is the gradient of error and *H* is the hessian matrix of the cost function. [12]
The levenberg-marquardt algorithm is like quasi-newton but it doesn't need to calculate hessian matrix where it can be estimated as follows:

$$H = J^T J \quad , \quad \nabla E = J^T e$$
$$W(k+1) = W(k) - [H + \mu I]^{-1} . \nabla E$$

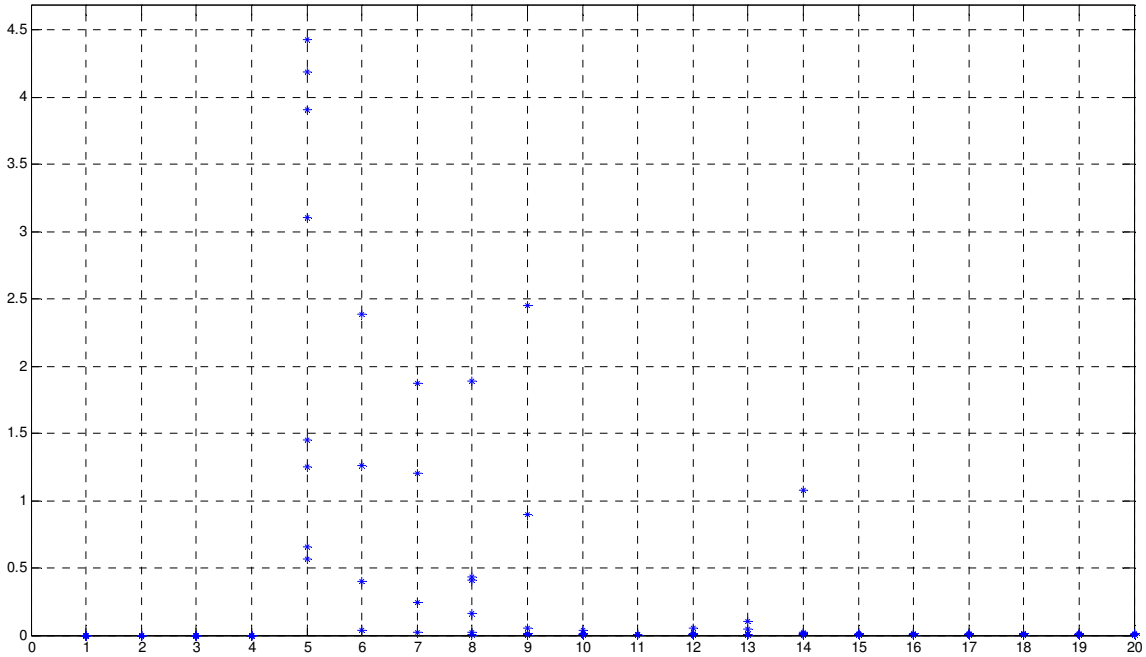

FIGURE 7: Diagram of mean squared error of the network output with 10 iterations for certain number of neurons

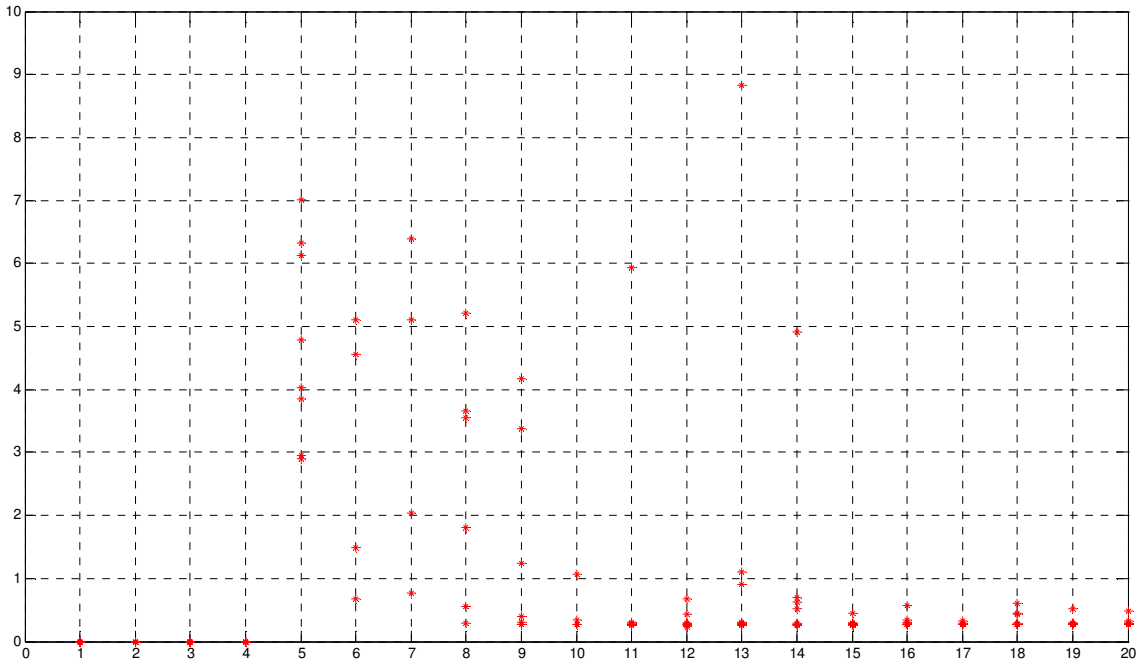

FIGURE 8: Diagram of maximum error of the network output with 10 iterations for certain number of neurons

The results of above algorithms have been collected in Table 2. Each row of the table is the result of average 40 iterations of each method. Evaluation criterion of adaptive systems was defined as following formula:

$$AveragePercentageError: APE = \frac{1}{N}\sum_{i=1}^{N}\left|\frac{e_i}{T_i}\right| * 100\%$$

Where T_i is the desired output and e_i is the output error. [13]

TABLE 2: Comparison of different algorithms used for predicting the concrete compressive strength

Row	Algorithm	Accuracy on data (%)				Ave. Time (second)
		Train	Validation	Test	Total	
1	Levenberg-Marquardt	99.436	99.389	99.397	99.407	7.7
2	Polak-Ribiere Conjugate Gradient	98.861	98.836	98.866	98.854	17.3
3	Fletcher-Powell Conjugate Gradient	98.713	98.675	98.695	98.694	12.4
4	Gradient Descent	98.584	98.567	98.606	98.586	24.3
5	Quasi-Newton	98.388	98.341	98.423	98.384	89.2
		Maximum Error (kg/cm2)				epochs
1	Levenberg-Marquardt	5.830	5.056	4.437	5.108	58
2	Polak-Ribiere Conjugate Gradient	9.686	8.536	7.652	8.635	571
3	Fletcher-Powell Conjugate Gradient	10.758	9.457	8.597	9.604	368
4	Gradient Descent	11.897	10.376	9.018	10.430	1833
5	Quasi-Newton	13.825	11.539	10.691	12.018	1999

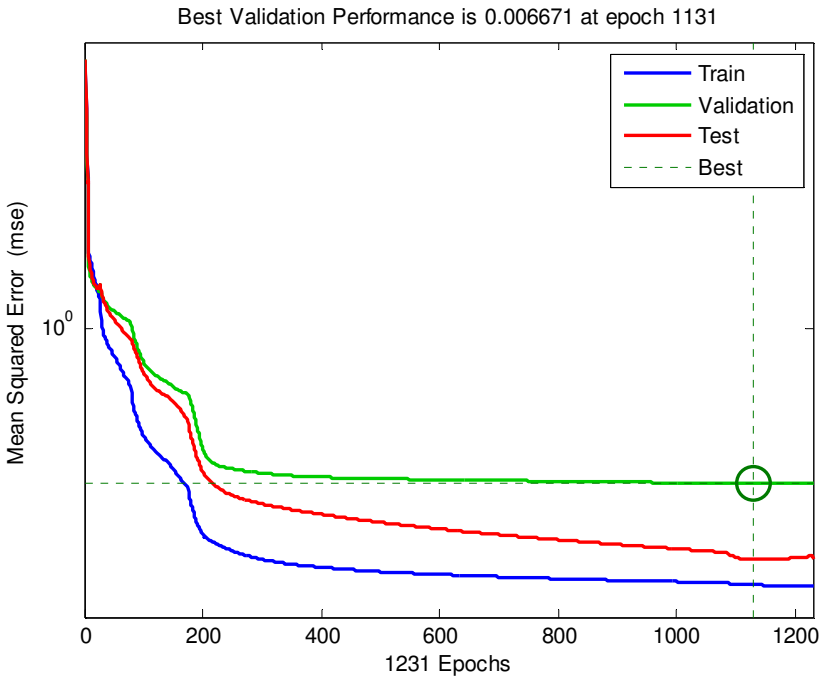

FIGURE 9: Diagram of mean squared error in the feed-forward neural network

It is conceived from table 2, that the best structure for prediction of concrete strength is the first method with levenberg-marquardt algorithm.
Figure 9 shows the mse diagram of the cost function reduction for training, validation and test data. The following results are being conceived from this figure.

1. The final mse is small and admissible
2. The test dataset error and validation dataset error are almost equal.
3. Over fitting was not happened

The diagram of figure.10 also shows the linear regression between network output and desired output for training, validation, test and total data.

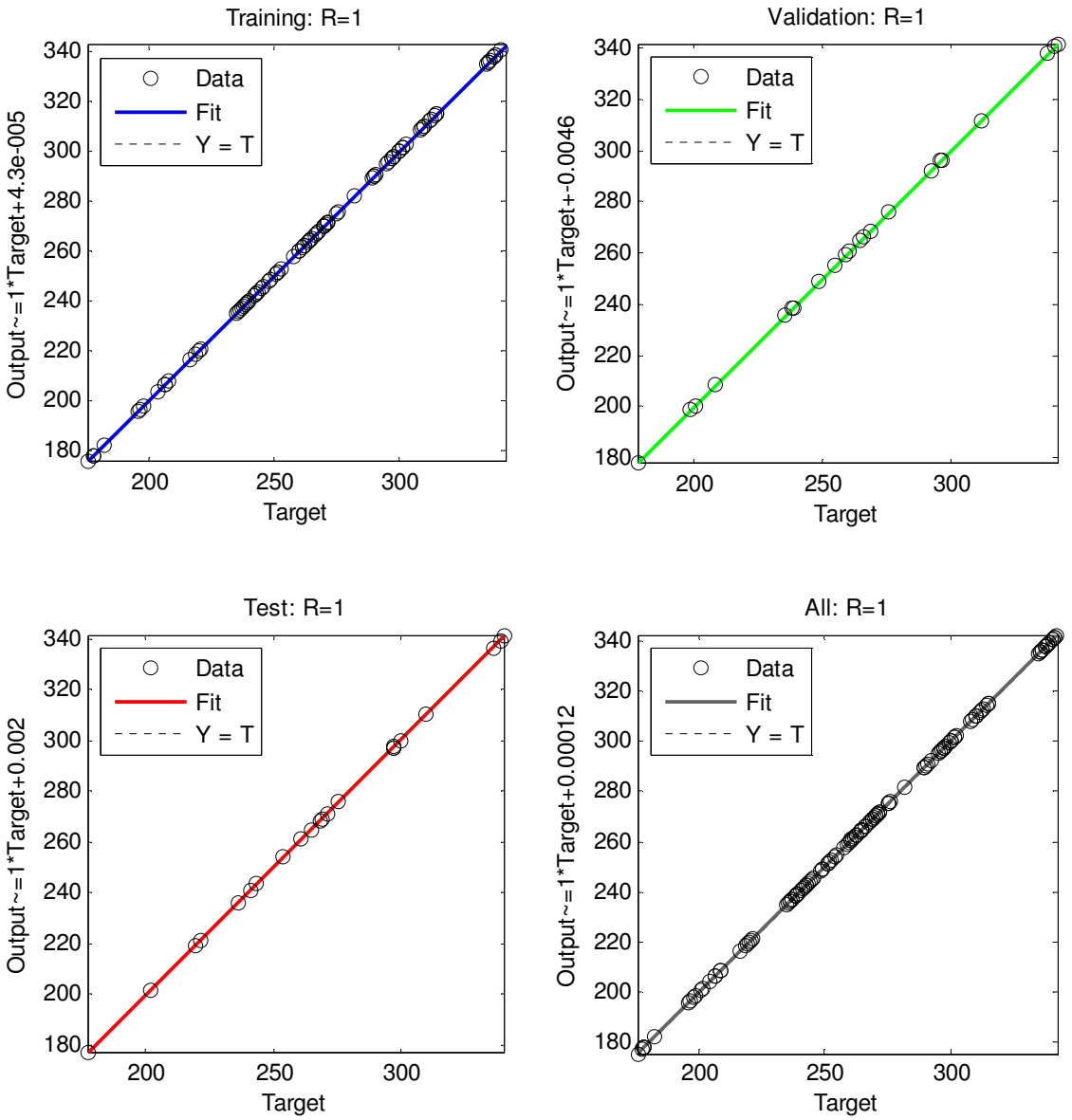

FIGURE 10: Diagram of the network output and desired output for train, validation, test and all data

16. CONCLUSION

In this paper, a practical approach has been presented for prediction of 28-day compressive strength of concrete. Basically, in all of the methods have been resented previously, the 3-day compressive strength of concrete was not considered as an important parameter.

From this point of view we can consider the proposed method as a new method in which the 3-day compressive strength parameter has been introduced as a very important index. [Ref: 13, 14, 15, 16]

The proposed technique can be used as a very useful tool for reducing the duration of the project execution in huge civil projects. For example, imagine if we have a massive concrete structure which requires 10 stages of concreting then we need at least 28×10=280 days to complete the total project regarding to standards. Therefore this project will be finished after about 1 year considering the frigid winter days which concreting is impossible.

Using the proposed tool we can have a precise prediction of the 28-day compressive strength of the concrete on the third day. Thereupon we need 3×10=30 days to complete this project and this is an important progress in order to reducing the duration of the civil projects execution.

17. REFERENCES

1. V. K. Alilou. *"Designing a learning machine for prediction of the compressive strength of the concrete by using Artificial neural networks"*. M.sc Thesis, Science and Research Branch, Islamic Azad University,Tehran,Iran, August 2009
2. *"Microsoft Encarta Encyclopedia",* Microsoft Corporation, (2009)
3. Chu Kia Wang, Charles G. Salmon. *"Reinforced Concrete Design"*, Harper & Row Publishers, USA, (1979)
4. M. Teshnehlab, V. K. Alilou, *"Concrete strength prediction using learning machine and neural networks".* In 2nd Joint Congress on Fuzzy and Intelligent Systems. Tehran, IRAN, 2008
5. J.D.Dewar. *"Computer Modeling of concrete mixture"*, E&FN Spon, LONDON, (1999)
6. Rishi. Garge. *"Concrete Mix Design using Artificial Neural Network"*. M.sc Thesis, Thapar Institute of Engineering and Technology, June 2003
7. Simon Haykin. *"Neural Networks – A Comprehensive Foundation"*, Prentice-Hall, (1999)
8. Danilo P. Mandic, Jonathon A. Chambers. *"Recurrent Neural Networks for Prediction"*, John Willey & Sons Inc., (2001)
9. Jerzy Hola, Krzysztof Schabowicz. *"Application of Artificial Neural Networks to determine concrete compressive strength based on non-destructive tests"*. Journal of civil Engineering and Management, 11(1):23-32, 2005
10. Howard Demuth, Mark Beale. *"Neural Network Toolbox"*, Mathworks, (1998)
11. Madan M.Gupta, Liang Jin, Noriyasu Homma. *"Static and Dynamic Neural Networks"*, Wiley-Interscience, (2003)
12. Martin T. Hagan, Howard B. Demuth, Mark Beale. *"Neural Network Design"*, University of Colorado Bookstore, (1996)
13. Ilker Bekir Topcu, Mustafa Saridemir. *"Prediction of compressive strength of concrete containing fly ash using Artificial Neural Networks and Fuzzy Logic"*. ScienceDirect, Computational Materials Science, 41(3):305-311, 2008
14. E. Rasa, H. Ketabchi, M. H. Afshar. *"Predicting Density and Compressive Strength of Concrete Cement Paste Containing Silica Fume Using Artificial Neural Networks"*. Scientia Iranica, 16(1):32-42, 2009
15. Jong In Kim, Doo Kie Kim. *"Application of Neural Networks for Estimation of Concrete Strength"*. KSCE Journal of Civil Engineering, 6(4):429-438, 2002
16. Ji Zong Wang, Xi-Juan Wang, Hong-Guang NI. *"An Algorithm of Neural Network and Application to Data Processing in Concrete Engineering"*. Informatica Institute of Mathematics and Informatics, 14(1):95-110, 2003

The influence of cement composition on superplasticizers' efficiency

Ghada Bassioni gbassioni@pi.ac.ae
Chemical Engineering Program
The Petroleum Institute
Abu Dhabi, P. O. Box 2533, United Arab Emirates
On leave from Chemistry Department, Faculty of Engineering
Ain Shams University
Cairo, Egypt

Abstract

Fundamental interactions between polymeric superplasticizers and cement are studied. Cements with different alite-, belite-, C_3A- and C_4AF-contents are used. The use of commercially available superplasticizers like melamine formaldehyde sulfite- (MFS) and β-naphthalene sulfonic acid formaldehyde-(NSF) resins is investigated. These superplasticizers (industrial products) are characterized by means of their molecular weights and polymeric radii, as well as by estimating the anionic charge density in water and in the cement filtrate of four CEM I cements. Application data of the eight cement-superplasticizer-combinations (heat flow calorimetry and mini-slump tests) are obtained and the surface chemistry of the superplasticizers with cement (zeta potentials and superplasticizer adsorption on cement) is studied.

Keywords: cement, superplasticizers, adsorption, zeta potential, charge density.

1. INTRODUCTION

The arising request for modern building materials that show better workability and durability can only be fulfilled by the application of different construction-chemical admixtures. Although some very good recipes have been developed e.g. for dry mix mortars, problems of compatibility between cement and organic admixtures have arisen. For this reason, the interaction of some superplasticizers on cement is studied. The results give some fundamental understanding in how far the cement industry can reduce the cement production and consequently the CO_2-emission which is of high environmental interest.

The relation between the C_3A content and naphthalene based-superplasticizers adsorption has been investigated by many researchers. It is clear that a large amount is adsorbed on C_3A of ordinary Portland cement [1]. The adsorption is also determined by the cement fineness [2]. It has been reported that hydration reactivity corresponds to high calcium aluminate contents [3, 4]. Generally, a certain amount of anionic superplasticizers are adsorbed on the surface of the cement grain or its hydrated phases to obtain a dispersing effect. The impact of these superplasticizers can be understood considering that polycondensates possess many $-SO_3^{2-}$-groups and therefore a high negative charge. The grain surface will be also negatively charged, once these superplasticizers adsorb. Due to the repulsion forces between equal charges, a good dispersing effect is obtained and reagglomeration is avoided.

The information about variation in adsorption behavior of polycondensates with the different types of cements is very important for application to give an indication about the dosages necessary related to the type of cement. In extreme cases, adsorption can be as low as 10 % and no liquefaction of the cement paste is observed. This would confirm the cement "incompatibility" with polycondensate-superplasticizers and emphasize the need for intensive research in this area. Another important factor for this "incompatibility" can rely on the type and availability (solubility) of the sulfate carrier in the cement.

The aim of this research work is to establish fundamental interactions between polymeric superplasticizers and cement. For this purpose, cements with different alite-, belite-, C_3A- and C_4AF-contents are used. The use of commercially available superplasticizers like melamine formaldehyde sulfite- (MFS) and a β-naphthalene sulfonic acid formaldehyde-(NSF) resin and four CEM I (A-D) cements of different chemical composition is investigated. The adsorption behavior of the superplasticizer on cement is studied.

2. EXPERIMENTAL

The experiments are performed with aqueous suspensions of the different cements CEM I (A-D). Their medium particle size D_{50} is determined by using laser granulometry (Cilas 1064; Co. Cilas). The densities of these cements are established by a helium pycnometer.

The MFS- and NSF- resins are industrial products and are used without further purification. The solid content of the polymeric solutions are established by using an IR-balance. The characterization of the polymers is made by GPC, coupled with a refractive index and light scattering detector. This equipment permits calculation of molecular weights and radii of the polymers. Moreover polymer solutions with a concentration of 10 mg / mL (with respect to the polymeric solid content) are prepared. The solvent used is a 0.1 mol/L $NaNO_3$ solution; pH = 12.0; adjusted with NaOH). The column material (Co. Waters) used contained three columns consecutively connected (Ultrahydrogel 120, Ultrahydrogel 250, Ultrahydrogel 500). They cover a separation area of 5,000 – 400,000 Dalton. Each sample is injected with a syringe containing a forwarded spaced filter (0,2 µm) in a 2-mL-GPC-sample holder, out of which the GPC-apparatus injects 100 µL into the system. Therefore the polymeric solution needed for one run is 1.0 mg. The evaluation is carried out with the GPC-Software Astra 4,908 (Co. Wyatt Technologies). To calculate the averaged molecular weights, a 3rd order fit is used.

The anionic charges of the superplasticizers under investigation are measured by means of the particle charge detector PCD 03 pH (Co. Mütek). 100 mL standard solutions of polymeric concentration of 200 mg/L are used. The filtrates of cement pastes with a w/c-value necessary to produce a flow value of 18 ± 0.5 cm (mini-slump test) are used as a solvent for the polymers to measure the anionic charge in the pore solution. The charge density is determined by means of a titration experiment with the polymer poly-dadmac (0.001 N), a cationic polyelectrolyte.

Adsorption measurements are carried out at RT by determining the organic carbon content via High TOC II analyser (Elementar) of the centrifugate (20 min at 8500 rpm) previously produced from the cement pastes with polymeric admixtures.

The zeta potentials of the cement pastes with different amounts of polymers are measured using Model DT-1200 electroacustic spectrometer (Dispersion Technology, Inc.). The following mixing procedure is used to prepare the cement pastes: cement is added to water (according to the necessary w/c-value) within 1 min. This paste is let sit for one more minute. Then, the mixture is vigorously stirred for 2 min in a casserole by using a spoon. The filtrate is taken for the measurement of the ionic background of the cement paste that is subtracted from the zeta potential values of the cement pastes containing the polymers.
To estimate the flow value, the superplasticizer dosages given in table 6 are poured into the mixing water in a porcelain casserole. After cement is added, the resulting paste is poured into a

VICAT-ring (h = 40 mm, $d_{inner,above}$ = 70 mm, $d_{inner,below}$ = 80 mm). After lifting up the VICAT-ring the diameter of the paste is determined.

3. RESULTS AND DISCUSSION

3.1 Characterization of the four types of cement

The analysis of the four types of cement is performed by using the Rietveld analysis- method. The results are listed in (table 1).

TABLE 1: Rietveld analysis of the cements CEM I (A-D).

Cement type / Mineral Phase	CEM I (A)	CEM I (B)	CEM I (C)	CEM I (D)
Alite	67.3	60.1	69.8	61.0
Belite	10.9	22.4	6.9	22.0
C3A (cub.)	5.7	2.3	1.3	0.4
C3A (orth)	5.6	0.0	4.6	1.1
Na2O	0.27	0.21	0.18	0.27
K2O	0.67	0.63	0.72	1.27
C4AF	1.7	12.2	6.8	14.0
Al2O3	4.47	3.55	3.63	4.15
Fe2O3	1.2	4.56	2.38	2.46
CaSO4*2H2O	0.1	2.5	0.1	1.1
CaSO4	2.5	0.0	2.4	0.0
CaO free	0.3	0.2	1.1	0.3
w/c	0.6	0.46	0.47	0.6

It can be seen that CEM I (C) has the highest alite content, while CEM I (B) & (D) comparably have the highest belite content. The highest C3A content, whether cubic or orthorhombic, is found for CEM I (A).

3.2 Characterization of the superplasticizers

The solid content determined by an IR-balance is found to be 38.71 % and 8.47 % for MFS- and NSF- resins, respectively. The pH-values of the polymeric solutions differed slightly from one another and found to be 8.47 in case of MFS-resin and 7.47 for the NSF-resin.

The GPC- analysis of the MFS-resin is listed in (table 2). Because the NSF-superplasticizer NSF-resin could not be analyzed chromatographically in aqueous medium because of adsorptive effects with the column material, a "batch"-measurement is carried out. The polymer samples of different concentrations are injected directly into the cell of the light scattering detector. Adsorptive Interactions of the polymers with the column are excluded. The "batch"-measurement gave the weight-average molecular weight M_w, the z-average radius of gyration Rg_z as well as the QELS (quasi elastic light scattering) – correlation function of the average hydrodynamic radius $Rh_{(avg)}$. Because of the absence of concentration information out of the refractive index detector, no values for M_n, M_z, Rg_n, Rg_w, Rh_n, Rh_z and polydispersity are obtained.

The "batch"-analysis via ZIMM-Plot is successful using double extrapolation. The first extrapolation occurs on the concentration zero. This is necessary to eliminate the intermolecular

interactions, because the scattered light intensity of a single molecule should be measured. The second extrapolation occurs on the scattering angle zero to eliminate the intramolecular influence. In the ZIMM-Plot all measured points are applied and connected to straight lines. From the slope of these straight lines the values of the 2nd virial coefficient A2 and the z average radius of gyration Rg_z are obtained. With this information the weight-average molecular weight M_w of the NSF-resin could be deduced (table 3). It is clear that the molecular weights of the polycondensates are very high. The molecular weights and the polymeric radii lie within expectations [5].

TABLE 2: GPC-Analysis of MFS-resin and "batch" - analysis of the NSF-resin.

Property	**MFS – resin**	**NSF – resin ("Batch"-analysis)**
Molecular weight [g/mol] Mn	77670	
Molecular weight [g/mol] Mw	109800	193500 (4 %)
Poly-dispersity [Mw/Mn]	1.41	
R.M.S. Radius (Rg) [nm] Rgn	12.0	
R.M.S. Radius (Rg) [nm] Rgw	13.5	
R.M.S. Radius (Rg) [nm] Rgz	16.9	38.7 (8 %)
QELS Hydro dynamic Radius moment [nm] Rhn	7.5	
QELS Hydro dynamic Radius moment [nm] Rhw	8.4	
QELS Hydro dynamic Radius moment [nm] Rhz	10.7	
QELS Hydro dynamic Radius moment [nm] Rh(avg)	5.8	

According to the calculated Burchard-Parameter ($[Rg_z/ Rh_{(avg)}] = 2.56$) it is found that the MFS-resin in solution lies in form of steady chains.

3.3 Estimation of the specific anionic charge density

The results of the specific anionic charge density measurements are found in figure 1.

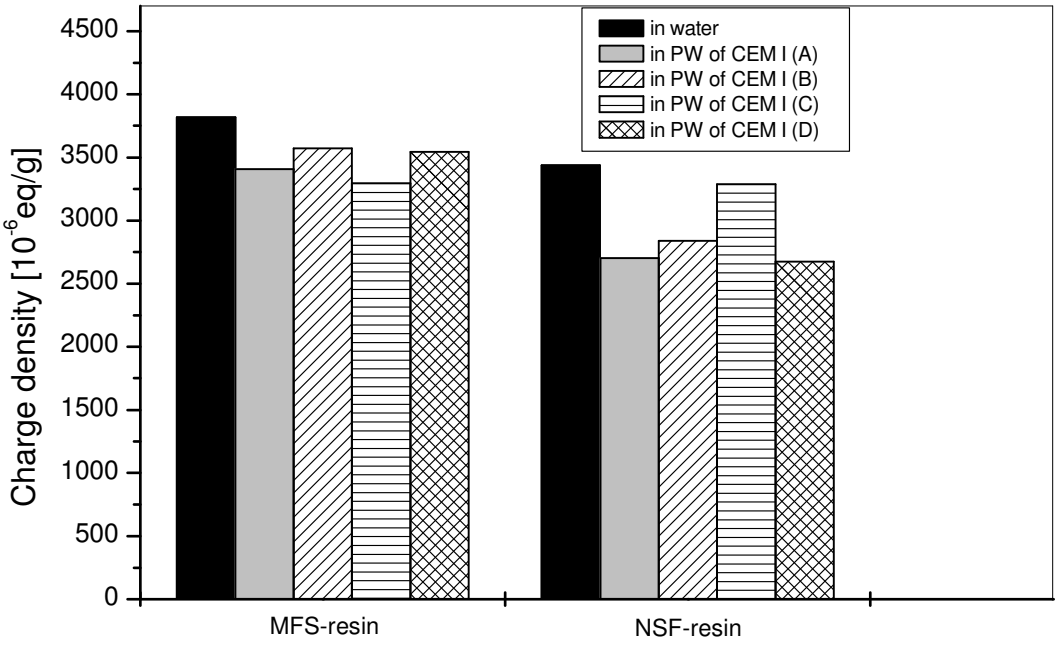

FIGURE 1: Anionic charge densities of the superplasticizers.

As expected, the polycondensates (MFS and NSF) show in salt free water as well as in the pore water of the four cements very high anionic charge densities.

While in water, the anionic charge density of the superplasticizers appear higher than in the different pore waters of the cements under investigation, due to the fact that pore water contains Ca^{2+} ions which form complexes with the superplasticizers. The two superplasticizers behave differently depending on the amount of free Ca^{2+} ions present in the pore solution and the affinity to form complexes with them.

3.4 Liquefying effect of the superplasticizers

The dosage (w.r.t cement) for each superplasticizer is estimated according to that necessary to produce a flow value of 26 ± 0.5 cm (mini-slump test). The blank value is a cement paste with a w/c-value for which the flow value is 18 ± 0.5 cm. By adding each superplasticizer, the dosage is adjusted so that a flow value of 26 ± 0.5 cm is obtained. The water content in the polymeric solutions is considered.

The dosages necessary to obtain a flow value of 26 ± 0.5 cm are similar for both polycondensates (table 6). Among all cements *CEM I (B)* is liquefied the best i.e. with the least dosage of superplasticizer, the best result is obtained. This is attributed to its low C_3A-content. Comparable behaviour is given by *CEM I (A).*

The cements *CEM I (C)* and *CEM I (D)* need much higher dosages.

TABLE 3: Dosages of the superplasticizers necessary to obtain a flow value of 26 ± 0.5 cm.

Cement; w/c	MFS-resin	NSF-resin
CEM I (A); w/c = 0.6	0.15 %	0.15 %
CEM I (B); w/c = 0.46	0.12 %	0.1 %
CEM I (C); w/c = 0.47	0.25 %	0.25 %
CEM I (D); w/c = 0.6	0.25 %	0.25 %

This can be explained by the high sulfate content - especially the rapidly soluble sulfates like arcanite. The free sulfate adsorbs on the surface of cement hydration phases and prevents the superplasticizers to adsorb and function as liquefiers [6]. Another reason for the bad compatibility of the superplasticizer with cement is the free CaO content.

3.5 Estimation of the superplasticizers adsorption on cement

First, the TOC-content in the pore solution without superplasticizer is estimated as background. Then the superplasticizer dosages listed in table 3 are examined by adsorption measurements determining the TOC-content in the filtrate of non-adsorbed superplasticizer. Subtraction from starting dosages leads to the amount adsorbed. The results are shown in figure 2.

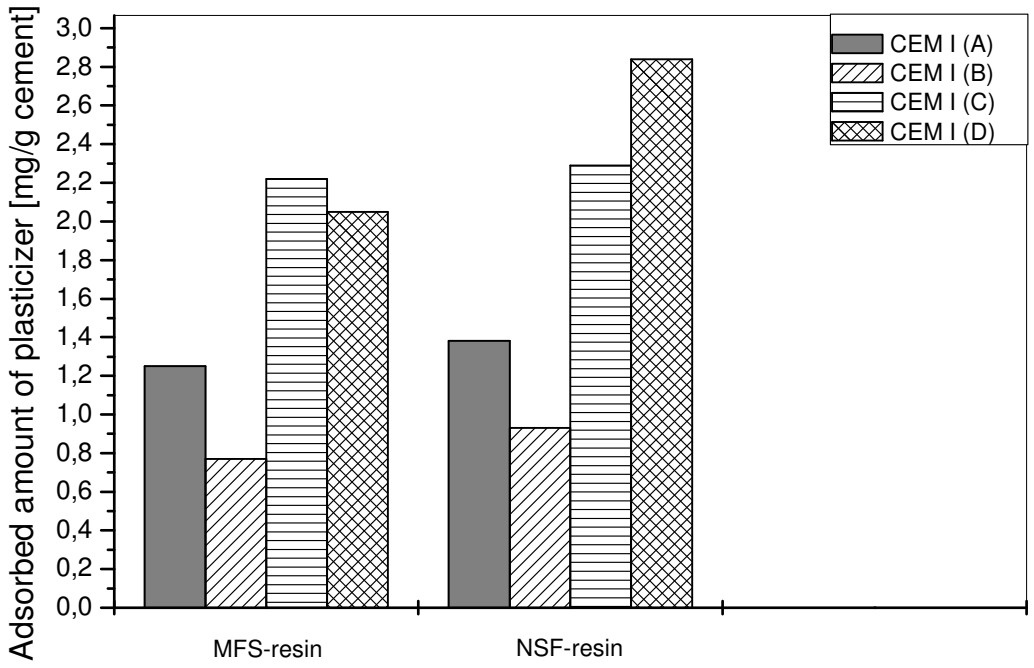

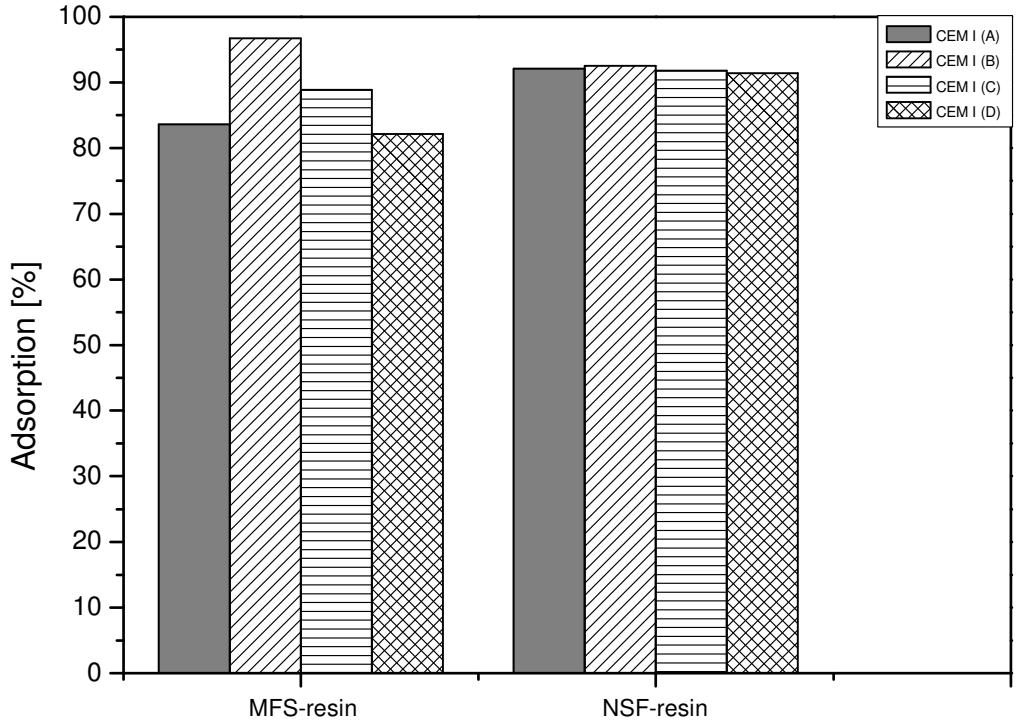

FIGURE 2: Adsorbed amount of superplasticizers in mg/g cement (above) and percent adsorption of the superplasticizers (below).

As expected, the C_3A-poor cement *CEM I (B)* adsorbed the least amount of superplasticizers, while *CEM I (C)* and *CEM I (D)* adsorbed the most. These results are consistent with the finding about dependence of adsorbed amount on the formation of ettringite [7]. In accordance with this, the high contents of sulfate and free CaO of *CEM I (C)* resulted in a high consumption of superplasticizers although it has a moderate C_3A-content.

Regarding the adsorbed amount of superplasticizers, the adsorption behaviors of MFS-resin und NSF-resin are very similar. The values of percental adsorption of these products indicated their limited function as superplasticizers (bad slump loss – behavior). These superplasticizers are good for precast concrete, because they show a high starting liquefaction of cement pastes with low dosages.

3.6 Zeta potential measurements

The zeta potentials are determined first without then with superplasticizer (figure 3) according to the dosages listed in table 3. The physical data needed to execute such experiments are given in as follows:
CEM I (B) - (D) have a density of 3.14 g/ cm^3, while CEM I (A)'s density is 3.12 g/ cm^3. The particle sizes D50 [µm] of the CEM I (A) – (D) are 7.5, 11.28, 17.49 and 8.81, respectively.

The zeta potential of the cement pastes are -2.6 mV for CEM I (A), -8.3 mV for CEM I (B), -1.9 mV for CEM I (C) and -2.8 mV for CEM I (D) without superplasticizers addition (figure 3). The zeta potentials of the pure cements depend on their C_3A-content. Cements with higher C_3A- and sulfate contents can form higher amounts of ettringite during the hydratation process which

shows a stronger positive zeta potential [8]. *CEM I (C)* has the least negative zeta potential of -1.9 mV. Apparently, this cement builds more ettringite due to its very high sulfate content than the *CEM I (A)*, which is richer in the C_3A-content. This effect is even more intensified due to the fact, that *CEM I (C)* possesses the biggest particle size. In the contrary to that, *CEM I (B)* shows a very negative zeta potential, because it can form less ettringite. Besides it has a higher content of silicates that produce a negative surface charge.

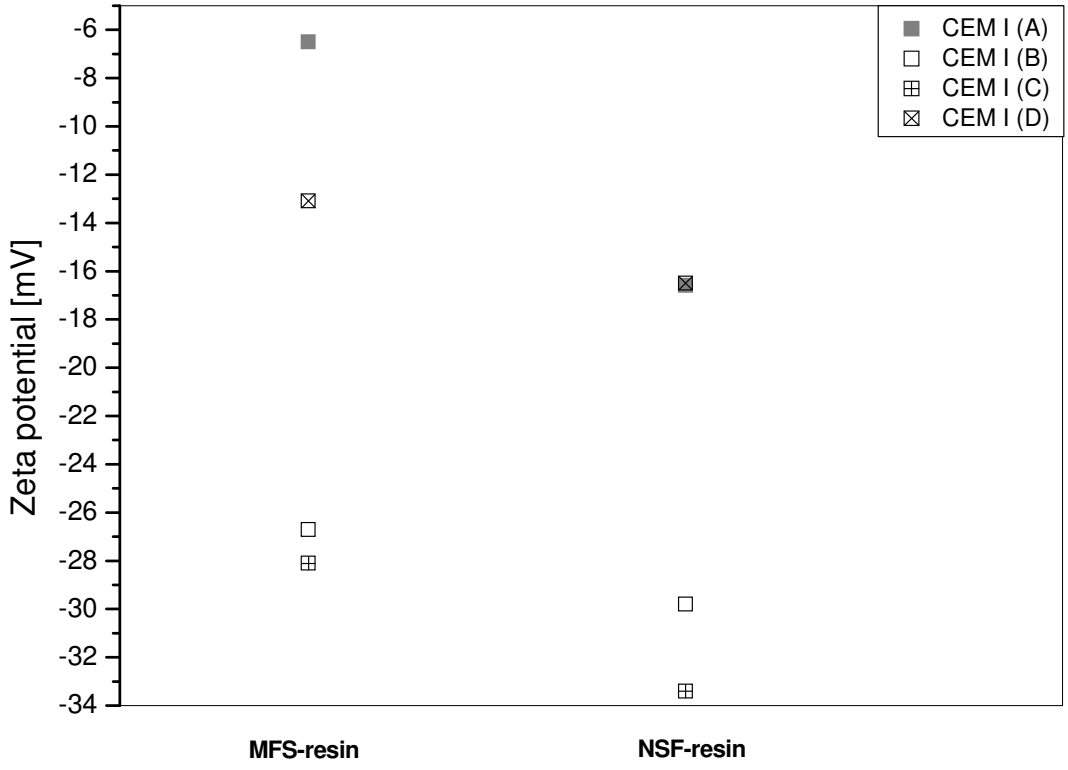

FIGURE 3: Zeta potentials of the superplasticizers on the four cements CEM I (A-D).

3.7 Heat flow calorimetry

For the evaluation of a probable retarding effect of superplasticizers, the samples are prepared according to the dosages listed in table 3 with the different types of cement. Regarding the data obtained from the heat flow calorimetry (figures 4 and 5), all cements are not retarded by the superplasticizers under investigation. Nevertheless, remarkable are the differences in the maximum heat of hydration of the pure cements. The results showed the coherence to the C_3A- and sulfate contents. Astonishing is the low heat of hydration of *CEM I (C)*. This can be attributed to the relatively big particle size of 17.49 µm.

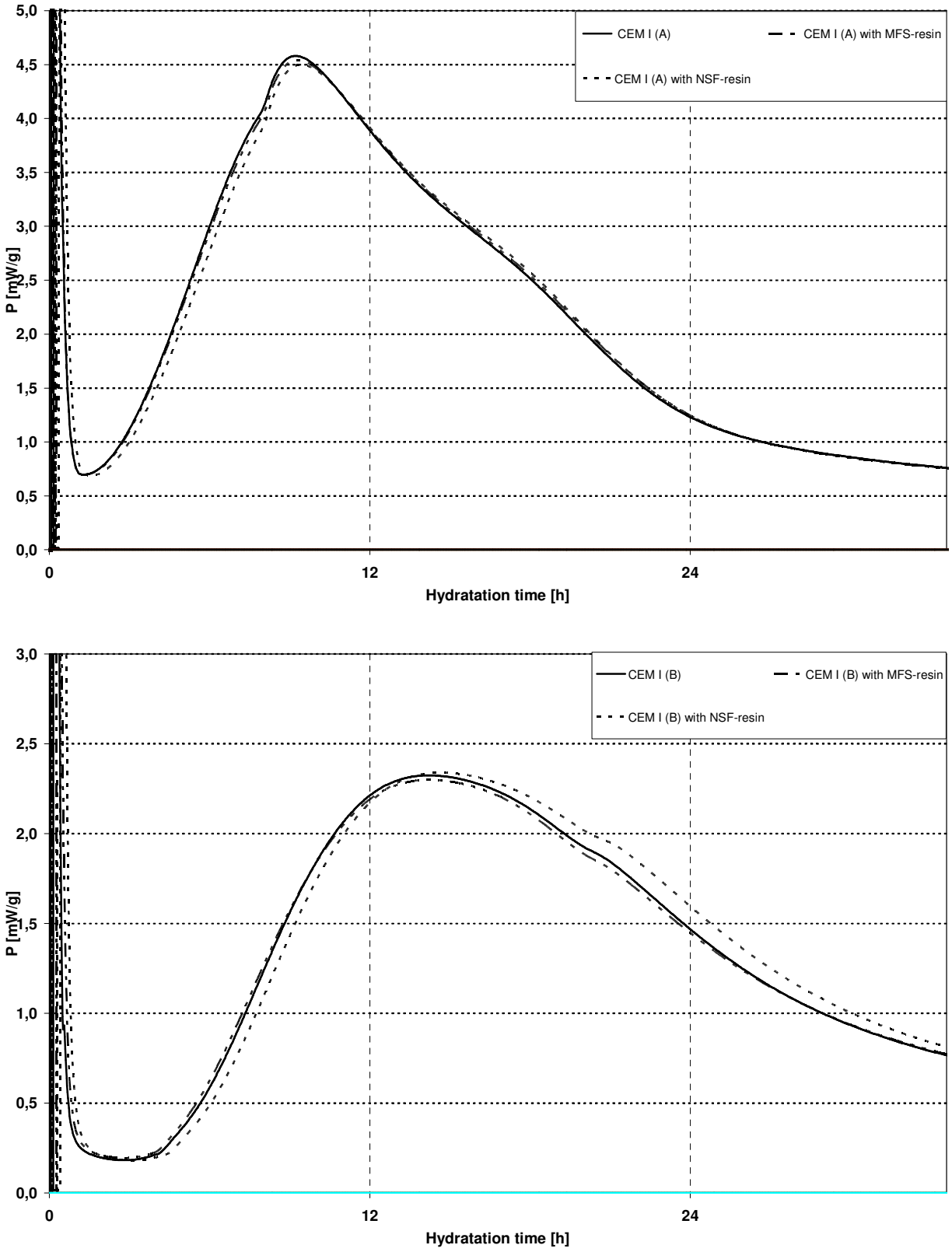

FIGURE 4: Heat flow calorimetry of the superplasticizers with CEM I (A) (above) and CEM I (B) (below).

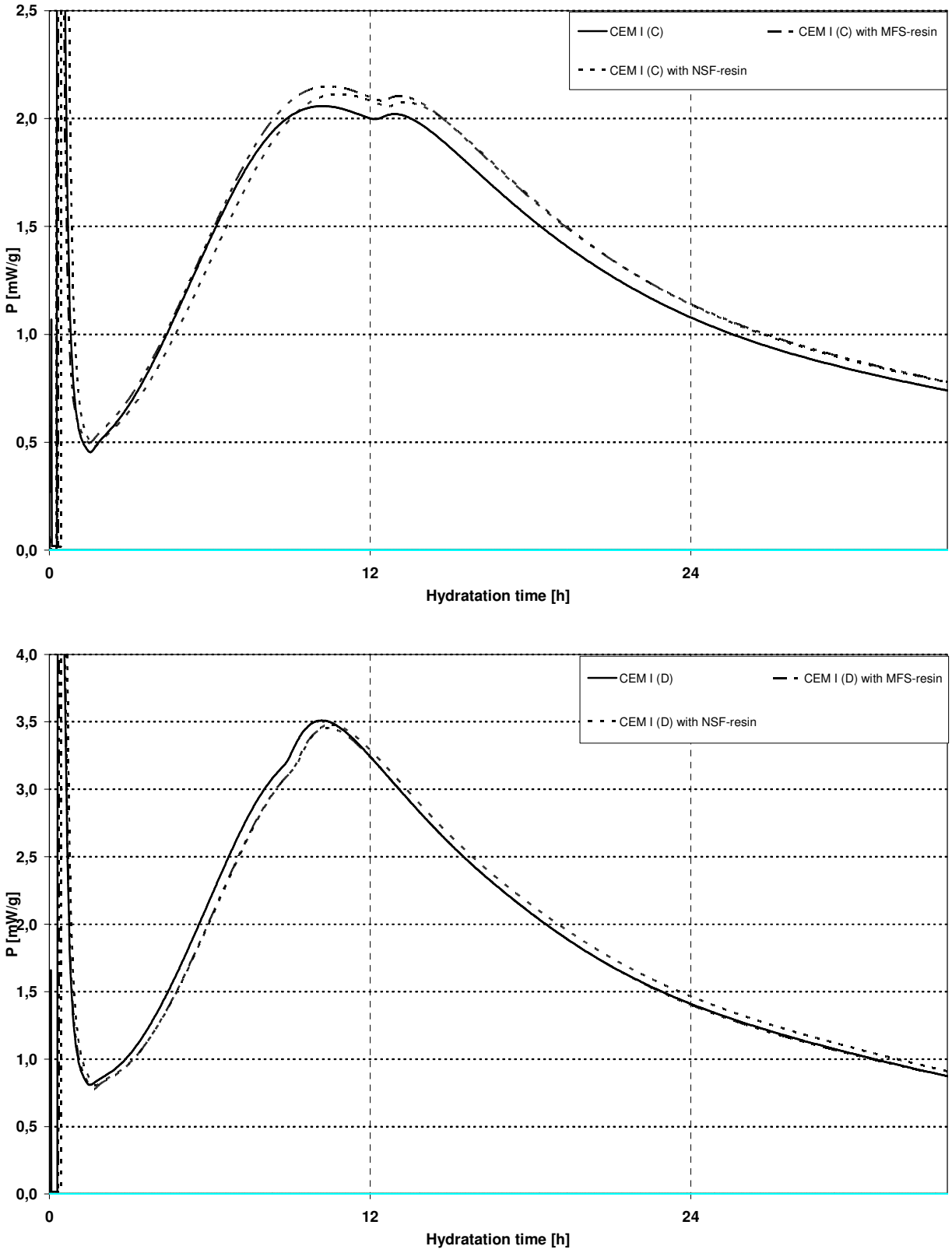

FIGURE 5: Heat flow calorimetry of the superplasticizers with CEM I (C) (above) and CEM I (D) (below).

4. CONSLUSION & FUTURE WORK

The interaction of two superplasticizers with four different types of cement is studied. Characterization of the polycondensates, MFS- and NSF-resins, showed that they have very high molecular weights. In solution, the MFS-resin lies as a steady chain according to the Burchard-Parameter. The adsorption behavior is affected by the anionic charge of the polymers in water and in the pore solutions of the four cements: The higher the anionic charge, the better the adsorption [9]. On the basis of low C_3A-content it is observed that *CEM I (B)* shows the best liquefying effect. The two cements *CEM I (C)* and *CEM I (D)* need higher dosages of superplasticizers to obtain the same result due to their high content of sulfate and free CaO. The adsorbed amounts of the superplasticizers in mg / g cement correlated with the dosages to obtain a flow value of 26 ± 0.5 cm. The C_3A-poor cement *CEM I (B)* adsorbed in all cases the least amount of superplasticizer. Regarding the heat flow values, no significant differences are observed for the cement combinations with superplasticizers. The results give an insight in how far the cement production (and consequently the CO_2 -emission) can be minimized by using admixtures which give good workability and compatibility which is of high environmental value.

5. REFERENCES

[1] a) S. Suzu, E. Okada and K. Hattori, *"Adsorption of superplasticizers on cement"* CAJ Review, 108-110, 1981. b) S. Goyal, M. Kumar, B. Bhattacharjee, *"Effect of relative proportion of pozzolana on compressive strength of concrete under different curing conditions*", Int. J. Eng., 2(1): 20-34, 2008.

[2] E. Asakura, H. Yoshida and H. Nakae, *"Influence of superplasticizers on fluidity of fresh cement paste with different clinker phase composition"*, In Proceedings of 9th Int. Cong. Chemistry of Cement, New Delhi, India, 5: 570-576, 1992.

[3] K. Yamada, S. Ogawa and S. Hanehara, *"Working Mechanism of Poly-Beta-Naphthalene Sulfonate and Polycarboxylate Superplasticizer Types from Point of Cement Paste Characteristics"*, In Proceedings of. 6th CANMET/ACI Int. Conf. on Superplasticizers, Nice, France, 195: 367-382, 2000.

[4] a) E. Sakai, J. K. Yamada and A. Ohta, *"Molcular Structure and Dispersion-Adsorption Mechansims of Coomb-Type Superplasticizers used in Japan"*, J. Adv. Concr. Tech. 1(1): 16-25, 2003. b) P. P. Bansal, M. Kumar, S. K. Kaushik *"Effect Of Wire Mesh Orientation On Strength Of Beams Retrofitted Using Ferrocement Jackets*", Int. J. Eng. 2(1): 8-19, 2008.

[5] G. Bassioni, *"Global warming and Construction Aspects"*, In Proceeding of the 7th International Scientific and Practical Conference on Environmental Technology Resources, Rezekne, Latvia, 2: 78-86, 2009.

[6] G. Bassioni, J. Plank, *"Untersuchungen zur kompetitiven Adsorption anorganischer Anionen am Modellsystem Kalksteinmehl"*, GDCh Monographie, 36: 225-232, 2006.

[7] J. Plank, G. Bassioni, Z. Dai, H. Keller, B. Sachsenhauser, N. Zouaoui, *"Neues zur Wechselwirkung zwischen Zementen und Polycarboxylat-Fließmitteln"*, ibausil-Tagungsband, 16: 579-598, 2006.

[8] a) J. Plank, Ch. Hirsch, *"Superplasticizer Adsorption on Synthetic Ettringite"*, In Proceedings of 7th CANMET/ACI Conference on Superplasticizers in Concrete, Berlin, Germany, 217: 283-298, 2003. b) A. Elazhary, Hassan Soliman, *"Analytical Investigation of the Flow Hydrodynamics in Micro-Channels at High Zeta Potentials*", Int. J. Eng., 3(3): 267-279, 2008.

[9] J. Plank, G. Bassioni, *"Adsorption of Carboxylate on $CaCO_3$ surface"*, Z. Naturforsch. B, 62b: 1277-1284, 2007.

The Effect of a Porous Medium on the Flow of a Liquid Vortex

Fatemeh Hassanipour fatemeh@utdallas.edu
Department of Mechanical Engineering
University of Texas at Dallas
Richardson, TX 75080, USA

Jose L. Lage
Department of Mechanical Engineering jll@lyle.smu.edu
Southern Methodist University
Dallas, TX 75205, USA

Abstract

This study investigates the predominant criteria in the persistence or decay of vortex flows in porous media. A simple approach is used to build a pair of vortices in a fluid. The vortices impinge on a permeable wall, thus allowing a study of the interaction of vortices with the porous medium. New insights are obtained, among them that permeability has a more important effect on this interaction compared with either porosity or the vortex transport velocity.

Keywords: vortex flow, porosity, permeability

1. INTRODUCTION

Modeling and simulation of vortical flow through permeable (porous) media are essential for the design of new devices and the prediction of a myriad of natural and man-made processes, such as metal (alloy) processing, beach erosion, forest fires, snow avalanche, grain storage, underground flow, and alveolar respiration. In forestry, accurate simulation of turbulent air flow through the vegetative porous medium can predict the spread of forest fires as well as the spreading of seeds that result in biodiversity. Dispersion of smog in heavily built cities can be accurately modeled by turbulent flow in porous media. The aerial spreading of hazardous substances in a city is similarly modeled, with applications in homeland security. Detection of biological and biochemical compounds in permeable fabrics via turbulent air “puffs” is yet another application. In energy exploration, the flow of oil and gas along a radial-inward path in an oil well is accelerated by turbulence arising as the flow reaches a more permeable region (the well).

Our study involves vortex flows and porous media, two subject matters that can individually be complex and interesting on their own. The issue of vortex flow in porous media begins with transition from laminar flow behavior to turbulence flow. Transition to turbulence in porous media is among the interesting topics reviewed by Getachew et al [1] who discussed several experimental studies related to transition to turbulence in porous media, and by Inoue et al [2]. Vortex rings are also used by other investigators to unveil the basic structure of a turbulent round jet by Lau and Fisher [3] and the dynamics of coherent structures in turbulent boundary layers by

Lim [4]. Moreover, Chu and Falco [5] used laminar vortex rings interacting with an inclined, moving wall to reproduce some of the features observed in turbulent boundary layers. In addition to laminar vortex rings, other investigations have studied the entrainment, growth, and turbulence production in turbulent vortex rings to better understand the role of coherent structures in turbulence by Maxworthy [6], Glezer et al. [7] and Olcay et al.[8]. However, the behavior of vortex flow in porous media has not been directly studied.

The interaction of vortex flows and porous media is on the cutting edge of knowledge in fluid mechanics. Vortex flows are inherently nonlinear and are known to display intriguing behavior while interacting with boundary conditions and various flow conditions. Porous media also with their various morphologies are a challenging area of ongoing study. When these two subject areas come together, an even richer set of conditions emerge and, as shown by the analysis in the sequel, display interesting behaviors.

The current study investigates the transport of large vortical structures through permeable obstructions. The focus on large-scale vortical structures is motivated by their intricate local transport behavior depending on the characteristics of the permeable obstruction. This study aims at building a protocol for predicting the behavior of vortical flow based on permeable media and flow characteristics. Numerical simulations demonstrate the effect of permeable media properties and vortex strength on the transport of vortex flow in porous medium.

2. MODEL CONFIGURATION

A simplified two-dimensional model is used, shown in Figure 1. The vortex ring generator is a piston–cylinder mechanism located in a 160 x 60 x 60 cm water tank. The cylinder is 50 cm long with a diameter of 5cm, which is used to produce a finite-duration jet pulse. The jet velocity program is trapezoidal to create a vortex flow, Fig 2.

The vortex ring impinges to a 40 x 20 x 20 cm porous medium located within 40 cm in front of it. Porous media with various morphologies are characterized by the porosity $(\emptyset)$ and permeability (K).

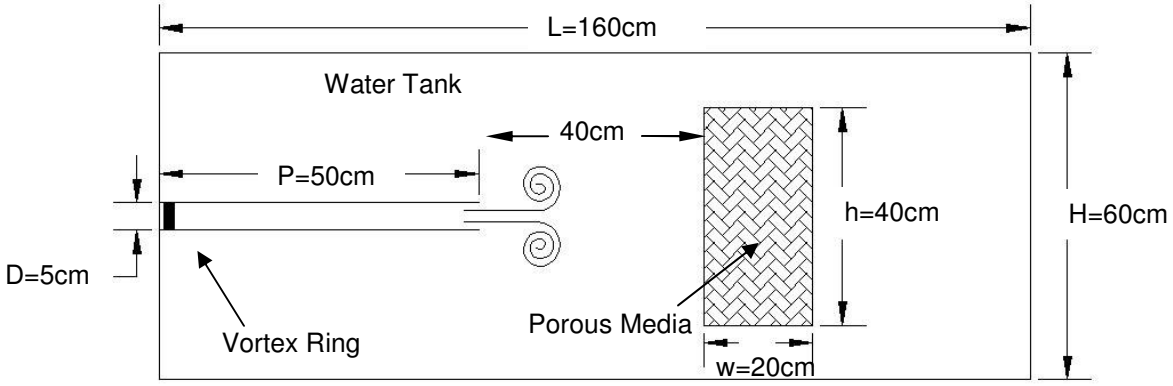

FIGURE 1: Schematic model configuration

The test is repeated with two different velocities of 0.179 $\frac{m}{s}$ and 0.058 $\frac{m}{s}$. Jet Reynolds number (Re) is calculated based on the piston's maximum velocity(U), piston diameter (D) and the fluid viscosity (ν), namely,

$$Re_j = \frac{UD}{\nu} \qquad (1)$$

Two velocity profiles by the vortex ring generator are:

Case 1: Re (jet)=9000

$$\begin{cases} u(t) = 0.324 * t & \text{if} \quad t < 0.554 \\ u(t) = 0.179 & \text{if} \quad 0.554 \leq t \leq 4.978 \\ u(t) = -0.323 * t + 1.79 & \text{if} \quad t > 4.978 \end{cases} \qquad (2)$$

Case 1: Re (jet)=3000

$$\begin{cases} u(t) = 0.104 * t & \text{if} \quad t < 0.554 \\ u(t) = 0.058 & \text{if} \quad 0.554 \leq t \leq 4.978 \\ u(t) = -0.104 * t + 0.577 & \text{if} \quad t > 4.978 \end{cases} \qquad (3)$$

These profiles are obtained based on the extracted data from experimental set up made.

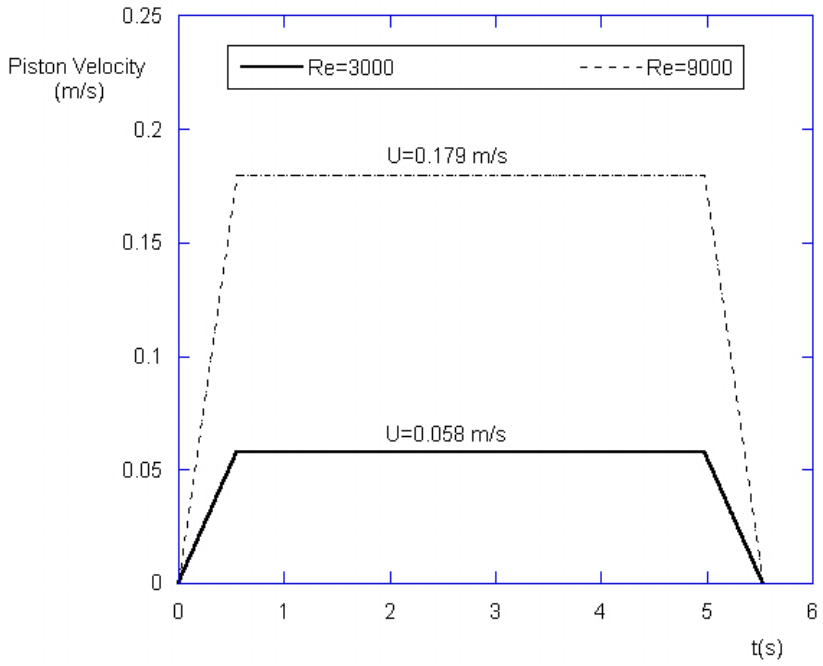

FIGURE 2: Typical Trapezoidal piston velocity for Re=3000 and Re=9000

3. THEORETICAL FORMULATION

The general equation for fluid flow through an isotropic, rigid, homogenous porous medium is Brinkman-Hazen-Dupuit-Darcy equation: [1]

$$0 = -\nabla(\phi\bar{p}) + \mu_e\nabla^2 u' - \left[\frac{\mu}{K}\phi u' + C\rho\phi^2|u'|u'\right] \qquad (4)$$

Observe that Equation 4 has six physical properties: fluid density ρ, fluid dynamic viscosity μ, effective viscosity μ_e , permeability K , form coefficient C , and porosity ϕ. The latter is defined as:

$$\phi = {A_f}/{A_t} \qquad (5)$$

A_f is the area occupied by the fluid and A_t is the total volume of the mateiral. Parameter ρ, μ, ϕ can be measure independently but the other three namely μ_e, K and C depends on the geometry of the permeable medium. They cannot be measured directly, nor calculated analytically, because there is no model relating them to more basic (measurable) quantities valid for all porous media. In principle, these quantities should be obtained simultaneously by matching the solution of Equation 4 to experimental data.

The Brinkman-Hazen-Dupuit-Darcy equation also has an alternative form where C is replaced by $\frac{C_f}{\sqrt{K}}$. The constant C_f is often takes the value 0.55.

$$C = \frac{C_f}{\sqrt{K}} \qquad (6)$$

In our study K varies from 10^{-8} to 10^{-2}. Porosity changes from 0.2 to 0.8, and the value for C varies accordingly, as listed in Table 1.

$K\ (m^2)$	ϕ	$C\ (1/m)$
$10^{-8} \rightarrow 10^{-2}$	$0.2 \rightarrow 0.8$	$5.5 \rightarrow 5500$

TABLE 1: Tables Representative of porous media properties

4. SIMULATION

A structured grid technique is adopted for accelerating the convergence to the steady-state. As a reference criterion, average vorticity of the flow is calculated by numerical methods to achieve an optimum grid (ΔG) and time interval (Δi) size. Vorticity (ω) is found mathematically at a point for each element of fluid that is a vector and is defined as the curl of the velocity

$$\vec{\omega_i} = \vec{\nabla} \times \vec{V_i} = \left(\frac{\partial v_i}{\partial x} - \frac{\partial u_i}{\partial y}\right) \qquad (7)$$

The average vorticity, $\vec{\omega}_{avg}$ in a small region of fluid flow is defined as the circulation around the boundary of the small region, divided by the area A of that region.

$$\vec{\omega}_{avg} = \frac{\sum_{i=1}^{n} \vec{\omega_i}}{w \times h} \qquad (8)$$

Where w and h are the porous medium dimensions.

In Table 2, representative results for ω_{avg} show that the optimum grid size of 0.5 cm and interval time of 0.125 seconds are good values for running the simulation.

ΔG (cm)	Δi (s)	1/s)
1.00	0.500	0.0086
0.50	0.500	0.0118
0.25	0.500	0.0104
1.00	0.250	0.0080
0.50	0.250	0.0096
0.25	0.250	0.0093
1.00	0.125	0.0078
0.50	0.125	0.0093
0.25	0.125	0.0092

TABLE 2: Representative grid and time interval accuracy for Re=9000

The mathematical formulation for the vortex flow behavior in porous media is solved by the finite volume method with successive over-relaxation. The Solver method is segregated and second-order accurate in space. The porous media object is modeled by the addition of a momentum source term to the standard fluid flow equations. The source term is composed of two parts: a viscous loss term (Darcy) and an inertial loss term:

$$0 = -\nabla(\phi\bar{p}) + \mu_e \nabla^2 u' + [S_i] \qquad (8)$$

where $$S_i = \left(\frac{\mu}{\alpha} v_i + C_2 \frac{1}{2} \rho |v|_{mag} v_i\right) \qquad (9)$$

α is the permeability, $\frac{1}{\alpha}$ is the viscous resistance coefficient (1/m2), and C_2 is the inertial resistance factor (1/m). If we compare Equations 4,8 and 9, then:

$$\frac{\mu}{K}\phi = \frac{\mu}{\alpha} \quad \rightarrow \quad \frac{1}{\alpha} = \phi\frac{}{K} \qquad (10)$$

and

$$C_2 \frac{1}{2} \rho = C\rho\phi^2 \quad \rightarrow \quad C_2 = 2C\phi^2 \qquad (11)$$

Table 3 shows the modified values based on the new parameters in Equation 8 for running the simulation to investigate the transport phenomena of vortex flow in porous media.

Re	ϕ	$K\ (m^2)$	$C\ (1/m)$	$C_2\ (1/m)$	$\frac{1}{\alpha\left(\frac{1}{m}^2\right)}$
3000	0.2	10^{-2}	5.5	0.44	0.2×10^2
3000	0.2	10^{-8}	5500	440	0.2×10^8
3000	0.8	10^{-2}	5.5	7.04	0.8×10^2
3000	0.8	10^{-8}	5500	7040	0.8×10^8
9000	0.2	10^{-2}	5.5	0.44	0.2×10^2
9000	0.2	10^{-8}	5500	440	0.2×10^8
9000	0.8	10^{-2}	5.5	7.04	0.8×10^2
9000	0.8	10^{-8}	5500	7040	0.8×10^8

TABLE 3: Properties of various porous media and vortex strength used in simulation

5. RESULTS

Numerical analysis and simulations are performed to illustrate the transport of vortical flow with various velocities through porous media with various morphologies. The significance, expansion, contraction and separation of vortex flow is distinguishable in color-coded figures. Table 4 lists these figures and their relevant parameters.

Figure	Re	$K(m^2)$	ø
3-a	3000	10^{-2}	0.2
3-b	3000	10^{-8}	0.2
3-c	3000	10^{-2}	0.8
3-d	3000	10^{-8}	0.8
3-e	9000	10^{-2}	0.2
3-f	9000	10^{-8}	0.2
3-g	9000	10^{-2}	0.8
3-h	9000	10^{-8}	0.8

TABLE 4: Vortex flow experiments and their parameters

In our numerical experiments, Reynolds number changes from 3000 to 9000 and porous media are used with different permeability and form-coefficient.

In Figure 3(a,c), vortex flow passes through the porous media for the minimum Reynolds number and maximum permeability. While propagating into the porous object, the lower vortex ring expands and partly blocks the upper vortex from traveling. Observation shows that the amount of porosity affects proportionally the size of vortex expansion.

For the same low Reynolds number but minimum permeability, the vortex pair does not pass through the porous object. The vortices mostly survive and return to the fluid with identical velocities. As observed in Fig. 3(b,d) separation of vortex rings does not occur. Investigation shows that in low permeability porous media and small Reynolds number flows, porosity has no effect on the behavior of vortex flow.

In another test, the Reynolds number was increased to 9000 and simulations repeated with the same porous permeability and porosities. When permeability is at maximum, the lower vortex ring expands, covers the whole porous medium and propagates through. Due to this quick expansion, it prevents the upper vortex from passing through the porous medium and makes it bounce back before making contact with the porous media. Returning to the flow, the upper vortex breaks into smaller vortexes in front of the porous object. Results show that the size and quantity of the split vortices are proportional to the porosity of the domain. See Fig. 3(e,g).

For the same Reynolds number of 9000 but minimum permeability, both vortex rings bounce back. In both porosities, a part of the lower vortex passes the porous medium and creates a new small vortex behind the porous medium (see Fig.3(f,h)). So, porosity does not affect the flow term when the Reynolds number is large and permeability of the porous medium is very low.

If compare the four figures, we observe that regardless of Reynolds number, vortex flows bounce back and cannot pass through a low-permeability porous medium. However, Reynolds numbers affect the expansion, breaking and return velocity of vortex rings. Permeability also plays an important role in the transport of vertical flow in the porous domain.

Figure 5 also shows the process of vortex flow movement in the porous media for case 1 and 8 for a duration of 312 seconds. Shots are taken in equal time intervals. Simulation reveals the areas in the domain that are more susceptible to the vortex streamlines.

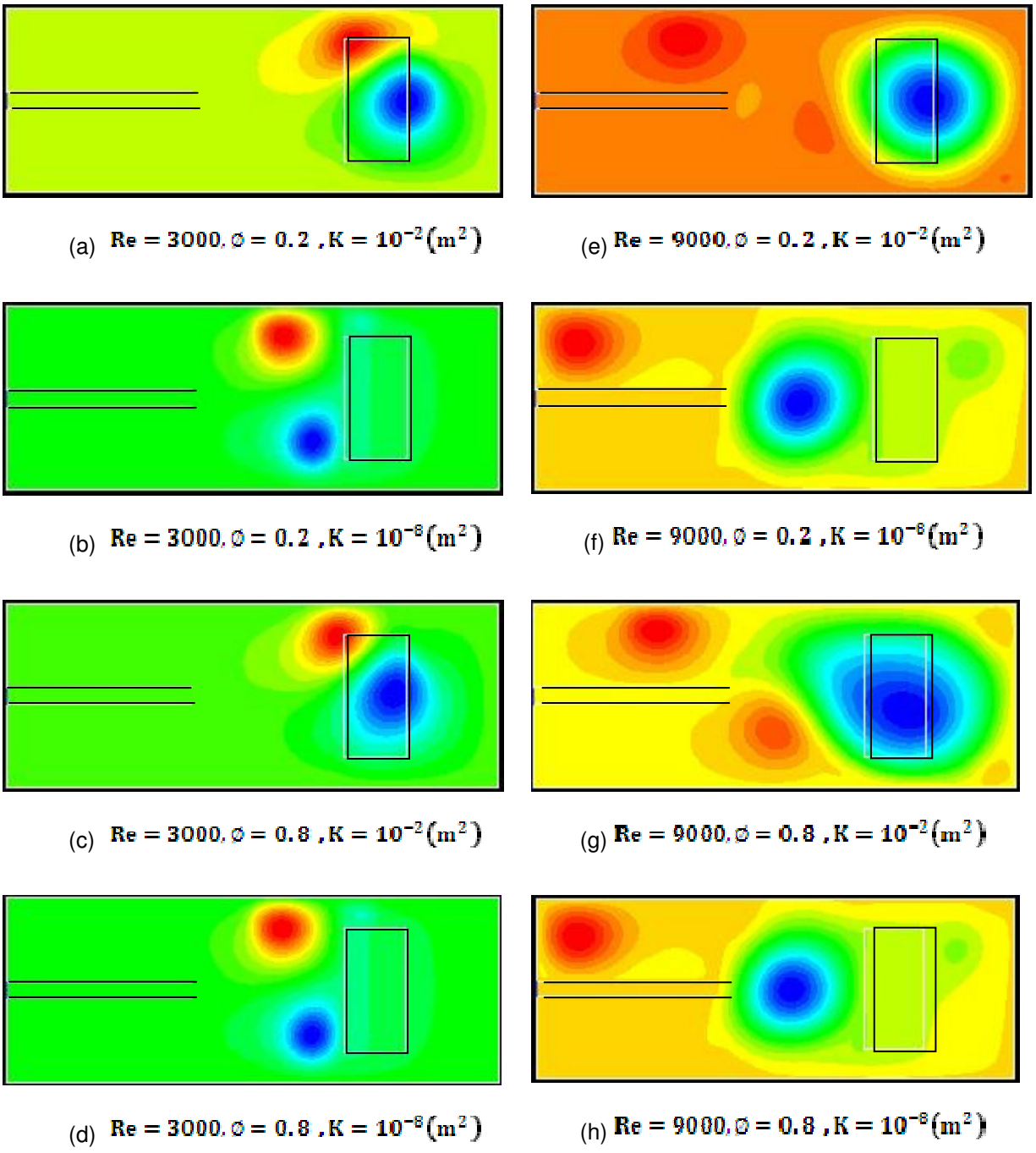

(a) $\mathbf{Re = 3000, \varnothing = 0.2\ , K = 10^{-2}(m^2)}$

(e) $\mathbf{Re = 9000, \varnothing = 0.2\ , K = 10^{-2}(m^2)}$

(b) $\mathbf{Re = 3000, \varnothing = 0.2\ , K = 10^{-8}(m^2)}$

(f) $\mathbf{Re = 9000, \varnothing = 0.2\ , K = 10^{-8}(m^2)}$

(c) $\mathbf{Re = 3000, \varnothing = 0.8\ , K = 10^{-2}(m^2)}$

(g) $\mathbf{Re = 9000, \varnothing = 0.8\ , K = 10^{-2}(m^2)}$

(d) $\mathbf{Re = 3000, \varnothing = 0.8\ , K = 10^{-8}(m^2)}$

(h) $\mathbf{Re = 9000, \varnothing = 0.8\ , K = 10^{-8}(m^2)}$

FIGURE 3: Local transport behavior of vertical flow in porous domain

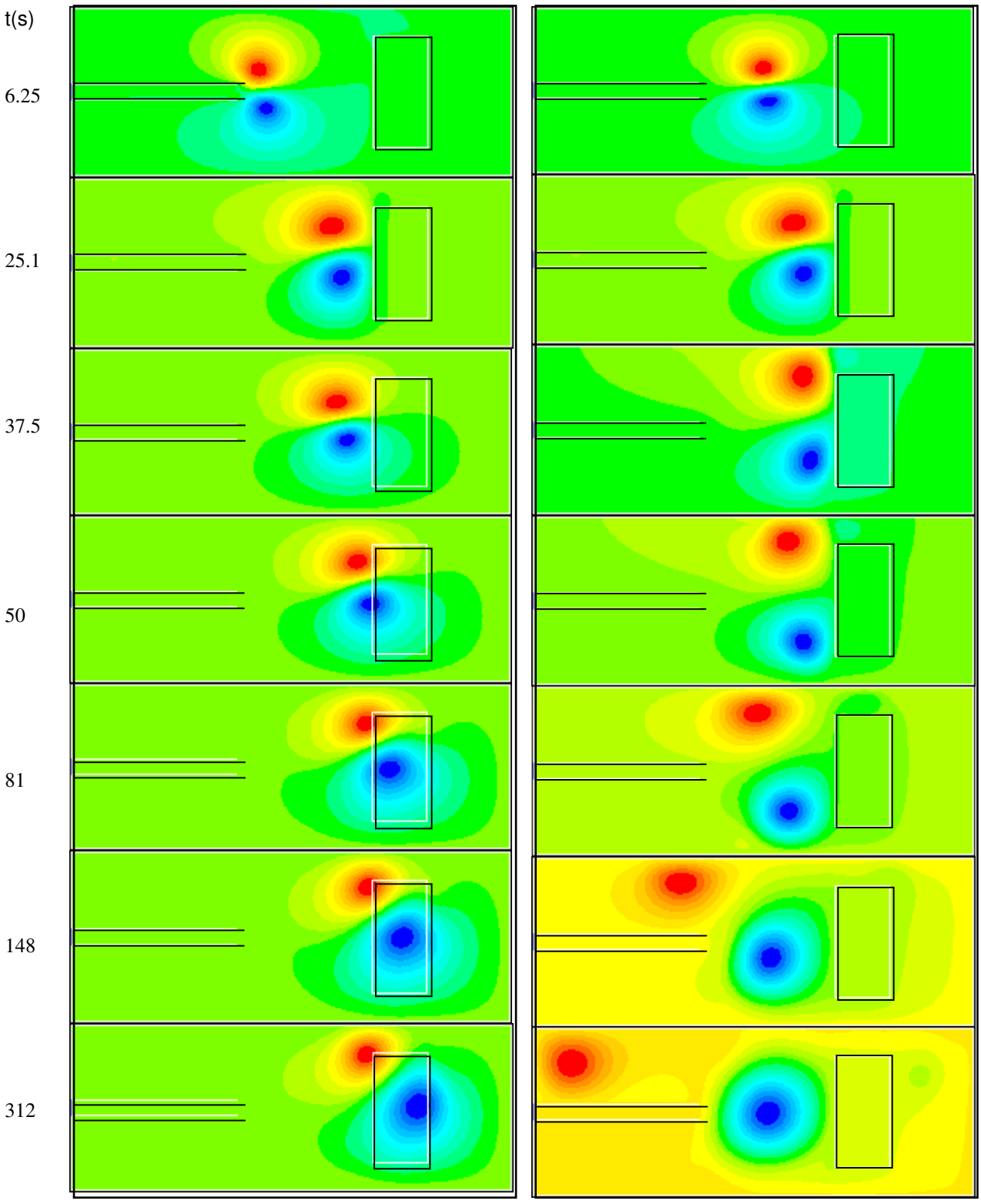
t(s)
6.25
25.1
37.5
50
81
148
312

FIGURE 4: Process of vortex movement: Re=3000, $\emptyset = 0.2, \quad K = 10^{-2}(m^2)$ (left), Re=9000, $\emptyset = 0.8, K = 10^{-8}(m^2)$ (right)

6. REFERENCES

1. D. Getachew, W.J. Minkowycz, J.L. Lage, "A modified form of the κ–ε model for turbulent flows of an incompressible fluid in porous media". International Journal of Heat and Mass Transfer, 43(16):2909-2915, 2000.
2. T Inoue, T Masuoka, Y Takatu, Flow Transition to Turbulence in Porous Media, National Heat Transfer Symposium of JAPAN 2000 - Japan Heat Transfer Society; 1999.
3. J.C. Lau, M.J. Fisher, "The vortex-street structure of turbulent jets", Part 1, Journal of Fluid Mechanics Digital Archive: 299-337, 2006.
4. T.T. Lim, "On the breakdown of vortex rings from inclined nozzles", Physics of Fluids, 1998.
5. C.C. Chu, R.E. Falco, "Vortex ring/viscous wall layer interaction model of the turbulence production process near walls". Journal of Experiments in Fluids, 305-315, 1987.
6. T. Maxworthy, Journal of Fluid Mechanics Digital Archive, 465-495, 1977.
7. A. Glezer, D. Coles, "Journal of Fluid Mechanics Digital Archive, An experimental study of a turbulent vortex ring": 243-283, 1990
8. A.B. Olcay, P. Krueger, "Measurement of ambient fluid entrainment during laminar vortex ring formation". Journal of Experiments in Fluids: 235-247, 2007

New PID Tuning Rule Using ITAE Criteria

Ala Eldin Abdallah Awouda Ala_awouda@yahoo.com
Department of Mechatronics and Robotics,
Faculty of Electrical Engineering,
Universiti Teknologi Malaysia,
Johor, 83100, Malaysia
rosbi@fke.utm.my

Rosbi Bin Mamat
Department of Mechatronics and Robotics, rosbi@fke.utm.my
Faculty of Electrical Engineering,
Universiti Teknologi Malaysia,
Johor, 83100, Malaysia

Abstract

This paper demonstrates an efficient method of tuning the PID controller parameters using the optimization rule for ITAE performance criteria. The method implies an analytical calculating the gain of the controller (K_c), integral time (T_i) and the derivative time (T_d) for PID controlled systems whose process is modeled in first order lag plus time delay (FOLPD) form. Firstly A mat lab program with objective function is written to find the optimum value for the PID controller parameters which can achieve most of the systems requirements such as reducing the overshoot, maintaining a high system response, achieving a good load disturbances rejection and maintaining robustness. The objective function is selected so as to minimize the integral of Time Absolute Error (ITAE) performance index. Using crave fitting technique, equations that define the controller parameters is driven. A comparison between the proposed tuning rules and the traditional tuning rules is done through the Matlab software to show the efficiency of the new tuning rule.

Keywords: ITAE criteria; AMIGO; Z-N tuning rule; PID;

1. INTRODUCTION

Controlling the process is the main issue that rises in the process industry. It is very important to keep the process working probably and safely in the industry, for environmental issues and for the quality of the product being processed. In order for the controllers to work satisfactorily, they must be tuned probably. Tuning of controllers can be done in several ways, depending on the dynamics desired strengths of the system, and many methods have been developed and refined in recent years. The proportional-integral-derivative (PID) controller is widely used in the process industries. The main reason is their simple structure, which can be easily understood and implemented in practice. Finding design methods that lead to the optimal operation of PID controllers is therefore of significant interest. It has been stated, for example, that 98% of control loops in the pulp and paper industries are controlled by PI controllers (Bialkowski, 1996) and that, in more general process control applications, more than 95% of the controllers are of PID type (Åström and Hägglund, 1995). In order for the PID controller to work probably it has to be tuned which mean a selection of the PID controller parameters has to be made [8]. The requirement to choose either two or three controller parameters has meant that the use of tuning rules to determine these parameters is popular. There are many tuning rules for the PID controller as it has been noted that 219 such tuning rules in the literature to specify the PI controller terms, with 381 tuning rules defined to specify the PID controller parameters (O'Dwyer,

2003), Though the use of tuning rules is practically important [3, 11]. Even though, recent surveys indicate, 30 % of installed controllers operate in manual, 30 % of loops increase variability, 25 % of loops use default settings and 30 % of loops have equipment problems [1, 10]. Most PID tuning rules are based on first-order plus time delay assumption of the plant hence cannot ensure the best control performance. Using modern optimization techniques, it is possible to tune a PID controller based on the actual transfer function of the plant to optimize the closed-loop performance. In this paper optimization method is being used to obtain PID controller parameters. A search of one parameter to be optimized lead to select the Integral of Time multiply by Absolute Error (ITAE) index performance criterion, since it can provide controllers with a high load disturbance rejection and minimize the system overshoot while maintain the robustness of the system.

The Integral of Time multiply by Absolute Error (ITAE) index is a popular performance criterion used for control system design. The index was proposed by Graham and Lathrop (1953), who derived a set of normalized transfer function coefficients from 2nd to 8th-order to minimize the ITAE criterion for a step input [10].

This paper is organized as follows: - an overview of the traditional and a best performance tuning rule is covered in section 2. The proposed tuning rule which derived from optimization method is outlined in section 3. Section 4 outlines the optimized PID parameters values that obtained from using the ITAE criteria performance index. In section 5 graphical results showing the performance and robustness of FOLPD processes, compensated with the proposed PID tuning rule. The process is modeled as a first order lag plus time delay (FOLPD) model, and compensated by PID controllers whose parameters are specified using the proposed tuning rule. The results of the proposed tuning rule are plotted and are used to be compared in the face of the performance, robustness and load disturbance rejection against the traditional tuning rule and more over against a well performance tuning rule. Conclusions of the work are drawn in Section 6.

2. CONTROLLER TUNING

Controller tuning methods provide the controller parameters in the form of formulae or algorithms. They ensure that the obtained control system would be stable and would meet given objectives. Also, great advances on optimal methods based on stabilizing PID solutions have been achieved. These methods require certain knowledge about the controlled process. This knowledge, which depends on the applied method, usually translates into a transfer function [9]. In fact, since Ziegler–Nichols proposed their first tuning rules [5], an intensive research has been done from modifications of the original tuning rules to a variety of new techniques: analytical tuning; optimization methods; gain and phase margin optimization, just to mention a few. Recently, tuning methods based on optimization approaches with the aim of ensuring good stability and robustness has received attention in the literature [2, 6]. In this section some of PID tuning algorithms is considered.

2.1 Ziegler-Nichols tuning rule

Ziegler-Nichols tuning rule was the first such effort to provide a practical approach to tune a PID controller. According to the rule, a PID controller is tuned by firstly setting it to the P-only mode but adjusting the gain to make the control system in continuous oscillation. The corresponding gain is referred to as the ultimate gain (K_u) and the oscillation period is termed as the ultimate period (P_u). Then, the PID controller parameters are determined from K_u and P_u using the Ziegler-Nichols tuning table.

Table 1:- Ziegler-Nichols tuning rule

controller	K_c	T_i	T_d
P	$K_u/2$		
PI	$K_u/2.2$	$P_u/1.2$	
PID	$K_u/1.7$	$P_u/2$	$P_u/8$

The key step of the Ziegler-Nichols tuning approach is to determine the ultimate gain and period [5]. However, to determine the ultimate gain and period experimentally is time consuming.

2.2. AMIGO tuning rules

AMIGO tuning rule consider a controller described by:-

$$u(t) = k(by_1sp(t) - y_1f(t)) + k_1i\int_1 0^t t\,i(y_1sp(\tau) - y_1f(\tau)\,\mathbb{I}\,) \text{ d}\tau + k_d\left(\frac{Cdy_{sp}(t)}{dt} - \frac{y_f(t)}{dt}\right) \ldots\ldots(1)$$

Where u is the control variable, ysp the set point, y the process output, and y_f is the filtered process variable, i.e. $Y_f(s) = G_f(s)Y(s)$ The transfer function $G_f(s)$ is a first order filter with time constant T_f , or a second order filter if high frequency roll-off is desired [7].

$$G(s) = \frac{1}{(1+sT_t)^2} \ldots\ldots\ldots\ldots(2)$$

Parameters b and c are called set-point weights. They have no influence on the response to disturbances but they have a significant influence on the response to set point changes. Neglecting the filter of the process output the feedback part of the controller has the transfer function

$$C(s) = K\left[1 + \frac{1}{sT_i} + sT_d\right] \ldots\ldots(3)$$

The advantage by feeding the filtered process variable into the controller is that the filter dynamics can be combined with in the process dynamics and the controller can be designed designing an ideal controller for the process P(s) $G_f(s)$. The objective of AMIGO was to develop tuning rules for the PID controller in varying time-delay systems by analyzing different properties (performance, robustness etc.) of a process test batch. The AMIGO tuning rules are based on the KLT-process model obtained with a step response experiment. The AMIGO tuning rules are

$$K_c = \left(0.2 + 0.45 * \frac{T}{L}\right) \ldots\ldots(4)$$

$$T_i = \left(\frac{0.4L + 0.8T}{L + 0.1T}\right)L \ldots\ldots(5)$$

$$T_d = 0.\frac{5LT}{0.3L + T} \ldots\ldots\ldots(6)$$

In order to use the PID controller with filtering, the rules are extended as follows:

$$\begin{cases} k_c = K_c \\ K_i = \dfrac{K_c}{T_i} \\ k_d = K_c * T_d \end{cases} \qquad \begin{cases} b = \begin{cases} 0 \text{ if } \tau \leq 0.5 \\ 1 \text{ if } \tau > 0.5 \end{cases} \\ c = 0 \\ T_f = \begin{cases} 0.\dfrac{05}{\omega_{gc}} \text{if } \tau \leq 0.2 \\ 0.1 * L \text{ if } \tau > 0.2 \end{cases} \end{cases} \ldots\ldots\ldots(7)$$

Where: - ω_{gc} is the gain crossover frequency and $\tau = L/(L+T)$ is the relative dead-time of the process, which has turned out to be an important process parameter for controller tuning [4, 7].

3. THE PROPOSED TUNING RULE

The proposed tuning rule is driven using several steps

- Step 1:- Find relations between the controller tuning parameters and process parameters as stated below:-

  $K_c = f_1(K_P; L; T)$; $T_i = f_2(K_P; L; T)$; $T_d = f_3(K_P; L; T)$

Function f_1, f_2 and f_3 should be determined such that the load disturbances response is minimized and the robustness constraint is satisfied.

- Step 2:-, Create dimension less expressions through diving and multiplying the factors of the process parameters with appropriate scale factors of each other such as L/T or ; T_i/L or T_i/T ; T_d/L or T_d/T ; K_c*K_P

- Step 3:- Select one factor of the above to find the relations between the tuning parameters and the process parameters. In this paper the factor (L/T) is being selected.
  $K_c* K_P = K_1$ (L/T) ; $T_i/L = K_2$ (L/T) ; $T_d/L = K_3$ (L/T)

- Step 4:- For a defined values of the factor L/T determine the optimal value of the tuning parameters K_c; T_i; T_d which minimize a specific performance criteria (ITAE). In order to take FOPDT processes with a very small, medium and fairly long value of dead time into account, the values of the dimensionless factor L/T are considered from 0.1 to 2.

- Step 5:- Find the values of $K_c* K_P$; T_i/L; T_d/L corresponding to the values of L/T.

- Step 6:- Drive the equations of K_1; K_2; K_3 using carve fitting techniques.

In step 4 a Matlab m-file is defined to calculate the ITAE index (the objective function) which is mathematically given by:-

$$IATE = \int_0^{\infty} [t\,|\,e(t)dt]\,| \quad \ldots\ldots\ldots..(8)$$

Where t is the time and e (t) is the error which is calculated as the difference between the set point and the output. A function of Matlab optimization toolbox (f*minsearch*) is called to calculate the minimum of the objective function. Like most optimization problems, the control performance optimization function is needed to be initializing and a local minimum is required. To do so, the initial controller parameters are set to be determined by one of existing tuning rules. In this way, the controller derived is at least better than that determined by the tuning method. The stability margin based Ziegler-Nichols is used for initial controller parameters and for performance comparison.

On each evaluation of the objective function, the process model develop in the simulink is executed and the IATE performance index is calculated using multiple application Simpson's 1/3 rule. The simulation s repeated with different values of the process parameters (T; L; K_P)

4. RSEULTS

Using Matlab simulation tools several processes with different parameters were taken under test. A record of the controller parameters (K_c, T_i and T_d) that minimize ITAE performance criteria was observed as shown in table (2). The processes under test were first order plus dead time (FOPDT) process.

$$P_{KTL}(S) = \frac{K_P}{Ts+1} * e^{-Ls} \quad \ldots\ldots\ldots.(9)$$

Table 2:- Controller parameters for different Process parameters

Kp = 5 T = 4				
L	L/T	KC	Ti	Td
0.1	0.025	2.2829	4	0.0336
1	0.25	0.4171	4.009	0.3333
2	0.5	0.2204	4.2592	0.699
3	0.75	0.1602	4.555	0.9955
4	1	0.131	4.8604	1.2591
5	1.25	0.1133	5.1709	1.5046
Kp = 2 T = 3				
L	L/T	KC	Ti	Td
0.1	0.033	8.1627	3	0.0335
1	0.33	0.8009	3.0347	0.3626
2	0.667	0.4358	3.3332	0.672
3	1	0.3273	3.6418	0.944
4	1.33	0.2718	3.9496	1.1847
5	1.67	0.2404	4.2664	1.4205
Kp = 3 T = 3				
L	L/T	KC	Ti	Td
0.1	0.03	4.8005	3	0.0335
1	0.33	0.5339	3.0347	0.3626
2	0.67	0.2906	3.3351	0.672
3	1	0.2182	3.6419	0.944
4	1.33	0.1812	3.9497	1.1847
5	1.667	0.1603	4.2665	1.4205
Kp = 2 T = 2				
L	L/T	KC	Ti	Td
0.1	0.05	5.4418	2	0.0334
0.5	0.25	1.0633	2.005	0.1667
1	0.5	0.5509	2.1298	0.344
2	1	0.3273	2.4278	0.6227
3	1.5	0.2554	2.7456	0.8689
4	2	0.2198	3.0588	1.0861
Kp = 1 T = 3				
L	L/T	KC	Ti	Td
0.1	0.033	17.574	3	0.0335
0.5	0.167	3.1872	3	0.1634
1	0.33	1.6018	3.0347	0.3626
2	0.67	0.8715	3.3331	0.672
3	1	0.6547	3.6418	0.944
4	1.33	0.5435	3.9497	1.1847
5	1.67	0.4808	4.2664	1.4205
Kp = 1 T = 2				
L	L/T	KC	Ti	Td
0.1	0.05	11.1413	2	0.0334
1	0.5	1.1018	2.1298	0.3442
2	1	0.6547	2.4279	0.6227
3	1.5	0.5109	2.7458	0.8687
4	2	0.4397	3.0588	1.0861
Kp = 5 T = 1				
L	L/T	KC	Ti	Td
0.1	0.1	0.9602	1	0.0328
0.5	0.5	0.2199	1.0615	0.1433
1	1	0.1312	1.217	0.3146
1.5	1.5	0.1022	1.373	0.4369
2	2	0.0871	1.5198	0.5423
Kp = 4 T = 1				
L	L/T	KC	Ti	Td
0.1	0.1	1.4645	1	0.0328
0.5	0.5	0.2749	1.0616	0.1433
1	1	0.164	1.2171	0.3146
1.5	1.5	0.1277	1.373	0.4367
2	2	0.1109	1.5389	0.5424
Kp = 3 T = 1				
L	L/T	KC	Ti	Td
0.1	0.1	1.8139	1	0.0355
0.5	0.5	0.3666	1.0616	0.1433
1	1	0.2186	1.2172	0.3146
1.5	1.5	0.1703	1.373	0.4429
2	2	0.1479	1.5389	0.5321
Kp = 2 T = 1				
L	L/T	KC	Ti	Td
0.1	0.1	2.7668	2	0.0328
0.5	0.5	0.5499	2.005	0.1433
1	1	0.3279	2.1298	0.3146
1.5	1.5	0.2555	2.2712	0.4425
2	2	0.2219	2.4279	0.5184
Kp = 1 T = 1				
L	L/T	KC	Ti	Td
0.1	0.1	5.8578	1	0.0328
0.5	0.5	1.1016	1.0647	0.1433
1	1	0.6559	1.2171	0.3146
1.5	1.5	0.5109	1.373	0.4425
2	2	0.4354	1.5199	0.5184

Using carve fitting techniques the tuning rule are found as shown below.

$$K_c = \left(0.3 + 0.38 * \frac{T}{L} + 0.007 * \left(\frac{T}{L}\right)^2\right) \ldots\ldots\ldots (10)$$

$$T_i = L * \left(0.5 + 0.5 * \frac{T}{L} + 0.01 * \left(\frac{T}{L}\right)^1 .5\right) \ldots\ldots (11)$$

$$T_d = \frac{1.4 * LT}{0.9 * L + 2.9 * T} \ldots\ldots\ldots\ldots\ldots\ldots\ldots (12)$$

5. MATLAB SIMULATION RESULTS

Several process models were examined in this analysis representing different types of processes. After finding the controller settings for the different processes, the responses of the systems were plotted. All processes were Fist order Plus Dead Time. A reduction procedure is used to modulate the higher order models in the FOPDT model.

$$G_1(s) = \frac{1 * e^{-5s}}{(3s+1)(s+1)} = \frac{0.99 * e^{-3.64s}}{2.85s+1}$$

Table 3: Controller settings of AMIGO and proposed tuning rule for process $G_1(s)$

Algorithm	K_C	T_i	T_d
Z-N	0.9238	7.7556	1.9389
AMIGO	0.432	4.3178	1.7695
Proposed tuning rule	0.499	4.4020	1.6868

Table 4: The response parameters values of Z-N, AMIGO and Proposed tuning rule for the process $G_1(s)$.

Algorithm	Rise time (s)	Settling Time (s)	Set point overshoot %	IAE
Z-N	10.2	22.8	11.42	83.28
AMIGO	15.5	17.2	4.19	100.36
Proposed tuning rule	13.5	14.6	7	88.54

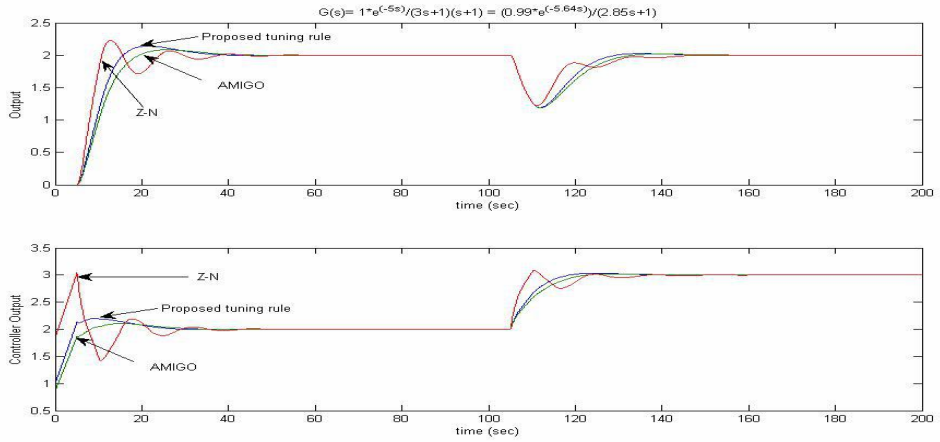

Figure 1:- Step response for the second order process with delay

$$G_2(s) = \frac{10 * e^{-s}}{(s+1)(s+2)(s+3)(s+4)} = \frac{0.419 * e^{-1.2s}}{(s^2 + 2s + 1)} = \frac{0.4167 * e^{-2.16s}}{1.1696s + 1}$$

Table 5: Controller settings of Z-N, AMIGO and proposed tuning rule for process $G_2(s)$

Algorithm	KC	Ti	Td
Z-N	2.7819	2.7641	0.6910
AMIGO	1.065	1.707236	0.694965
Proposed tuning rule	1.219	1.71901	0.662852

Table 6: The response parameters values of Z-N, AMIGO and Proposed tuning rule for the process $G_2(s)$.

Algorithm	Rise time (s)	Settling Time (s)	Set point overshoot %	IAE Yd
Z-N	3.2	6	18.13	9.94
AMIGO	6.2	7.3	0.9	16.03
Proposed tuning rule	5.3	9	2.36	14.10

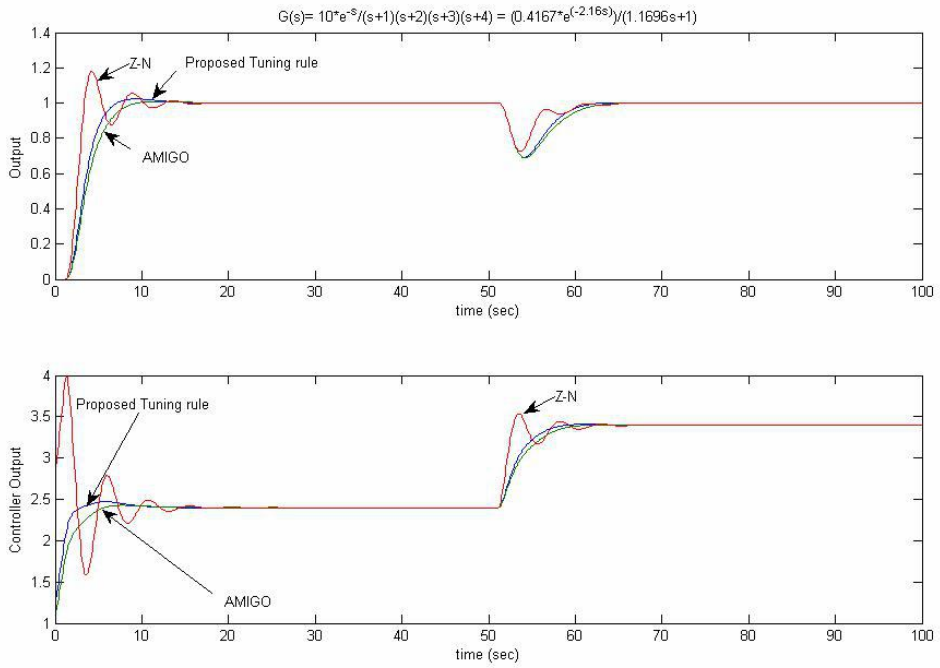

Figure 2:- Step response for the high order process with delay

$$G_3(s) = \frac{1 * e^{-3s}}{(2s+1)(s+1)^2} = \frac{0.9993 * e^{-4.69s}}{2.61s+1}$$

Table 7: Controller settings of AMIGO and proposed tuning rule for process $G_3(s)$

Algorithm	K_C	T_i	T_d
Z-N	1.0345	6.4481	1.6120
AMIGO	0.451	3.755031	1.523637
Proposed tuning rule	0.514	3.762972	1.354542

Table 8: The response parameters values of AMIGO and Proposed tuning rule for the process $G_3(s)$.

Algorithm	Rise time (s)	Settling Time (s)	Set point overshoot %	IAE Yd
Z-N	7.6	17.7	14.45	65.5
AMIGO	12.8	15	1.48	83.33
Proposed tuning rule	10.9	11.9	3.66	72.99

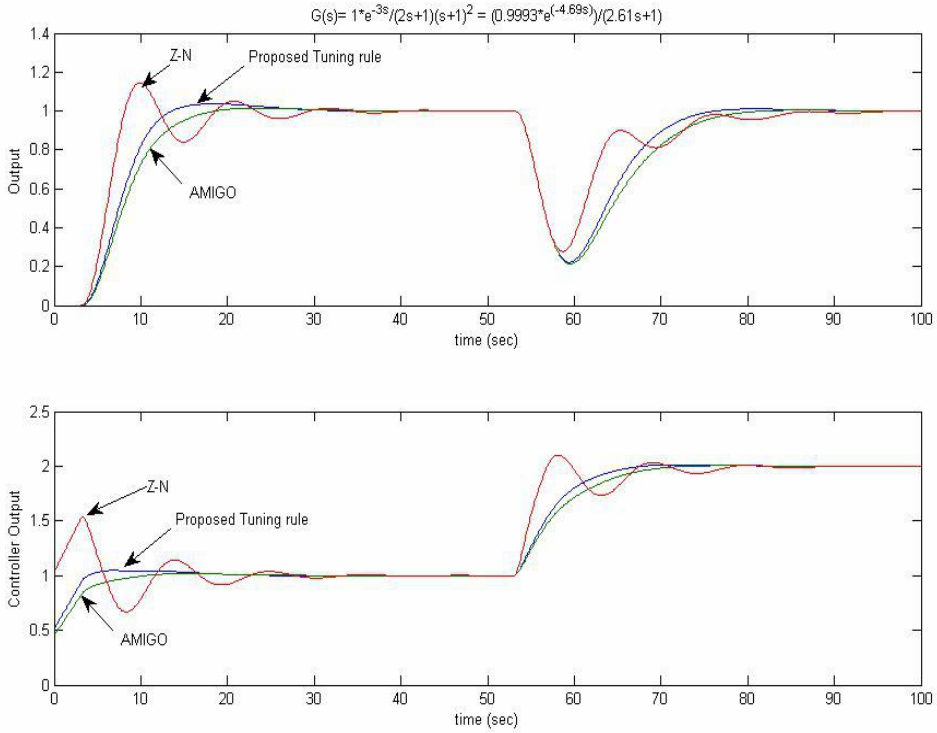

Figure 3:- Step response for the third order process with delay

$$G_4(s) = \frac{1 * e^{-4s}}{(2s+1)}$$

Table 9: Controller settings of AMIGO and proposed tuning rule for process $G_4(s)$

Algorithm	K_C	T_i	T_d
Z-N	0.9101	5.4901	1.3725
AMIGO	0.425	3.047619	1.25
Proposed tuning rule	0.492	3.113137	1.191489

Table 10: The response parameters values of AMIGO and Proposed tuning rule for the process $G_4(s)$.

Algorithm	Rise time (s)	Settling Time (s)	Set point overshoot %	IAE
Z-N	6.8	23	16.39	60.24
AMIGO	11.1	12.9	1.78	71.94
Proposed tuning rule	9.3	10.3	3.65	63.29

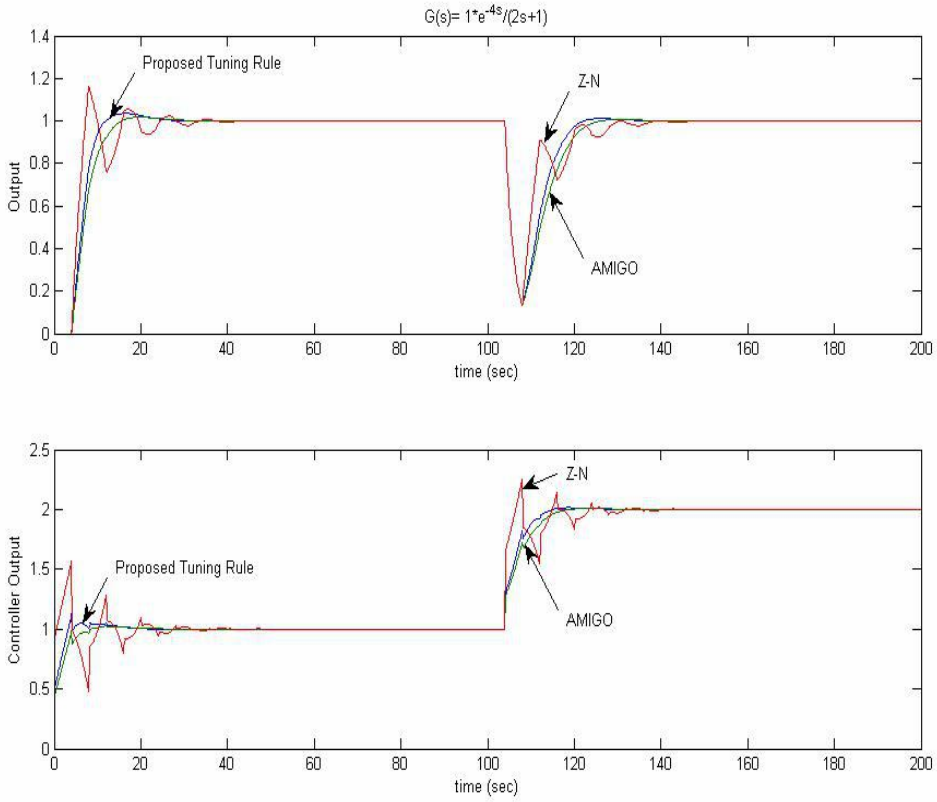

Figure 4:- Step response for FOPDT process

$$G_5(s) = \frac{10}{(s+1)(s+2)(s+3)(s+4)} = \frac{0.419 * e^{-0.8s}}{(s^2 + 2s + 1)} = \frac{0.416 * e^{-1.14s}}{1.1696s + 1}$$

Table 11: Controller settings of AMIGO and proposed tuning rule for process $G_5(s)$

Algorithm	K_C	T_i	T_d
Z-N	7.5449	1.4050	0.3512
AMIGO	1.591	1.262184	0.441037
Proposed tuning rule	1.676	1.16577	0.422533

Table 12: The response parameters values of AMIGO and Proposed tuning rule for the process $G_5(s)$.

Algorithm	Rise time (s)	Settling Time (s)	Set point overshoot %	IAE
Z-N	1.3	44.18	4.1	1.86
AMIGO	3.4	4.91	3.8	7.93
Proposed tuning rule	3.1	8.64	6.7	6.95

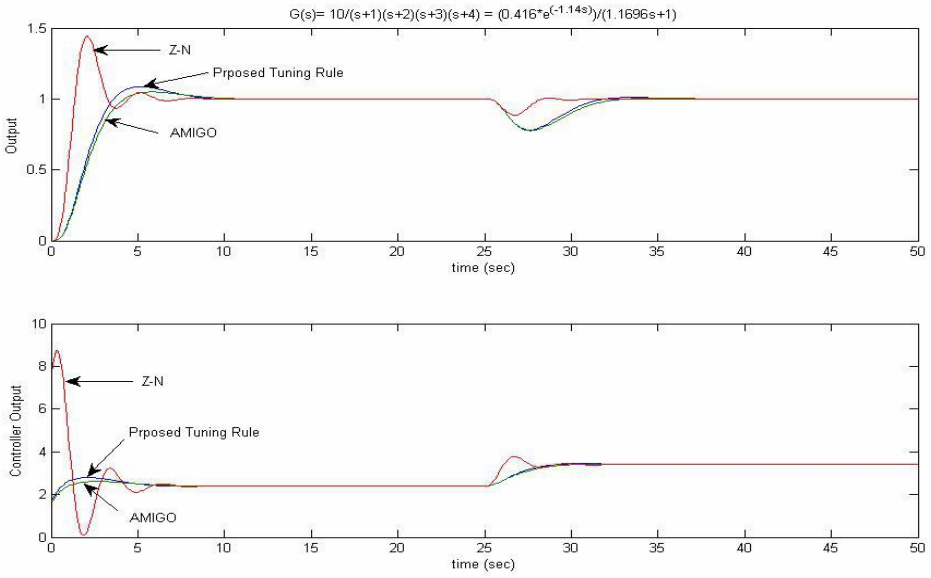

Figure 5:- Step response for high order process without delay

6. CONCLUSION

The analysis shows that the proposed tuning and AMIGO settings give the least oscillatory response than Z-N setting. It is also seen that the IAE (integral of absolute error) for the disturbance for the proposed tuning settings is less than the AMIGO setting but slightly higher than Z-N setting. The proposed tuning setting give a small rise time comparing to that of the AMIGO tuning, but slightly higher than ZN setting. In the other hand the proposed tuning gives a settling time faster than Z-N's. Test batch of different process had been used to simulate the proposed tuning. The most important advantage of this design is in the use of the IATE performance criteria index to find the new tuning rule since it can provide the controller with a good performance. As it appears from the simulation, the proposed tuning rule is able to deal with the possible variation of system parameters. It is so obvious that the proposed tuning rule has the same or better performance than AMIGO tuning rule and a much better performance than Z-N tuning rule. The observation from those results shows that a high overshoot appears in the output of the system for some cases of processes. This overshoot appears as expense of achieving a high response and a better load disturbance rejection. In the other hand the proposed tuning rule maintain robustness. The concluded important contributions in this paper regarding the use of the proposed tuning rule are that it proves the ability of the proposed tuning rule in tuning the PID controller probably. Also it validates the flexibility of the proposed tuning rule to deal with different modeling systems with different parameters. As a future work, the proposed tuning rule can be used in a practical experiment so as to prepare this proposed tuning rule to be used in the practical industrial applications.

7. REFRENCES

1. C.-Y. Kao and B. Lincoln, "Simple stability criteria for systems with time-varying delays," Automatica, vol. 40, pp. 1429-1434, Aug. 2004.
2. Dingyu Xue, YangQuan Chen. Derek P. Atherton. "Linear Feedback Control" Society for Industrial and Applied Mathematics. 2007.
3. Guillermo J. Silva, Aniruddha Datta. S. P. Bhattacharyya. "PID Controllers for Time-Delay Systems". Boston. ISBN 0-8176-4266-8.2005.

4. Hang, C.C, K.J.Astrom and W.K. Ho, “refinement of Ziegler-Nichols Tuning Formula”, IEE Proc. Pt. D, Vol. 138, pp. 111-118 .1991.
5. J. G. Ziegler and N. B. Nichols, “Optimum Settings for Automatic Controllers,” Trans. ASME, Vol. 64, pp. 759-768, 1942.
6. K. J. Astrom and T. Hagglund, “The Future of PID Control,” IFAC J. Control Engineering Practice, Vol. 9, pp. 1163-1175, 2001.
7. K.J.Astrom, T.Hagglund, “Revisiting the Ziegler–Nichols step response method for PID control”, Journal of Process Control 14,635–650, Department of Automatic Control, Lund Institute of Technology. 2004.
8. Lasse M. Eriksson and Mikael Johansson, “PID Controller Tuning Rules for Varying Time-Delay Systems”, Proceedings of the 2007 American Control Conference ,New York City, USA, July 11-13, 2007.
9. L. Eriksson and T. Oksanen, ”PID Controller Tuning for Integrating Processes: Analysis and New Design Approach,” In Proc. Fourth International Symposium on Mechatronics and its Applications, harjah, UAE, Mar. 2007
10. Panagopoulos H., Astrom K. J., Hagglund T., “Design of PID Controllers Based on Constrained Optimisation”, IEE Proc., Control Theory Appl., Vol. 149, No. 1. – P. 32–40. 2002.
11. P. Cominos and N. Munro, “PID Controllers: Recent Tuning Methods and Design to Specification,” IEE Proc. D, Control Theory and Applications, Vol. 149, No. 1, pp. 46-53, 2002.

Performance Analysis of Continuous Wavelength Optical Burst Switching Networks

Aditya Goel adityagoel2@rediffmail.com
Department of Electronics & Communication
MANIT (Deemed University)
Bhopal-462051, India

Vitthal J. Gond vitthal_g@rediffmail.com
Department of Electronics & Communication
MANIT (Deemed University)
Bhopal-462051, India

R K Sethi sethirk@hotmail.com
Department of Electronics & Communication
MANIT (Deemed University)
Bhopal-462051, India

And
A K SINGH akhil26783@gmail.com
Department of Electronics & Communication
MANIT (Deemed University)
Bhopal-462051, India

Abstract

Considering the economic and technical aspects of wavelength converters, full wavelength conversion capability will not be available throughout optical networks in the foreseeable future. In this paper we have used balanced static wavelength assignment (BSWA) algorithm. It is a technique to improve the performance of an all-optical network in respect of blocking probability & other parameters to provide cost effective optical communication system. We carried out the performance analysis of wavelength-continuous optical burst switching network-using BSWA for the network topologies namely NSFNET and INTERNET2NET with the initial assumption that there is no wavelength converter or optical buffer in the networks. For simulation we have used a powerful tool MatplanWDM. The performance analysis of burst loss probability v/s traffic load using BSWA algorithm shows that its performance is better than other static wavelength assignment algorithm. We have also explored the performances of NSFNET and INTERNET2NET networks on the basis of channel utilization, message delay, and the ratio of traffic transferred in single hop to total traffic offered against percentage of reused wavelength in the network. It has been observed that channel utilization becomes the maximum for 40% of reused wavelengths per fiber and beyond that cost of network unnecessary increases. By the performance analysis of message propagation delay for both network Topology, it is observed that message propagation delay, is minimum at 40% of reused wavelength per fiber and it becomes constant beyond that. It is therefore recommended that reused wavelengths per fiber should not exceed 40 % of the total available wavelength so as to yield cost effective solution with optimum performance.

Keywords: BSWA: Balanced Static Wavelength Assignment, OBS: Optical Burst Switching, OADM: Optical Add/Drop Multiplexers, OXC: Optical Cross-Connect, TBS: Terabit Burst Switching, PWA: Priority Wavelength Assignment.

1. INTRODUCTION

Due to the introduction of various wide band applications, such as video conferencing, broadband wireless communication [1] etc the demand of transmission capacity is growing exponentially. This has motivated the researcher to device & employ different techniques [2,3] to enhance the existing transmission capacity of optical terrestrial and wireless networks. In order to accommodate this wide capacity requirement, efficient and cost-effective wavelength division multiplexing (WDM) can be used between network nodes [4]. Today up to several Tbit/s traffic can be carried by the optical link over long distances. e.g. in an ultra-dense WDM transmission total capacity of 50 Tbit/s have already been experimentally demonstrated [5]. However, with the introduction of very high capacity WDM optical transmission techniques, the discrepancy between optical transmission capacity and electronic switching capability increases. Moreover, due to cost and complexity aspects, it is advantageous to keep data in the optical domain and to avoid bit-level signal processing. Burst switched WDM optical networks are coming up as suitable network architectures for future Optical Internet backbones [6]. Optical Burst Switching (OBS) has emerged as a new paradigm for an optical Internet [7]. During the past years, there are large efforts to realize OBS. Although the concept of burst switching had already been known since the 1980s, it has never been a big success in electrical networks. The main reason is that its complexity and realization requirements are comparable to that of more flexible electronic packet switching techniques. Optical circuit switching (OCS) does not support fine switching granularity on the packet-level. Only poor bandwidth utilization is obtained due to the absence of statistical multiplexing. On the other hand, Optical Packet Switching (OPS) are still too complex to be realized in the near future. Therefore, a hybrid approach like burst switching seems promising for the WDM-based optical networks. Optical burst switching (OBS) was proposed in the late 1990 [7,8] and it tries to exploit the advantages of both OCS and OPS approaches and avoid a part of their limitations. OBS is considered as one of the most promising approaches to implement IP over WDM [9]. At the moment, due to the fast development of this new approach and the large number of new proposals, OBS is still at its definition phase and no common definition of OBS can be found. However, among several different definitions two main definitions can be found. One is more oriented towards fast wavelength switching. Synonyms like optical flow switching (OFS) [10] and wavelength routed OBS (WR-OBS) [11,12,13] can be found in the literature. Here, an acknowledged two-way reservation is generally used. A burst will be only transmitted after having received a positive acknowledgement of its reservation request. Another most widely used definition for OBS is more packets oriented and was proposed by Qiao and Turner [14,7,8].

To realize an OBS network, a new optical layer is mandatory. Furthermore, an OBS network will be only possible if fast and efficient switching nodes can be built. To constitute the OBS network nodes several key components are needed e.g. optical space switches, tunable filters/lasers, wavelength converters etc. Most of the studies on OBS networks assume that full wavelength conversion is available throughout the network. However, such capability is not at present a realistic assumption. Although use of wavelength converters give better performance with respect to blocking probability but it is quite expensive. So, the absence of (full) wavelength conversion capabilities calls for good and efficient wavelength assignment policies. The Wavelength Assignment Algorithm is a method to improve the performance in respect of blocking probability and to provide cost effective communication system. To solve the above problems there have been developed number of wavelength assignment techniques e.g. Random, FF-TE, BSWA etc. Traditional first-fit or random wavelength assignment algorithm in OCS network is not appropriate for wavelength-continuous OBS networks, since the burst is transmitted without knowledge of the wavelength occupation status of the following links.

Out of the number of wavelength assignment techniques we have selected Balanced Static wavelength assignment (BSWA) algorithm. The BSWA algorithm is new and improved wavelength assignment policy [15] In BSWA wavelength order lists are carefully designed during

the network-planning phase, and no extra information exchange or signaling is needed. The BSWA improves the performance of blocking probability vs. traffic load than other existing static wavelength assignment policies. The BSWA also reduces the cost of communication system because it reduces the number of wavelength converters, which is too costly. The BSWA has improved the performance in respect of blocking probability as compared to other static approaches. Numerical results show that BSWA reduces the burst loss probability in comparison with existing static approaches, and almost achieves the same performance as PWA (Priority Wavelength Assignment) with the advantage that no extra dynamic information is needed. In this work performance analysis for NSFNET and INTERNET2NET networks have been carried out for various crucial parameters like burst loss probability, message propagation delay and channel utilization.

1.1 Optical Burst Switching (OBS)

The main characteristics of OBS can be summarized as follows:

- Client layer data (IP-Packet) is aggregated and assembled into variable length optical bursts in edge nodes. OBS assumes more extensive burst aggregation, to realize bursts with payloads typically carrying tens of Kbytes.
- There is a separation between control information (header) and user information (data) in space and in time. Control header packets are sent on a separate wavelength (out-of-band) and processed electronically in all OBS core nodes to set up the switch matrix before the data bursts arrive.
- Data bursts are asynchronously switched in core nodes and stay in the optical domain until they reach their destination edge node. Only wavelength conversion and/or some degree of regeneration are applied to the signal.
- Resources are allocated by using one-pass reservation, i.e., burst transmission is not delayed until an acknowledgment of successful end- to-end path setup is received but is initiated after the burst was assembled and the control packet was sent out.
- Burst switching does not require buffering inside the core network.

2. BSWA ALGORITHM & IMPLEMENTATION

To reduce the blocking probability, wavelength assignment techniques play an important role in OBS Network, which are not having full wavelength conversion capability. To address the burning problem of network congestion along with low cost, various wavelength assignment algorithms have been developed like First-Fit, Random, First-Fit-TE, etc. In this paper we have carried out the performance analysis of newly developed wavelength assignment algorithm, Balanced Static Wavelength Assignment algorithm. BSWA is capable of reducing the burning problem of network congestion to a substantial amount in comparison to other traditional wavelength assignment algorithm.

2.1 BSWA Algorithm

BSWA algorithm is static approach, which does not require the exchange of any information among network routers. Thus, the assignment rules are determined during the network-planning phase, depending on certain properties of the network like topology, routing paths, and traffic. In this work we used traffic information for wavelength assignment. In this BSWA tries to fully balance the traffic that shares common links between different source-destination pairs among wavelength on those links.

An OBS network is represented by a graph G (V, E), where V = $\{V_1, V_2,...,V_N\}$ is the set of nodes, and E=$\{E_1, E_2,\ldots,E_M\}$ is the set of unidirectional fiber links. The link $E(V_s, V_d)$ connects V_s to V_d and contains W different wavelengths labeled arbitrarily, say, , $\lambda_1, \lambda_2, \ldots\ldots, \lambda_w$. By $P\{V_s, V_d\}$, we denote the routing path from V_s to V_d, and $\rho(V_s, V_d)$ is the given traffic load from V_s to V_d. We define virtual_wl_cost(V_i, V_j, λ_k) to be the virtual cost of wavelength λ_k on link $E(V_i, V_j)$, and path_cost(V_s, V_d, λ_k) to be the cost of the the path on λ_k along which the source V_s sends bursts to the destination V_d. Thus , path_cost(V_s, V_d, λ_k) is calculated as

$$\text{path\_cost}(V_s, V_d, \lambda_k) = \sum_{E(V_i, V_j) \in P(V_s, V_d)} \text{virtual\_wl\_cost}(V_i, V_j, \lambda_k) \quad (1)$$

Balanced static wavelength assignment (BSWA) algorithm:
Input: G(V,E), $P(V_s, V_d)$, $\rho(V_s, V_d)$ for all s,d ϵ {1,2,……..,n}
Output: $WA(V_s, V_d, t)$ for all s,d ϵ {1,2,……..,n}, t ϵ {1,2,……..,w}
Initialization: virtual_wl_cost $(V_i, V_j, \lambda_k) = 0$ for all i, j ϵ {1,2, ... ,N},
t ϵ {1,2, ... ,W}
FOR t← from 1 to W
FOR s← from 1 to N
FOR d← from 1 to N
Step 1: Compute the path_cost for each wavelength that has not been assigned before for this s-d pair.
Step 2: Choose the λ_k that has the least path_cost, and make it the wavelength assigned in this loop.That is, $WA(V_s, V_d, t) = \lambda_k$.
Step 3: Update virtual_wl_cost(V_i, V_j, λ_k) for all $E(V_i, V_j) \epsilon P\{V_s, V_d\}$ by virtual_wl_cost(V_i, V_j, λ_k) = virtual_wl_cost$(V_i, V_j, \lambda_k) + \rho(V_s, V_d)$ (2)

The process of BSWA is stated as follows. First the cost of each wavelength on all links, virtual_wl_cost(V_i, V_j, λ_k) is initialized to 0. Then we begin to assign wavelengths for s-d pairs one by one. The value of path_cost(V_s, V_d, λ_k), k ϵ {1, 2, ….,w}, is calculated for each (V_s, V_d) pair, and λ_k that has the least path_cost is chosen as the wavelength assigned for the (V_s, V_d) pair.Every time we assign a wavelength (e.g. λ_k) for an s-d pair, we increase virtual_wl_cost(V_i, V_j, λ_k) on all the passing links of $P\{V_s, V_d\}$ by $\rho(V_s, V_d)$ so that the wavelength is less likely to be chosen by other s-d pairs if it is already heavily loaded. We continue to do this for all s-d pairs, so that each pair is assigned a wavelength. The process described is called searching loop W times, we can get a list of the wavelength assignment order for each s-d pair.

2.2 Implementation of BSWA Algorithm

To reduce the data congestion with low cost, we have used balanced static wavelength assignment algorithm to assign the wavelength for each source-destination pair (s-d pair). The programming of the BSWA algorithm has been coded in Matlab. We have used a very powerful tool named as Matplan-wdm to implement the coded algorithm. This works on the platform of Matlab7.0 or above version. The optimization in this tool will be done with the help of Tomlab, which is also a powerful tool for optimization. The algorithm has been implemented in two network topology namely NSFNET & INTERNET2NET as shown in Figure 1 & Figure 2 respectively. The NSFNET consist of 14 nodes and 21 bi-directional fiber links, where as INTERNET2NET consist of 9 nodes and 13 bi-directional fiber links. The traffic loads have been taken in erlangs per wavelength. The NSFNET have 40 maximum wavelengths per fiber where as INTERNET2NET have 32 maximum wavelengths per fiber. It is assumed that there are not available wavelengths converters and optical buffers in both networks. We have used the Dijkastra's shortest-path algorithm to calculate the route for each s-d pair [15]. In this algorithm each s-d pair will select shortest path in network to transfer the data. This algorithm has been also coded in Matlab. We have analyzed the burst loss probability by varying the traffic load in erlangs per wavelength. Similarly we have done performance analysis of channel utilization, traffic transferred in single hop, message propagation delay by varying the number of wavelengths per fiber. The channel utilization has been calculated as how many wavelengths channels are being used to transfer the data out of total wavelengths channels available in the network. The traffic transferred in single hop has been calculated as ratio of traffic transferred in single hop to total traffic offered in percentage. The message propagation delay has been calculated as the difference between the time that message being transmitted at transmitter and that is being received at receiver. It is assumed that burst dropped at transmitter have negligible propagation delay. The number of wavelengths per fiber varied as percentage of maximum wavelengths used per fiber in the particular network. For example in NSFNET maximum wavelengths per fiber is 40 and in INTERNET2NET that is 32.

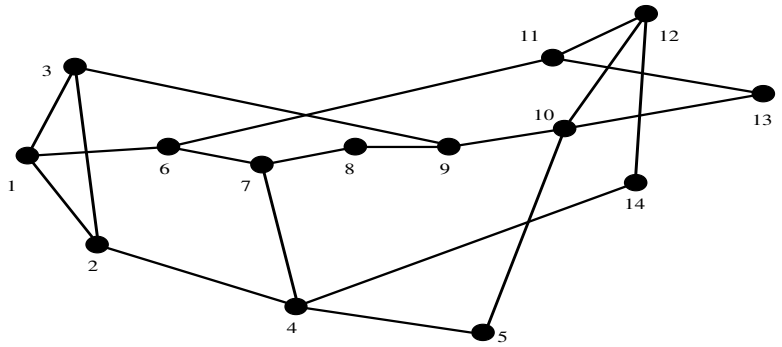

FIGURE 1: NSFNET (14 Nodes, 21 Bi-directional Link)

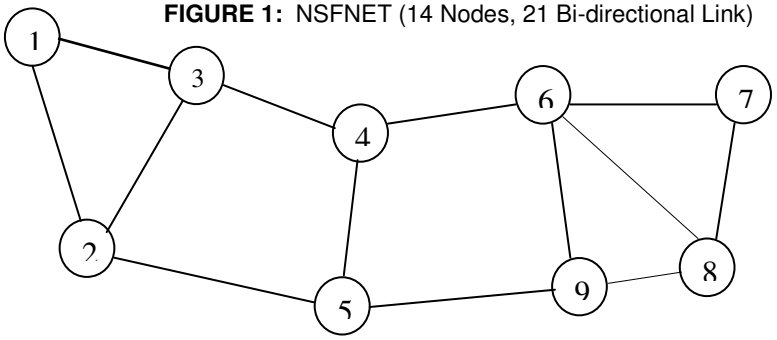

FIGURE 2:INTERNET2NET (9 Nodes, 13 Bi-directional Link)

2.3 Validation of BSWA

We have validated our simulated results generated through our code with the previously published results [15] as reported by Chunlei Zhu, Wenda Ni at all in their paper titled "New and Improved Approaches for Wavelength Assignment in Wavelength-Continuous Optical Burst Switching Network," By The tabular comparison of the two shows that the simulated result is in reasonably good agreement with the reported result [15]. The comparison of result is for NSFNET with 14 nodes and 21 bidirectional fiber links. The load is taken in erlangs per wavelength.

Table: 2.1 Result Validations

LOAD (Erlang)	Published Result (1)	Simulated
0.1	0.0015	0.002
0.2	0.009	0.009
0.3	0.026	0.03
0.4	0.05	0.06
0.5	0.08	0.08
0.6	0.12	0.12
0.7	0.15	0.15
0.8	0.2	0.19
0.9	0.25	0.26
1.0	0.30	0.30

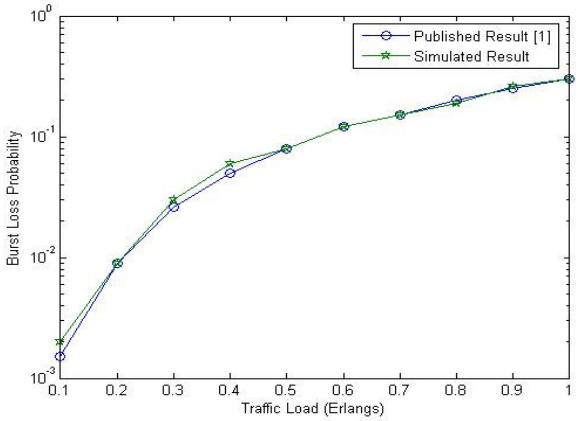

FIGURE 3: Result validation

The Figure 3 shows that there is small variation of simulated result from that with published result [15] up to 0.5 erlangs of traffic load and after 0.5 erlangs of traffic load the simulated result and published result [15] are almost coincident. Hence this shows that simulated results are in good agreement reasonably with that of published reported results [15]. Once the validation has been done, it is ensured that the simulated code is free from logical & other errors. Hence we can apply our code to other networks and applications.

2.4 Comparison of Various Wavelength Assignments

The comparision of various wavelength assignment policies with respect to burst loss probability have been shown in the Figure. 4. In this we can see at low load, burst loss probability is minimum for BSWA.This comparision is demonstrated for NSFNET network with 14 nodes, 21 bidirectional link.The load is in *erlangs per wavelength*. At high load burst loss probability is almost same as PWA which is dynamic wavelength assignment algorithm. Thus BSWA is giving optimum performance because it is giving almost the same result as PWA with the advantage that no extra dynamic information is needed.

The Figure 4 shows that up to 0.2 erlangs, the BSWA is giving optimum performance. After 0.2 erlangs load BSWA shows the same performance as PWA with small variation in burst loss probability and after 0.9 erlang it shows almost same performance as PWA. The advantage of BSWA is that it shows almost same performance as PWA without incorporating any extra dynamic information exchange.

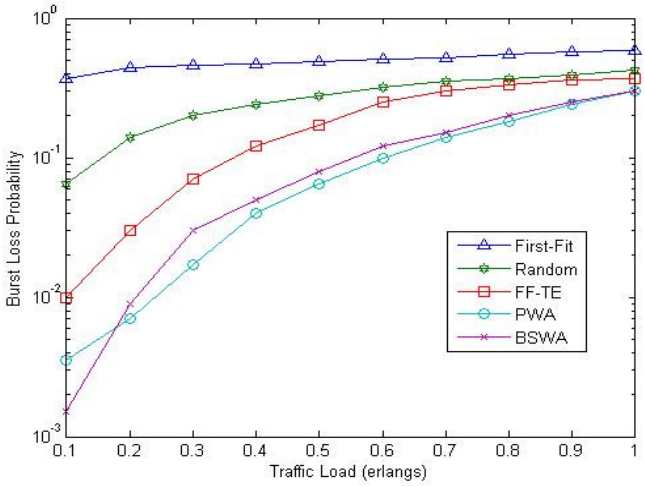

FIGURE 4: Traffic Load vs. Burst Loss Probability for Various Wavelengths Assignments Policies (NSFNET, 14 Nodes, 21 Bi-directional Link)

2.5 Performance Analysis

The performance analysis of wavelength-continuous optical burst switching network [17 has been carried out, by evaluating the performance of following parameters: -

2.5.1 Burst loss probability

Burst loss probability [17 is given by,

$$P_b = \frac{(\text{Numer of burst dropped})}{(\text{Total number of arrivals})} \quad (3)$$

Here we have assumed that if any route is blocked then coming burst through this rote will be dropped. Hence the burst loss probability has been calculated as the average blocking probability P_b for the network and is defined as average of the blocking probabilities on all the routes and is given by,

$$P_b = \frac{\sum_{r=1}^{R} Br}{R} \quad (4)$$

Where R is the total number of routes in the network.

Br is the blocking probability of a route r, which involves multiple links (say n links), is given by,

$$Br = 1 - \prod_{i=1}^{n}(1-Pi) \quad (5)$$

Where P_i is the blocking probability of a link i with capacity C (number of wavelengths on link) and is given by

$$P_i = R(L(i), C) = \frac{L(i)^C}{C!}\left[\sum_{n=0}^{C}\frac{L(i)^n}{n}\right]^{-1} \quad (6)$$

Where L (i) is carried traffic on link i which has frequency of usage, F_i and is given by,

$$L(i) = \sum_{j=1}^{F_i} L_r = \frac{L \times F_i}{R} \quad (7)$$

Where L_r is the load on any route r and is given by,

$$L_r = \frac{L}{R} \quad (8)$$

Where L is the total load (erlangs) on the network and is given by,

$$L = l \times N \quad (9)$$

and R is the total number of bi-directional routes and is given by,

$$R = \frac{N \times (N-1)}{2} \quad (10)$$

2.5.2 Channel Utilization

Channel Utilization [17] s given by,

$$U = \frac{\text{Average value of occupied channels in the network}}{\text{Total available channels in the network}} \quad (11)$$

$$= \frac{\sum_{i=1}^{J}\sum_{m=0}^{C-1}(C-m)P_i(C-m)}{C * J} \quad (12)$$

Total Available Channels = C × J (13)

Here Occupied channels = $\sum_{i=1}^{J}\sum_{m=0}^{C-1}(C-m)P_i(C-m)$; where $\sum_{m=0}^{C}P_i(m)=1$ (14)

Where $P_i(C\text{-}m) = q_i(m)$ (15)

≅ Probability of finding C-m wavelengths occupied in link i

≅ Probability of finding m wavelengths free on link i

Where $q_i(m)$ is the probability of finding m idle or free wavelengths on link i and from the Birth-death model, $q_i(m)$ is given as,

$$q_i(m) = \frac{C(C-1).....(C-m+1)}{L_{eff}(i)^m} q_i(0);\ m = 1,2,.....C \quad (16)$$

Where

$$q_i(0) = \left[1+\sum_{m=1}^{C}\frac{C(C-1).....(C-m+1)}{L_{eff}(i)^m}\right] \quad (17)$$

and $L_{eff}(i)$ is the effective carried traffic on link I and is given by,

$$L_{eff}(i) = \sum_{r=1}^{F_i} L_r(1+P_i-B_r) = L_r\left[F_i+F_i\times P_i-\sum_{r=1}^{F_i}B_r\right] \quad (18)$$

Since in the formula of channel utilization given, channel utilization mainly depends on value of occupied channels so we have simulated the result for average Occupied Channel used against total channel available.

2.5.3 Message propagation delay

This is the difference between the times of Message being transmitted from source and message being received at receiver. The assumption has been taken that dropped burst have no transmission delay.

2.5.4 Ratio of single hop traffic to total traffic offered

It is the ratio of traffic being transmitted in single hop to total traffic offered to network. In our simulation traffic is being transmitted through Dijkastra's shortest path [15].

2.6 Burst loss calculation for OBS Network using full wavelength converter capability

The objective of calculation of burst loss probability for full wavelength conversion capability network is to show that wavelength converters have very important roll to reduce the burst loss probability. The disadvantage of wavelength converter is, it is too costly. So to reduce the cost wavelength assignment policies is being used. Let in the OBS Network, there are (M+1) wavelengths per fiber link. In (M+1) wavelengths one wavelength is used as reservation channel for signaling and other M wavelengths channel carry data bursts. The bursts loss probability B on each fiber link is the same and is given by using the well known Erlang loss formula [16,17] with

$$B(A,M) = (A^M / M!) / \left(\sum_{i=0}^{M} A^i / i!\right), \quad (19)$$

Where A is the offered traffic load and M the number of wavelengths (which will carry data bursts) per out put fiber. Therefore A/M is the normalized offered traffic, which corresponds to utilization of output fiber of the node.

3. Results and Discussion

The typical network topologies we have used in this simulation are NSFNET (14 nodes, 21 bi-directional fiber links) and INTERNET2NET (9 nodes, 13 bi-directional fiber links) as shown in Figure 1 and Figure 2 respectively. We initially assume wavelength converters are not available. Dijkstra's shortest-path algorithm is used to calculate the route for each **s-d pair**. The performance of BSWA has been investigated by evaluating the performance of following parameters:

1. Burst loss probability vs. traffic load in Erlangs with BSWA.
2. Number of used wavelength channels v/s. % of wavelengths used per fiber.
3. Message propagation Delay v/s % of wavelengths used per fiber.

Further we have also calculated the blocking probability of OBS Network with full wavelength conversion capability using Erlangs Loss formula for NSFNET.

3.1 Burst Loss Probability with BSWA Algorithm

3.1.1 NSFNET Topology

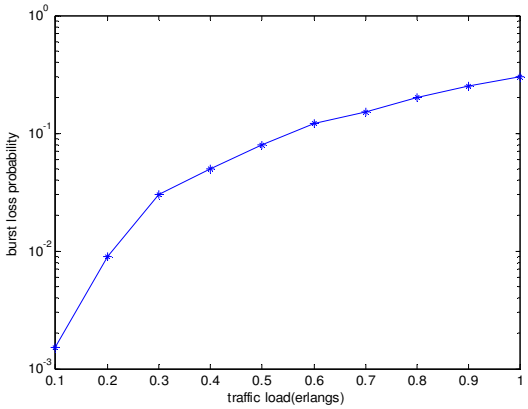

FIGURE 5: for NSFNET Topology

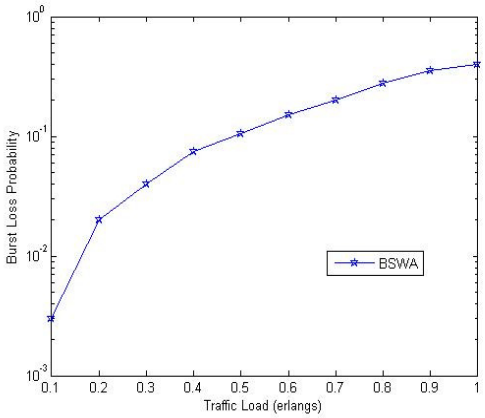

FIGURE 6:for INTERNET2NET Topology

The results of burst loss probability vs traffic load with BSWA algorithm have been shown in Figure 5 for NSFNET. We observe that as the load increases burst loss probability also increases. From Figure 5 it is evident that up to 0.3 erlangs traffic load, burst loss probability increases rapidly and at 0.3 erlangs it is approximately 3×10^{-2}.beyond 0.3 erlangs of traffic load, burst loss probability increases at aslower pace and after 0.8 erlangs it becomes nearly uniform (burst loss probability is approximately 0.2 to 0.3 as traffic load ranges between 0.8 erlangs to 1.0 erlangs) .

3.1.2 INTERNET2NET Topology

The results of burst loss probability vs traffic load with BSWA algorithm have been shown in Figure 6 for INTERNET2NET. We observe from Figure 6 as load increases burst loss probability also increases. From Figure 6 it is clear that up to 0.2 erlangs of traffic load, burst loss probability increases rapidly and between 0.2 erlangs to 0.5 erlangs of traffic load, burst loss probability increases but at a slower rate. At 0.1 erlangs burst loss probability is approximately 3×10^{-3} and at 0.2 erlangs of traffic load it is approximately 2×10^{-2}. Beyond 0.5 erlangs of load, burst loss probability increases at a much slower rate while after 0.8 erlangs it becomes almost uniform, so no need was felt to simulate for more than 1.0 erlags of traffic load.

3.2 Number of Used Wavelength Channels vs. % of Wavelengths Used per Fiber

3.2.1 NSFNET Topology

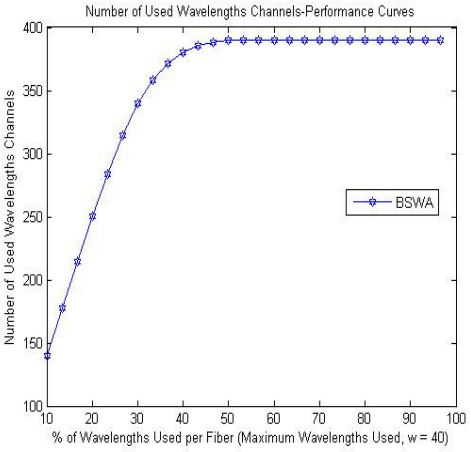

FIGURE 7: for NSFNET Topology.

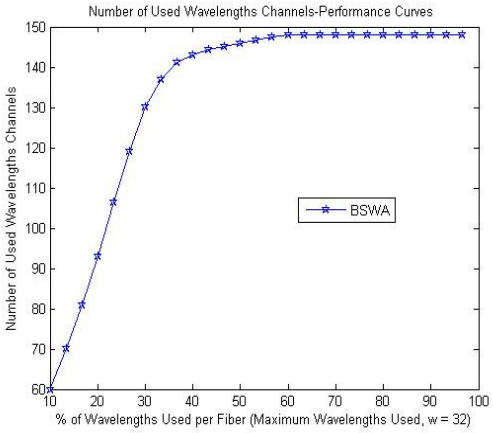

FIGURE 8:for INTERNET2NET Topology

For simulation we have taken number of wavelengths per fiber equal to 40 for NSFNET network. The simulation results are shown in Fig. **7** for traffic load of 0.2 erlangs. In Figure 7 at 10% of wavelengths used per fiber, number of used wavelengths channels are 140 and it increases with the % of wavelengths used per fiber. Again at 40% of wavelengths used per fiber (i.e. number of wavelengths per fiber w =16), the number of used wavelengths channels is 360 and that is almost constant after 40% of wavelengths used per fiber. Hence beyond 40 % , wavelengths reused per fiber more than 40% are unnecessary going to augment overall cost of the network.

3.2.2 INTERNET2NET Topology

Here for simulation we have taken maximum number of wavelengths per fiber = 32 . The simulation results are shown in Figure 8 for traffic load of 0.2 erlangs. As shown in Figure **8**, for 10% of wavelengths used per fiber, number of used wavelengths channels are 60 and it increases with the % of wavelengths used per fiber. Again at 40% of wavelengths used per fiber (i.e. number of wavelengths per fiber w = 12), the number of used wavelengths channels is 145 and thereafter it is almost constant. Hence here also the % of wavelength reused per fiber should not be allowed to exceed 40 %.

3.3 Message Propagation Delay vs. % of Wavelengths Used Per Fiber

3.3.1 NSFNET Topology

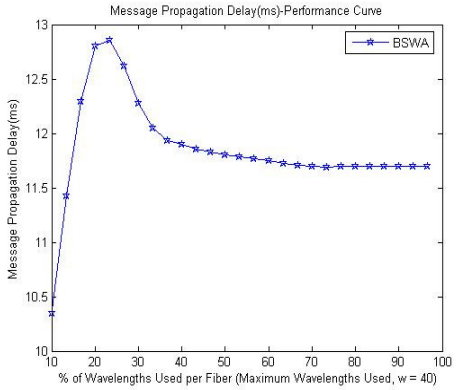

FIGURE 9: for NSFNET Topology.

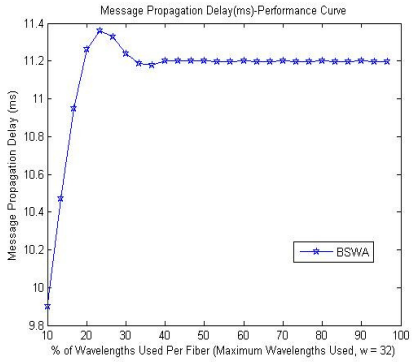

FIGURE10: for INTERNET2NET.Topology

we have assumed maximum number of wavelength per fiber W = 40 . The simulation results are shown in Figure 9 for traffic load of 0.2 erlangs. From Figure 9 we noticed that message propogation delay increases upto 25 % of wavelengths used per fiber and then it suddenly decreases. It become nearlyuniform 40 % of wavelength used per fibr. As % of wavelengths used per fiber increases up to 25%, message reaches from source to destination with significant delay and therefore initially the message propagation delay also increases.

However after 25% of wavelengths used per fiber, number of available wavelength channels also increases and more message are being propagated through single hop which led to decrease in delay up to 40% of wavelengths used per fiber. Thereafter it becomes saturated because all traffic is being propagated through the single hop. This investigation also reveals that wavelength used per fiber should be confined within 40 %.

3.3.2 INTERNET2NET Topology

For simulation we have taken maximum number of wavelength per fiber = 32 .The simulation result are demonstrated in Figure 10 for traffic load of 0.2 erlangs. Here also up to 25% of wavelengths per fiber, message propagation delay increases with a further decreases till 40 % and thereafter becomes nearly uniform . As % of wavelengths used per fiber increases up to 25%, message reaches from source to destination with a significant delay,thereby resulting in increase of message propogation delay.

Since after 25% of wavelengths used per fiber, number of available wavelength channels increases and more message are being propagated through the single hop which ultimately results in decrease of delay up to 40% of wavelengths used per fiber. Thereafter delay becomes

saturated because all traffic is being propagated through the single hop. Hence the above investigation also reveals that % of wavelength used per fiber should be confined to 40 % as far as message delay is concerned.

3.4 Burst Loss Probability with full wavelength converter Capability with 8,16,24,32 wavelengths per fiber

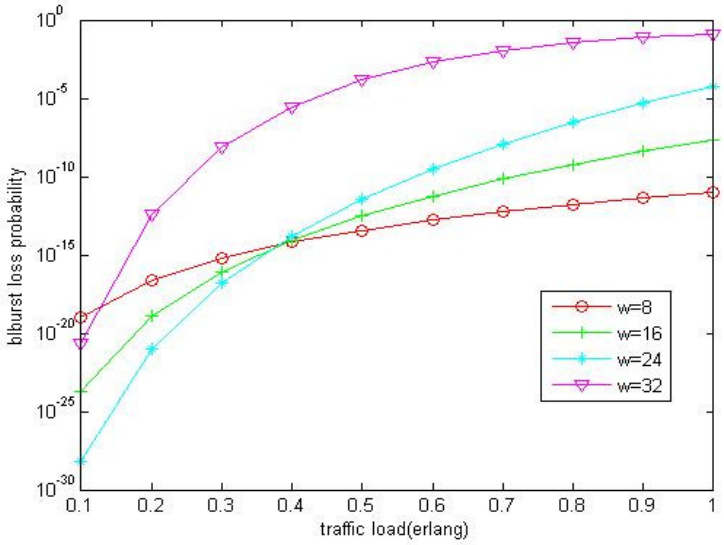

FIGURE 11: Burst Loss Probability vs.Traffic Load for full wavelength converters OBS Network

In FIGURE 11 burst loss probability vs traffic load per wavelength in erlangs have been shown for different number of wavelength per optical fiber. We can see at high traffic load beyond 0.4 erlags, number of wavelengths per fiber w = 8 is giving minimum blocking probability. The decreasing performance order is w = 8, 16, 24, 32 for traffic load per wavelength more than 0.4 erlangs. The decreasing performance order is w=24, 16, 8, 32 for traffic load per wavelength between 0.15 and 0.4 erlags. The decreasing order is w =24, 16, 32, 8 for traffic load per wavelength for traffic load less than 0.15 erlangs. Therefore from the above study we conclude that wavelength factor w=16,24 are giving better performance for different traffic loads as compared to 8 & 32.

4. CONCLUSION

In this paper we have discussed a novel static wavelength assignment approach, called BSWA, which can greatly reduce the burst loss probability by balancing the traffic that shares common links among wavelengths on those links. We have compared also the burst loss probability of various wavelength assignment policies and observed that at the starting of traffic load BSWA is giving relatively better performance among others. It has been also observed that without incorporating extra dynamic information and signaling cost, BSWA can achieve almost the same performance as dynamic techniques like PWA. The performance of BSWA algorithm with NSFNET and INTERNET2NET network has also been studied and it is observed that approximately 40% of wavelengths used per fiber give reasonably good results with respect to the parameters: message propagation delay and channel utilization. The performance with respect to various parameters can be individually summarized as follows: -

A. The performance analysis of burst loss probability vs. traffic load for both networks shows that it has been improved by BSWA algorithm as compared to other static wavelength assignment algorithm and it is almost same as PWA (dynamic wavelength assignment algorithm).

B. The performance analysis of number of used wavelengths channels vs. % of wavelengths Used per fiber shows that after approximately 40% of wavelengths used per fiber (i.e. for NSFNET 16 & INTERNET2NET 12 wavelengths per fiber), number of used wavelengths Channels become uniform. Hence it is recommended that beyond 40% of wavelengths reused per fiber the cost of network will increase without improvement in the overall performance.

C. The performance analysis of message propagation delay vs. % of wavelengths used per fiber shows that after approximately 40% of wavelengths used per fiber (i.e. for NSFNET 16 and INTERNET2NET 12 wavelengths per fiber), message propagation delay is minimum and nearly uniform. Here again it is observed that % of wavelengths used per fiber must be confined to 40 %, as there is no significant improvement in the performance beyond that.
Further we have also analyzed the performance with wavelength converters for different number of wavelengths per fiber and it is observed that wavelengths factor w = 16 and 24 reduces the blocking probability more efficiently in comparison with w= 8 & 32.

The above investigations ultimately conclude that % of wavelengths reused per fiber should not be allowed to exceed 40% as otherwise it augments the overall network cost without any further significant improvement in the performance of the network. The Performance analysis of Optical Burst Switching Networks for INTERNET2NET and NSFNET can also be carried out in future by using dynamic wavelength techniques. The possibility of optimizing an arbitrary network topologies to yield better network performance can also be explored in future.

REFERENCES

1. Aditya Goel, Ajaii Sharma "Performance Analysis of Mobile ADOC Network using AODV Protocol" International Journal of Computer Science and Security Volume 3 Issue 5 pages 334-343, 2009.
2. Aditya Goel, R K Sethi "Integrated Optical wireless network for next generation wireless Systems", Signal Processing – An International Journal, vol. 3 Issue 1, Pages 1-13, 2009.
3. Aditya Goel, Ravi Shankar Mishra Remote Date Acquisition Using Wireless SCADA System International Journal of Engineering Volume 3 Issue 1 pages 58 – 64, 2009.
4. Shikha Nema, Aditya Goel, R P Singh, "Integrated DWDM and MIMO-OFDM system for 4G High capacity mobile communication System" Signal Processing – An International Journal Volume 3 Issue 5 pages 132-143, Nov/Dec 2009.
5. F. Kukuchi et al.,"10.92-Tbits/s triple-band / ultra dense optical repeated transmission Experiment," in Proceedings of Optical Fiber Communication Conference (OFC), Anaheim, California, USA, March 2001 number PD24.
6. X. Wang, H. Morikawa, and T. Aoyama, " Priority-based wavelength assignment algorithm for burst switched WDM optical networks," IEICE Trans. Commun E86-B (5), 1508–1514 (May 2003)
7. C. Qiao and M. Yoo, "Optical burst switching (OBS)—a new paradigm for an optical Internet," J. High Speed Networks. 8(1), 69–84(1999)
8. J S Turner, "Terabit burst switching," J. High-Speed Networks, vol.8, no.1, pp.3-16, Jan.1999.
9. Jiangtao Luo , Jun Huang, Hao Chang et.al. ," ROBS: A novel architecture of Reliable Optical Burst Switching with congestion control," J. High-Speed Networks, vol.16, No.2, pp.123-131, 2007
10. C.H. Xin and C.Qiao, "A comparative study of OBS and OFS," in Proceedings of Optical Fiber Communication Conference (OFC), Anaheim, California, USA, no. ThG7-1, Mar 2001
11. M. Düser and P. Bayvel, "Analysis of a dynamically wavelength-routed optical burst switched Network architecture," IEEE J. of Light wave Technology, vol. 20, no. 4, pp. 574-585, April 2002.
12. De Miguel, M. Düser, and P. Bayvel, "Traffic load bounds for optical burst switched networks with Dynamic wavelength allocation," in Proc. of the IFIP TC6 5th International Working Conference on Optical Network Design and Modeling (ONDM 2001), Vienna, February 2001.
13. M. Düser and P. Bayvel, "Bandwidth utilization and wavelength re-use in WDM optical burst-Switched packet networks," in Proc. of the IFIP TC6 5th International Working Conference on Optical Network Design and Modeling (ONDM 2001), Vienna, February 2001.
14. C. Qiao and M. Yoo, "Choices, features and issues in Optical Burst Switching," Optical Networks Magazine, vol. 1, no. 2, pp. 37-44, April 2000.
15. Chunlei Zhu, Wenda Ni, Yu Du, Yanhe Li, Xiaoping Zheng, Yili Guo and Hanyi Zhang, "New and Improved Approaches for Wavelength Assignment in Wavelength-Continuous Optical Burst Switching Network," Optical Engineering September 2007/vol.46 (9).
16. L. Kleinrock, Queueing Systems - Volume I: Theory, John Wiley & sons, New York, 1975.

17 Rajalakshmi P and Ashok Jhunjhunwala, "Analytical performance computation for all optical networks

With wavelength conversion, "*IETE Journal of Research*, Vol. 54, No.1, Jan-Feb 2008, pp 31-38.
18 P.J. Kühn, Teletraffic Theory and Engineering, Lecture at University Stuttgart, 2002/2003.

Knowledge – Based Reservoir Simulation – A Novel Approach

M. Enamul Hossain menamul@kfupm.edu.sa
Department of Petroleum Engineering
King Fahd University of Petroleum & Minerals
Dhahran 31261, Saudi Arabia

M. Rafiqul Islam rafiq.islam@dal.ca
Department of Civil and Resource Engineering
Dalhousie University
Sexton Campus, 1360 Barrington Street, Halifax, NS B3J 2X4, Canada

Abstract

It is well known that reservoir simulation studies are very subjective and vary from simulator to simulator. While SPE benchmarking has helped accept differences in predicting petroleum reservoir performance, there has been no scientific explanation behind the variability that has frustrated many policy makers and operations managers and puzzled scientists and engineers. In a recent book by the research group of R. Islam, a new approach is taken to add the Knowledge dimension to the problem. For the first time, reservoir simulation equations are shown to have embedded variability and multiple solutions that are in line with physics rather than spurious mathematical solutions. With this clear description, a fresh perspective in reservoir simulation is presented. Unlike the majority of reservoir simulation approaches available today, the 'knowledge-based' approach does not stop at questioning the fundamentals of reservoir simulation but offers solutions and demonstrates that proper reservoir simulation should be transparent and empower decision makers rather than creating a black box. Mathematical developments of new governing equations based on in-depth understanding of the factors that influence fluid flow in porous media under different flow conditions are introduced. Behavior of flow through matrix and fractured systems in the same reservoir, heterogeneity and fluid/rock properties interactions, Darcy and non-Darcy flow are among the issues that are thoroughly addressed. For the first time, the fluid memory factor is introduced with a functional form. The resulting governing equations are solved without linearization at any stage. A series of clearly superior mathematical and numerical techniques are also presented that allow one to achieve this objective. Mathematical solutions that provide a basis for systematic tracking of multiple solutions that are inherent to non-linear governing equations. This was possible because the new technique is capable of solving non-linear equations without linearization. To promote the new models, a presentation of the common criterion and procedure of reservoir simulators currently in use is provided. The models are applied to difficult scenarios, such as in the presence of viscous fingering, fractures, and others. It is demonstrated that the currently available simulators only address very limited range of solutions for a particular reservoir engineering problem. Examples are provided to show how the Knowledge-based approach extends the currently known solutions and provide one with an extremely useful predictive tool for risk assessment.

Keywords: Emulation, Newtonian Mechanics, New Energy Balance Formulation, Energy Pricing, Non-Linear Mathematics

1. INTRODUCTION

In reservoir simulation, the principle of GIGO (Garbage in and garbage out) is well known [1]. This principle implies that the input data have to be accurate for the simulation results to be acceptable. Petroleum industry

has established itself as the pioneer of subsurface data collection [2]. Historically, no other discipline has taken so much care in making sure input data are as accurate as the latest technology would allow. The recent superflux of technologies dealing with subsurface mapping, real time monitoring, and high speed data transfer is an evidence of the fact that input data in reservoir simulation are not the weak link of reservoir modelling.

However, for a modelling process to be knowledge-based, it must fulfill two criteria, namely, the source has to be true (or real) and the subsequent processing has to be true [3]. As indicated earlier, the source is not a problem in the petroleum industry. The potential problem lies within the processing of data. For the process to be knowledge-based, the following logical steps have to be taken:

- Collection of data with constant improvement of the data acquisition technique. The data set to be collected is dictated by the objective function, which is an integral part of the decision making process. Decision making, however, should not take place without the abstraction process. The connection between objective function and data needs constant refinement. This area of research is one of the biggest strength of the petroleum industry, particularly in the information age.
- The gathered data should be transformed into Information so that they become useful. With today's technology, the amount of raw data is so huge, the need for a filter is more important than ever before. However, it is important to select a filter that doesn't skew data set toward a certain decision. Mathematically, these filters have to be non-linearized [4]. While the concept of non-linear filtering is not new, the existence of non-linearized models is only beginning to be recognized [2].
- Information should be further processed into 'knowledge' that is free from preconceived ideas or a 'preferred decision'. Scientifically, this process must be free from information lobbying, environmental activism, and other forms of bias. Most current models include these factors as an integral part of the decision making process [5], whereas a scientific knowledge model must be free from those interferences as they distort the abstraction process and inherently prejudice the decision making. Knowledge gathering essentially puts information into the big picture. For this picture to be distortion-free, it must be free from non-scientific maneuvering.
- Final decision making is knowledge-based, only if the abstraction from 1) through 4) has been followed without interference. Final decision is a matter of Yes or No (or True or False or 1 or 0) and this decision will be either knowledge-based or prejudice-based. Figure 1 shows the essence of the knowledge based decision making.

The process of aphenomenal or prejudice-based decision-making is illustrated by the inverted triangle, proceeding from the top down (Figure 2). The inverted representation stresses the inherent instability and unsustainability of the model. The source data from which a decision eventually emerges already incorporates their own justifications, which are then massaged by layers of opacity and disinformation.

The disinformation referred to here is what results when information is presented or recapitulated in the service of unstated or unacknowledged ulterior intentions [6]. The *methods* of this disinformation achieve their effect by presenting evidence or raw data selectively, without disclosing either the fact of such selection or the criteria guiding the selection. This process of selection obscures any distinctions between the data coming from nature or from any all-natural pathway, on the one hand, and data from unverified or untested observations on the other. In social science, such manoeuvering has been well known, but the recognition of this aphenomenal model is new in science and engineering [7].

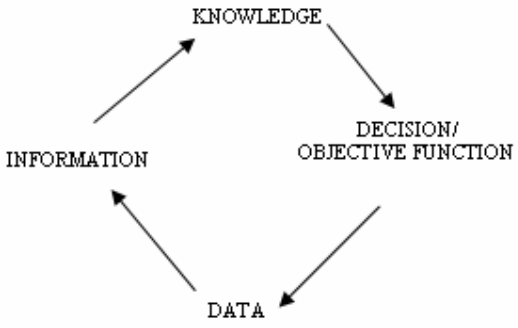

FIGURE1: The knowledge model and the direction of abstraction

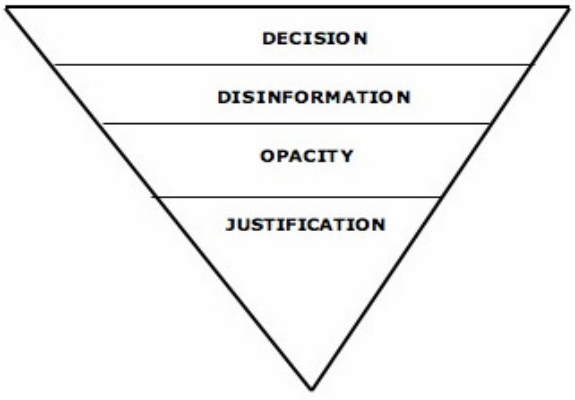

FIGURE 2: Aphenomenal decision-making

2. SHORTCOMINGS OF THE CONVENTIONAL APPROACH

Recently, Mustafiz and Islam [8] published a comprehensive review of currently available reservoir simulation approaches. In this paper, the discussion is limited to finite difference approach because that is the most commonly used technique in the petroleum reservoir modelling community.

The history of differential calculus dates back to the time of Leibnitz and Newton. In this concept, the derivative of a continuous function to the function itself is related. In the core of differential calculus is the Newton's formula that has the following approximation attached to it: the magnitude and direction change independently of one another. There is no problem in having separate derivatives for each component of the vector or in superimposing their effects separately and regardless of order. That is what mathematicians mean when they describe or discuss Newton's derivative being used as a "linear operator". Following this, comes Newton's difference-quotient formula. When the value of a function is inadequate to solve a problem, the rate at which the function changes, sometimes, becomes useful. Therefore, the derivatives are also important in reservoir simulation. In Newton's difference-quotient formula, the derivative of a continuous function is obtained. This method relies implicitly on the notion of approximating instantaneous moments of curvature, or infinitely small segments, by means of straight lines. This alone should have tipped everyone off that his derivative is a linear operator precisely because, and to the extent that, it examines change over time (or distance) within an already established function. This function is applicable to an infinitely small domain, making it non-existent. When, integration is performed, however, this non-existent domain is assumed to be extended to finite and realistic domain, making the entire process questionable.

Zatzman and Islam [9] identified the most significant contribution of Newton in mathematics as the famous definition of the derivative as the limit of a difference quotient involving changes in space or in time as small as anyone might like, but not zero, *viz.*

$$\frac{d}{dt}f(t) = Lim_{\Delta t \to 0}\ \frac{f(t+\Delta t)-f(t)}{\Delta t} \qquad (1)$$

Without regards to further conditions being defined as to when and where differentiation would produce a meaningful result, it was entirely possible to arrive at "derivatives" that would generate values in the range of a function at points of the domain where the function was not defined or did not exist. Indeed: it took another century following Newton's death before mathematicians would work out the conditions – especially the requirements for continuity of the function to be differentiated within the domain of values – in which its derivative (the name given to the ratio-quotient generated by the limit formula) could be applied and yield reliable results. Kline [10] detailed the problems involving this breakthrough formulation of Newton. However, no one in the past did propose an alternative to this differential formulation, at least not explicitly. The following figure (Figure 3) illustrates this difficulty.

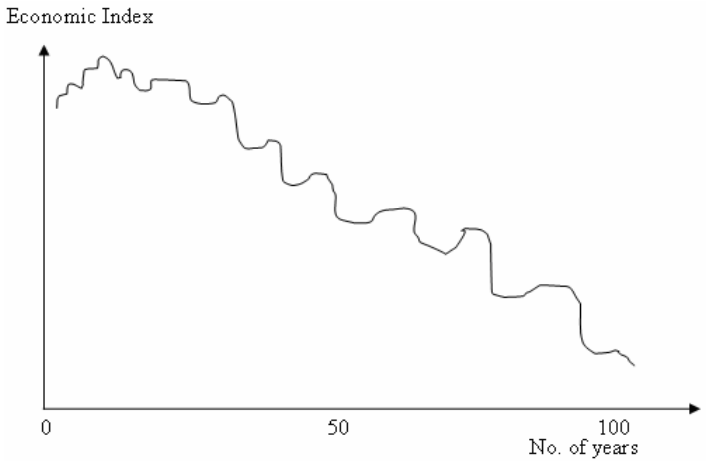

FIGURE 3: Economic wellbeing is known to fluctuate with time

In this figure, economic index (it may be one of many indicators) is plotted as a function of time. In nature, all functions are very similar. They do have local trends as well as global trend (in time). One can imagine how the slope of this graph on a very small time frame would quite arbitrary and how devastating it would be to

take that slope to a long-term. One can easily show the trend, emerging from Newton's differential quotient would be diametrically opposite to the real trend. Zatzman and Islam [9] provided a basis for determining real gradient, rather than local gradient that emerges from Newtonian's differential quotient. In that formulation, it is shown that the actual value of Δt, over which a reliable gradient has to be observed, needs to be several time greater than the characteristic time of a system. The notion of Representative Elemental Volume (REV), as first promoted by Bear [11] is useful in determining a reasonable value for this characteristic time. The second principle is that at no time Δt be allowed to approach 0 (Newton's approximation), even when the characteristic value is very small (e.g. phenomena at nano scale). With the engineering approach, it turns out such approximation is not necessary [12] because this approach bypasses the recasting of governing equations into Taylor series expansion, instead relying on directly transforming governing equations into a set of algebraic equations. In fact, by setting up the algebraic equations directly, one can make the process simple and yet maintain accuracy [4]. Finally, initial analysis should involve the extension Δt to ∞ in order to determine the direction, which is related to sustainability of a process [13].

Figure 4 shows how formulation with the engineering approach ends up with the same linear algebraic equations if the inside steps are avoided. Even though the engineering approach was known for decades (known as the control volume approach), no one identified in the past the advantage of removing in-between steps. In analyzing further the role of mathematical manipulation in solving a natural problem, the following extremely simple example can be cited. Consider the function, $y = 5$. Following steps show how this function simple function can take route of knowledge or prejudice, based on the information that is exposed or hidden, respectively.

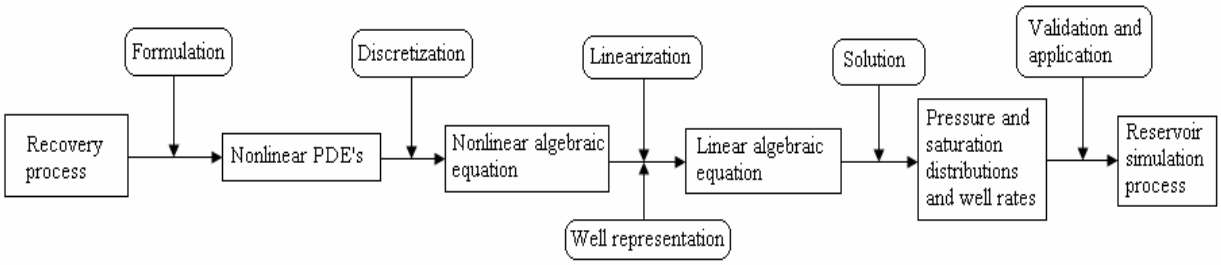

FIGURE 4: Major steps used to develop reservoir simulators (redrawn from Abou-Kassem et al., 2006, Hossain et al., 2009)

Step 1: $y = 5$. This is an algebraic equation that means, y is a constant with a value of 5. This statement is an expression of tangibles, which becomes clear if the assumptions are pointed out. The assumptions are: a) y has the same dimension as 5 (meaning dimensionless); b) nothing else matters (this one actually is a clarification of the condition a). Therefore, the above function implies that y cannot be a function of anything (including space and time). The mere fact that there is nothing in nature that is constant makes the function aphenomenal. However, subsequent manipulations (as in Step 2) make the process even more convoluted.

Step 2: $dy/dx = 0$. This simple derivation is legitimate in calculus that originates from Newton's ratio of quotient theory. In this, even partial derivative would be allowed with equal legitimacy as nothing states in conventional calculus that such operation is illegitimate. By adding this derivative in x (as in x direction in Cartesian coordinate), a spurious operation is performed. In fact, if Step 1 is true, one can add any dimension to this the differential would still be 0 – statement that is 'technically' true but hides background information that becomes evident in Step 3.

Step 3: If one integrates dy/dx, one obtains, y = C, where C is a constant that can have infinite number of values, depending on which special case it is being solved for. All of a sudden, it is clear that the original function. All of a sudden, it is clear that the original function (y = 5) has disappeared.

Step 4: One special case of $y = C$ is, y = 5. To get back the original and unique function (as in Step 1), one now is required to have boundary conditions that are no longer attached to the mathematical formulation. If a special case of C = 5 is created, similarly one can have y=1, 2, 3, 4, 5, 6,... How does one know which solution will give the 'true' solution. In this particular case, all but one solution are called 'spurious' solutions, because they failed to match the solution of interest, i.e., y = 5.

This simple example shows how imposing Newton's differential and integrating procedure convolutes the entire process, while losing information that would allow anyone to trace back the original algebraic function.

On the other hand, if one is looking at an actual phenomenon, then dy/dx = 0 could mean that we are at the very start of something, or at the very end of something. If we look at ∂y/∂x, on the other hand, then we have to look also at Δy/Δt, and then we also have to consider the situation where Δy/Δx=0 but Δy/Δt is non-0. This might very well be a branch-point, a point of bifurcation or, generally speaking, something marking a change from an old state to a new state. Branch-points in physical natural reality clearly imply infinite solutions, since the process could go, literally, anywhere from that branch-point. This approach of locating bifurcation phenomena has eluded previous researchers engaged in modelling chaos [14]. With the engineering approach, the following steps can be taken. Note the similarity of these steps with the one shown above regarding a simpler function.

Step 1) Mass balance + Darcy's law → It is an algebraic equation.
Step 2a) Time variable is added to it through Newton's differential quotient → time increment is allowed to approach to 0.
Step 2b) Space variable is added through Newton's differential quotient → space increment is allowed to approach 0.
Step 2c) Differential equations emerge, burying assumptions added in 2a and 2b.
Step 3) Differential equation integrated analytically, original solutions will not be recovered. The integrated values will have the possibility of having infinite solutions, depending on the boundary conditions, initial conditions, etc.
Step 4) Three special cases (out of infinite number of solutions possible) are identified as part of the integrated solution of the Differential equation in Step 3. They are:
Step 4a) Steady state, compressible. This is Mass balance and Darcy's law as in Step 1.
Step 4b) Unsteady state, slightly compressible fluid. This is the typical equation that gives rise to the Diffusivity equation. This one would have liquid density as the only equation of state (density as a function of pressure).
Step 4c) Unsteady state, compressible fluid case. This is the typical gas flow equation. This would have gas compressibility (z factor that is a function of pressure and temperature). Here the term 'unsteady' means there is a time derivative. As time extends to infinity, this term drops off, making the model steady state. This alone shows that these 'unsteady state' models are not dynamic models and do not emulate nature that is dynamic at all time.
Step 5) Because analytical methods are very limited in solving a PDE and require their additional assumptions regarding boundary conditions, numerical techniques were introduced. This one essentially involves discretisation through Taylor series approximation and subsequent elimination of higher order terms, arguing that at higher order they are too small (e.g. if Δx is less than 1, Δx^2 is << 1; Δx^3 <<< 1).
Step 6) The removal of higher order terms, as in Step 5, is equivalent to eliminating the additions of space and time variables as in Steps 2a and 2b. We, therefore, recover original mass balance and Darcy's law (Momentum balance equation) as in Step 1. The Engineering approach works with these algebraic equations (Step 1) rather than working with PDE and subsequent discretized forms. This explains why Engineering approach coefficients are the same as the 'mathematical approach' coefficients.

When we go from y = 5 to dy/dx = 0, we add the possibility of adding an infinite series. When we then go from dy/dx to y = constant, we are left with infinite solutions, all because of the previous addition. On the other hand, if we do this integration numerically (by invoking Taylor series approximation), we end up having the original solution only if we ignore the left over terms of the infinite series that may or may not be convergent. It is important to see the actual derivation of Taylor series expansion.

3. NUMERICAL CHALLENGES

3.1. Theory of Onset and Propagation of Fractures due to Thermal Stress

Fundamental work needs to be performed in order to develop relevant equations for thermal stresses. Similar work has been initiated by Wilkinson et al. [15], who used finite element modelling to solve the problem. There has been some progress in the design of material manufacturing for which in situ fractures and cracks are considered to be fatal flaws. Therefore, formulation complete equations are required in order to model thermal stress and its effect in petroleum reservoirs. It is to be noted that this theory deals with only transient state of the reservoir rock.

3.2. 2-D and 3-D solutions of the governing equations

In order to determine fracture width, orientation, and length under thermal stresses as a function of time, it is imperative to solve the governing equations first in 2-D. The finite difference is the most accepted technique to develop the simulator. An extension of the developed simulator to the cylindrical system is useful in designing hydraulic fractures in thermally active reservoirs. The 3-D solutions are required to determine 3-D stresses and the effects of permeability tensor. Such simulation will provide one with the flexibility of determining fracture orientation in the 3-D mode and guide as a design tool for hydraulic fracturing. Although the 3-D version of the hydraulic fracturing model can be in the framework put forward earlier [15], differences of opinion exist as to how thermal stress can be added to the in situ stress equations.

3.3 Viscous fingering during miscible displacement

Viscous fingering is believed to be dominant in both miscible and immiscible flooding and of much importance in a number of practical areas including secondary and tertiary oil recovery. However, modelling viscous fingering remains a formidable task. Only recently, researchers from Shell have attempted to model viscous fingering with the chaos theory. Islam (1993) has reported in a series of publications that periodic and even chaotic flow can be captured properly by solving the governing partial differential equations with improved accuracy (Δx^4, Δt^2). This needs to be demonstrated for viscous fingering. The tracking of chaos (and hence viscous fingering) in a miscible displacement system can be further enhanced by studying phenomena that onset fingering in a reservoir. It eventually will lead to developing operating conditions that would avoid or minimize viscous fingering. Naami et al. [[16] conducted both experimental and numerical modelling of viscous fingering in a 2-D system. They modelled both the onset and propagation of fingers by solving governing partial differential equations. Recent advances in numerical schemes [17 – 18] can be suitably applied in modelling of viscous fingering. The scheme proposed by Bokhari and Islam [18] is accurate in the order of Δx^4 in space and Δt^2 in time. This approach has been used to model viscous fingering with reasonable agreement with experimental results [19]. Similar approach can be extended for tests in a 3-D system in future. Modelling viscous fingering using finite element approach has been attempted as well [20].

4. CHALLENGES OF MODELLING SUSTAINABLE PETROLEUM OPERATIONS

Recently, Khan and Islam [21 – 22] outlined the requirements for rending fossil fuel production sustainable. This scientific study shows step by step how various operations ranging from exploration to fuel processing can be performed in such a manner that resulting products will not be toxic to the environment. However, modelling such a process is a challenge as the conventional characterization of matter does not make any provision for separating sustainable operations from unsustainable ones. In order to avoid some of the difficulties associated with conventional approach, Khan et al. [23] recently introduced simultaneous characterization of matter and energy. This renders time a characteristic of matter itself within the overall context of mass-energy-momentum conservation. In other words, time ceases to be mainly or only a derivative of some spatial displacement of matter. In this way, it becomes possible at last to treat time, consistently, as a true fourth dimension — and no longer as merely the independent variable. This description is consistent with Einstein's revolutionary relativity theory, but does not rely on Maxwell's equations as the starting point. The resulting equation is shown to be continuous in time, thereby allowing transition from mass to energy. As a result a single governing equation emerges. This equation is solved for a number of cases and is shown to be successful in discerning between various natural and artificial sources of mass and energy. With this equation, the difference between chemical and organic fertilizers, microwave and wood stove heating, and sunlight and fluorescent light can be made with unprecedented clarity. This analysis would not be possible with conventional techniques. Finally, analysis results are shown for a number of energy- and material-related prospects. The key to the sustainability of a system lies within its energy balance. Khan et al. recast the combined energy-mass balance equation in the following form:

$$\int_{t=0}^{t=\infty} \int_{s=1}^{s=\infty} m\, v = constant \qquad (2)$$

Dynamic balances of mass, energy and momentum imply conditions that will give rise to multiple solutions, at least with the currently available mathematical tools. When it comes to the Nature, a portion of the space-time continuum in which real physical boundary conditions are largely absent, a mathematics that requires $\Delta t \rightarrow 0$ is clearly inappropriate. What is needed are non-linear algebraic equations that incorporate all relevant components (unknowns and other variables) involved in any of these critical balances that must be preserved by any natural system. In this context, Eq. 2 is of utmost importance. This equation can be used to define any process, for which the following equation applies:

$$Q_{in} = Q_{acc.} + Q_{out} \qquad (3)$$

In the above equation classical mass balance equation, Q_{in} in expresses Eq. 2 for inflow matter, Q_{acc} represents the same for accumulating matter, and Q_{out} represents the same for outflowing matter. Q_{acc} will have all terms related to dispersion/diffusion, adsorption/desorption, and chemical reactions. This equation must include all available information regarding inflow matters, e.g., their sources and pathways, the vessel materials, catalysts, and others. In this equation, there must be a distinction made among various matter, based on their source and pathway. Three categories are proposed: 1) biomass (BM); 2) convertible non-biomass (CNB); and 3) non-convertible non-biomass (NCNB). Biomass is any living object. Even though, conventionally dead matters are also called biomass, we avoid that denomination as it is difficult to scientifically discern when a matter becomes non-biomass after death. The convertible non-biomass (CNB) is the one that due to natural processes will be converted to biomass. For example, a dead tree is converted into methane after microbial actions, the methane is naturally broken down into carbon dioxide, and plants utilize this carbon dioxide in presence of sunlight to produce biomass. Finally, non-convertible non-biomass (NCNB) is a matter that emerges from human intervention. These matters do not exist in nature and their existence can be only considered artificial. For instance, synthetic plastic matters (e.g. polyurethane) may have similar composition as natural polymers (e.g. human hair, leather), but they are brought into existence through a very different process than that of natural matters. Similar examples can be cited for all synthetic chemicals, ranging from pharmaceutical products to household cookwares. This denomination makes it possible to keep track of the source and pathway of a matter. The principal hypothesis of this denomination is: all matters naturally present on Earth are either BM or CNB, with the following balance:

$$\text{Matter from natural source} + CNB_1 = BM + CNB_2 \quad (4)$$

The quality of CNB_2 is different from or superior to that of CNB_1 in the sense that CNB_2 has undergone one extra step of natural processing. If nature is continuously moving to better environment (as represented by the transition from a barren Earth to a green Earth), CNB_2 quality has to be superior to CNB_1 quality. Similarly, when matter from natural energy sources come in contact with BMs, the following equation can be written.

$$\text{Matter from natural source} + B_1M = B_2M + CNB \quad (5)$$

Applications of this equation can be cited from biological sciences. When sunlight comes in contact with retinal cells, vital chemical reactions take place that results in the nourishment of the nervous system, among others [24]. In these mass transfers, chemical reactions take place entirely differently depending on the light source, the evidence of which has been reported in numerous publications [25]. Similarly, sunlight is also essential for the formation of vitamin D, which is in itself essential for numerous physiological activities. In the above equation, vitamin D would fall under B_2M. This vitamin D is not to be confused with the synthetic vitamin D, the latter one being the product of artificial process. It is important to note that all products on the right hand side are of greater value than the ones on the left hand side. This is the inherent nature of natural processing – a scheme that continuously improves the quality of the environment and is the essence of sustainable technology development.

Following equation shows how energy from NCNB will react with various types of matter.

$$\text{Matter from unnatural source} + B_1M = NCNB_2 \quad (6)$$

An example of the above equation can be cited from biochemical applications. For instance, if artificially generated UV is in contact with bacteria, the resulting bacteria mass would fall under the category of NCNB, stopping further value addition by nature. Similarly, if bacteria are destroyed with synthetic antibiotic (pharmaceutical product, pesticide, etc.), the resulting product will not be conducive to value addition through natural processes, instead becoming trigger for further deterioration and insult to the environment.

$$\text{Matter from unnatural source} + CNB_1 = NCNB_3 \quad (7)$$

An example of the above equation can be cited from biochemical applications. The $NCNB_1$ which is created artificially reacts with CNB_1 (such as N_2, O_2) and forms NCNB3. The transformation will be in negative direction, meaning the product is more harmful than it was earlier. Similarly, the following equation can be written:

$$\text{Matter from unnatural source} + NCNB2_1 = NCNB_2 \quad (8)$$

An example of this equation is that the sunlight leads to photosynthesis in plants, converting NCBM to MB, whereas fluorescent lighting would freeze that process can never convert natural non-biomass into biomass.

4.1 Implications of the Simultaneous Characterization

The principles of the knowledge-based model proposed here are restricted to those of mass (or material) balance, energy balance and momentum balance. For instance, in a non-isothermal model, the first step is to resolve the energy balance based on temperature as the driver for some given time-period, the duration of which has to do with characteristic time of a process or phenomenon. Following the example of the engineering approach employed by Abou-Kassem, [12] and Abou-Kassem et al. [2], the available temperature data are distributed block-wise over the designated time-period of interest. Temperature being the driver, as the bulk process of interest, i.e., changes with time, a momentum balance may be derived. Velocity would be supplied by local speeds, for all known particles. This is a system that manifests phenomena of thermal diffusion, thermal convection and thermal conduction, without spatial boundaries but giving rise nonetheless to the “mass” component.

The key to the system’s sustainability lies with its energy balance. Here is where natural sources of biomass and non-biomass must be distinguished from non-natural, non-characteristic industrially synthesised sources of non-biomass.

Figure 5 envisions the environment of a natural process as a bioreactor that does not and will not enable conversion of synthetic non-biomass into biomass. The key problem of mass balance in this process, as in the entire natural environment of the earth as a whole, is set out in Figure 6: the accumulation rate of synthetic non-biomass continually threatens to overwhelm the natural capacities of the environment to use or absorb such material.

In evaluating Eq. 3, it is desirable to know all the contents of the inflow matter. However, it is highly unlikely to know the all the contents, even at macroscopic level. In absence of a technology that would find the detailed content, it is important to know the pathway of the process to have an idea of the source of impurities. For instance, if de-ionised water is used in a system, one would know that its composition would be affected by the process of de-ionisation. Similar rules apply to products of organic sources, etc. If we consider combustion reaction (coal, for instance) in a burner, the bulk output will likely to be CO_2. However, this CO_2 will be associated with a number of trace chemicals (impurities) depending upon the process it passes through. Because, Eq. 3 includes all known chemicals (e.g. from source, adsorption/desorption products, catalytic reaction products), it would be able to track matters in terms of CNB and NCNB products. Automatically, this analysis will lead to differentiation of CO_2 in terms of pathway and the composition of the environment, the basic requirement of Eq. 2. According to Eq. 4, charcoal combustion in a burner made up of clay will release CO_2 and natural impurities of charcoal and the materials from burner itself. Similar phenomenon can be expected from a burner made up of nickel plated with an exhaust pipe made up of copper.

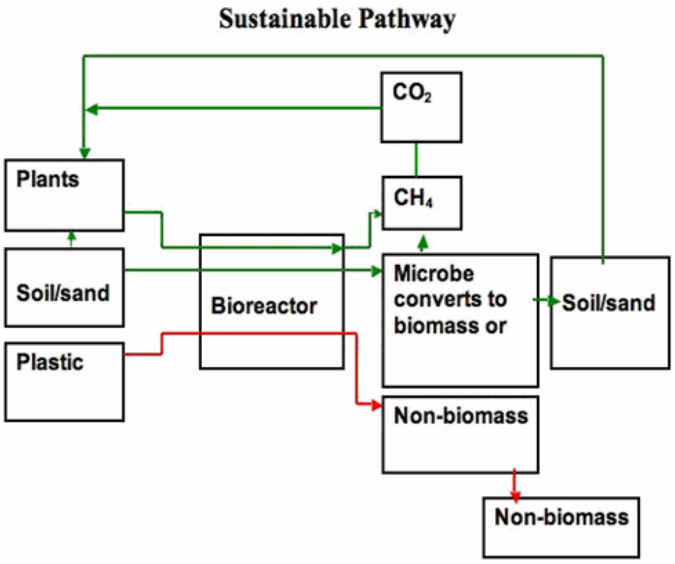

FIGURE 5: Sustainable pathway for material substance in the environment

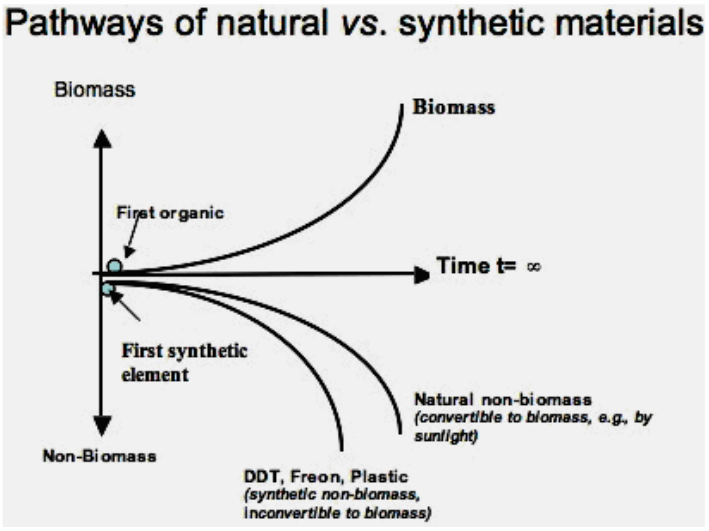

FIGURE 6: Transitions of natural and synthetic materials

Anytime, CO_2 is accompanied with CNB matter, it will be characterised as beneficial to the environment. This is shown in the positive slope of Figure 7. On the other hand, when CO_2 is accompanied with NCNB matter, it will be considered to be harmful to the environment, as this is not readily acceptable by the eco-system. For instance, the exhaust of the Cu or Ni-plated burner (with catalysts) will include chemicals, e.g. nickel, copper from pipe, trace chemicals from catalysts, beside bulk CO_2 because of adsorption/desorption, catalyst chemistry, etc. These trace chemicals fall under the category of NCNB and cannot be utilised by plants (negative slope from Figure 7). This figure clearly shows that on the upward slope case is sustainable as it makes an integral component of the eco-system. With conventional mass balance approach, the bifurcation graph of Figure 7 would be incorrectly represented by a single graph that is incapable of discerning between different qualities of CO_2 because the information regarding the quality (trace chemicals) are lost in the balance equation. Only recently, the work of Sorokhtin et al. [26] has demonstrated that without such distinction, there cannot be any scientific link between global warming and fossil fuel production and utilisation. In solving Eq. 3, one is likely encounter a set of non-linear equations. These equations cannot be linearised. Recently, Moussavizadegan et al. [27] proposed a method of solving non-linear equations. The principle is to cast Eq. 3 in engineering formulation, as outlined by Abou-Kassem et al. [2], whose principles were further elaborated in Abou-Kassem [12].

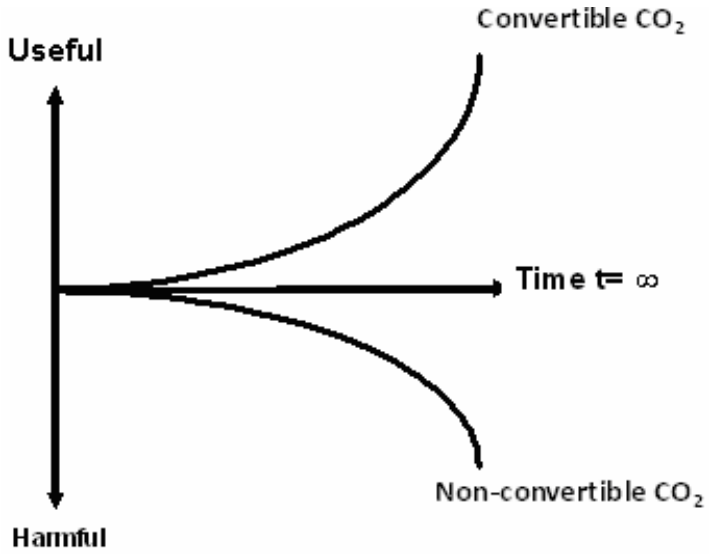

FIGURE 7: Divergent results from natural and artificial

The non-linear algebraic equations then can be solved in multiple solution mode. Mousavizadegan [27] recently solved such an equation to contemporary professionally acceptable standards of computational efficiency. The result looked like what is pictured in Figure 8.

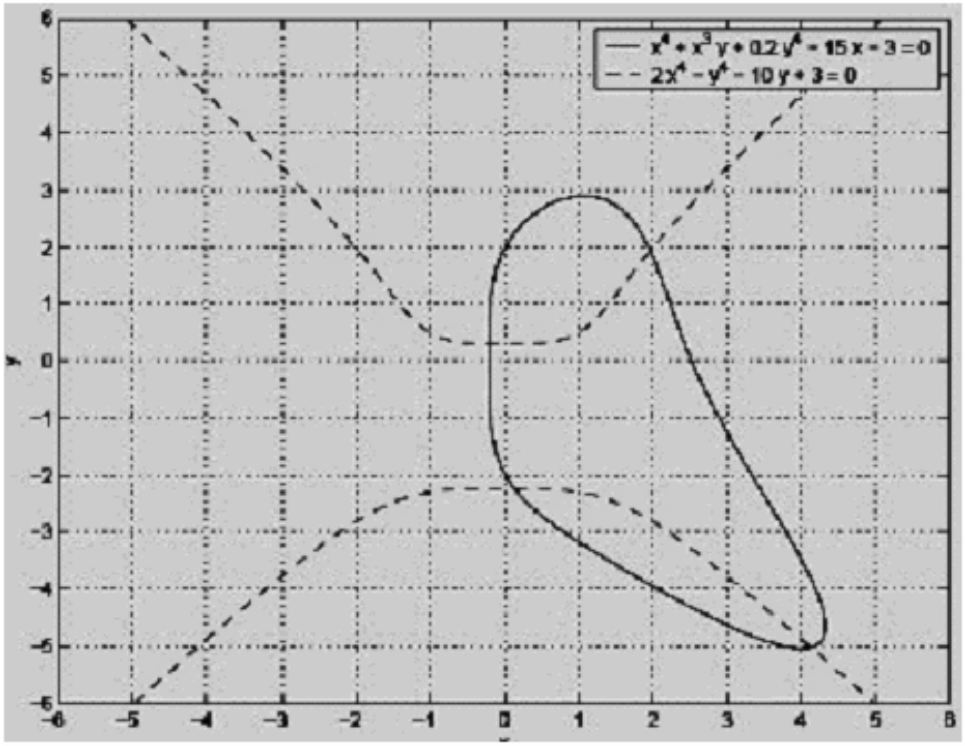

FIGURE 8: The solution behaviour manifested by just two non-linear bivariate equations, $x^4 + x^3y + 0.5y^4 - 15x - 3 = 0$ and $2x^4 - y^4 - 10y + 3 = 0$, suggests that a "cloud" of solutions would emerge.

5. EXAMPLES OF KNOWLEDGE-BASED SIMULATION

A series of computer simulation runs were performed, using the knowledge-based approach. The first series involved the solution of the 1-D multiphase flow problem. The Buckley-Leverett approach involves neglecting the capillary pressure term, leading to spurious multiple solutions. In order to remedy this problem, the well known 'shock' is introduced. While this approach is a practical solution to the problem, it is scientifically inaccurate. The knowledge-based approach requires that à priori simplification and/or linearisation be avoided. The governing 1-D multiphase equation, including the capillary pressure term, was solved using Adomian domain decomposition technique. This technique is capable of solving non-linear equations. The details of the approach are available elsewhere [28]. Figure 9 shows the results obtained for this case. This figure shows how the spurious multiple solutions disappear in favour of a set of monotonous functions. However, one would easily recall that such solutions also appear with conventional finite difference approach, even though this method does use linearisation, albeit at a later stage (during matrix inversion).

In order to determine the role of this linearisation, a series of numerical runs was performed using a non-linear solver. No linearisation was performed during the solution of these multiphase flow problems.

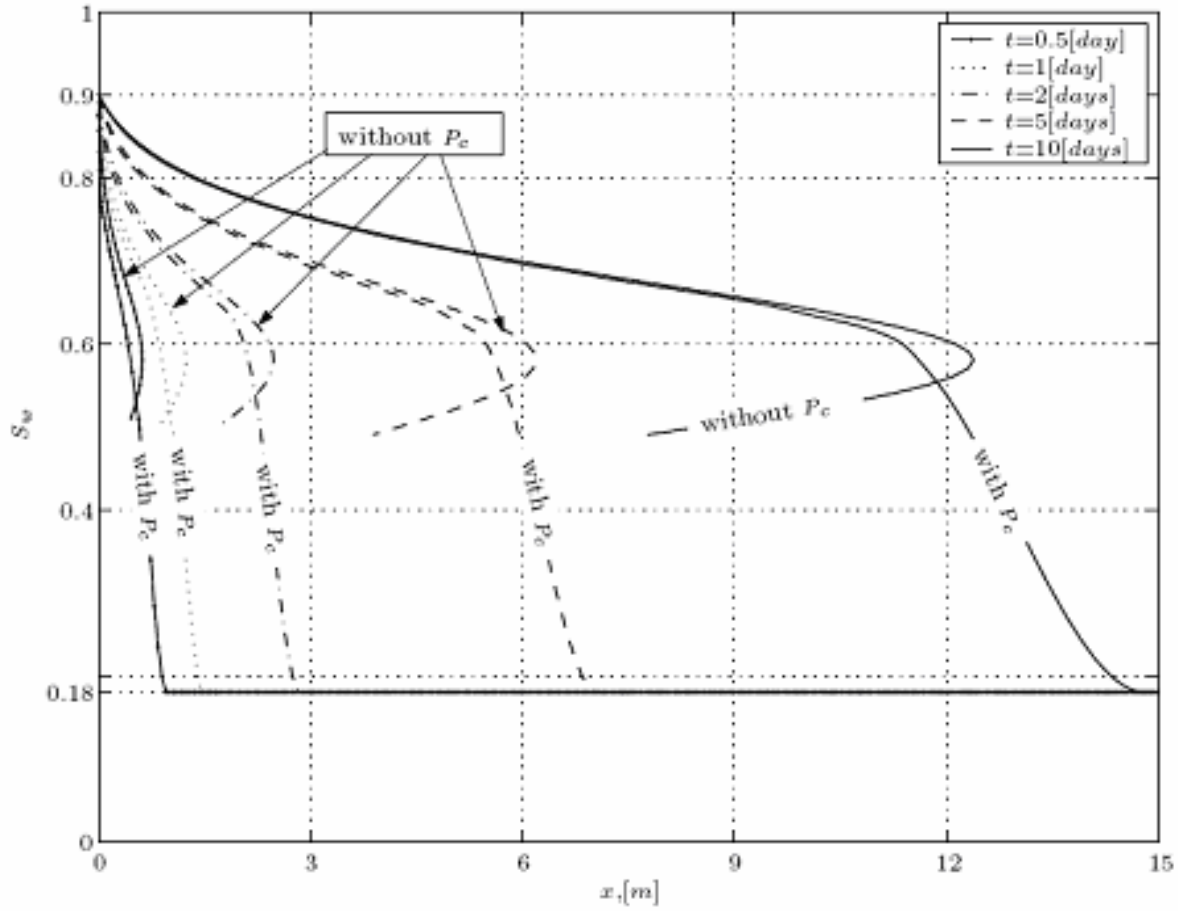

FIGURE 9: 1D multiphase problem solved without linearisation (classical Buckley Leverett equation)

The flow depends on two types of parameters. The first types are those that is changed with the variation of pressure, such as the fluid formation volume factor, the viscosity of the oil and the porosity of the formation. The second type depends on the variation of water saturation. These are the relative permeability of oil and water and the capillary pressure. The parameters are categorised based on their dependency on the pressure or water saturation and the effect of each group are studied separately. A complete description of these runs is available elsewhere [29]. In the first series of runs, the value of the fluid formation volume factor in the process of oil production was varied between 1.2063 to 1.22 from the reservoir pressure to the bubble point pressure. We neglect the compressibility of the fluid and take that B_o = 1.22 during the production process. The pressure and water saturation distribution are computed for a year with Δt = 1(day) and n = 256. The result for t = 3, 6, 9 and 12 (months) are given in Figure 10. The obtained results are then compared with the solutions when the fluid formation volume factor is changed with change in pressure. There are no significant differences at early months of production. But, the differences are increased with time and with the increase in production time. However, it shows that the variation of B_o has a minor effect on the distribution of p_o and S_w.

The variation of the viscosity with the pressure is neglected and it is assumed that μ_o = 1.1340 cp during the production process. This corresponds to the viscosity at the initial reservoir pressure, P_R = 4000 psia. The computations are carried out for a year with Δt = 1(day) and m = 256. The pressure and water saturation distributions are shown in Figure 11 for t = 3, 6, 9 and 12 (months). The results are compared with the the case when $\mu_o = f(p_o)$ as given in (4). There are not significant differences between the results when μ_o = Const. and $\mu_o = f(p_o)$ for various depicted times. It indicates that the variation of viscosity has not a major effect on the pressure and water saturation distributions.

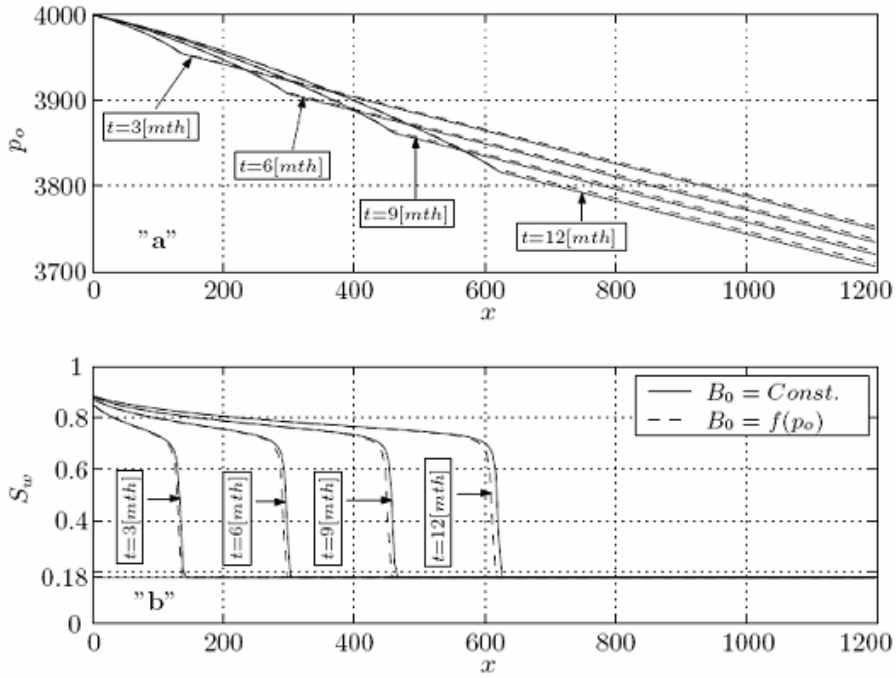

FIGURE 10: Distribution of oil phase pressure and water saturation for constant and variable fluid formation volume factors

The porosity variation due to pressure change is neglected in this part. It is assumed that $\varphi = \varphi_0 = 0.27$ during the production process. The computations are carried out for a year with $\Delta t = 1$(day) and $m = 256$. The pressure and water saturation distributions do not demonstrate any difference between two cases of φ = Const. and $\varphi = f(p_o)$. The pressure and water distributions are shown in Figure 12. There is not any difference between the graphs at a certain time with constant and variable φ, respectively, and the diagrams coincide completely.

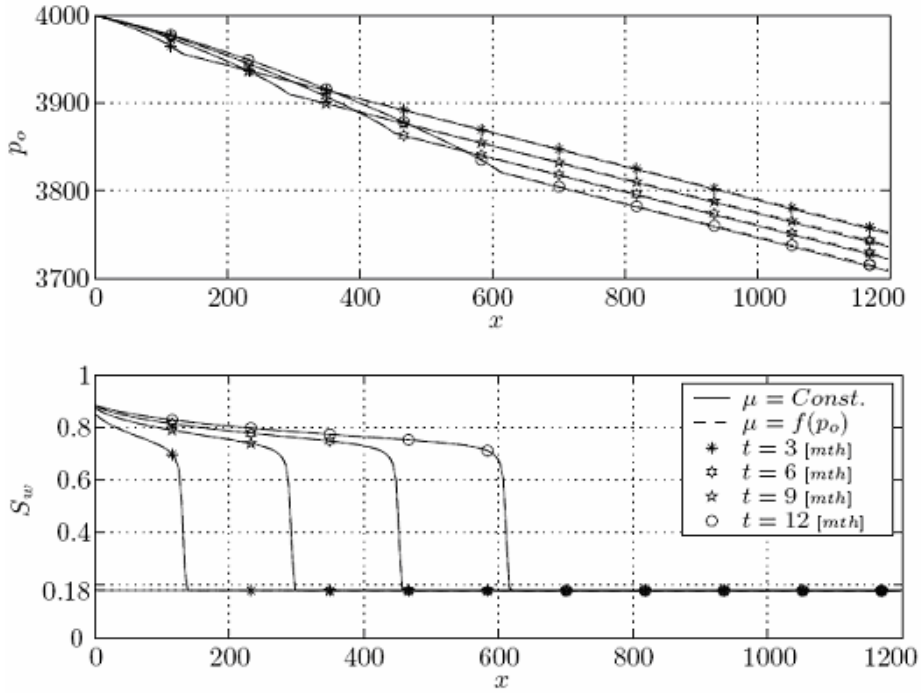

FIGURE 11: The distribution of oil phase pressure and water saturation for constant and variable oil viscosity

In order to study the combined effects, a series of runs was conducted. It was assumed that Bo = 1.22, μ_o = 1.1340 cp and $\varphi = \varphi_o = 0.27$ during the production process. The computations are carried out for a year with Δt = 1(day) and n = 256. The pressure and water saturation distributions are given in Figure 12 for t = 1(year). The results are compared for various cases. Note that, all the results were obtained without linearization at any stage. From these results, it appears that the oil formation volume factor, Bo has major effects while the porosity variation has the minor effect on the oil pressure and water saturation distributions. The water permeability of water and oil and the capillary pressure are dependent on the variation of water saturation. The pressure distribution of the single and double phase flows are given for t = 1(year) in Figure 13. The pressure distribution with neglecting the variation of the pressure dependent parameters is also depicted to provide a comparison and to find out the effect of different parameters on the final results. The effect of the pressure dependent parameters is very small compared with the influence of the water saturation variation.

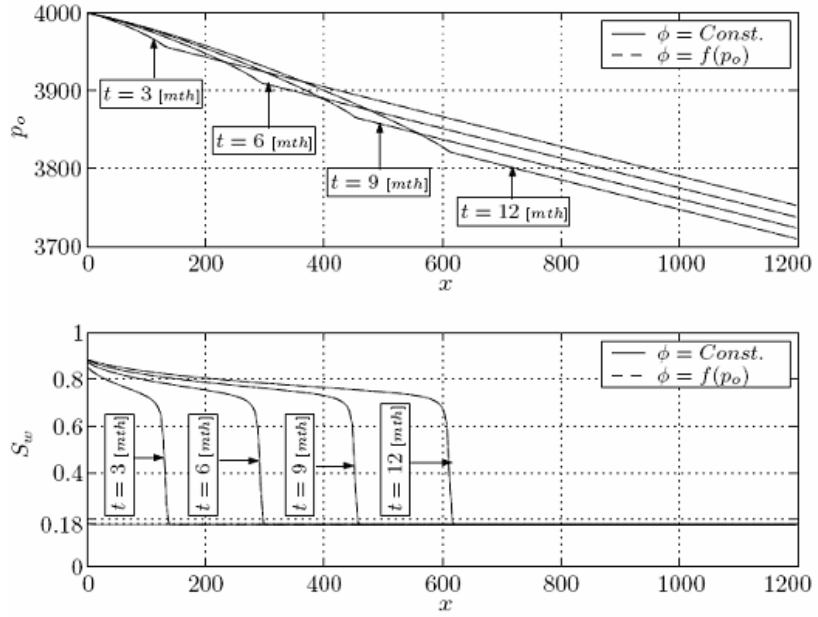

FIGURE 12: Distribution of oil phase pressure and water saturation for constant and variable porosity

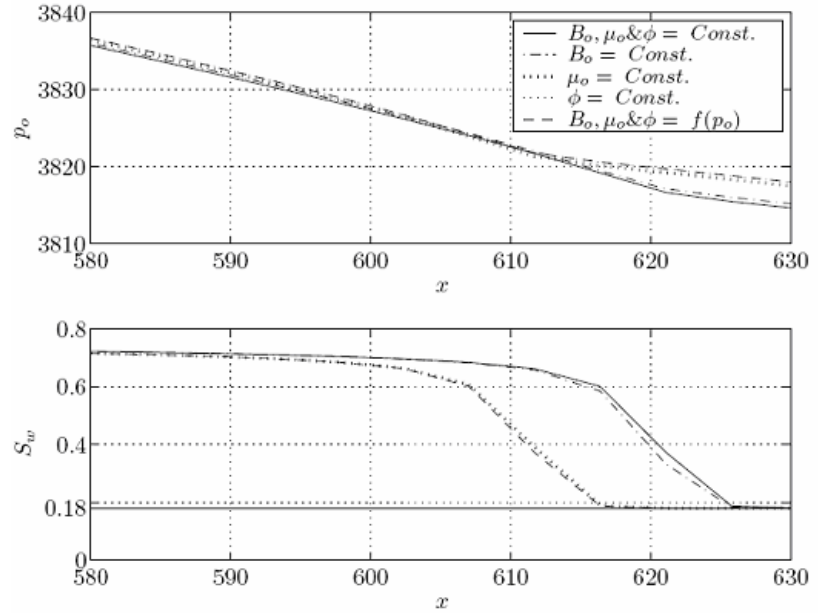

FIGURE 13: Distribution of oil phase pressure and water saturation for constant and variable pressure dependent parameters

The effective permeabilities to water and oil and the capillary pressure are dependent on the variation of water saturation. The pressure distribution of the single and double phase flows are given for t = 1(year) in Figure 14. The pressure distribution with neglecting the variation of the pressure dependent parameters is also depicted to provide a comparison and to find out the effect of different parameters on the final results. The effect of the pressure dependent parameters is very small compared with the influence of the water saturation variation.

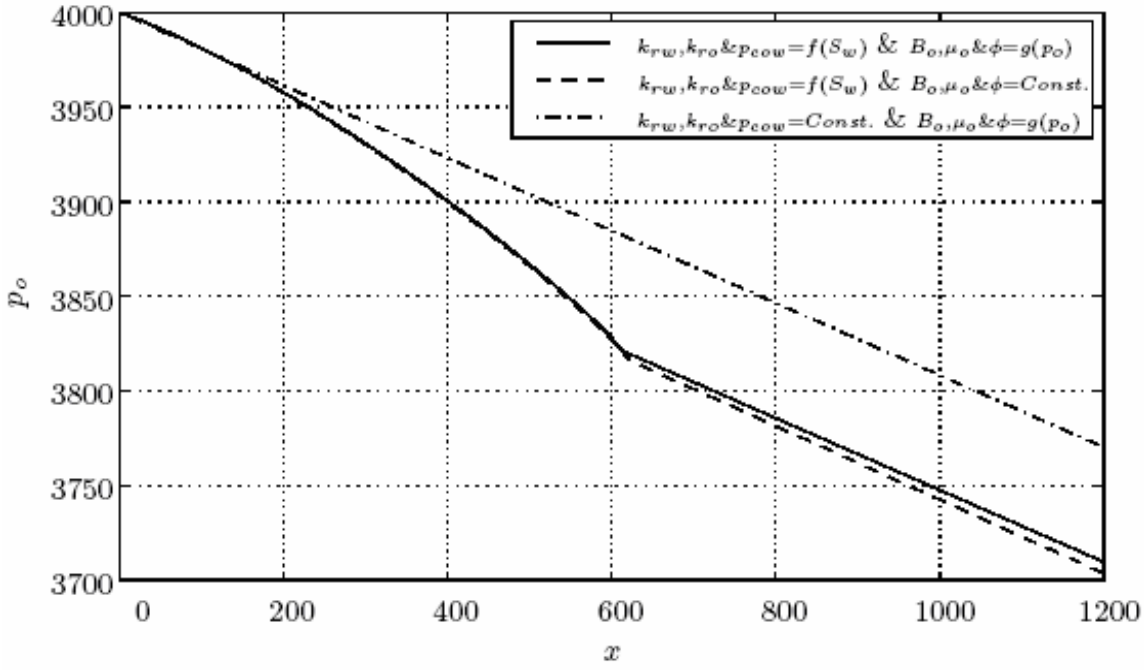

FIGURE 14: Distribution of pressure and water saturation for constant and variable cases

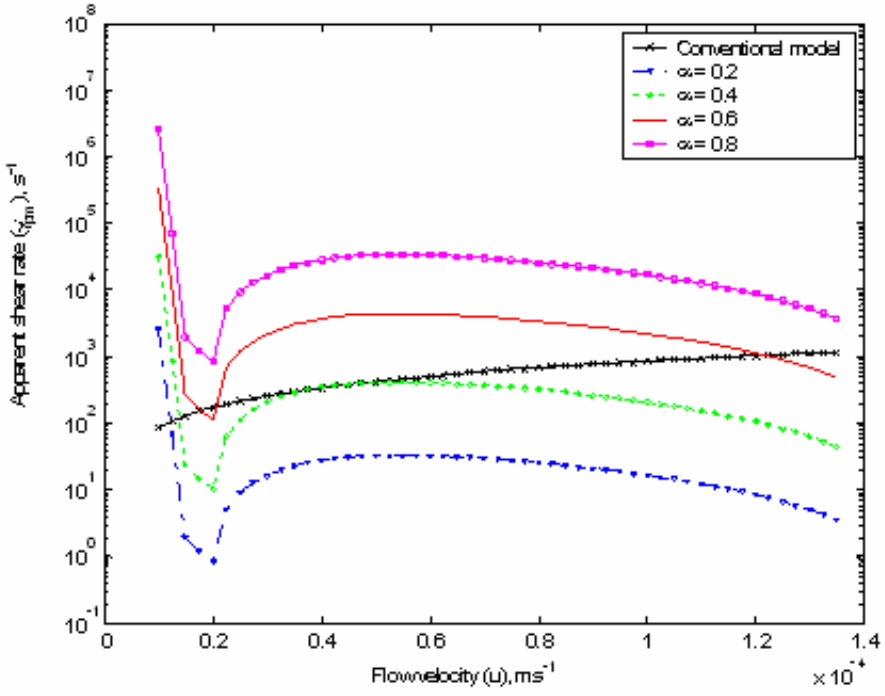

FIGURE 15: The role of memory function in determining apparent viscosity

Finally, results using a recently developed fluid rheology model that includes fluid memory are presented in Figure 15. Once again, fluid memory is considered to be the continuous time function. With the inclusion of the memory, results deviate significantly from the conventional approaches. When, this rheology is coupled with the momentum balance equation, classical cases of multiple solutions arise. Because the exact form of the memory is never known, this depiction would give one an opportunity to refine the prediction envelop, rather than putting too much emphasis on a single solution. Further details of this technique are available in recent work of Hossain and Islam [30].

6. FUTURE RESEACH

Recent research has shown, the source of this uncertainty is the linearization of all governing equations – a standard practice in reservoir simulation. If this linearization is eliminated, the accuracy of the results can improve as much as 30%. A more accurate scenario of the reservoir would add science to the risk analysis, which is often left to arbitrary assignment of the risk factor. A more accurate range of predicted values will reduce the uncertainty to a great extent. The most important aspect of the knowledge-based approach is that it leaves the open the option of multiple solutions, generating a set of cloud points rather than single point solution. The same model is applicable to other fields of engineering, including aviation engineering and biomedical engineering.

Concrete justifications on their results in order to prove that with their knowledge-based approach, results are significantly different for most of the solution regime.

The results and successes reported by recent works of Mousavizadegan et al. (2007), Mustafiz et al. (2008a, 2008b), and Mousavizadegan et al. (2008) in solving equations without linearization promise the success of the knowledge-based approach The benefits of the knowledge-based approach are two-fold. For a specific study, if the results show significant differences between the solutions of the linearized and non-linearized models, the stage will be set to seriously consider the new approach in reservoir simulation. If however the results show insignificant differences for a given range of parametric values, then the proposed research reaffirms that current method of linearization of model equations is appropriate for the given range and, therefore, delineates the range for which fine tuning of the current techniques is necessary.

7. CONCLUSION

In the paper, the concept of knowledge-based modelling is presented. Proposals are made to overcome a number of challenges encountered during modelling of petroleum reservoirs. It is shown that with the knowledge-based approach, results are significantly different for most of the solution regime. This finding would help determine more accurate range of risk factors in petroleum reservoir management. With the proposed technique, sustainable petroleum operations can be modelled to yield different results from unsustainable practices. This also allows one to distinguish between materials that cause global warming and the ones that don't. Such distinction was not possible with conventional modelling techniques.

8. ACKNOWLEDGMENTS

This paper summarizes recent work of a number of current and former PhD students, such as, Dr Shabbir Mustafiz, Dr Enamul Hossain, Dr Hadi Belhaj, and Mr M. Moniruzzaman Khan. They were funded by various funding agencies and industries. That funding is gratefully acknowledged. The first author gratefully acknowledges the support of King Fahd University of Petroleum & Minerals during the preparation of the manuscript.

9. NOMENCLATURE

All symbols and notations are explained in the text.

10. REFERENCES

1. Rose W. Myths about later-day extensions of Darcy's law. J. Pet. Sci. Eng. 2000: 26(1-4), May; 187-198.
2. Abou-Kassem JH, Farouq Ali, SM. and Islam, MR. A Basic Approach to Reservoir Simulation. Gulf Publishing Co., Houston, Texas, 2006; 455.
3. Zatzman GM and Islam MR. Truth, consequences and intentions: The study of natural and anti-natural starting points and their implications. J. Nature Science and Sustainable Technology 2007; 1(3): 169-174.
4. Mustafiz S. Mousavizadegan H. and Islam, MR. The effects of linearization on solutions of reservoir engineering problems. Pet. Sci. Tech. 2008: 26(11-12): 1224-1246.
5. Eisenack K. Matthias KB. Lüdeke MKB. Petschel-Heldl G. Scheffran J. and Kropp JP. Qualitative modelling techniques to assess patterns of global change, in advanced methods for decision making and risk management in sustainability science, Kropp, J. and Scheffran, J. (eds.), Nova Science Publishers 2007; 83-127.
6. Zatzman GM. and Islam MR. Truth, consequences and intentions: The study of natural and anti-natural starting points and their implications. J. Nature Science and Sustainable Technology 2007a; 1(2): 169-174.
7. Shapiro R. Zatzman GM. and Mohiuddin Y. Towards understanding disinformation. J. Nature Science and Sustainable Technology 2007; 1(3): 471-504.
8. Mustafiz S. and Islam MR. State of the art of reservoir simulation. Pet. Sci. Tech. 2008; 26(11-12): 1303-1329.
9. Zatzman, GM. and Islam MR. Economics of intangibles. Nova Science Publishers: 431; 2007b.
10. Kline M. Mathematical thought from ancient to modern times. Oxford University Press, New York, USA, 1238: 1972.
11. Bear J. Dynamics of fluids in porous media. American Elsevier Publishing Co., New York, 761; 1972.
12. Abou-Kassem JH. Engineering approach vs the mathematical approach in developing reservoir simulators, J. Nature Science and Sustainable Technology. 2007; 1(1): 35-68.
13. Zatzman GM. Khan MM. and Islam MR. The use of newly formulated comprehensive mass and energy balance equation to develop an atmospheric model. paper ID: 588-301, WSEAS Transaction; 2008.
14. Gleick J. Chaos – making a new science. Penguin Books, NY; 352; 1987.
15. Wilkinson DS. Maire E. and Embury JD. The role of heterogeneity on the flow and fracture of two-phase materials. Materials Science and Engineering. A. Structural 997; 233: 145-154.
16. Naami AM. Catania P. and Islam MR. Numerical and experimental modelling of viscous fingering in two-dimensional consolidated porous medium. CIM paper no. 118, CIM conference, Regina, Oct. 1999.
17. Aboudheir A. Kocabas I. and Islam MR. Improvement of numerical methods in petroleum engineering problems. Proceedings IASTED International Conference, Applied Modelling and Simulation, Cairns, Australia, Sept. 1-3. 1999.
18. Bokhari K. and Islam MR. Improvement in the time accuracy of numerical methods in petroleum engineering problems – A new combination. Energy Sources 2005; 27(1-2): 45-60.
19. Bokhari K. Mustafiz S. and Islam MR. Numerical modelling of viscous fingering under combined effects of thermal, solutal and mixed convection in liquid-liquid miscible displacements. Journal of Petroleum Science and Technology. accepted for publication, May, 2006.
20. Saghir, Z., Chaalal, O. and Islam, M.R., 2000, "Experimental and Numerical Modeling of Viscous Fingering", *J. Pet. Sci. Eng.*, vol. 26(1-4), 253-262.
21. Khan MI. and Islam MR. The petroleum engineering handbook: sustainable operations. Gulf Publishing Co., Houston, USA, 461: 2007.
22. Khan MI. and Islam MR. True Sustainability in technological development and natural resources management. Nova Science Publishers, New York, USA, 381: 2007b.
23. Khan MM. Zatzman GM. and Islam MR. The formulation of a comprehensive mass and energy balance equation, ASME International Mechanical Engineering Congress and Exposition, Nov. 2-6, Boston, MA.: 2008.
24. Chhetri AB. and Islam MR. Inherently sustainable technology developments, Nova Science Publishers, New York, 452; 2008.
25. Lim, M.L., Land, M.F., 2007, "Sex-specific UV and Fluorescence Signals in Jumping Spiders", Jan. 26:315 (5811), pp. 481.
26. Sorokhtin OG. Chilingar GV. and Khilyuk LF. Global warming and cooling. Elsevier, 313; 2007.

27. Mousavizadegan SH. Mustafiz S. and Rahman M. The adomian decomposition method on solution of non-linear partial differential equations, J. Nature Science and Sustainable Technology 2007; 1(1): 115-131.
28. Mustafiz S. Mousavizadegan H. and Islam MR. Adomian decomposition of Buckley Leverett equation with capillary terms, Pet. Sci. Tech.: in press.
29. Islam MR. Mousavizadeghan and Mustafiz S. Handbook of knowledge-based reservoir simulation. Gulf Publishing Company, Houston, TX, to be published in March 2009.
30. Hossain, ME and Islam, MR. An Advanced Analysis Technique for Sustainable Petroleum Operations. VDM Verlag Dr. Muller Aktiengesellschaft & Co. KG, Germany, 2009.
31. Hossain, M.E., Mousavizadegan, S.H. and Islam, M.R. (2009). The Mystery and Uncertainty Cloud during Reservoir Simulation in Petroleum Industry. *Advances in Sustainable Petroleum Engineering Science*, in press.

TGA Analysis of Rubber Seed Kernel

Noorfidza Yub Harun Noorfidza.Yub_Harun@unb.ca
Graduate Student
Faculty of Forestry and Environmental Management
University of New Brunswick
Fredericton, E3B 5A3, Canada

M.T. Afzal mafzal@unb.ca
Associate Professor
Faculty of Forestry and Environmental Management
University of New Brunswick
Fredericton, E3B 5A3, Canada

Mohd Tazli Azizan tazliazizan@petronas.com.my
Graduate Student
Chemical Engineering Department
University College of London
Gower Street,
London, WC1E 6BT,
United Kingdom

Abstract

This project investigated the possibility of converting biomass wastes into solid fuels by undergoing torrefaction process. Rubber seed kernel was used to produce torrefied material and the factors affecting torrefaction were investigated. Samples of rubber seed kernel were dried, ground, sieved, heated and cooled to obtain the torrefied material. It was found that minimum 30% of the moisture content was removed from its original value during torrefaction process. Almost 100% of the calorific value in all the samples can be retained or increased by up to 10% from the original waste calorific value. The proximate analysis was carried out using Thermo Gravimetric Analyzer (TGA) where rubber seed kernels exhibited high fixed carbon region at the respective temperature. At the optimum condition of temperature 280℃ and particle size of 0.025 mm, the torrefied material produced is viable to be promoted at a larger scale.

Keywords: Torrefaction, Biomass, Temperature, Particle Size.

1. INTRODUCTION

Nowadays, the increasing demands on fossil fuel have awakened the oil and gas industry due to the limiting resources of its reserved. Apart from that, concerning the environmental effect, continuous and increasing use of petroleum will intensify local air pollution and magnify the global warming problems caused by CO_2. In order to meet rapidly increasing energy demand as well as to conserve the world, alternative energy sources should be utilized effectively.

Of all alternative energy resources, biomass has a great potential today and in the future, since it is renewable, in contrast to the nature of the fossil fuels [3]. Biomass is seen as one of the best options that can provide a renewable fuel which can be utilized in a range of energy conversion technologies and also has the added advantage of being CO_2 neutral [7]. It is biodegradable and non-toxic. It has low emission profiles and thus is environmentally beneficial. There are many biomass resources available in the world and one of those is rubber seed kernel which is not edible. Rubber seed kernel can be converted into source of energy via biomass processes which are torrefaction and fast pyrolysis.

Peninsular Malaysia, comprising 12 of the 14 states in the Malaysian federation is among the world's most important rubber growing area. Rubber is also grown in Sabah (formerly North Borneo) and Sarawak, which, known together as East Malaysia. Altogether Malaysia produces almost 20% of the world's natural rubber. More than half Malaysia's rubber comes from thousands of privately owned small landholdings, which are usually about 2 hectares. The rest is grown on big estates owned by various companies; each can cover over a thousand hectares. Altogether, Malaysia has 1.7 million hectares of rubber plantation [19]

Torrefaction produces solid product of carbon sources material like biomass, retaining approximately 70% of the initial weight and 80%-90% of the original energy content [4]. As the temperature increases, biomass begins to be brown and gives off moisture, carbon dioxide, and large amount of acetic acid with some phenols [5].

This project studies the possibility of using rubber seed kernel to produce biofuel via torrefaction. As the annual rubber seed production in Malaysia is high, this makes the source unlimited and renewable throughout the years.

2. METHODOLOGY

The biomass waste of rubber seed kernel was obtained from a local supplier. It was dried at 110 ℃ for 2 hours, then grinded into smaller particles and finally sieved into two mesh sizes i.e. 250 and 500 µm, respectively. Each sample weighing 10 grams underwent torrefaction process where it was heated for 1.5 and 3 hours respectively in a special furnace called Fixed Bed Activation Unit at two different temperatures i.e. 240 ℃ and 280 ℃, in the presence of inert nitrogen. The torrefied material was then cooled to room temperature and reweighed to determine the weight loss from the material due to the torrefaction process.

2.1 Sample Analysis

2.1(a) Moisture Content Analysis

The moisture content of material was analyzed by using Halogen Moisture Analyzer (HMA). It is an important indication and method to determine the moisture content loss of the biomass sample after undergoing torrefaction or pyrolysis process. The measurement was conducted two times, which are before and after the torrefaction or pyrolysis process.

2.1(b) Ultimate Analysis

The ultimate analysis was conducted by using Carbon Hydrogen Nitrogen Sulphur (CHNS) Analyzer. The samples were weighed around 1.5 milligrams to 2.0 milligrams in aluminium container prior entering the analyzer. The analyzer will then display the composition of that carbon, hydrogen, nitrogen, and sulphur contained within the material in percentage value. The oxygen composition is calculated by difference method.

2.1(c) Calorific Value Analyses

The calorific value of biomass sample before and after undergoing torrefaction or pyrolysis was determined using Bomb Calorimeter by IKA which technology approved by DIN 51900, ASTM 240D, ISO 1928 and BSI.

2.1(d) Weight Loss Analyses

The weight loss of the heated material is determined by weighing the initial and final mass of the sample before and after heating.

$$\text{Percentage of weight loss} = \frac{A - B}{A} \times 100$$

Where;
A: weight of the sample before heating, g
B: weight of the sample after heating, g

The moisture content is determined by establishing the loss in the weight of the sample when heated under rigidly controlled conditions of temperature, time and atmosphere, sample weight, and equipment specification. The percentage of moisture in the analysis sample is calculated as follows:

$$\text{Percentage of moisture} = \frac{A - B}{B - C} \times 100$$

Where;
A: mass of container and wet sample, g
B: mass of container and dry sample, g
C: mass of container, g

2.1(e) TGA Analyses

The proximate analysis conducted by using Thermal Gravitational Analyzer (TGA). The samples are weighed approximately 5mg to 10mg to fit the small pan of TGA. A set methodology was programmed to the TGA controller to ensure the result obtained aligned with the objectives. The method was set as followed:

i. Hold for 1 minute at 50℃
ii. Heat from 50℃ to 800℃ at 40.00℃/min with nitrogen flow rate of 20ml/min

Next, the TGA procedure was followed to complete the analysis. The outcome of the analysis will be displayed in term of decomposition regime graph, and then further analysis will be carried on. TGA is used to determine elements of:

i. Moisture content
ii. Volatile matter
iii. Fixed carbon
iv. Ash

3. RESULT AND DISCUSSION

3.1 Sample Pretreatment

The drying process took place in an oven having muffle temperature of 110℃ for more than two hours. The weight of the biomass sample is taken periodically every 15 minutes until the weight is constant. Figure 1 shows a gradual decrease in the weight of the sample is observed for the first two hours. After two hours, the rate of weight loss is lower and remains constant until 24 hours.

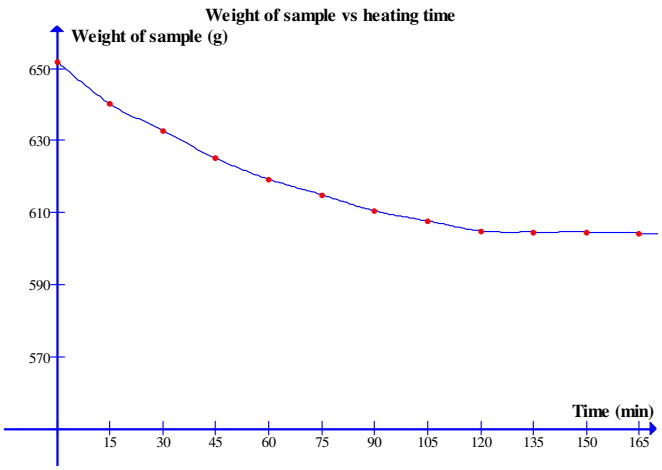

Figure 1: Weight of rubber seed kernel versus heating time

Referring to Alves and Figueiredo [19], when heat is applied into wood particles, it will begin to dry more intensely at the outer boundary with the increasing temperature. The bound and free water tend to move outwards by convection and diffusion, while some may migrate towards the inner, which is the colder part of the solid where condensation occurs. However, as the drying process proceeds, the penetration of heat into the deeper part of the wood particle and moisture movement to the surface becomes harder due to material resistance. This results in the rate decrease of drying.

This concept can also be applied to the pre-treatment process of rubber seed kernel via drying in the oven. This is because, the concept applied is similar in both cases where heat is applied to the wet raw material in order to remove the bound and free water; in this case; rubber seed kernel. The drying is considered finished when the weight of sample remains constant. During this time, it is assumed that all bound and free water have been released. The rate of weight loss gradually decreases because as time goes by, the moisture content in the raw material becomes lower and lower. Therefore, less water is removed from the sample from time to time throughout the drying period until the weight remains constant.

3.2 Sample Analysis

Sample analysis before heating is carried out using CHNS Analyzer. The equipment only evaluates the carbon, hydrogen, nitrogen, and sulphur composition of the material. The remaining composition of the material is oxygen which is determined by difference method. In this case, oxygen value is 50.25%. This is done to compare the composition of the sample before and after heating. From this analysis, the major components of rubber seed kernel initially are carbon and oxygen. This result will be compared with the composition obtained from the samples undergoing the heating process.

From CHNS analysis also, it is found out that hydrogen, nitrogen, and sulphur are minor components of rubber seed kernel. The percentages of those components are acceptable after comparison made with other torrefied biomass wastes used as solid biofuel production such as beech, willow, larch, and straw [9] as shown in the Table 1.

Apart from the CHNS analysis, the initial calorific value of the raw sample is also determined using bomb calorimeter before the heating process takes place which is 17218 J/g. From the first look also, rubber seed kernel is seen as a good viable source of alternative solid fuel as by nature.

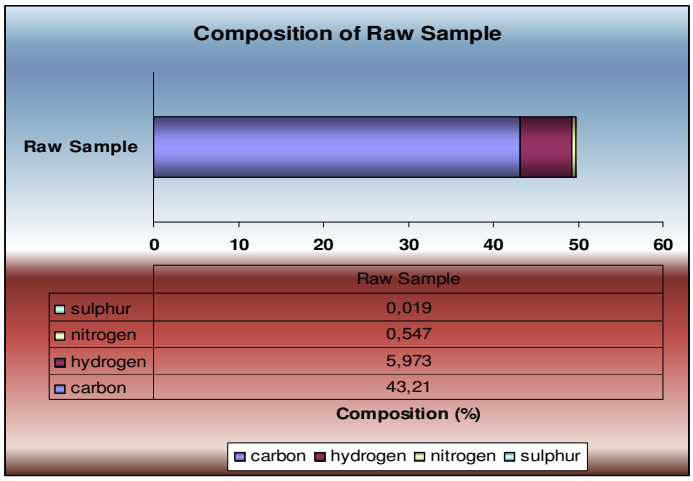

Figure 2: Composition of fresh rubber seed kernel

Biomass Type	% Carbon	% Hydrogen	% Nitrogen
Beech	47.2	6.0	0.40
Willow	47.2	6.1	0.34
Larch	48.8	6.1	0.10
Straw	44.3	5.8	0.40
Rubber Seed Kernel	**43.2**	**6.0**	**0.55**

Table 1: Compositions of hydrogen and nitrogen of torrefied biomass wastes

3.3 Experimental Results

3.3(a) Color Changes

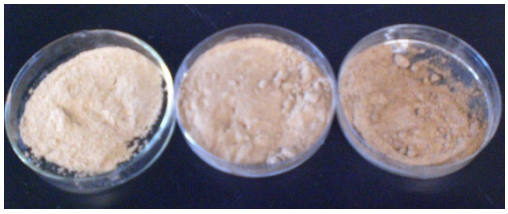

A **B** **C**

Figure 3: Colour change of samples

A is the sample taken before heating process takes place. B and C are samples observed when heated in the fix bed activation unit at temperature 240℃ and 280℃ respectively. From Figure 3, the colour of samples becomes darker as the temperature of heating increases. According to J. Bourgeois [5], he has proven from his research that as temperature increases, biomass begins to be browned off and gives off moisture, carbon dioxide and large amounts of acetic acid with some phenols. The colour turns into darker due to the increasing carbon content of the heating sample.

3.3(b) Effect of Duration, Temperature and Particle Size to Weight Loss

During torrefaction process where sample is heated at temperature range between 225℃ to 300℃, two main reactions occur which are dehydration and carbonization. In general, higher process temperature and longer time period result in lower production of solid product as more biomass is converted to gas and liquid. This is proven by research done by Farah Dila [7] where longer reaction time from 1.5 hours to 4 hours produce higher liquid yield for pyrolysis process and lower product yield. This can also be applied to torrefaction. However, the portion of liquid

and gas produced during torrefaction is lower compared to pyrolysis due to the difference in temperature ranges.

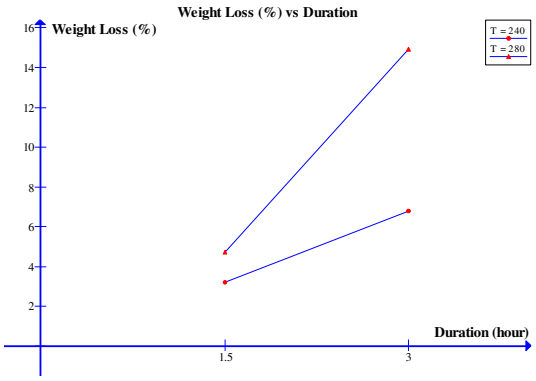

Figure 4: Effect of duration

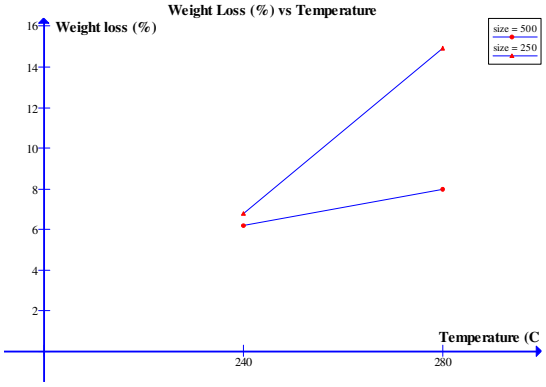

Figure 5: Effect of Temperature

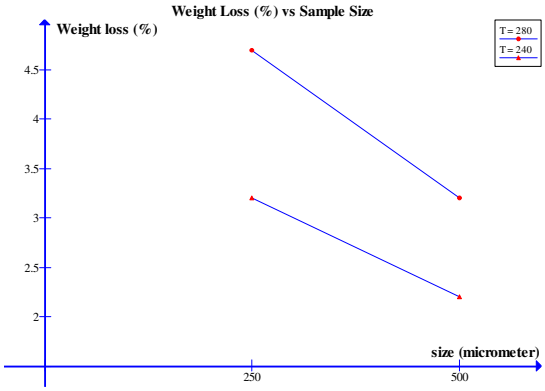

Figure 6: Effect of Size

By referring to Figure 4, heating time gives a massive impact to the weight loss. As the reaction time is increased, more weight loss is observed. This is expected because, as time goes by, more water in the sample, which constitutes as the major contribution to the mass, is evaporated leaving behind the solid. This is true since the greater the size is, the longer time is needed to convert to the torrefied material.

From Figure 5, it is observed that, as the heating temperature is increased, the weight loss is also increased. When the biomass is heated, drying process takes place first. Further heating removes new amount of water from chemical reactions through thermo-condensation process, which occurs at temperature above 160℃, as well as the formation of carbon dioxide gas begins. This results to the weight loss of the sample as the heating process takes place. As the heating temperature is increased, the rate of evaporation of water in the material becomes higher, thus the weight loss increases. That is why it is observed that, at temperature 240℃ the weight loss is 8.0% while at temperature 280℃, 14.9% weight loss is exhibited which is nearly two times of the previous value.

Referring to Herlina [6] and Farah Dila [7], both concluded that higher temperature promotes higher evaporation and changes the solid to gaseous form. This is because, more cracking occurs at higher temperature resulting in higher gas yield and lower solid yield. From this study, the highest weight loss occured at temperature 280℃ and reaction time of 3 hours with the smaller particle size of rubber seed kernel.

As the size increases, weight loss is decreased. This is because, as the size of particles increase, the surface area exposed to the heating process decreases. Therefore, less water can be

evaporated as the process takes place. This is within expectation because as time goes by within 1.5 hours, there are still more water evaporated, leaving behind the solid. The greater the size is, the longer time is needed to convert to torrefied material. This is also proven by the moisture loss analysis which exhibits higher value in smaller sample size compared to the bigger one which will be discussed further in the next part.

Apart from that, with less surface area exposed, less contact area is established for the reaction to take place, either for dehydration or degradation of biomass sample. As a result, less degradation of solid to convert to gas exhibits lesser weight loss for bigger sample size and vice versa.

3.3 (c) Effect of Duration, Temperature and Particle Size Composition

Figure 7 shows the comparison of the rubber seed kernel composition before and after heating at different duration of time. The torrefied materials still exhibit carbon and oxygen content as the major composition while others remain as minor ones. However, as the raw material undergoes heating process and the heating duration increases, the carbon content also increases. Thus, the torrefied material contains higher percentage of carbon compared to the raw material. In addition, the increase is more significant at longer time period and higher temperature. In contrast, the oxygen content become lesser as the duration is longer and carbon content is higher.

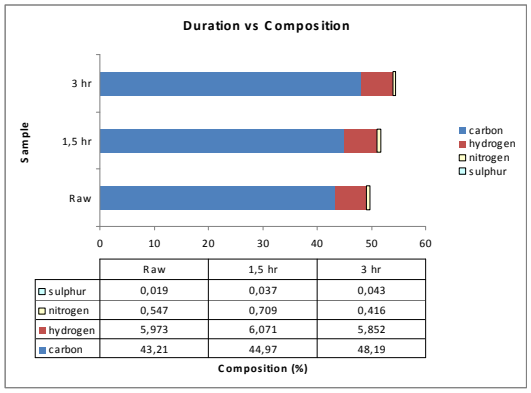

Figure 7: Effect of Duration

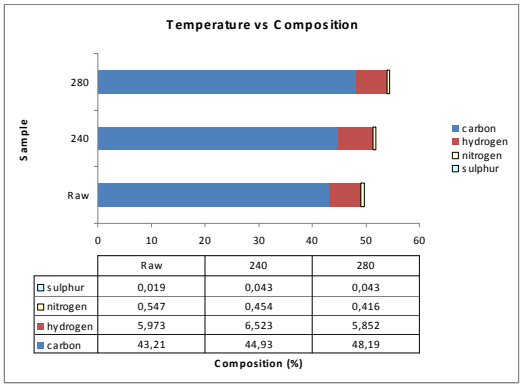

Figure 8: Effect of Temperature

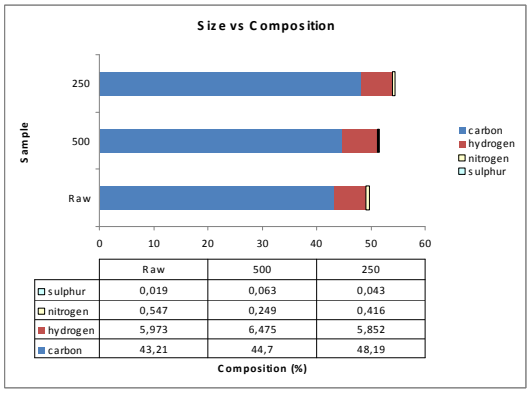

Figure 9: Effect of Size

According to Patrick *et. al* [20], in torrefaction process biomass loses relatively more oxygen and hydrogen compared to carbon. Water from dehydration is the best example, but also all organic reaction products (acetic acid, furans, methanol) and gases (mostly CO_2 and CO) contain a considerable amount of oxygen. Therefore, torrefied material has higher carbon content and

lower oxygen content compared to the raw sample. Due to removal of water and CO_2, the composition of torrefied material has a lower Oxygen/Carbon and Hydrogen/Carbon ratio.

As longer duration takes place, more water and gases are removed from the biomass sample, therefore lower oxygen content exhibits lower Oxygen/Carbon ratio which is 0.9 and thus the torrefied product becomes a better biofuel. However, the common Oxygen/Carbon ratio according to Prins [8] is 0.69 to 0.72 which is quite low compared to the result obtained. It can be concluded that, the oxygen content in the torrefied product is still high to be accepted as a good biofuel.

Figure 8 shows nitrogen and hydrogen decrease while the carbon content exhibits higher composition at higher temperature. In conjunction with that, the oxygen content decreases as the temperature increases. In this study, the highest percentage of carbon content is at 280℃, which is the maximum temperature of the experiment.

Rapid breakdown of the biomass structure increases tremendously at higher temperature, leaving the decreased amount of torrefied product as discussed in the weight loss section previously. The reason is, at high temperature, the reaction achieves complete conversion to form more stable form of solid. Besides, at higher temperature, greater amount of raw material is oxidised with other component exist in it. With high burn-off rate, most of the original sample has undergone complete reaction with oxygen. Therefore, more water and gas are released from the biomass sample as the temperature increases. That is why hydrogen and nitrogen components decrease while the carbon content increases.

The decrease in Oxygen/Carbon ratio from 1.2 to 0.9 as the heating temperature increases exhibit better biofuel. However, as discussed earlier, the ratio does not meet the torrefied wood ratio which is from 0.69 to 0.72. In addition, the changes in composition is significant only at higher temperature and longer time period as the increase of carbon content is higher compared to at lower temperature and shorter time period.

Figure 9 shows the relationship between the particle size and composition of torrefied material. Theoretically, the lower the particle size, the higher the surface and contact area exposed to the heating process as well as the reaction to take place. High surface area can induce more evaporation of water and other volatile products such as CO and CO_2 to leave the sample quickly and thus, resulting in lower volatile matter in the product and higher fixed carbon content. The removal of those water and volatile matter reduces the hydrogen and nitrogen content as well as Oxygen/Carbon ratio which results to better biofuel product. Furthermore, the result is more significant at longer heating time as the change in composition is more compared to at shorter heating time.

From the analysis done to the torrefied products composition with the effect of reaction time, temperature, and sample size, the best biofuel product exhibited is at 280℃ for 3 hours reaction time of 250 µm sample which has 48.19% carbon with 0.9 Oxygen/Carbon ratios.

3.3 (d) Effect of Duration, Temperature and Particle Size to Moisture Loss

Basically, all the effects studied for moisture content loss are similar to weight loss behaviour. Figure 10 shows the effect of reaction time to the moisture loss of the torrefied material. It is observed that as the reaction time increases, the moisture loss also increases. This is because, as the heating process takes place, water is removed from the biomass sample. Thus, as more time left for the biomass to be heated, more and more water can be removed as time goes by.

Apart from that, the moisture content loss is also affected by temperature where the higher the temperature, the higher the moisture loss is. This is proven by Figure 11. Referring to Zanzi *et. al* [9], at temperatures between 180℃ and 270℃ an exothermically reaction takes place, as well as the degradation of hemicelluloses goes on. Biomass begins to be brown and gives off moisture, carbon dioxide and large amounts of acetic acid with some phenols. As the temperature

increases, more water can be removed from the biomass sample due to higher heating rate applied to the sample. Therefore, higher moisture content is lost at higher temperature. However, from the graphs, it is observed that time is not really significant as the changes in moisture loss at longer duration are very less compared to other parameters.

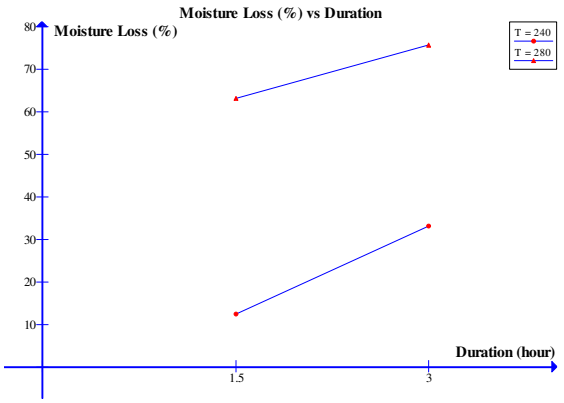

Figure 10: Effect of Duration

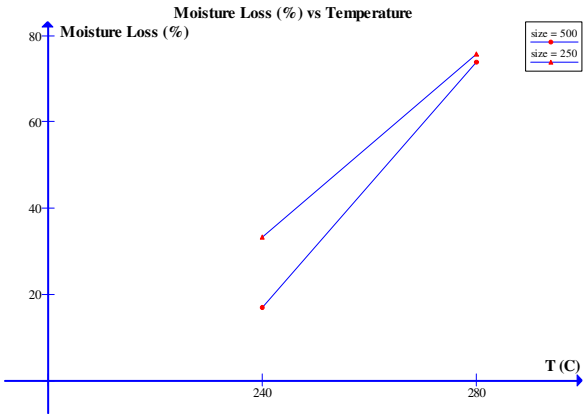

Figure 11: Effect of Temperature

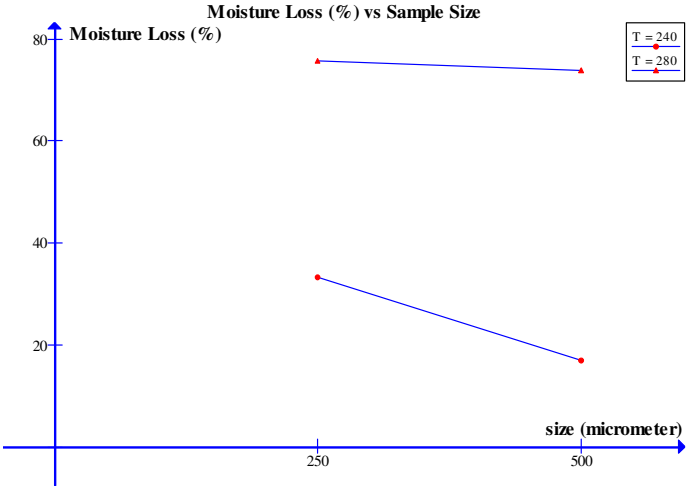

Figure 12: Effect of Particle Size

The third parameter studied is the effect of sample size to the moisture loss. The smaller sample size exhibits higher moisture content loss. This is due to higher surface area exposed to the hot environment during the heating process. Higher surface area removes more water from the sample thus induces higher moisture content loss.

From the analysis done on the moisture content, it is observed that, the moisture content loss increases with temperature and reaction time. However, for sample size, moisture content loss decreases with the increase of sample size. The maximum moisture content loss is at 280℃ for 3 hours long of 250µm sample size which is 75.62%. Thus, the properties of the product can behave like hydrophobic nature that has resistance to absorb water again.

3.3 (e) Effects of Duration, Temperature and Particle Size to Calorific Value

For calorific value analysis, the reading was taken by bomb calorimeter before and after torrefaction process. The raw sample calorific value before heating is 17218 J/g.

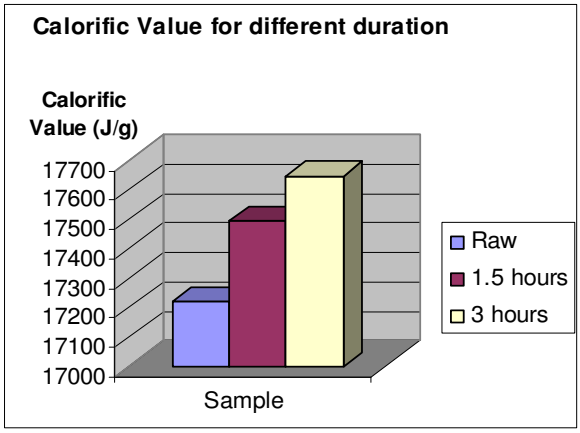

Figure 13: Effect of Duration

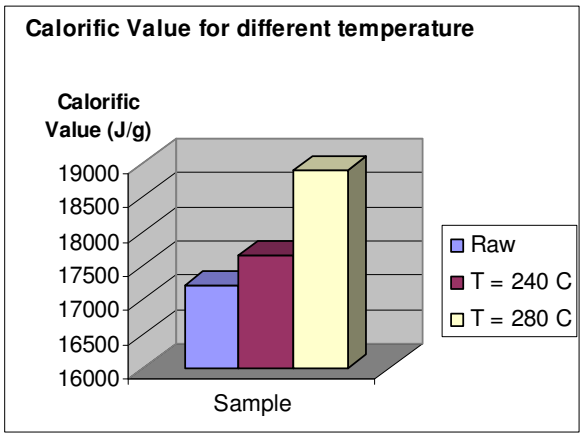

Figure 14: Effect of Temperature

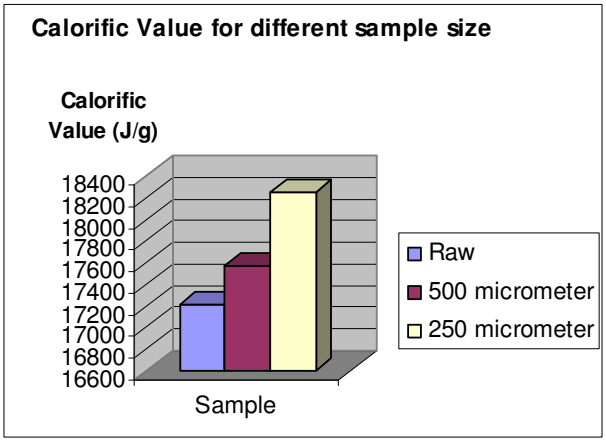

Figure 15: Effect of Particle Size

Referring to Figure 13, 14 and 15, it is clearly seen that, the torrefied materials can retain the calorific value almost 100% of the initial value. The research done by Itebe *et. al* [23] that torrefaction process can retain up to 90% of the original energy is proven. In fact, the values increase with the increasing heating temperature and reaction time. However, the calorific value decreases with the increasing sample size. The higher the calorific value, the better the torrefied material will be as it provides enough energy to be an alternative fossil fuel.

According to Patrick *et. al* [20], an increase of the calorific is the main result from the increasing carbon content and decreasing O/C ratio with the removal of water and gas during torrefaction. Depending on the torrefaction conditions, the low heating value dry of biomass, specifically wood can be increased from 17-19 MJ/kg to 19 to 23 MJ/kg. Also referring to R. Zanzi *et.* Al [9], at higher temperature, the carbon content in the product increases while the contents of H and O decrease. H/C and O/C atomic ratios decrease with the temperature. As a result, the calorific value (CV) of the solid product increases with the temperature and at longer residence time.

3.3(f) TGA Analysis

Based on the TGA graph obtained, there are three main regions which are the moisture content represented by the first slope, the volatile matter represented by the second slope, and the fixed carbon represented by the third slope.

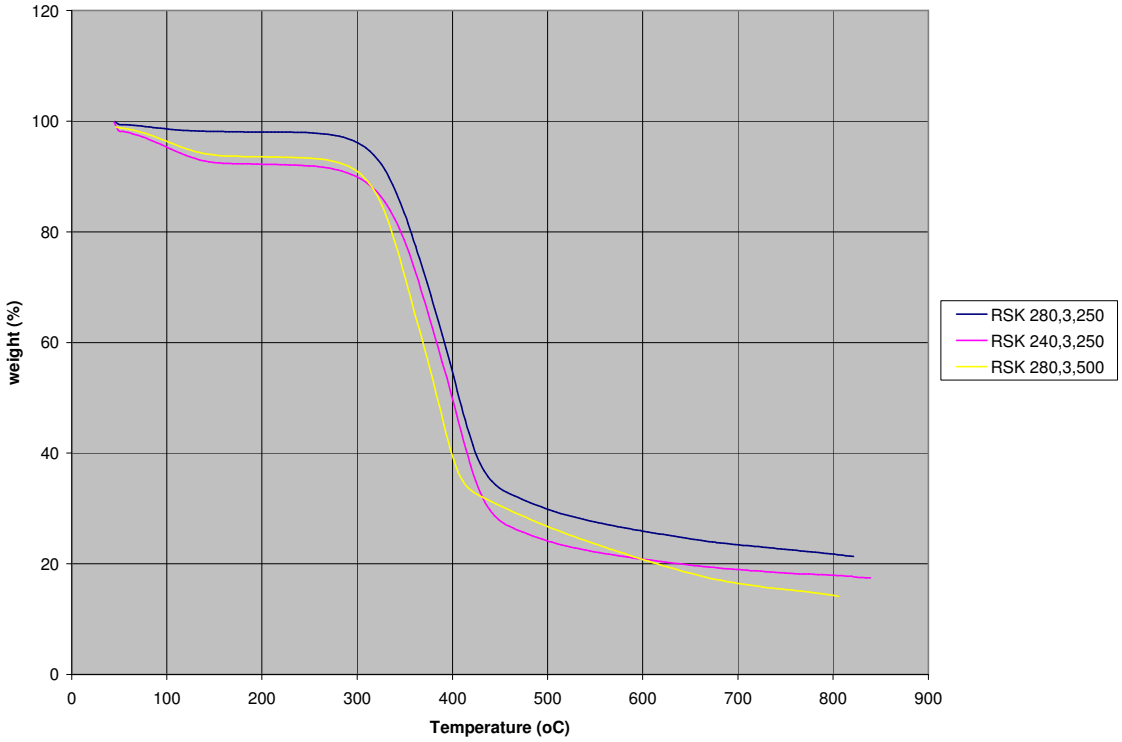

Figure 16: TGA graph of Rubber Seed Kernel for each torrefaction condition

From Figure 16, rubber seed kernel of 250 µm that torrefied at 280°C has shown lesser weight reduction than torrefied at 240°C in the first slope, which region referred as moisture content. Water content has been removed approximately 7% difference between the two conditions. However, for rubber seed kernel of 500 µm has shown to remove about 6% more than 250 µm sample condition. At same temperature condition bigger particle size gives off lower moisture content and lower burn off rate due to smaller surface area in contact to reaction.

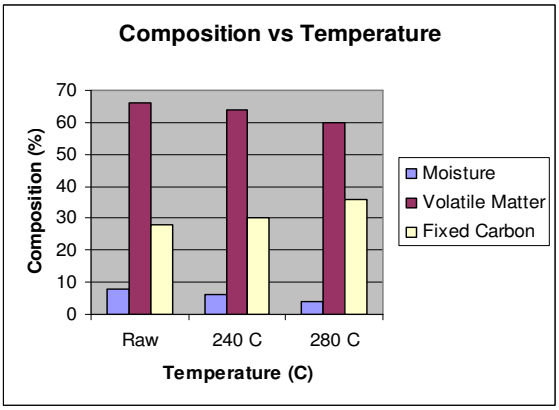

Figure 17: Effect of Temperature

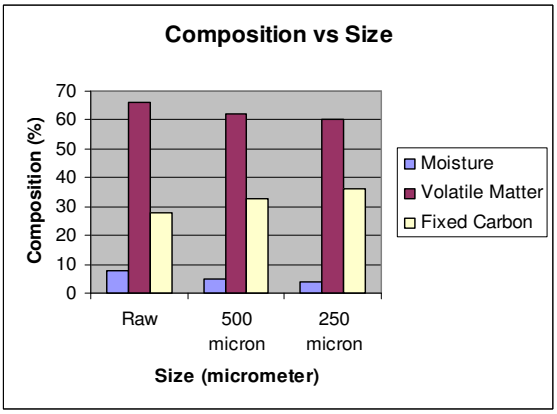

Figure 18: Effect of Size

From Figure 17, it is observed that, the moisture content and volatile matter compositions are reduced slightly as temperature increases. As discussed previously, the reduction is due to the increase in drying rate of the sample at higher temperature. Therefore, more water and volatile matter is removed at 280℃ compared to at 240℃. The moisture content is the first element which is decomposed normally at temperature 100 ℃ to 150 ℃ where at this temperature the recondensation and depolymerisation occur to remove the moisture. It is important to analyze the behaviour of torrefied material as hydrophobic nature which has the resistance to absorb water. Thus, it is expected that the moisture content within the material has lower value for this purpose. As the temperature increases, more moisture can be removed from the torrefied material.

According to Herlina [6], the volatile matter indicates the by-product of torrefaction which includes non-condensable and condensable gases. High values of volatile matter are a result of high number of functional groups and low number of aromatic structures in organic materials. High volatile charcoal may be easy to ignite but it burns with heavy smoke. In addition, with high volatility, the material commonly will be less friable than ordinary material with low volatile matter. Devolutilisation occurs at temperature of 150 ℃ to 220 ℃. The volatile matter should exhibit low value for it to be more friable. In addition, rate of volatile matter removal increases as temperature increases.

Apart from that, the fixed carbon content increases as heating process takes place and the value also increases at higher temperature. High fixed carbon content illustrates high heating capacity as discussed before. As the temperature increases, more volatile matter is being discharged to the environment which leads to a higher amount of carbon left in the torrefied product. However, the increase is very slight. As referred to Herlina [6], the fixed carbon should illustrate high content for torrefied materials. The fixed carbon content induces high calorific value and hence contributes to become potential fossil fuels for its high energy content. Normally, the carbonization for torrefaction occurs at temperature between 250 ℃ to 300 ℃.

From the composition analysis done using CHNS Analyzer, the percentage of carbon content determined for torrefied material at 280 ℃ is 48.19%, while the fixed carbon analyzed by TGA Analyzer is 36%. Therefore, we can conclude that about 25% of carbon is burnt as volatile hydrocarbon and 75% of total carbon content remains. On the other hand, the percentage of carbon content of torrefied material at 240 ℃, analyzed by CHNS Analyzer is 44.88% while the fixed carbon analyzed by TGA Analyzer is 30%. In total, the remaining carbon content left in the torrefied material is about 67% which is much lower compared to at 280 ℃.

Figure 18 shows the relationship between size and the composition of the torrefied products. The results obtained shows that the moisture and volatile matter content decrease as the sample size decreases while the fixed carbon increases. High surface area of smaller sample size causes the evaporation of water and volatile matter to leave the charcoal quickly and thus, resulting in lower volatile matter in the product and higher fixed carbon content. This is due to the decrease in Oxygen/Carbon and Hydrogen/Carbon ratio. However, the changes are not so much that the amounts of those three components are almost equal for different sizes of material.

For the torrefied material with size of 500 μm, the CHNS Analyzer gives carbon content of 44.2% while the TGA Analyzer gives fixed carbon value of 33%. This shows that the remaining carbon left is about 75% while the rest is burnt as volatile hydrocarbon. In comparison, the torrefied material with size of 250 μm also has carbon content left of 75%. This proves that the particle size of the sample does not give much effect to the torrefied material.

4. CONCLUSION

It is observed that temperature, particle size, and residence time do affect the physical and chemical characteristics of the torrefied products. Almost 100% of the calorific value in all the samples can be retained or increased by up to 10% from the original waste calorific value. From the Thermo Gravimetric Analysis (TGA), rubber seed kernels exhibited high fixed carbon region

at the respective temperature. At the optimum condition of temperature 280℃ and particle size of 0.025 mm, the torrefied material produced is viable to be promoted at a larger scale.

5. REFERENCES

1. Dewi Soraya. "*Torrefied Biomass Waste as Alternative Replacement to Fossil Fuel".* Final Year Project Dissertation, University Technology PETRONAS, Malaysia. 2008

2. A.V. Bridgwater, G.V.C. Peacocke. "*Fast pyrolysis processes for biomass"*. Renew. Sust. Energy Rev. 4(1): 1-73, 2000

3. E. Natarajan, A. Nordin, A.N. Rao. "*Overview of Combustion and Gasification of Rice Husk in Fluidized Bed Reactors*". Biomass and Bioenergy, 14(5): 533-546, 1998

4. J. Arcate. "*New process for torrefied wood manufacturing".* Bioenergy Update. 2(4), 2000

5. J. Bourgeois and J. Doat. "*Proceedings Conference on bioenergy".* Göteborg. Vol.3, 1985

6. M. Herlina. "*Production of Torrefied Materials from Waste Biomass".* Final Year Project Dissertation, University Technology PETRONAS, Malaysia. 2002

7. M. L. Farah Dila. "*Pyrolysis of Biomass for Production of Liquid Fuel".* Final Year Project Dissertation, University Technology PETRONAS, Malaysia. 2008

8. Mark J. Prins, Krzysztof J. Ptasinski, Frans J.J.G. Janssen. "*More efficient biomass gasification via torrefaction".* Energy, 31: 3458-3470. 2006

9. R. Zanzi, D. Tito Ferro2, A. Torres3, P. Beaton Soler2, E. Björnbom. "*Biomass torrefaction"*. http://hem.fyristorg.com/zanzi/paper/zanziV2A-17.pdf , Royal Institute of Technology (KTH), Stockholm, Sweden. 1989

10. Alberto J. Tsamba, Weihong Yang, Wlodzimierz Blasiak. "*Pyrolysis characteristics and global kinetics of coconut and cashew nut shells"*. Fuel Process Technology, 87(6): 523-530. 2006

11. A.S. Ramadhas, S. Jayaraj, C. Muraleedharan. "*Characterization and effect of using rubber seed oil as fuel in the compression ignition engines"*. Renewable Energy, 30(5): 795-803, 2005

12. A.S. Ramadhas, S. Jayaraj, C. Muraleedharan. "*Dual fuel mode operation in diesel engines using renewable fuels: Rubber seed oil and coir-pith producer gas"*. Renewable Energy, 33(9): 2077-2083, 2008

13. B.V. Babu, A.S. Chaurasia. "*Modeling, simulation and estimation of optimum parameters in pyrolysis of biomass"*. Energy Conversion Management, 44(13): 2135-2158, 2003

14. A.V. Bridgwater, G.V.C. Peacocke. "*Fast pyrolysis processes for biomass"*. Renewable Sustainability Energy Revision. 4(1): 1-73, 2000

15. Ersan Pu¨tu¨n , Funda Ates, Ays_e Eren Pu¨tu. « *Catalytic pyrolysis of biomass in inert and steam atmospheres"*. Fuel 87(6): 815-824, 2008

16. F. Fonseca Felfli, C. Luengo, G. Bezzon and P. Beaton. "*Bench unit for biomass residues torrefaction".* In Proceedings of Conference on Biomass for Energy and Industry. Würzburg, Germany. 1998

17. Joe¨l Blin, Ghislaine Volle, Philippe Girard, Tony Bridgwater, Dietrich Meier, *Biodegradability of biomass pyrolysis oils: Comparison to conventional petroleum fuels and alternatives fuels in current use*. Fuel. 86(17-18): 2679-2686. 2007

18. Mohamad K.M. Sabil. "*Study on the Production of Charcoal by Carbonization Using Mangrove Wood in Malaysia*". In Proceedings of Second Engineering Congression Engineering Innovation and Sustainability: Global Challenges and Issues. Sarawak, Malaysia. 2002

19. S.S. Alves, Figuereido. "*A model for pyrolysis for wet wood*". Chemical Engineering Science, 44(12): 2861-2869, 1989

20. Patrick C.A. Bergman, Jacob H.A. Kiel. "*Torrefaction for Biomass Upgrading".* In Proceedings of 14th. European Biomass Conference & Exhibition. Paris, France. 2005

21. Malaysian Rubber Review Third Quarterly Industrial Report 2006

22. International Energy Outlook 2007

23. http://library.thinkquest.org/11226/why.htm [retrieved on 11th March 2008]

24. http://en.wikipedia.org/wiki/Carbon_cycle [retrieved on 12th March 2008]

25. http://en.wikipedia.org/wiki/Kyoto_Protocol [retrieved on 12th March 2008]

26. http://unfccc.int/kyoto_protocol/items/2830.php [retrieved on 12th March 2008]

27. http://en.wikipedia.org/wiki/Biofuel [retrieved on 9th March 2008]

28. http://en.wikipedia.org/wiki/Second_generation_biofuels [retrieved on 9th March 2008]

29. http://www.cpeo.org/techtree/ttdescript/pyrols.htm [retrieved on 9th March 2008]

30. http://www.bioenergywiki.net/index.php/Pyrolysis [retrieved on 11th March 2008]

31. http://www.btgworld.com/technologies/pyrolysis.html [retrieved on 9th March 2008]

An improved mathematical model for assessing the performance of the SDHW systems

Imad A. Khatib imadk@ppu.edu
Renewable Energy and Environment Research Unit
Palestine Polytechnic University
Hebron, 19000, Palestinian Authority

Moh'd Awad mohdawad@ppu.edu
Renewable Energy and Environment Research Unit
Palestine Polytechnic University
Hebron, 19000, Palestinian Authority

Kathem Osaily kazema@ppu.edu
Renewable Energy and Environment Research Unit
Palestine Polytechnic University
Hebron, 19000, Palestinian Authority

Abstract

Short term testing of the SDHW system components is an essential prerequisite for assessing the system's long-term thermal performance. Relevant performance parameters are therefore, crucial in recommending systems outputs and feasibility. Short term testing methods based on ANSI/ASHRAE and ISO standards testing methods and the mathematical system energy input/output models used showed sensitivity to variation of the day length used in testing and to different levels of irradiance. On the bases of the thermal performance testing carried out for a SDHW system and the outcomes of the day-by-day long-term performance prediction, a new mathematical system energy model is proposed which may reduce the number of tests required, minimizes the dependency on the day length and the sensitivity of the levels of irradiance.

Keywords: SDHW Systems, Performance Testing, Long-Term Performance Prediction, Energy Input/output System Equation model.

1. INTRODUCTION

The potential of utilizing solar energy in Palestinian areas is so promising. Since the 1970s people began to use solar energy for heating water for domestic uses and after 36 years; i.e. in 2006, survey studies done by the Palestinian Central Bureau of Statistics [1] indicated that more than 70% of Palestinian dwellings are equipped with solar domestic hot water (SDHW) systems. The SDHW systems are manufactured locally using traditional manufacturing processes that make these products very competitive and feasible when compared to other similar imported products. Until very recently, evaluating the performance of the locally manufactured SDHW systems could not be realized as there exists no official standards institute to regulate the process, and even after the establishment of the Palestinian Standards Institution (PSI) until recently the relevant standards for testing the performance of the SDHW systems are inactive.

The establishment of the Renewable Energy and Environment Research Unit (REERU) at the Palestine Polytechnic University and its involvement in a multilateral project funded by the US-Citizen Exchange Program of the Department of State entails its cooperation with the Florida Solar Energy Center (FSEC) of the University of Central Florida and a consortium of universities in the Middle East. The outcome of the cooperation is the establishment of the solar energy testing facility at REERU and strengthening the required human capacity. Through cooperation among REERU, the Palestinian Standards Institute and the Ministry of Higher Education, REERU was assigned to evaluate the performance of the locally produced SDHW systems and to validate a standard performance testing procedure that enables understanding, predicting and comparing the performance of the different SDHW systems.

2. TESTING SDHW SYSTEM'S COMPONENTS

The SDHW system used is a thermo-siphon integrated two flat-plate collectors tested with a thermal storage tank in an open cycle. The thermal storage tank capacity is 126-Liters. Each collector is having an aperture area of 1.42m^2. The collector housing is made of galvanized steel with 30mm polyurethane insulation separating the housing from the flow risers and headers tubes that are made of iron. The absorber plate is made of black steel and above it are transparent glass plates. This configuration is usually used in all locally manufactured flat plate solar collectors. The storage tank core is non-enameled made of 4mm steel sheets insulated from the housing with 50mm polyurethane and it withstands a maximum attainable pressure of 12bar. The collector housing is made of a 0.4mm galvanized steel sheet.

Both the flat plate collectors and the storage tank were tested under transient conditions in accordance with ANSI/ASHRAE 93-2003 [2] and ISO 1995 [3] standards testing procedures and methods.

2.1. TESTING FLAT-PLATE SOLAR COLLECTORS

The method used to test the collectors operating with constant flow rate is the steady-state method. The method was first proposed by Hill and Kausuda [4], and later published in ASHRAE standard [5] and ISO 1995 [3]. The steady state testing method depends on measuring the instantaneous collector efficiency over a range of operating temperature. The data collected should correspond to stationary conditions over a period of 15 to 20 minutes. A straight line presentation is then plotted using the relationship:

$$\eta = \eta_o - UT^* \quad (1)$$

Where the reduced temperature difference T^* is computed using Eq. 2:

$$T^* = (T_m - T_a) / G_T \quad (2)$$

And T_m is the mean plate operating temperature, i.e.

$$T_m = (T_i + T_e) / 2 \quad (3)$$

The slope in Eq. 1 represents the collector heat loss coefficient; U and the intercept with the Y-axis (η_o) is the collector zero loss efficiency or the optical efficiency. For each testing point, the energy output of the collectors is calculated as:

$$Q_{out} = m_c \, c_P \, (T_e - T_i) \quad (4)$$

and the energy input as

$$Q_{in} = G_T \, A_C \quad (5)$$

The resulting of instantaneous efficiency η represented by the ratio of the output to the input (Q_{out}/Q_{in}) is plotted versus the reduced temperature difference T^* in the straight line presentation of Fig. 1, which represents the collector performance.

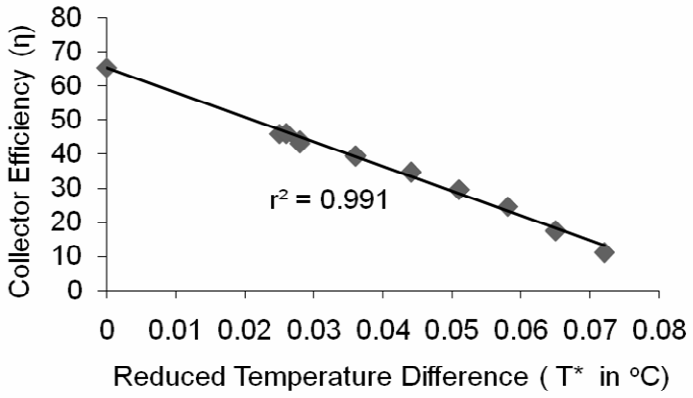

FIGURE 1: Solar collector testing results.

The results showed that the collectors have an optical efficiency (η_o) of 65%, which agrees well with optical efficiency values for similar collector types, and have a heat loss coefficient (U) of 7.2 $W/m^{2o}C$.

2.2. TESTING THERMAL STORAGE TANK

The thermal storage tank performance test is carried out to determine the storage heat loss coefficient UA_S. The test method is described in ASHRAE 93-2003. In this test, the storage tank is charged to a temperature 61.7 ^oC attained using the solar collectors and allowed to cool for 48 hours. During charging, no fluid is added to or extracted from the system. Hourly measurement is performed for the storage temperature and the ambient air temperature where the test is conducted.

By assuming a fully mixed storage losing heat to ambient temperature of T_a it is possible to integrate the storage tank energy balance equation (Eq. 6) over the test duration; i.e. *t* in seconds to compute the storage heat loss coefficient as in Eq. 7, i.e.

$$M_s\, c_p\, T_s = UA_s\, (T_a - T_s) \quad (6)$$

$$UA_s = -1/t\; M_s\, c_p\, \ln\{1-(T_{sf} - T_{si}) / (T_a - T_{si})\} \quad (7)$$

A plot (Fig. 2) showing the store temperature decrease over the testing time constitutes an indicator of the thermal storage performance.

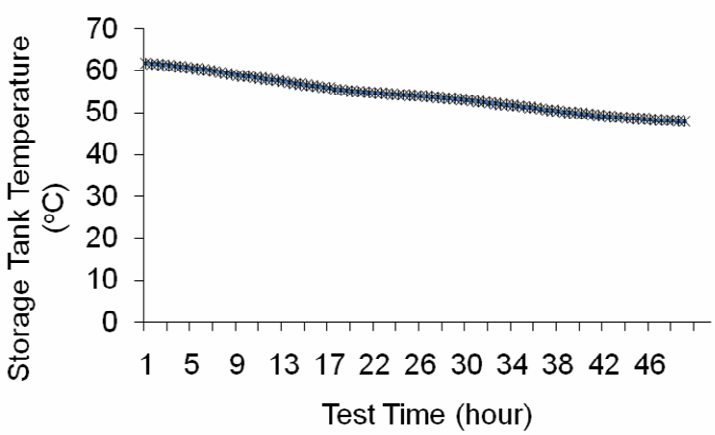

FIGURE 2: Storage tank temperature trend over the 48 hours.

The storage tank heat loss coefficient UA_S was computed at 1.42 W^oC^{-1}, a value considered relatively good for such thermal storage. However, in order to improve the thermal storage performance better insulation may be used including enameling the core of the storage tank.

2.3. TESTING IN SITU THE SDHW SYSTEM

It is clear that the ISO 9459-2 standard testing method is based on the European CSTG method [6]. The method assumes that for a fixed system and a fixed load, where there is little or no carry-over of energy from one day to the next, the climatic parameters which significantly affect daily system performance are:

- the daily solar irradiance on the plane of the collector H,
- the average ambient air temperature T_a during day time, and
- main cold water temperature supplied to the system T_C.

A correlation between these parameter is assumed which represents an approximate linear relationship between the solar irradiance and the system output which takes the form in Eq. 8:

$$Q_{out} = a_1 H + a_2(T_a - T_c) + a_3 \quad (8)$$

The correlation expressed in Eq. (8) forms the basis of the test method where, from results of several tests employing different values of H, T_a and T_c, the values a_1, a_2 and a_3 can be determined using a multi-regression fit method. It is worth mentioning that a_1 represent the irradiance part of the model equation, a_2 is the part of the energy lost or gained from the temperature difference and a_3 is the balance coefficient.

The test procedure carried out consists of one day tests which are independent of each other. For each test the system is first preconditioned bringing the store temperature to the cold water temperature. During that time collectors are covered to ensure no heat gained by solar radiation. The circulation of water through the store is stopped after ensuring that the temperature in the store is uniformly distributed. The system then charges by taking off the collectors' cover and exposing them to sun rays. Immediately after the charge phase a single draw-off of three times the store volume is performed in order to ensure that there was no carryover of energy to the next day.

The test is repeated over several days constituting different values of irradiance levels, ambient air temperatures, and mains water temperatures. During the course of each test the irradiance is measured over the plans of the collectors. And during the charging phase, hourly measurements are performed for the ambient air temperature, and the store temperature. The temperature difference between the outlet and the inlet to the store is also recorded over a time increment of 60 seconds.

The test is performed using an average flow rate of draw-off that is recommended by the testing method, which is 600 Liter/hour. The data obtained from the different tests are used in the mathematical thermal model equation (Eq. 8) and by using a multi-regression method the mathematical model coefficients a_1, a_2 and a_3 are identified for the different levels of irradiances (Table 1).

Irradiance Level	a1 (m^2)	a2 (MJ/K.day)	a3 (MJ/day)
Low	0.56	0.26	0.60
Medium	0.53	2.11	4.02
High	1.01	1.19	3.72

TABLE 1: Mathematical model constants (a-parameters).

The values of the model constants $a_1 - a_3$ are used then in predicting the long-term performance of the SDHW system.

2.4. SYSTEM DRAW-OFF TEST

The performance of the SDHW system depends on the internal operation of its component. One of the most influential parts of the SDHW system is the thermal storage tank. During extraction of energy the type of the store is dependent on the flow rate. The stratification will decrease with increase in the flow rate through the store due to increase in mixing between mains cold water entering the store and the hot water inside the store.

The system under test showed that its vertical storage tank type tends to be fully mixed during the energy charging phase. During extraction of energy the store appears to be stratified. The stratification increase with the increase in the energy input. In Fig. 3 below are the three curves showing different draw-offs under different irradiance levels. It could be seen that the discharged heat (Q_{out}) is proportional to the area under the curve.

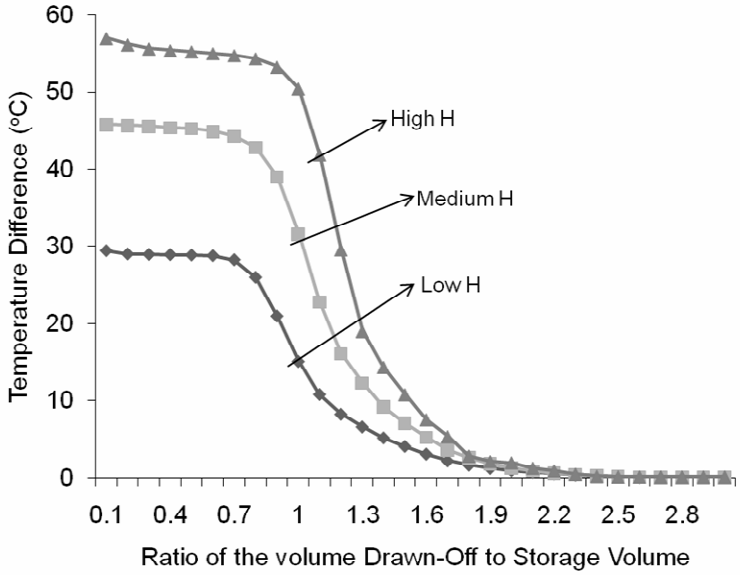

FIGURE 3: Draw-off curves for the different irradiance levels.

The draw-off curves that represent the energy output of the system when drawing 3 times its volume, could be used to measure the energy output from the system and the energy left over in the system by assigning the draw-off energy fraction f(v). By knowing the demand water volume that would be drawn-off (extracted) from the system, the fraction f(v) could be calculated. In this test a demand water volume of 150 Liter/day is considered, which constitute 1.19 times the tank volume of 126 Liter. Using the draw-off curves for the

different levels of irradiance, the different values of f(v) could be calculated as shown in Table 2. The same table shows the fraction of energy when extracting the same tank volume of 126 Liter.

Irradiance Level	f(v) for 150 Liter	f(v) for 126 Liter
Low	0.78	0.66
Medium	0.79	0.68
High	0.84	0.72

TABLE 1: Values of the fraction f(v) calculated for different levels of Irradiance.

2.4. SYSTEM MIXING TEST

While the draw-off profile represents the effect of temperature stratification in the storage tank, and mixing during discharging the system, there is a need to determine the effect of mixing during draw-off independent of the temperature stratification inside the store. This is achieved by discharging the system after establishing a uniform temperature distribution inside the store, and by using the same flow rate utilized in draw-off profiles.

The resulting mixing profile can be seen in Fig. 4. It is seen that after consuming a volume equals to store volume (i.e. 126 Liter), the fraction of energy extracted g(v) is approximately 0.86 of the total energy withdrawn, and 0.90 of the total energy is for a demand load of 150 Liter.

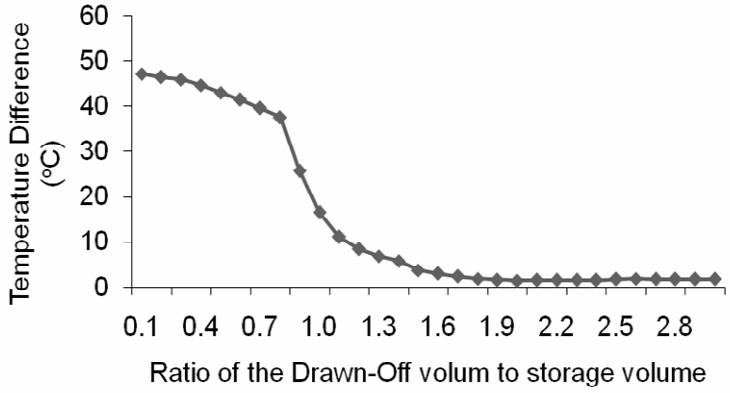

FIGURE 4: Mixing profile.

3. LONG-TERM SYSTEM PERFORMANCE PREDICTION

Long term performance prediction of the SDHW system is computed using a Day-by-Day method described in the European CSTG documents and later adopted by the ASHRAE 93-2003. The method requires several parameters to be pre-identified, i.e. those identified in the short-tem tests, as well as the dominant meteorological settings (or any other setting) for the location where the system is going to be installed. In addition daily mains cold water temperature recorded or calculated is considered essential for consistent calculations. In this respect, the British Standards (BS 5918) of 1982 [7] referenced a correlation for computing mains cold water temperature. This correlation was later modified to suit the Palestine climate and is written in the form:

$$T_c = 18 - 5.5 \times \cos((2 \times \pi / 365.5) \times (D + 11.25)) \quad (9)$$

For the long-term calculation, the annual climate data used is taken from the Meteorological Station of the Renewable Energy and Environment Research Unit (REERU).The weather station records values on time increment of 15 minutes and store them for each year.

The Day-by-Day method calculate the performance of the SDHW system for each day using the input meteorological values of that day, and taking into account any energy in the system that is carried over from the previous day. The method assumes that if the water in the storage tank is at a temperature higher than the cold water temperature at the beginning of the day, due to carry-over of energy from the previous day, this energy is equally spread over the tank volume at start of the next day (i.e. the storage tank is always in a fully mixed state with a uniform temperature at the start of each day).

The total energy captured by the first operating day is given by the Input\Output diagram. The draw-off temperature profile enables the division of this amount of energy into useful energy extracted during draw-off and energy carried over through using the fraction f(v).

The energy remaining in the storage tank will partly be lost overnight due to heat losses , and will force the system to start the next morning at a temperature higher than the cold supply temperature. At this stage, and for each of following days, the assumption mentioned before is made so that the energy is uniformly distributed over the store, leading to a uniform temperature at the beginning of the next day.

At the end of the second day and all the following days the system output can be calculated using the morning store temperature. A division is made in used and remaining energy using the draw-off profile f(v). This energy output represent only a part of the total energy output, as the system refilled with water at temperature T_c and not the morning store temperature. The division of the second part of the extracted and remaining energies is made based on the mixing-profile g(v). And so forth, the calculation is performed day-by-day, for each month and for the whole year. The output are the solar fraction for each month of the year (f_m), the yearly solar fraction (f), the energy output from the system and the energy delivered to the system.

3.1. LONG-TERM PREDICTION RESULTS

The system coefficients a_1, a_2 and a_3 computed are used in three consecutive model runs to predict the annual system performance. The annual delivered energy Q_{out}, which is the sum of the daily delivered energy, was calculated using a fixed demand volume of 150 Liters, and a demand temperature of 60 ^oC was chosen for the calculation.

The results of the annual performance prediction using the day-by-day performance prediction method is seen in Fig. 5 where both energy delivered to the SDHW system and energy extracted for each month of the year considered are presented in histograms.

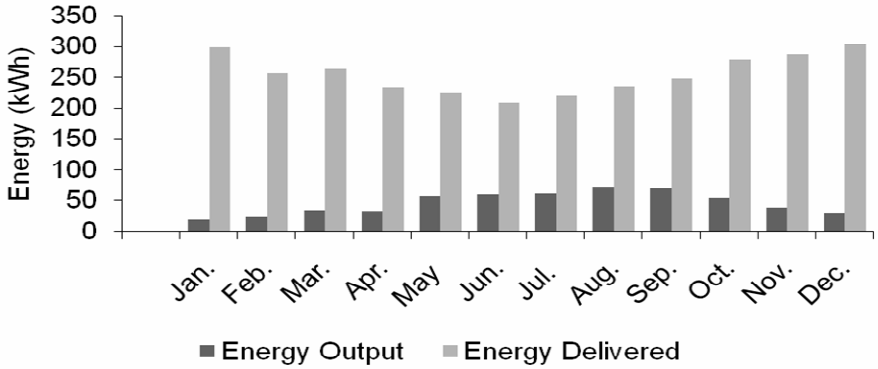

FIGURE 5: Histogram showing monthly variations between energy output and energy delivered.

The annaul solar fraction was computed at 0.18 which means in economic words an annual saving of more than US$120 and a payback period for the SDHW system of 6-7 years.

It should be mentioned here that the mathematical input/output model (Eq. 8) showed high sensitivity for the day length and the variation in the level of irradiance.

3.2. RECOMMEDNED MODIFIED MATHEMATICAL MODLE

The sub-task E of the International Energy Agency (IEA) has suggested a stationary model for the short-term testing of the SDHW systems [8]. The model was called the c-model that identifies 5 parameters, reduce the testing time and provide more variability of test data. The correlation model expressed in the form:

$$Q_{out}\,(1+c_3c_4\delta t / (M_L\,c_p)) = c_1\,\Sigma\,(G_T\,K_{\alpha\tau} - c_2\,\{T_c - T_a + c_4\,Q_{out} / (M_L\,c_p)\})^{+}\,\Delta t - c_3\,\delta t\,(T_c - T_a) - c_5\,\delta t\,(T_D - T_a) \quad (10)$$

The coefficient $c_1 - c_5$ are system parameters that can be identified by a best fit to test data. It is worth mentioning that the last term of Eq. 10 accounts for thermal auxiliary source during testing and hence for real testing the term could be excluded; i.e. c_5 accounts to zero. Marshall et al. [9] have added a term to Eq. 10 that accounts for carryover of energy, changing the model from stationary to non-stationary model as in Eq. 11:

$$Q_{out}\,(1+c_3c_4\delta t / (M_L\,c_p)) = c_1\,\Sigma\,(G_T\,K_{\alpha\tau} - c_2\,\{T_c - T_a + c_4\,Q_{out} / (M_L\,c_p)\})^{+}\,\Delta t - c_3\,\delta t\,(T_c - T_a) - M_s\,c_p\,\delta t\,(T_s^{n+1} - T_s^{n}) \quad (11)$$

Where, T_s^{n+1} and T_s^{n} are the store temperature at end of the test day and at the beginning of the test day respectively.

Eq. 11 could be written in terms of energy output (Q_{out}) as:

$$Q_{out} = c_1\Sigma(G_T - c_2\,\{T_c - T_a + c_4\,Q_{out} / (M_L\,c_p)\})^{+}\,\Delta t - c_3\,\delta t\,(T_c - T_a) - c_3\,c_4\,\delta t\,Q_{out} / M_L\,c_p) - M_s\,c_p\,(T_s^{n+1} - T_s^{n}) \quad (12)$$

By assuming that all energy is utilizable (the + sign) then the equation should be reduced to:

$$Q_{out}\,(1+(c_1c_2c_4 / M_L\,c_p)\Sigma\Delta t + c_3c_4\,\delta t / M_L\,c_p) = c_1\,\Sigma G_T\,\Delta t - c_1c_2\,(T_c - T_a)\Sigma\Delta t - c_3\,\delta t\,(T_c - T_a) - M_s\,c_p\,(T_s^{n+1} - T_n^{n}) \quad (13)$$

Or

$$Q_{out} = [c_1 / (1+d+e)]H + [c_1c_2\,\Sigma\Delta t + c_3\delta t\ / (1+d+e)]\,(T_a - T_c) + [-1 / (1+d+e)]\,\Delta Q_{store} \quad (14)$$

Assuming that the values:

$d = (c_1c_2c_4 / M_L\,c_p)\,\Sigma\,\Delta t$

$e = c_3c_4\,\delta t / M_L\,c_p$

$\Delta Q_{store} = M_s\,c_p\,(T_s^{n+1} - T_s^{n})$

Comparing the model Eq. 14 with the model Eq. 8 showed that the coefficients $a_1 - a_3$ are given by:

$a_1 = c_1 / (1+d+e)$

$a_2 = c_1c_2\,\Sigma\,\delta t + c_3\,t / 1+d+e$

$a_3 = -1 / 1+d+e$

By knowing either $a_1 - a_3$ or $c_1 - c_4$ the other parameters could be identified. This mathematical model assumes one day length and the four c - parameters depend primarily on the SDHW system operation conditions and its performance parameters. Hence, to reduce the sensitivity of the input/output model (Eq. 8) on the day length and the irradiance levels it is possible to perform few short-term tests using constant day length and solve the equation to find c-parameters and the corresponding a-parameters for the long-term calculations.

The mathematical model needs to be verified and hence future work will concentrate on testing the model and comparing the results with the previous ones.

4. CONCLUSIONS

Testing the performance of the locally manufactured SDHW system and its components using the ASHRAE 93-2003 and ISO 1995 and combining the resulted performance parameters to the day-by-day long-term performance prediction procedure brought relatively good results. However, it is found that the results of the mathematical input/output model and the testing procedure are sensitive to day length and to irradiance levels. A new mathematical model that is based on the IEA utilizable model and the input/output model used is proposed. It is suggested that the new model may minimizes the dependency of the input/output model on the day length and the irradiance levels.

4. CONSLUSION & FUTURE WORK

5. REFERENCES

1. PCBS "Households energy survey results - April 2008". Palestinian Central Bureau of Statistics, Palestinian Authority, 2008
2. ANSI/ASHRAE Standards 93-2003 "Methods of testing to determine the thermal performance of solar collectors". ASHRAE publication, Atlanta, GA30329, 2003
3. ISO 1995 "Solar heating-domestic water heating systems – part 2: outdoor test method for system performance characterization and yearly performance prediction of solar only systems". Ref. no. ISO 9459-2:1995(E), International Standards Organization, 2995
4. Hill, J.E. and Kausuda, T. "Methods of testing for rating solar collectors based on thermal performance". NBS Report, NBSIR, 74-635, 1974
5. ASHRAE Standards 95-1981 "Methods of testing to determine the thermal performance of solar domestic water heating systems". AHRAE publication, Atlanta, GA30329, 1981
6. European Solar and System Testing Group "Test method for solar water heating systems, Second international draft, Proceedings of the 6th meeting of the European Solar Collector and System Testing Group (CSTG), Joint Research Center, Ispra, Italy, 1987
7. BS 5918 "Code of practice for solar heating systems for domestic hot water". British Standards Institution, London, UK, 1982
8. Spirikl, W. "SDHW short-term test simulation using a utilizability based correlation model". Internal Report to the International Energy Agency (IEA), III-E Document, IEA, 1987
9. Marshall, R. and Barragan, F. A simulation study of the IEA system test procedure". Dept. of Mechanical Engineering and Energy studies, report no. 1440, University of Wales, Cardiff, U, 1988

Modeling and simulation of Microstrip patch array for smart antennas

K.Meena alias Jeyanthi, meena.jeyanthi@gmail.com
Assistant Professor,
PSNA College of Engineering & Technology,
Dindigul, Tamil Nadu, India.

A.P.Kabilan, apkabilan@yahoo.co.in
Principal,
Chetinad College of Engineering & Technology,
Karur, Tamil Nadu, India.

Abstract

The aim of the paper is two fold. One is to design and simulate an antenna array suitable for wireless applications and the other is the design of beamforming algorithm. In this paper, the first module presents the design of multiple microstrip rectangular patch elements suitable for beamforming technique in wireless applications in the range of 1.8 - 2.4 GHz. By designing 1x8 patch array, it is possible to achieve 15 dB gain and 58% more directivity compared to the conventional patches. The second module suggests a NLVFF-RLS algorithm for beamforming technique to concentrate the power in the desired direction and nullify the power in the interferer direction with HPBW of 13°.The results are analyzed for the scanning sector of -60° to 60°. The modeling and simulation of antenna array is computed using Agilent's ADS. The beamforming algorithm is designed in Matlab.

Key words: Adaptive antennas, antenna arrays, microstrip patch, beamforming.

1. INTRODUCTION

The rising importance of wireless communication and multimedia services increasing the efforts to the design and implementation of novel microstrip patch structures from miniaturized electronic circuits to the antenna arrays[2]. The main advantages of microstrip patches are light weight, low cost, planar or conformal and ability of integration with electronic or signal processing circuitry. Microstrip antenna elements radiates efficiently as devices on microstip printed circuit boards. Microstrip antenna array consists of microstrip antenna elements, feed and phasing networks.Designing microstrip structure requires understanding of both mathematical relatives and applications[2].The microstrip array is very reliable since the entire array is one continous piece of copper.

Microstrip patch antenna consists of a radiating patch on one side of a dielectric substrate with a continuous metal layer bonded to the opposite side of the substrate which forms a ground plane. The patch is generally made of conducting material such as copper or gold and can take any possible shape. A patch antenna is a narrowband, wide-beam antenna fabricated by photo etching the antenna element pattern in metal trace on the dielectric substrate shown in figure 1.

1.1 Design of microstrip patch array

The following are the design equations of the single patch[2],
The actual Length of the Patch is,

$$L = \frac{\lambda}{2\sqrt{\varepsilon_r}} \quad (1)$$

Effective relative dielectric permittivity,

$$\varepsilon_{reff} = \frac{\varepsilon_r + 1}{2} + \frac{\varepsilon_r - 1}{2}\left[1 + 12\frac{h}{W}\right]^{-\frac{1}{2}} \quad (2)$$

the effective Length of the Patch is,

$$L_{eff} = \frac{c}{2 f_o \sqrt{\varepsilon_{reff}}} \quad (3)$$

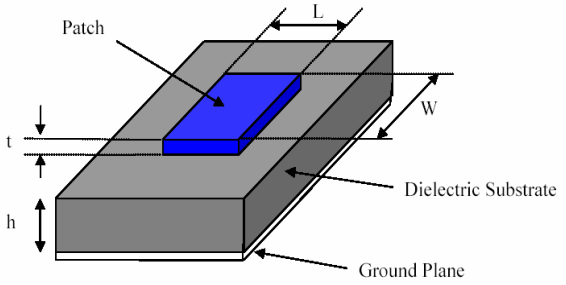

FIGURE 1: Rectanular microstrip antenna element

The Extension Length due to fringing field,

$$\Delta L = 0.412h\frac{\left(\varepsilon_{reff} + 0.3\right)\left(\frac{W}{h} + 0.264\right)}{\left(\varepsilon_{reff} - 0.258\right)\left(\frac{W}{h} + 0.8\right)} \quad (4)$$

The coaxial feed is a very common technique used for feeding microstrip patch antennas as shown in figure 2.

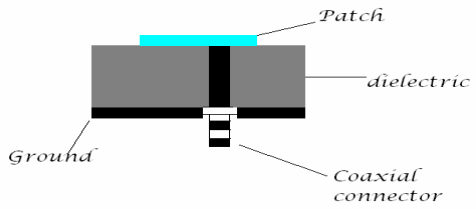

FIGURE 2: side view of element with coaxial feed

1.2 Simulation of single and multiple array

A single patch antenna provides a maximum directive gain of around 6-9 dB. It is relatively easy to print an array of patches on a single (large) substrate using lithographic techniques[2]. Patch arrays can provide much higher gain than a single patch at little additional cost; matching and phase adjustment can be performed with printed microstrip feed structures. The ability to create high gain arrays in a low-profile antenna is one reason that patch arrays are common in all wireless applications[2]. The antenna model is simulated by Agilent's ADS which is a powerful tool in the design of multilayer micostrip antennas. In early days, most of the designers uses graphical tool for the design of antennas[10,11]. Figure 3 shows the return loss of -13 dB for single patch and figure 4 shows the return loss of -18dB for 1x8 patch array for the center

frequency of 1.85GHz. Even the fractal antennas have the S_{11} of -27dB which is comparable with this.[9].Figure 3 & 4 shows the return loss is obtained for the same resonant frequency of 1.85GHz accurately.

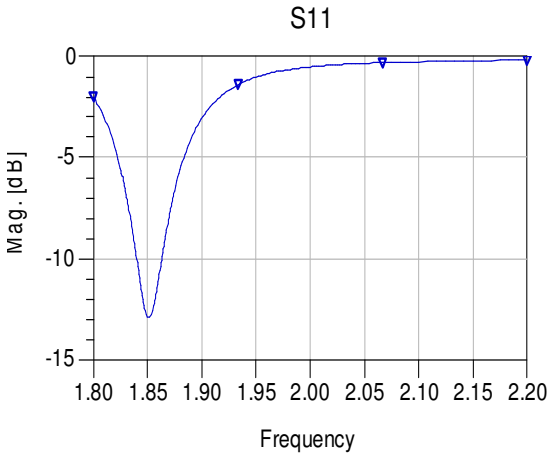

FIGURE 3: Return loss of single patch

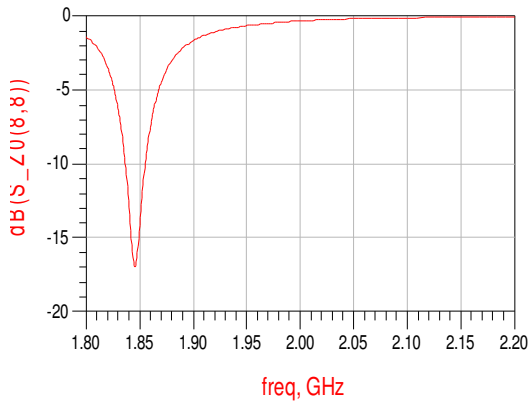

FIGURE 4: return loss of 1x8 elements

2. DESIGN OF ARRAY OF PATCHES

2.1 Substrate selection

It is important to choose a suitable dielectric substrate of appropriate thickness' h' and loss tangent 'δ'. A thicker substrate are mechanically strong, will increase the radiated power, reduce conductor loss and improve the impedance bandwidth[2]. A high loss tangent increases the dielectric loss and therefore reduces antenna efficiency. Here the substrate selected as 1/32in(1.58mm)and loss tangent of 0.024 for the operating frequency ranges from 1.8-2.4GHz.

2.2 Element width and Length

Patch width has a minor effect on the resonant frequency and radiation pattern of the antenna. With the proper excitation, a patch width 'W' greater than the patch length 'L' without exciting undesired modes. The patch width affects the cross polarization characteristics.

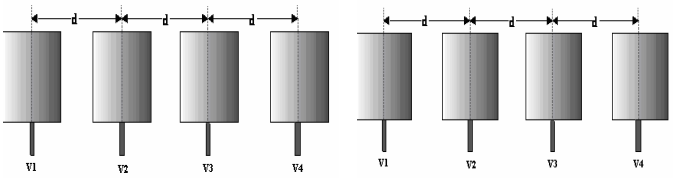

FIGURE 5: Array of 8 patches

In this paper, a broadband rectangular microstrip patch antenna using the permittivity of ε_r of 4.28, log tan δ of 0.024. The length and breadth of the patch is 51.25mm and 40.01mm respectively. The uniform linear array of patches with spacing of 0.5λ are arranged as shown in figure 5.

2.3 Radiation pattern

The radiation pattern of an antenna is prime important in determining most of the characteristics which include beamdwidth,beam shape, sidelobe level, directivity and radiated power. Radiation pattern is computed using method of moments in ADS.

2.4 Beamwidth

The half power beamwidth(HPBW) of an antenna is equal to the angular width between the directions where radiated fields reduced to $1/\sqrt{2}$ times the maximum value.

2.5 Directivity and gain

The directivity is a measure of the directional properties of an antenna compared to the isotropic antenna. Directivity is generally high for array antennas. The gain of the antenna directly depends on the radiation efficiency and the directivity of the antenna[2]. It is observed that directivity increases with increase of substrate thickness and patch width. Conversely, the beamwidth is expected to decrease for higher values of 'h 'and 'W'.

Figure 6 shows the E plane beamwidth of the array. The dimensions and the antenna parameters are tabulated in table 1.

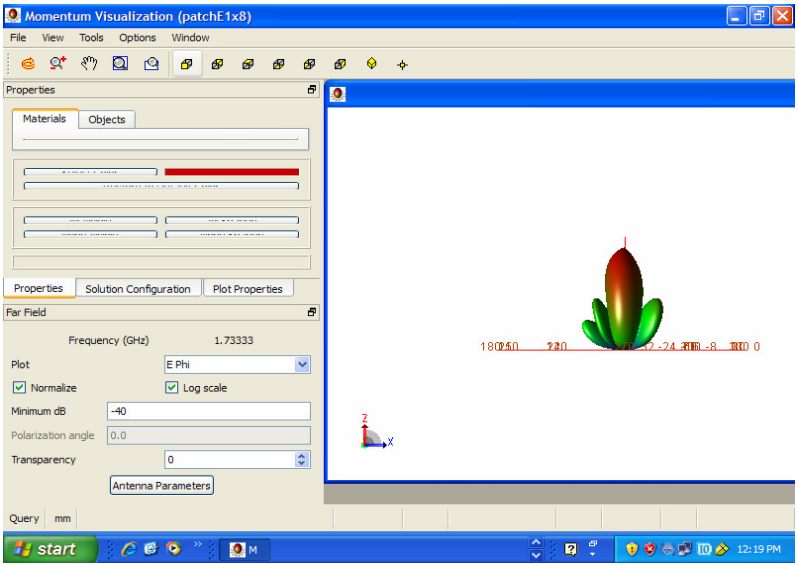

FIGURE 6: Radiation pattern of 1x8 patches

The conventional single patch has the directivity of 7-8dB.But it is observed that the directivity of 1x8 array is improved by 6 dB compared to the single patch. The gain of the array is found to be 15 dB.

Operating frequency(fo)	1.85 GHz	Power radiated(Watts)	0.046
Width of single patch(W)	51.25mm	Effective angle(deg)	0.41 steradian
Length of single patch(L)	40.01mm	Directivity(dB)	14.832
Height	1.5 mm	Gain(dB)	14.8287
No.of elements	8	Intensity(Watts)	0.112
Distance between elements	0.5 λ	E(theta)	81.68
Feed line length	9.5 mm	E(phi)	82.68
Radius of the field	0.5 mm		

Table 1: Antenna parameters

3. SMART ANTENNAS

Smart antennas gain more space in modern wireless communication systems using the important property of spatial filtering[8]. The increasing demand for mobile communication services in a limited RF spectrum motivates the need for better techniques to improve spectrum utilization as well as the development of new high bit rate applications[1]. A smart antenna is an antenna array system aided by some smart algorithm designed to adapt to different signal environments[2]. In this paper our approach is presented by designing an adaptive algorithm using a linear arrangement of rectangular antenna array, with 8 elements, a high degree-of-freedom exists to synthesize very sophisticated radiation patterns[7].

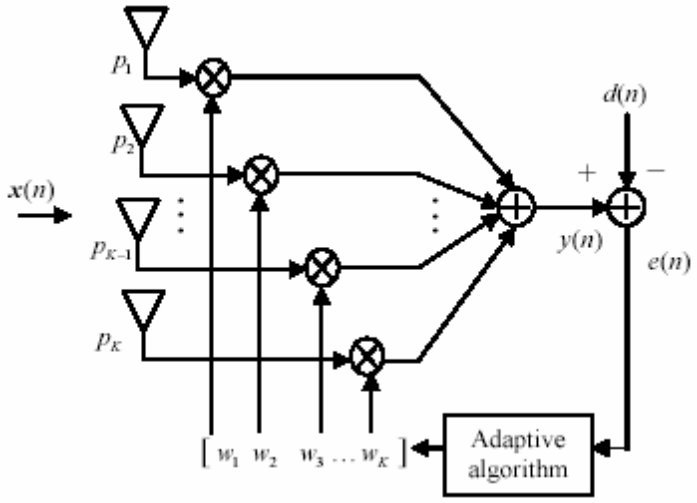

FIGURE 7: Structure of the adaptive array

A linearly arranged and equally spaced array of antenna forms the structure of a beam former. In order to form a beam, each user input signal is multiplied by a set of complex weights and then transmitted from the array to the distant point, the signal emitted from the antennas in the array differ in phase as well as amplitude. If the weights are computed and updated in real time, the process is known as adaptive beam forming [3]. The structure of the adaptive antenna array is shown in figure 7.

Adaptive process permits narrower beam and improving the signal to noise ratio only in the direction of that particular user. This technique drastically reduces the interference in the system. In digital beamforming, the received RF signals are down converted to intermediate frequency (IF) and then digitized by Analog-to-digital converters (ADC). The availability of digital signals enables the use of a considerable number of processing algorithms, because the adaptation can be performed by the controlling software at a lower frequency.

3.1. Non linear variable forgetting factor recursive least squares algorithm (NLVFF-RLS)

The Recursive Least Squares (RLS) algorithm offers an alternative to the LMS algorithm as a tool for the solution of adaptive filtering problems. This algorithm uses the least squares estimate of the tap weight vector of the filter at iteration n-1, to compute the updated estimate of the vector at iteration 'n' upon the arrival of new data. Hence this algorithm is referred as the Recursive Least Squares (RLS) algorithm.
The recursive equation for updating the tap- weight vector is,

$$\bar{W}(n) = W(n-1) + \bar{k}(n)\xi^*(n) \tag{5}$$

$$\xi(n) = d(n) - u^T(n)\bar{W}^*(n-1), \tag{6}$$

is the a priori estimation error.
k(n) is the gain vector. k(n) is expressed as

$$k(n) = \frac{\pi(n)}{\lambda + u^H(n)\pi(n)} \tag{7}$$

The intermediate quantity $\pi(n)$ is computed as

$$\pi(n) = P(n-1)u(n) \tag{8}$$

The inverse correlation matrix is computed as

$$P(n) = \lambda^{-1}P(n-1) - \lambda^{-1}k(n)u^H(n)P(n-1) \tag{9}$$

3.2 Forgetting factor

In the case of non stationary environment, the algorithm[3] uses the forgetting factor λ €(0,1). Here the constant forgetting factor used is λ =0.95.The constant forgetting factor will not produce the optimal performance. Hence the nonlinear variable forgetting factor is preferred. RLS approach leads to higher complexity, but provides a higher speed of convergence and performs better in flat fading channels. The nonlinear forgetting factor can be obtained by error measurements and updating the constant forgetting factor λ non linearly .The optimal filtering gain k should be chosen in such a way that the equalization error is an uncorrelated noise sequence.

$$\lambda_i = \frac{\lambda_{i-1}(1 + u^H(n)P(i-1)u(i-1))}{S_i} \tag{10}$$

where $\lambda^{-1}P(n-1)u_i - k_i S_i = 0,$

This algorithm produces feed back control by updating the gain and forgetting factor λ based on the nonstationary environment.

4. RESULTS AND DISCUSSION

The simulated system consists of an eight element uniform linear array spaced at half wavelength. The operating frequency selected as 1.8GHz. The channel is modeled as additive white Gaussian channel. The received signals are modeled in the base band processing and modulated by MSK (Minimum Shift Keying) signals. The modulated signals are multiplied by steering vectors to simulate array processing technology. Inverse correlation matrix was computed, and the weights are updated.

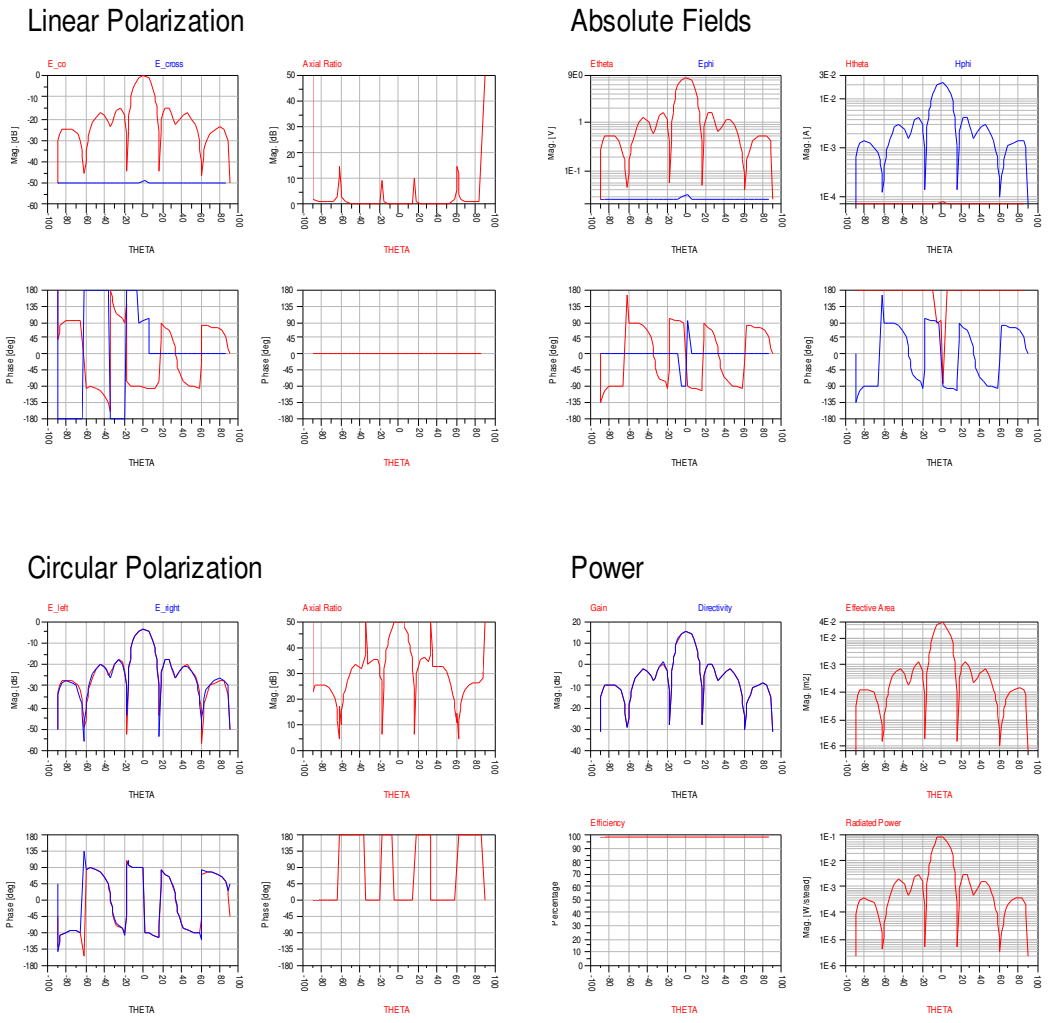

FIGURE 8: Amplitude response of the array

Figure 8 shows the Amplitude response the 1x8 antenna array. Figure 9 shows the power pattern comparison of NLVFF-RLS and RLS algorithm which is scanning efficiently with half power beam width of 13 º for the scanning sector of -60º to 60º . The side lobe level is varying between -14 dB to -18dB which is appreciable value compared to the conventional methods [12].

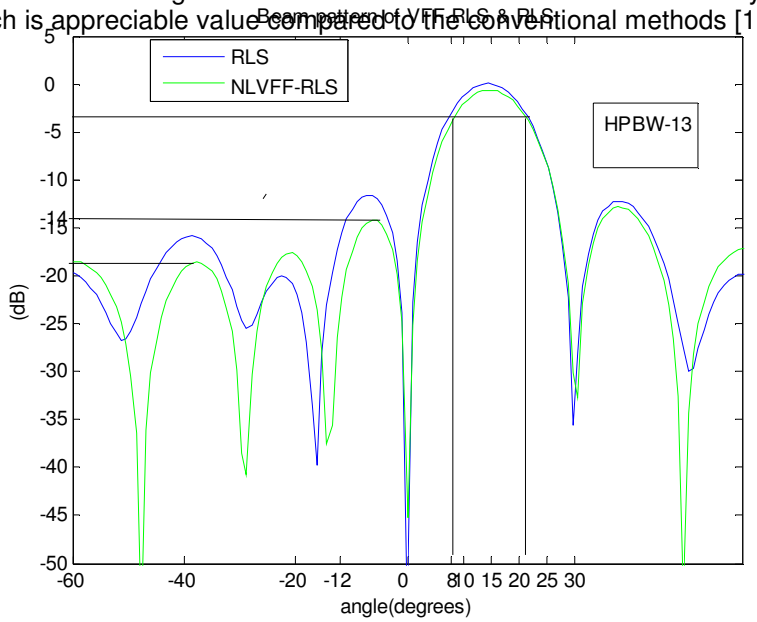

Figure 9: Beam pattern comparison of NLVFF-RLS and RLS

The various parameters are computed for the scanning sector of -60° to 60° are half power beam width(HPBW), null point suppression and compared with the conventional LMS and RLS algorithms are shown in table 2.

Algorithm	HPBW (deg)	SLL (db)	No.of Iter	Null point Supp (db)
LMS	14	12	25	30
RLS	18	14	15	40
NLVFF-RLS	13	14	10	50

Table 2: Comparision of algorithms

4. CONCLUSION

Due to the high cost and complexity of the design for planar and high resolution array, the design focused on the development of uniform linear array antenna. The array designed using method of moments in ADS to obtain the directivity of 14 dB (58% increase compared to the normal patch).The proposed structure uses the spacing 0.5 λ, provides the return loss of 18 dB referenced to the center frequency 1.85 GHz. The second goal is achieved by concentrating the power in the specified direction with a HPBW of 13° in the scan sector of -60° to 60°. Simulation results showed that NLVFF-RLS provides remarkable improvement in null point suppression of 50dB, convergence rate of 10 iterations and minimum mean square error over that of RLS. The

presented algorithm confirms the adaptive antennas are able to sustain a large number of simultaneous communication with respect to directional and switched beam technologies.

5. REFERENCES

1. Simon Haykin, “Adaptive Filter Theory”, Fourth edition n, 2002

2. Ramesh Gharg, Prakash Bhartia, ”Microstrip Antenna design Handbook”, Artech House, 2000

3. Jeffrey H. Reed, ”Software Defined radio”, Pearson education, 2006

4. M.Mukhopadhyay, B.K.Sarkar, ”Augmentation of antijam GPS system using smart antenna with a simple DoA estimation algorithm”, PIER, 67, 231-249,2007.

5. L. J. Griffith and C. W. Jim, “An Alternative Approach to Linearly Constrained Adaptive Beamforming”, *IEEE Trans. AP*, 30(1): 27–34, 1982.

6. K.Meena alias Jeyanthi, Dr.A.P.Kabilan, “A simple adaptive beamforming allgorithm with interference suppression”, International journal of Engineering and Technology, vol.1, N0.1, pp 67-70, April 2009.

7. K.Meena alias Jeyanthi, Dr.A.P.Kabilan, “A NLVFF-RLS approach to adaptive beamforming for wireless communication”, ICCCNET,2008.

8. A.P. Kabilan, P. Elizabeth Caroline, X. Susan Christina, “An optical beamformer for smart antennas in mobile broadband communication”, International journal of mobile communications, vol.7, no.6, pp-683-694, 2009.

9. Niruth Prombutr, Prayoot Akkaraaektharm, ”Analysis and design of Hilbert curve fractal antenna feed with coplanar wave guide for multiband wireless communications”, International Journal of Engineering, volume 2, Issue 3, 2003.

10. Z.Rostamy, “Determination of resonant requency of dominant and higher order modes in thin and thick circular mcrostrip patch antennas with superstrate by MWM”, International journal of Engineering,volume 16, November 2003.

11. M.R. Doushabchizadeh, S. Taromi and A.Radji, ”TV and OR FM transmitting antennas design using computer graphic system”, volume 7, International Journal of Engineering, August 1994.

12. Ali Varahram, Jalil Rashed Mohassel, K.Mafinezhad, ”Optimization of array using modified genetic algorithm”, Vol. 17, No 4, IJE Transactions: Applications, Dec 2004.

CALL FOR PAPERS

International Journal of Engineering (IJE) is devoted in assimilating publications that document development and research results within the broad spectrum of subfields in the engineering sciences. The journal intends to disseminate knowledge in the various disciplines of the engineering field from theoretical, practical and analytical research to physical implications and theoretical or quantitative discussion intended for both academic and industrial progress.

Our intended audiences comprises of scientists, researchers, mathematicians, practicing engineers, among others working in Engineering and welcome them to exchange and share their expertise in their particular disciplines. We also encourage articles, interdisciplinary in nature. The realm of **International Journal of Engineering (IJE)** extends, but not limited, to the following:

- Aerospace Engineering
- Agricultural Engineering
- Biomedical Engineering
- Chemical Engineering
- Civil & Structural Engineering
- Computer Engineering
- Control Systems Engineering
- Education Engineering
- Electrical Engineering
- Electronic Engineering
- Engineering Mathematics
- Engineering Science
- Environmental Engineering
- Fluid Engineering
- Geotechnical Engineering
- Industrial Engineering
- Manufacturing Engineering
- Materials & Technology Engineering
- Mechanical Engineering
- Mineral & Mining Engineering
- Nuclear Engineering
- Optical Engineering
- Petroleum Engineering
- Robotics & Automation Engineering
- Telecommunications Engineering

CFP SCHEDULE

Volume: 4
Issue: 1
Paper Submission: January 31 2010
Author Notification: February 28 2010
Issue Publication: March 2010

CALL FOR EDITORS / REVIEWERS

CSC Journals is in process of appointing Editorial Board Members for ***International Journal of Engineering (IJE)***. CSC Journals would like to invite interested candidates to join **IJE** network of professionals/researchers for the positions of Editor-in-Chief, Associate Editor-in-Chief, Editorial Board Members and Reviewers.

The invitation encourages interested professionals to contribute into CSC research network by joining as a part of editorial board members and reviewers for scientific peer-reviewed journals. All journals use an online, electronic submission process. The Editor is responsible for the timely and substantive output of the journal, including the solicitation of manuscripts, supervision of the peer review process and the final selection of articles for publication. Responsibilities also include implementing the journal's editorial policies, maintaining high professional standards for published content, ensuring the integrity of the journal, guiding manuscripts through the review process, overseeing revisions, and planning special issues along with the editorial team.

A complete list of journals can be found at http://www.cscjournals.org/csc/byjournal.php. Interested candidates may apply for the following positions through http://www.cscjournals.org/csc/login.php.

Please remember that it is through the effort of volunteers such as yourself that CSC Journals continues to grow and flourish. Your help with reviewing the issues written by prospective authors would be very much appreciated.

Feel free to contact us at coordinator@cscjournals.org if you have any queries.

Contact Information

Computer Science Journals Sdn BhD
M-3-19, Plaza Damas Sri Hartamas
50480, Kuala Lumpur MALAYSIA

Phone: +603 6207 1607
+603 2782 6991
Fax: +603 6207 1697

BRANCH OFFICE 1
Suite 5.04 Level 5, 365 Little Collins Street,
MELBOURNE 3000, Victoria, AUSTRALIA

Fax: +613 8677 1132

BRANCH OFFICE 2
Office no. 8, Saad Arcad, DHA Main Bulevard
Lahore, PAKISTAN

EMAIL SUPPORT
Head CSC Press: coordinator@cscjournals.org
CSC Press: cscpress@cscjournals.org
Info: info@cscjournals.org

COMPUTER SCIENCE JOURNALS SDN BHD
M-3-19, PLAZA DAMAS
SRI HARTAMAS
50480, KUALA LUMPUR
MALAYSIA